High Contrast Interferometry and Finite Temperature Coherence of Bose-Einstein Condensates

Christopher Hugh Carson

Experimental Quantum Optics and Photonics
Department of Physics and SUPA

University of Strathclyde

A thesis presented in the fulfilment of the requirements for the degree of

Doctor of Philosophy

March 2015

‘This thesis is the result of the author’s original research. It has been composed by the author and has not been previously submitted for examination which has led to the award of a degree.’

Signed: Date:

To my parents, family and friends.

In memory of Gran and Granny.

Abstract

This thesis outlines the main experimental results of a Bose-Einstein condensate (BEC) interferometer and the finite temperature coherence of elongated BECs.

Cold atom and BEC-based interferometers take advantage of the wave nature of atoms as they are cooled and can be used for precision measurements of fundamental physics, fundamental constants, rotations and gravitational gradients. The coherence properties of atomic matter-waves are of great interest, in particular phase coherence, which has played an important role in fundamental research involving BEC interferometry. When subject to high cloud aspect ratios, BECs become elongated and exhibited phase fluctuations, which can have a dramatic affect on the performance of matter-wave interferometers.

A brief overview of the history and basic theory of Bose-Einstein condensates is presented as well as introducing the various studies and applications in metrology involving BECs. The theory of the techniques used to create a BEC, such as laser cooling, trapping and evaporation, are discussed along with the dynamics of BECs, matter-wave interference and phase fluctuations.

The experimental chapters describe the various concepts, techniques and mechanisms used to experimentally observe matter-wave interference fringes. The interference fringes are a result of realising two BECs from a double-well potential, which is created using a combination of magnetic and optical potentials, and allowing them to expand and overlap.

The main interferometry results are then discussed, this includes the observation of single-shot interference fringes with contrast $\geq 95\,\%$, which has a strong dependence on the detuning of the imaging beam. Also, a strong dependence on fringe contrast with the focal location of the camera is observed, which can now be clearly attributed to the Talbot effect. This is the first reported observation of the spatial Talbot effect of light interacting with period BEC fringes, revealing the drastic effect it can have on the interference signal.

The major results regarding phase fluctuations in elongated condensates are presented. These include the existence of large regular period phase fluctuations, which should normally be of random phase and size. By dynamically changing the aspect ratio of the condensate during an experimental sequence, a controlled generation and removal of phase fluctuations in a Bose-Einstein condensate is observed, indicating a phase revival.

The thesis concludes by considering potential improvements and future experiments, which could be used towards the experimental implementation of a BEC interferometer.

Acknowledgements

Now to thank all the people who have not only helped me over the past three and a half years, but also made the time during my PhD enjoyable.

The first (and biggest) mention must go to my supervisor Dr. Aidan Arnold, who is responsible for at least 80 % of my knowledge on BECs. Aidan, thank you for agreeing to take me on as your student and your unrelenting patience during the countless visits to your office asking for help with the experiment and Mathematica. Discussions with you always made any issues easier to understand and solve, without this I wouldn't have managed to get through my PhD and I am extremely grateful.

Prof. Erling Riis, thank you for all the useful suggestions during the weekly group meetings, these were invaluable in the lab and stopped me going off on tangents. In moments when nothing was working and no one else knew what to do you always had an idea......which always worked.

My unofficial third supervisor Dr. Paul Griffin, thank you for never complaining about the many times I came into your office and said "Griff, can I borrow you for a minute?" Turns out it was very rarely a minute, but you were always happy to help whenever I was stuck in the lab or needed help or advice, I really appreciated it.

My lab partner Dr. Yueyang Zhai, you started two years into my PhD and saved me from being lonely, was nice having an extra pair of hands. I really appreciate you taking the time to explain any problems I had clearly and share your physics knowledge with me.

My PhD student and Postdoc companions in the Experimental Quantum Optics and Photonics group (EQOAP), thanks for making it such an enjoyable and fun place to work. When I first started there was only a few of us in one office, now there is more than twenty over eight offices, it's a good place to be! The weekly "friendly" football match was always a highlight, sorry for all the moaning! I wish all the luck and success to everyone still at EQOAP: James, Billy, Pedro, Savino, Ivor, Andrew, James, Dylan, Jesus, Vicki, Rachel, Elmar, Bruno, Stuart, Calum, Andrew and Dominic, and to all the past members: Yoann, Jakob, Aline and Chris. It has been a delight getting to

know and working with you guys!

Outside of research I would like to thank my family and friends. Mum and dad, thank you for all the love and support you have given me, not only during my PhD, but through my whole life. I'll never be able to thank you enough and I wouldn't be where I am today without you. My sisters and nephew, thank you for putting up with me and always being there, I couldn't have asked for a better family. My close friends, thank you for always being there for me when times have been tough, both personally and my research. Thanks for keeping my sane by taking my mind off research (probably too often) and helping me relax on my days off, really couldn't have done it without you guys! Finally Hayley, we haven't known each other for too long but already I feel like I've known you for years. You've made me realise that there's much more to life and for that I am forever indebted to you. Who knows what the future holds but I can't wait for us to find out together!

"Physics isn't the most important thing. Love is."

— Richard P. Feynman

Contents

List of Figures

List of Tables

Chapter 1

Introduction

1.1 Is colder better?

To answer this question we must first ask ourselves what it actually means. The fact that we are to able cool elements down, by narrowing the width of the systems velocity distribution, allows us to see remarkable phase transitions in every day life, such as vapour to liquid and then liquid to solid. Extraordinary advances in recent decades have allowed atoms to be cooled, trapped and controlled at ultra low temperatures, which enables phase transitions and quantum phenomena to be observed in cold atom labs around the world. As atomic systems approach zero temperature, macroscopic quantum effects become extremely pronounced and this provides an incredibly powerful tool to explore phase transitions [1, 2], build quantum simulators [3, 4, 5], develop quantum computing [6], test fundamental physics [7, 8] and make precision measurements [9] just to name a few. It has rapidly become apparent that ultracold atoms have the potential to probe and discover phenomena about the quantum world, therefore research in this area has grown dramatically. In this thesis we discuss experiments that take advantage of the condensation of a weakly interacting dilute atomic system at low temperature.

1.2 Condensation of a quantum gas

In quantum mechanics particles can be classed into one of two groups, either bosons, which have integer spin, or fermions, which have half integer spin. These two spin states exhibit different properties. This difference is evident when considering the occupancy of the quantum state. Bosons have no limit to how many can be in the same quantum state, however the Pauli exclusion principle allows only fermion in the same quantum state.

The different restrictions on the number of particles allowed in each state between these two types of particles means that a gas of bosons and a gas of fermions have differing properties at low temperatures. In 1924, Bose and Einstein introduced the first theoretical description of an ensemble of bosonic atoms in the same quantum state [10, 11], this provided the framework for a whole area of physics. In this paper they predicted that if an atomic system of bosons could be cooled to its lowest possible temperature, by minimising the kinetic energy, then the atoms will all condense into the lowest quantum ground state. When this happens one can observe a macroscopic occupation of a single quantum ground state. This phenomenon in which a bosonic ensemble can condense into a single quantum state is known as a Bose-Einstein condensation (BEC) [12, 13].

The phase transition of an ensemble of bosons to a Bose-Einstein condensate occurs when both the temperature and density reach a critical value, at this point the atomic separation between the atoms approaches the de Broglie wavelength. In the simplified picture represented in Figure 1.1, atoms can be considered as quantum-mechanical wavepackets, which have a size on the order of the de Broglie wavelength λ_{dB}. The de Broglie wavelength of the wavepackets is defined as

$$\lambda_{dB} = \frac{\hbar}{\sqrt{2\pi m k_B T}} \ , \tag{1.1}$$

where m is the mass of the particle, k_B is the Boltzmann constant, $\hbar$ is Planck's constant divided by 2π and T is the temperature. At low temperatures (Figure 1.1 a)) $\lambda_{dB} = h/mv \propto T^{-1/2}$, however as the temperature of the wavepackets is decreased the de Broglie wavelength gets longer until it reaches a critical value, at which point λ_{dB} becomes as large as the inter-particle spacing (Figure 1.1 b)). At this point the wavepackets overlap and the atoms become indistinguishable from one another and Bose-Einstein condensation can occur. As the temperature continues to decrease the atoms condense into the same quantum state and form a giant matter wave (Figure 1.1 c)), which can be described by the same wavefunction.

The quantity that is commonly used to describe this phase transition, which is

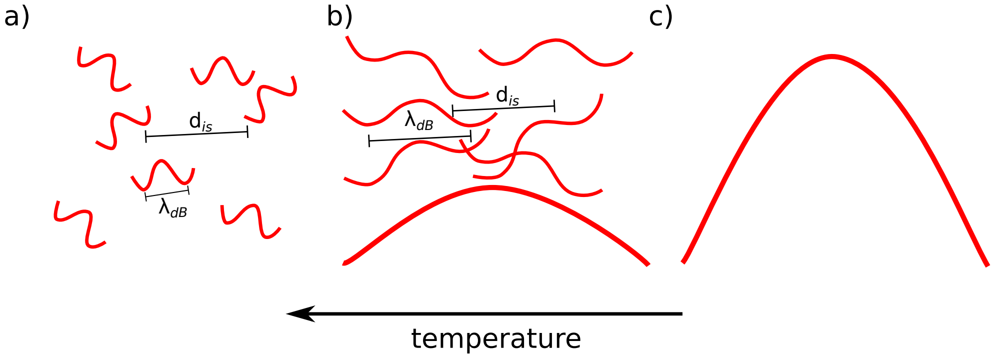

Figure 1.1: De Broglie waves as a function of temperature showing the stages from a thermal gas to a Bose-Einstein condensate. a) Thermal atoms which have a λ_{dB} smaller than the interparticle spacing, d_{is}. b) Close to the BEC transition temperature where the two length scales become comparable and the wavefunctions start to overlap each other. c) All atoms have condensed into the same ground state to form a pure BEC and can be described by the one wavefunction. Figure adapted from [14].

written in terms of the spatial number density and the de Broglie wavelength to give a unitless number, is known as the phase space density (PSD)

$$\mathrm{PSD} = n\lambda_{dB}^3 \ , \tag{1.2}$$

where n is the number density and λ_{dB} is the de Broglie wavelength. From the above equations it can be seen that the phase space density and de Broglie wavelength are both temperature and density dependent, meaning the ideal situation to reach the BEC transition would involve maximising the density and minimising the temperature. As mentioned previously the BEC transition occurs at a very specific temperature known as the critical temperature, which is given by

$$T_C = \frac{\hbar\bar{\omega}}{k_B}\left(\frac{N}{\zeta(3)}\right)^{1/3} \ , \tag{1.3}$$

where $\bar{\omega}$ is the geometric mean of the trapping frequencies $\bar{\omega} = (\omega_x\omega_y\omega_z)^{1/3}$, N is the number of atoms and $\zeta(x)$ is the Riemann Zeta function. The phase space density can also be written in terms of the trapping potential and temperature

$$\mathrm{PSD} = N\left(\frac{\hbar\bar{\omega}}{k_B T}\right)^3 = \zeta(3)\left(\frac{T_C}{T}\right)^3 \ . \tag{1.4}$$

The BEC transition for a three-dimensional harmonic potential occurs when the phase space density PSD=$\zeta(3) = 1.202$ [15] (the critical phase space density changes depending on the trapping potential [16] and is sometimes quoted as $\zeta(3/2) = 2.612$, which is for an ideal Bose gas in a three-dimensional box or a free gas [17]).

If you consider atoms at room temperature that move with velocities of a few hundred metres per second, this corresponds to de Broglie wavelengths of the order of picometres. However, atoms approaching the BEC transition have velocities of the order of millimetres per second, which increases the de Broglie wavelengths to micrometres. The orders of magnitude in phase space densities between room temperature atoms and atoms at the BEC transition has made it a very challenging prospect of experimentally observing such a phase transition since it's first prediction in 1924.

The road to creating a BEC has not been an easy one, many technical problems reared their heads many times, but out of this challenging time many new and vital tools have come about, such as laser cooling [18, 19] and trapping of atoms [20, 21], magneto-optical traps (MOT) [22], magnetic trapping of atoms [23, 24] and evaporative cooling [24, 25]. After over 70 years since it was first predicted, cold atom physicists were rewarded for their hard work and the first ever Bose-Einstein condensate was observed by the research group of Eric Cornell and Carl Wieman at the University of Colorado (JILA) in early June 1995 [26]. Shortly after in September of that year Wolfgang Ketterle's research group at the Massachusetts Institute of Technology (MIT) successfully produced a BEC, which contained 100 times more atoms [27]. For their achievements Cornell, Wieman, and Ketterle received the 2001 Nobel Prize in Physics. It is these experiments and this exotic state of matter that have opened up a whole new world of physics to be explored.

Since the first experimental realisation of a Bose-Einstein condensate in 1995, research in this field has grown dramatically and BECs have been made in many different atomic species including H [28], metastable helium ^{4}He [29, 30], ^{7}Li [31], ^{23}Na [27], ^{39}K[32], ^{40}Ca [33], ^{41}K [34], ^{52}Cr [35], ^{84}Sr [36, 37], ^{85}Rb [38], ^{86}Sr [39], ^{87}Rb [26], ^{88}Sr [40], ^{133}Cs [41], ^{160}Dy [42], ^{162}Dy [42], ^{164}Dy [43], ^{164}Yb [44], ^{168}Er [45], ^{170}Yb [46], ^{174}Yb [47], ^{176}Yb [44], and photons in a cavity [48].

Bose-Einstein condensates have also been used for a variety of studies including the ability to tune the interaction strength between particles using Feshbach resonances [49, 50, 51]. Theoretical predictions of the properties of BECs have now been compared with experimental data, such as collective excitations [52, 53, 54] and the formation of vortices [55, 56, 57]. Due to their unique properties, BECs have been used to produce a coherent beam of atoms, a so-called atom laser [58, 59]. BECs have also been observed non-destructively [60] so their formation [61] and the flow of a superfluid can be probed [62, 63]. Another field that has grown since the first observation of a BEC is interferometry [64, 65, 66] and condensates have been used to enhance measurement sensitivity [67].

1.3 Interferometry

Interference was first observed by Thomas Young in 1801 through his famous double slit experiment [68]. This experiment shows that light behaves as a wave. This discovery was as important to physics in the nineteenth century as the quantum field was to physics in the twentieth century. The discovery by Young revolutionised the field of physics and optics and had a crucial hand in the discovery of light as an electromagnetic wave [69]. A short time after it was realised that the interference of light could be used to make very precise measurements. Through the ground-breaking experiments and efforts of Michelson, Morley, Rayleigh, Mach, Zehnder, Fabry and Perot optical interferometers grew and flourished into an important and ever expanding field of research. Interferometers of that period could measure path differences with a precision of the order of one wavelength of light [70].

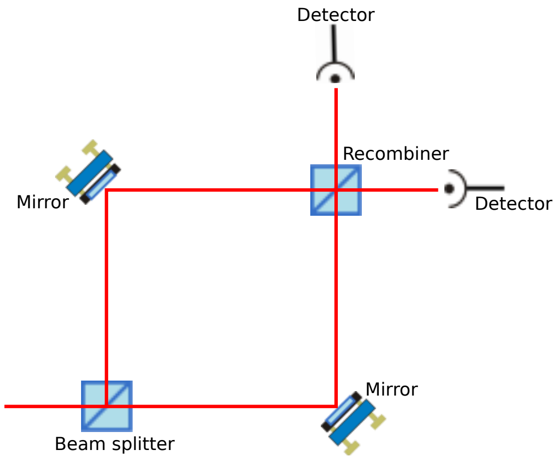

Figure 1.2: Schematic diagram of a Mach-Zender interferometer

Although there are many different types of optical interferometers, they can be split into four different basic groups, Michelson, Mach-Zehnder, Sagnac and Fabry-Perot interferometers. All these interferometers rely on the same basic principles, that is, a incoming beam (single mode) is split into two, the two separate parts are allowed to evolve in time before they are recombined and then any acquired phase difference can be measured.

In 1924, de Broglie proposed in his doctoral dissertation that matter, like light, should behave like a wave [71]. Shortly after the first proposal by de Broglie, electron diffraction experiments showed wave-like phenomena [72, 73]. The first electron interferometer was observed in 1954 [74] and in 1962 a neutron interferometer was experimentally realised [75].

1.3.1 Atom interferometry

Interferometry performed with atoms has many advantages compared to photons or electrons, these include a wider selection of atomic properties, larger cross section for scattering and higher precision [76]. The de Broglie wavelength of thermal atoms are of the order of 30 000 times smaller than wavelengths for visible light, which enables much smaller signals to be detected with increased sensitivity. A wide variety of atomic properties can be chosen, for instance the atomic mass, magnetic moment and polarisability. Furthermore, atoms can be manipulated and controlled by lasers with high levels of precision.

By analogy with its optical counterparts, atom interferometry uses the wave nature of atoms and seeks to exploit wave interference as a tool for precision metrology. The basic principle behind atom interferometry is similar to that of optical interferometry, both can be realised by combining matter waves and light waves. In the case of atom interferometers (schematic shown in Figure 1.3), the atom itself propagates and interferes instead of the light wave, and is coherently split and recombined using light fields. The relative phase is given as the difference in path lengths and determines the output interference signal.

Atom interferometry is still a young area of research. It was first demonstrated in 1991 [77, 78] where periodic potentials of light were used as diffraction gratings. In this method three identical gratings are used, the first acts as a beamsplitter, second as a mirror and third as the second beamsplitter to recombine the atoms. A few months

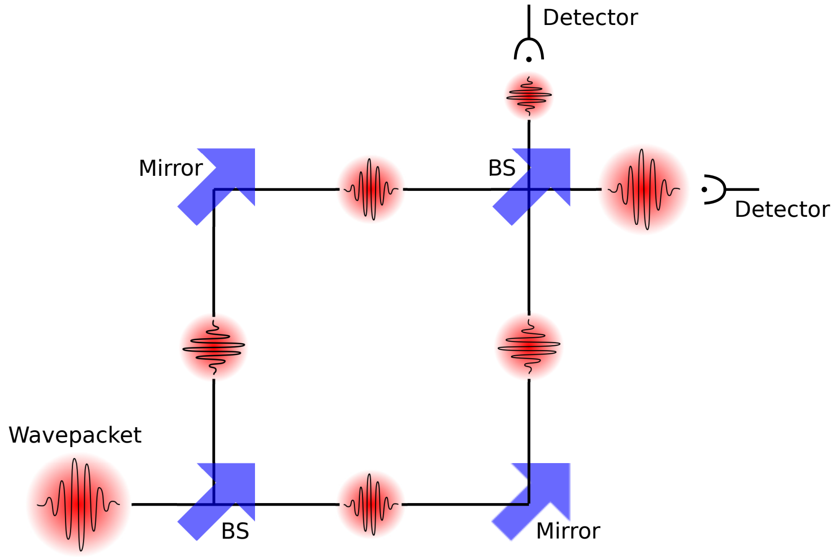

Figure 1.3: Schematic diagram of an atom interferometer, where the atom itself propagates and interferes and light waves (blue arrows) act as beamsplitters (BS) and mirrors. The two atom wavepackets propagate along different paths and if the two paths differ from one another then a phase shift will build up and this can be measured at the detector.

after the first demonstration a second type of atom interferometer was developed using stimulated Raman scattering to control the atoms [79, 80]. This type of interferometer works by applying off-resonant Raman light pulses to transfer momentum onto the atoms and thus split and recombine them.

An atom wave has mass and internal structure, hence the atom can experience potentials from the Earth's gravitational field, magnetic field, electric field and atom-atom interaction. Therefore the atom can accumulate phase shifts due to these fields during the interrogation time of the interferometer. For this reason atom interferometry has been used to provide standards of time, frequency and length [81] and also used for some of the most precise measurements of fundamental constants [82, 83], gravity gradients [84, 85], fundamental physics [86, 87, 88], rotations [89, 90, 91], accelerations [92, 93], quantum decoherence [94] as well as practical uses [95, 96].

1.3.2 Atoms v light

One may ask "why use atoms instead of light?" The Sagnac effect is an example that answers this question and demonstrates the power of atom interferometry [97]. The phase shift for an interferometer of area A, which is rotating with an angular velocity Ω, can be expressed as [98]

$$\Delta\Phi = \frac{4\pi A\Omega}{\lambda v} \ , \tag{1.5}$$

where λ is the wavelength and v is the propagation velocity. If two identical interferometers, which enclose the same area are used, one with atoms and the other photons, then the sensitivity has a ratio of [76]

$$\frac{\Delta\Phi_{\mathrm{atom}}}{\Delta\Phi_{\mathrm{light}}} = \frac{\lambda_{\mathrm{photon}} c}{\lambda_{dB} v_{\mathrm{atom}}} = \frac{mc^2}{\hbar\omega_{\mathrm{light}}} \ . \tag{1.6}$$

The ratio of the energy of atoms ($E = mc^2$) compared to the energy of photons ($E = \hbar\omega$) shows that atoms have the possibility to measure inertial effects and rotations with a much higher precision. For ^{87}Rb and 780 nm light, the sensitivity per particle for atoms can be up to 5 x 10^{10} times larger than that of light [76]. As well as the potential of increased sensitivity, atom interferometers have far fewer atoms than photons and a much smaller area.

1.4 Cold atom or BEC based interferometry

Atom interferometers are essential tools for studying fundamental quantum mechanical phenomena, probing atomic properties and metrology. The next question one may ask is “what are the advantages of using cold atoms or even BECs?” The main reason for using cold atoms instead of hot atoms is the coherence time. For cold atomic ensembles the momentum spread is reduced, which results in a longer coherence time, which in turn leads to a longer interaction and therefore increased phase sensitivity. Using BECs rather than cold atoms in interferometry is similar to the transition from using laser light instead of white light, with all particles in the same mode [99]. However, in using a BEC atom number is sacrificed, therefore reducing sensitivity and the atomic interactions in a BEC cause unwanted phase shifts [76].

In a condensate, a macroscopic matter wave is formed, which means all the atoms are in the same quantum state. Since condensates exhibit large coherence lengths of the order of the condensate size of tens of μm, this means condensates can be thought of as analogous to lasers and thermal atoms (coherence lengths of 0.5 μm near the condensation temperature) are the analogue of white light sources, therefore making interference easy to observe [76]. The atoms in a condensate are so cold and monochromatic that the velocity spread Δv_{BEC} is much smaller than that of thermal atoms, which means they can be manipulated and controlled much more easily. Since the atoms propagate along the same path, they have a stable phase relationship, which leads to long temporal coherence times. The atoms in a BEC can be described by the same wavefunction, therefore over time they will evolve in the same way and every atom will remain in phase and thus be coherent across the whole condensate.

The relatively easy manipulation of BECs leads to translational states being used to separate the arms of an interferometer. In thermal atom interferometers the separation of the arms is normally realised by transferring the atoms into a superposition of internal atomic states [98]. The output is then formed by counting the number of atoms in each state. The atoms are sensitive to the phase of the driving field, so this effect introduces decoherence and limits the interaction time. Due to the precise control possible when using condensates, the separation between the arms can be achieved using translational states.

A major disadvantage when using atom interferometers is further heightened when using condensates. Low production rates can reduce the signal-to-noise ratio of atom interferometers compared to light interferometers, and for condensates the production rates worsen. Typical atom beam interferometers have flux rates of 10^9 particles per second, whereas the best BEC production rates are limited to 10^5 per second [100].

1.4.1 Double-well potential BEC interferometer

The basic principle of a double-well interferometer is a condensate formed in a single-well potential, which is then coherently split into a double-well potential before the trapping potentials are switched off and the two separated BECs are allowed to overlap with one another. In this type of interferometer the trap holding the BEC is continuously deformed into a double-well potential, with each of the two wells containing part of the wavefunction. Coherent splitting of the wavefunction by slowly deforming a single-well into a double-well trap can be thought of as the beam splitter for trapped atoms. The splitting in a double-well interferometer occurs in position space, which is a sharp contrast to to interferometers in which the splitting occurs in momentum space. In this interferometer the two atom waves are always confined and can be separated by moving the two wells apart.

The first experimental realisation of a double-well interferometer was demonstrated in 1997 by the group of Ketterle and Pritchard at MIT [64]. In this experiment the BECs were formed in a double-well potential created by a magnetic trap and a focussed blue-detuned laser beam. This produced two independent BECs, which were initially separated by 40 μm, and when allowed to ballistically expand and overlap with one another an interference pattern was observed. This result confirmed condensates as a good source of coherent matter waves. The second evolution of this experiment was demonstrated in 2004. In this setup a BEC was created in a single-well potential which was then coherently split into a double-well potential [65]. The double-well was created by a collimated laser beam passing through an acousto-optic modulator (AOM), which was driven at two frequencies. This produced two beams that propagate parallel to each other, the separation was controlled by the frequency difference and could achieve a separation of 13 μm with coherence times of 5 ms.

Another method in which a single-well was split into double-well potential on an atom chip using a two-wire scheme [101] was first demonstrated by the group at MIT [66]. The beamsplitter in this setup comprised two parallel wires with the same current and a perpendicular magnetic field. To achieve the splitting the magnetic field is varied and this can transform the single-well into a double-well potential.

The group of Jörg Schmiedmayer demonstrated a third method in which the condensate could be split [102, 103]. In this setup the double-well was created using radio-frequency (RF) induced adiabatic potentials [104] and when the interference fringes from the two condensates combining in time-of-flight were analysed it was determined the splitting was coherent, i.e. the phase was preserved. Using RF induced adiabatic potentials to split the atom cloud overcomes the weak confinement during the splitting and the extreme sensitivity to magnetic field fluctuations present in the two-wire setup. This method to separate the condensates allows control over the separation between the wells and could be used to separate the wells from 2 to 80 μm with coherence times of 2 ms for small separations. The large range of well separations enabled regimes of tunnelling wells and complete isolated sites to be accessed.

In the Strathclyde experiment the single-well potential is transformed into a double-well potential in a scheme very similar to Reference [64]. The BEC is created in a single-well magnetic trap which is then deformed into a double-well using a focused blue-detuned 658 nm laser beam [105]. At the focus the two wells are separated by 40

μm and by varying the power of the blue-detuned beam the separation of the wells can be altered.

1.4.2 Guided-wave BEC interferometer

By combining the concept of optical interferometers that use optical fiber wave guides with the rapid advances in confining, guiding and manipulating atoms, the next logical step is to consider wave guides for atoms and BECs. A wave guide BEC interferometer can be achieved by using a weakly confining magnetic field along the axis and using light pulses, which act as the beamsplitter, mirrors and re-combiner, to manipulate it. In this type of guided wave interferometer the BEC is split into two momentum components. The first experimental observation of a guided-wave BEC interferometer was in the group of Cornell at JILA [106]. This was a Michelson interferometer and had a coherence time of 10 ms. A modification of the Michelson interferometer was built by the group of Sackett [107] and had a coherence time of 44 ms. A third guided-wave BEC interferometer was based on a Mach-Zehnder interferometer and had a coherence time of 15 ms [108].

A toroidal trap acts a circular waveguide for the condensate, which spatially separates the two atom clouds, and benefits from symmetric two-dimensional confinement. The first ring trap for neutral atoms was a magnetic trap developed by the Chapman group [109]. Toroidal traps also have the advantage that since they guide the condensate back to its original position, only splitting and re-combination pulses are needed. Large enclosed areas with compact spatial extent can be achieved by using guided interferometers [110] where the atoms are confined during propagation, as in a ring trap. Phase noise is also reduced by guiding the condensate around the ring due to the Coriolis force, e.g. in gravity measurements [111]. Many different phenomena can be studied in a ring trap, for instance, superfluid properties of a BEC [62], vortex creation and decay [112, 113], atomic SQUIDS [63] and much more.

There are different types of toriodal traps including magnetic ring traps [114, 115], optical ring traps [63, 116] , RF ring traps [116, 117], inductively coupled magnetic trap ring traps [118, 119] and a combination of two different methods [62, 120, 121].

All of the different implementations of the ring trap have their own advantages and disadvantages, for instance magnetic ring traps are normally larger, optical and RF dressed ring traps are tuneable in size and inductively coupled ring traps have no

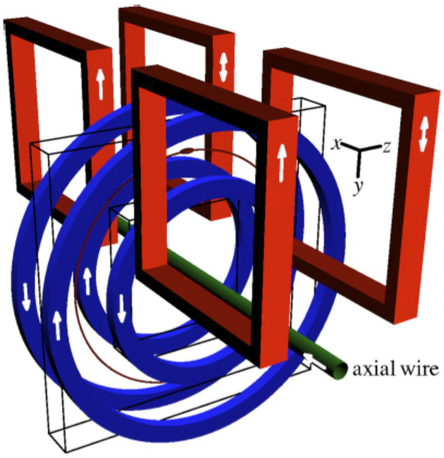

Figure 1.4: Toroidal magnetic storage ring trap for BECs (image from [115]). It shows the four circular current carrying wires, which create a quadrupole field that has a ring-shaped magnetic minimum. The axial wire adds an additional extra azimuthal magnetic field, this removes the zero field from the toroidal quadrupole field and avoids Majorana spin flips.

current carrying wires, so therefore no end effects. Sagnac interferometry is where ring traps come into their own, as free-propagating interferometers use standing waves to split and separate the condensate by the transfer of momentum. This limits the separation of the two arms of the interferometers, hence limiting the sensitivity that can be achieved. Ring traps can overcome this by the fact that the condensate is confined during the propagation and small compact ring traps can have a large enclosed area [107, 110].

The Strathclyde ring trap shown in Figure 1.4 can hold a BEC and has a magnetic lifetime which is 40 times longer than that of the first storage ring [109]. It can also hold 5 x 10^8 atoms and has an enclosed area of 72 cm^2, making it the largest ring trap in the world and has the potential to be used for ultra-sensitive Sagnac interferometry.

1.5 Thesis outline

In this thesis I will discuss the ongoing Bose-Einstein interferometry and finite temperature coherence experiments at Strathclyde and discuss the progress made during the duration of my PhD studies.

In Chapter 2 the theory and techniques used to create a Bose-Einstein condensate will be discussed, mainly laser cooling and trapping, magnetic trapping, evaporation and the dynamics of BECs. Then the concept of interference between condensates and the coherence of BECs at finite temperature will be introduced.

Chapter 3 will review the Strathclyde experimental setup, for instance the lasers and various trap geometries, as well as discussing the experimental parameters.

Chapter 4 gives a brief description on the main methods to create and control the BEC. The main features of the Strathclyde experiment, such as the dipole beam used to split the condensate and the magnetic levitation will be discussed.

Chapter 5 details the main experimental results from the interference of two condensates. It introduces the interference signal's dependence on various experimental parameters, maximum contrast interference, Talbot enhanced interferometry and the lifetime of the interference fringes.

In Chapter 6 the experimental studies of the coherence of BECs in elongated traps will be described and how the Strathclyde experiment allows the trapping potential to be dynamically changed. This feature enables the controlled creation and then removal of phase fluctuations in elongated condensates.

The thesis will conclude in Chapter 7, where the work during my PhD will be summarised and potential future improvements discussed.

Chapter 2

How to make a BEC

2.1 Rubidium

The alkali metals have dominated the laser cooling, trapping and Bose-Einstein condensate community due to their moderately simple energy level structure. Rubidium, like all alkali metals, belongs to the "hydrogen-like" group of atoms due to only having one valence electron and can be easily understood using an adapted hydrogen atom theory. Rubidium occurs naturally in two isotopes, ^{85}Rb with an abundance of 72% and ^{87}Rb with an abundance of 28% [122]. Both these isotopes have slightly different properties, one of these is their nuclear spins, ^{85}Rb has a nuclear spin of $I = 5/2$ whereas ^{87}Rb has a nuclear spin of $I = 3/2$.

Rubidium has two groundstate F hyperfine levels, which is a result of the coupling of the total angular momentum J and the nuclear angular momentum I, and results in a total angular momentum given by $F = I + J$, which can take values $|J - 1| \leq F \leq |J + I|$. The presence of a magnetic field further splits each of the F levels into additional, non degenerate, magnetic sublevels. Each of the hyperfine groundstates splits into $2F + 1$ magnetic sublevels m_F, which can take values of $-F, -F+1, ..., F+1, F$. The excited states are defined depending on the atomic transition, hence in ^{87}Rb the D1 transition at 795 nm has two excited state F levels ($F' = I \pm 1/2$), and the D2 transition at 780 nm has four excited state F levels ($F' = I \pm 1/2, I \pm 3/2$). The two excited states are known as the $5^2\mathrm{P}_{1/2}$ and the $5^2\mathrm{P}_{3/2}$ states and the D1 and D2 lines correspond to the respective transitions to these states from the $5^2\mathrm{S}_{1/2}$ ground state. The Strathclyde BEC is created using ^{87}Rb atoms trapped in the $|F = 2, m_\mathrm{F} = 2\rangle$ ground state, which is achieved using the D2 line which connects the $5^2S_{1/2} \rightarrow 5^2P_{3/2}$ ground and excited states, therefore only the energy level structure for ^{87}Rb ($I = 3/2$) will be presented in Figure 2.1.

2.1.1 Trap and repump lasers

The level diagram shown in Figure 2.1 helps illustrate the selection rules for absorption on the D2 line, which are $\Delta F=0,\pm1$ and $\Delta m_F=0,\pm1$. Transitions of the form $\Delta F=\Delta m_F=m_F=0$ are prohibited.

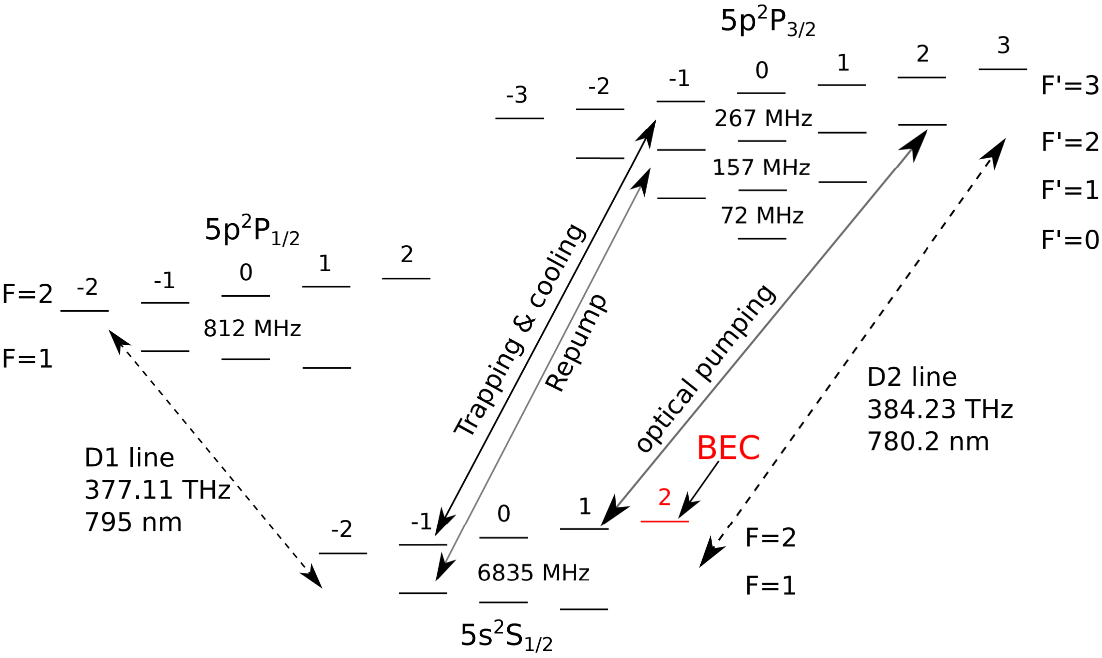

Figure 2.1: Energy level diagram for ^{87}Rb (not to scale). Red state indicates the quantum state where the Strathclyde BEC is made. Integers represent the m_F sublevels

In our experimental setup the laser which drives atomic transitions between $F = 2 \rightarrow F' = 3$ levels is used to cool the atoms, and is referred to as the 'trap laser'. When an atom is excited to the $F' = 3$ excited state its decay is governed by the selection rules and therefore the atom must decay to the $F = 2$ ground state, this cycle creates a closed loop and provides effective laser cooling. However, the trap laser is also able to address transitions to the $F' = 2$ and $F' = 1$ states. If an atom is excited to the $F' = 1$ or $F' = 2$ state instead of the $F' = 3$ state then it can decay to the $F = 1$

state, thus being lost from the closed cooling transition. Over time all the atoms will eventually accumulate in the $F = 1$ ground state and won't be able to absorb cooling light. To avoid this an additional laser is needed to pump the atoms out of the dark state and replenish the $F = 2$ ground state again so cooling can be performed. This laser is known as the 'repump' laser and is an essential component in laser cooling of atoms. The repump laser is tuned to the $F = 1 \rightarrow F' = 2$ transition and is overlapped with the trap beams.

As well as being able to create BECs in the $|F = 2, m_F = 2\rangle$ state, it is also possible to make BECs in the $|F = 1, m_F = -1\rangle$ state [123, 124, 125] and the $|F = 2, m_F = 1\rangle$ state [126, 127].

2.1.2 Optical pumping

In the cooling cycle provided by the trap and repump lasers, most of the atoms will eventually decay into the $F = 2$ ground state. During the decay process the atoms will be distributed amongst the magnetic sublevels of the ground state. This proves a problem when trying to create a BEC as it isn't possible to trap all the magnetic sublevels at the same time. The process in which the atoms can be reorganised and increase the population in the specific state where further cooling and trapping can be performed is known as optical pumping (OP). Optical pumping increases the number of trapped atoms and helps lead to the creation of a BEC. A more detailed explanation will be provided in Section 4.2.

2.2 Laser cooling

The first suggestion that light could exert a force on matter was back in the 17^{th} century, when Kepler noticed that comet tails always pointed away from the sun, which led him to the conclusion that it was due to light pressure. Although in the context of comet tails light plays little role, in 1901 Nichols and Hull showed the first experimental evidence of the existence of light radiative pressure [128]. It was 32 years later when Frisch preformed an experiment that proved that light could exert a force on matter [129]. In this experiment he saw a beam of sodium atoms being deflected by a resonant laser beam, due to the atoms absorbing the photons from the laser.

It took scientists many years before they could unlock the immense power of light exerting a force on matter and the major breakthrough that made this possible was the invention of the tuneable laser. The tuneable laser opened up a broad band of precision laser spectroscopy, and the narrow linewidth allowed resonant transitions in atoms to be explored. The first proposal that light could be used to transfer momentum to atoms and cool them was in 1975 by Hänsch and Schawlow at Stanford University [18] and Wineland and Dehmelt at the University of Washington [130]. Both these papers explained how light could be used to reduce the atom's kinetic energy and therefore cool the atom.

2.2.1 Light force on atoms

The first experimental realisation of radiation pressure was by Phillips and Metcalf in 1982 [131], where they decelerated an atomic beam by the absorption of counter-propagating resonant laser beams. In 1985, three-dimensional cooling of neutral atoms by resonance radiation pressure was reported by Chu *et al.* [19]. In this setup there was no confinement of the atoms but Section 2.2.2 shows how it played a major role in the creation of the atom trap.

To understand how the radiation force can be used to cool atoms we must first consider an atom travelling within a laser beam, which is tuned close to a resonance line of the atom. This atom will repeatedly absorb photons, each photon having a momentum equal to:

$$p = \frac{h}{\lambda} = \hbar k \ , \tag{2.1}$$

where h is Planck's constant, λ is the laser's wavelength and $\hbar$ is Planck's constant over 2π. Every time the atom absorbs or emits a photon this results in a change of its momentum.

In a two-level atom the rate at which it absorbs and spontaneously emits photons is given by the Lorentzian profile [132]:

$$R(I, \Delta) = \frac{\Gamma}{2} \frac{I/I_{\mathrm{sat}}}{1 + I/I_{\mathrm{sat}} + (2\Delta/\Gamma)^2} \ , \tag{2.2}$$

where the excited state lifetime $\tau = 1/\Gamma$, Γ is the natural linewdith of the transition, I is the light intensity, I_{sat} is the saturation intensity and Δ is the laser's frequency detuning from the atomic resonance. For ^{87}Rb, τ=26.6 ns, Γ=6.07 MHz, I_{sat}=1.67 mW/cm^2 (for the stretched state $|2,2\rangle \rightarrow |3,3\rangle$ transition) and the maximum acceleration a single atom can feel in a laser beam is 1.1×10^5 m/s [122]. If the frequency between the atom's ground and excited state is ω_0 and the laser's frequency is ω, then the detuning is defined as $\Delta = \omega - \omega_0$. Since the atom is absorbing photons at a rate R, which have a momentum of $\hbar k$, then the atom will feel a force due to radiation pressure, which can be derived from Newton's second law of motion

$$F = \hbar k R \ , \tag{2.3}$$

it is this force that leads to the atom being cooled.

2.2.2 Doppler cooling - optical molasses

Now consider a two-level atom with resonant frequency ω_0, traveling with velocity v, which is interacting with two counter-propagating laser beams (which originate from the same laser) as shown in Figure 2.2. If the two counter-propagating beams are red detuned from resonance (lower frequency), then there will always be a force which opposes the motion of the atom, due to the force imbalance from the two lasers. The momentum that the photon imparts during the absorption process results in reducing the atom's kinetic energy, which is related to reducing the temperature [133, 134]. Before the atom can absorb another photon it must emit one, this emission has no preferred direction so has no overall net effect on the atoms velocity, but random recoil momentum can result in the atom drifting from the laser field [135]. The spontaneous emission also causes inherent heating, which sets a limit on the achievable temperature using laser cooling.

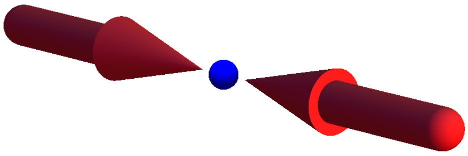

Figure 2.2: Two counter-propagating laser beams interacting with an atom travelling with velocity v.

Atoms travelling in the red detuned laser light will experience the Doppler effect,

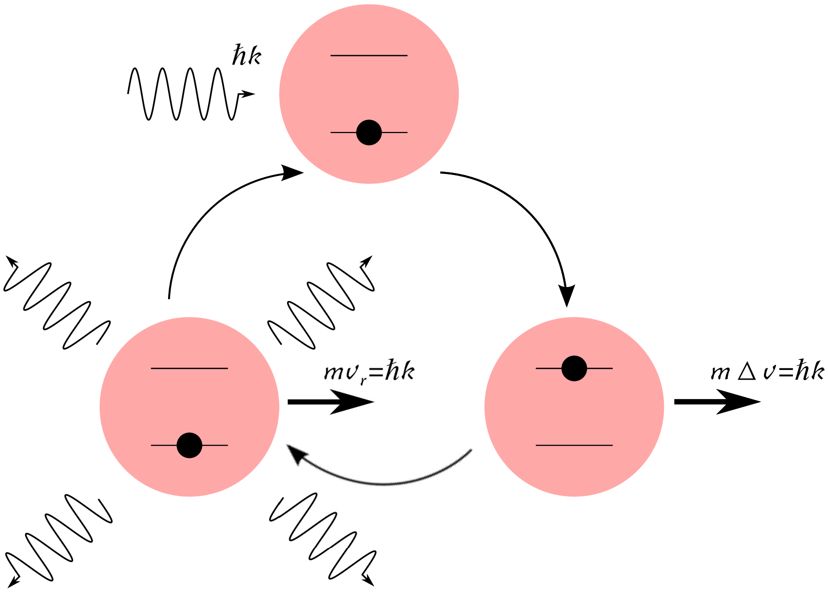

Figure 2.3: Absorption and emission cycle of laser cooling adapted from [136]: An atom absorbs an incident photon with momentum $\hbar k$ and is promoted to the excited state. When the atom absorbs the photon it will gain a momentum kick parallel to the direction the photon is travelling, thus causing the atom to recoil with a change of velocity of $\hbar k/m$. The atom will then emit a photon, which will again cause another momentum kick, in a random direction and return to the ground state. Since the emitted photon is in a random direction, over many absorption and emission cycles this will be symmetric and on average the atom will feel no momentum kick from the emitted photons.

which depends on the direction of the light. If the laser beam is travelling towards the atom, then the atom will see the light blue-shifted closer to resonance and therefore scatter more photons. Whereas, when the laser beam is travelling away from the atom the light will be further red-shifted from resonance and scatter fewer photons. The imbalance of the two forces from the two laser beams results in an average force which opposes the atom's motion. This Doppler shift results in two different detunings depending on the direction of the light: when the atom is travelling in the same direction as the photons the shifted angular frequency Δ_{same} is:

$$\Delta_{same} = \Delta - kv \ . \tag{2.4}$$

Therefore, when the atom is travelling in the opposite direction to the photons the

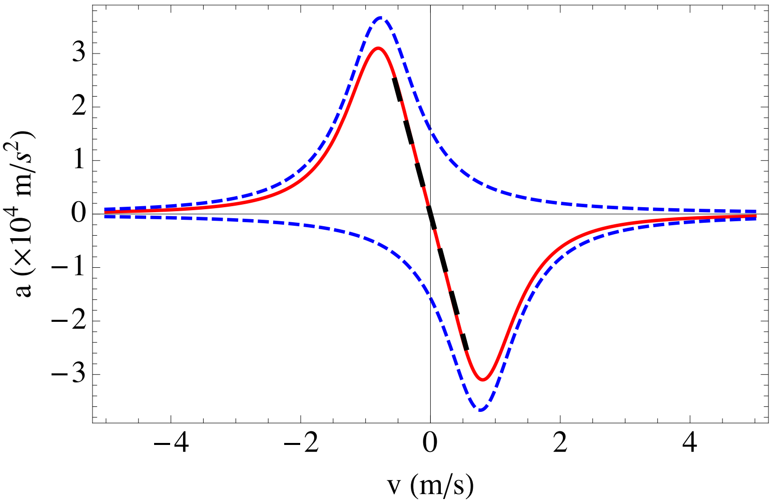

Figure 2.4: Velocity-dependent acceleration in optical molasses. Dashed blue lines are the Lorentzian profiles from both of the counter-propagating laser beams and the solid red line is the combination of the two. $I/I_{\text{sat}} = 1$, $I_{\text{tot}} = 2I$ and $\Delta = -\Gamma$.

shifted angular frequency Δ_{opp} is:

$$\Delta_{opp} = \Delta + kv \ . \tag{2.5}$$

The radiation pressure force the atom feels from in Equation 2.3 is now a function of intensity and detuning and in 1D takes the form:

$$F(I,\Delta)_{1D} = \hbar k[R(I,\Delta - kv) - R(I,\Delta + kv)] \ . \tag{2.6}$$

The damping or cooling force the atoms experience can be written as $F = -\alpha v$, where α is the dampening coefficient and is defined as [132, 136]:

$$\alpha = -4\hbar k^2 \frac{I}{I_{sat}} \frac{(2\Delta/\Gamma)}{[1 + sI/I_{sat} + (2\Delta/\Gamma)^2]} \ . \tag{2.7}$$

This force is depicted in Figure 2.4, when an atom is in the linear region (dashed black line) of the red curve it feels a net force pushing it towards ‘zero’ velocity. For red detuned lasers ($\Delta < 0$) this force has a cooling effect, so therefore reduces the width of the velocity distribution, whereas for blue detuned lasers ($\Delta > 0$) this causes heating.

The damping force on the atoms is a result of many absorption and emission cycles,

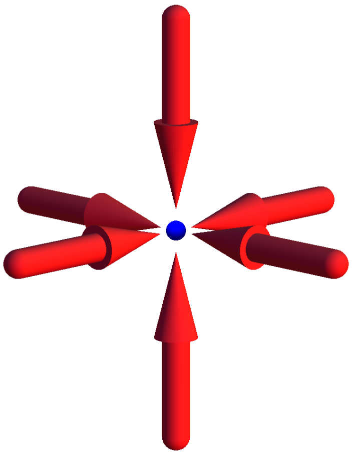

Figure 2.5: 3D optical molasses arrangement. The optical molasses setup consists of three pairs of orthogonal red-detuned laser beams. These provide a viscous force which opposes the atom's motion in all three dimensions.

the 1D setup can be extended to three dimensions [19], so the force becomes:

$$\mathbf{F}(I,\Delta)_{3D} = \hbar\mathbf{k} \sum_{3D=x,y,z} \left[R_{3D}(I,\Delta - \mathbf{k}\cdot\mathbf{v}_{3D}) - R_{3D}(I,\Delta + \mathbf{k}\cdot\mathbf{v}_{3D})\right] , \tag{2.8}$$

the 3D setup is simply constructed of three pairs of orthogonal counter-propagating beams and results in a viscous force for the atoms. The orientation of laser beams is depicted in Figure 2.5.

The 3D viscous field that the photons create for the atoms is commonly known as 'optical molasses' and was first demonstrated in 1985 by Chu *et al.*[19]. The viscous force of optical molasses will cool the atoms until a certain point, when there is a balance between the cooling force and the heating due to the random nature of photon absorption and emission. This leads to a quantity known as the Doppler temperature [132]:

$$T_D = \frac{\hbar\Gamma}{4k_B}\frac{1 + I_{\text{tot}}/I_{\text{sat}} + (2\Delta/\Gamma)^2}{-2\Delta/\Gamma} . \tag{2.9}$$

In the limit of low intensity, ($I_{\text{tot}} \ll I_{\text{sat}}$), and when $\Delta = -\Gamma/2$, the Doppler temperature has a minimum of

$$T_D = \frac{\hbar\Gamma}{2k_B} . \tag{2.10}$$

Since the Doppler temperature is a function of natural linewidth it varies depending on atomic species, for ^{87}Rb T_D=145 μK on the 780 nm transition.

2.2.3 Magneto-optical trap

Although optical molasses reduces the atoms velocity it doesn't confine them. For this an inhomogenous magnetic field is needed. In 1987, the first experiment in which atoms were not only cooled but also trapped was performed by Raab *et al.* [22]. This setup combined optical molasses with a quadrupole magnetic field, $\mathbf{B}$=$B_1(x, y, -2z)$, which originates from two current carrying wires in the anti-Helmholtz configuration and is known as the 'magneto-optical trap' (MOT) and is depicted in Figure 2.6. In optical molasses, the linear Doppler effect provides a velocity-dependent pressure imbalance in the laser beams and in a MOT, due to the linear Zeeman effect, this pressure imbalance is in addition spatially-dependant. The MOT configuration still has the velocity-dependant optical molasses cooling effect, thus creating cold and dense atomic

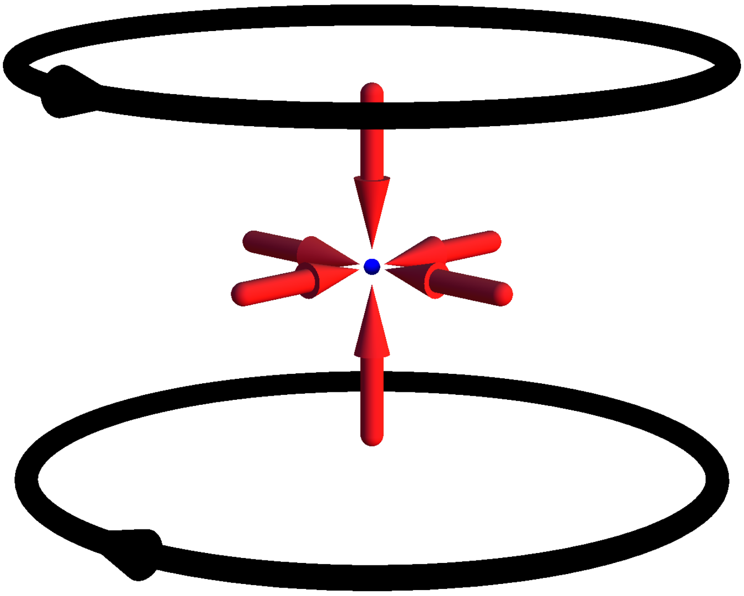

Figure 2.6: Schematic of a 3D MOT: This configuration combines both magnetic and optical components, which have correct polarisations, to cool and trap the atoms. Two coils (black) with current flowing in opposite directions (indicated by arrows) produce a quadrupole magnetic field. When combined with 3 pairs of orthogonal red-detuned beams with correct polarisation (red), this produces a restoring force that pushes the atoms to the centre of the trap.

ensembles.

When a magnetic field is applied, the excited state sublevels are split with the following energy difference [137]

$$\Delta E = g_F \mu_B \Delta m_F B \ , \tag{2.11}$$

where g_F is the Landè g-factor for a given state with angular momentum F, μ_B is the Bohr magneton and B is the amplitude of the static magnetic field. In the 1D case depicted in Figure 2.7 a linearly varying magnetic field $\vec{B}$ is applied, and the point at which the field amplitude vanishes is set to be $z = 0$. Two red-detuned counter-propagating laser beams are shone onto the atoms, with polarisations of the same handedness, i.e. for both of the beams the electric field vector rotates in the same

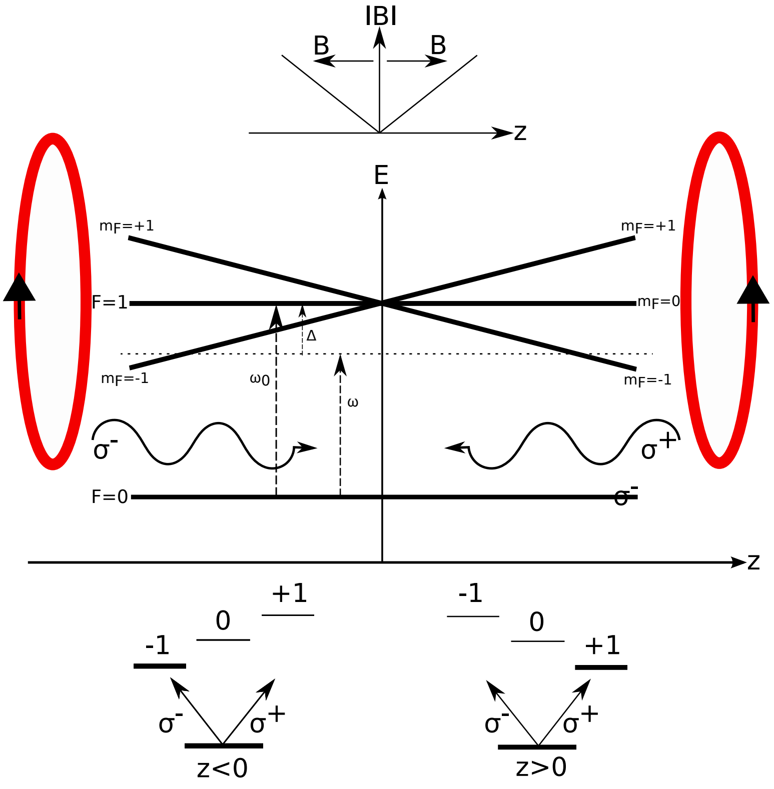

Figure 2.7: One dimensional MOT scheme. The laser beam travelling in the +z direction is σ^- polarised when $z < 0$ and is σ^+ polarised when $z > 0$. The polarisations are set so that σ^- light can only drive atoms to the $m_F = -1$ and σ^+ light can only drive the $m_F = +1$ state.

direction when looking along the wave vector of the beam. A laser beam travelling in the +z direction will be σ^- polarised for $z < 0$ and therefore will couple to the $m_F = -1$ transition. The same beam travelling along the +z direction will be σ^+ for $z > 0$ and will couple to the $m_F = +1$.

For an atom on the left side ($z < 0$), photons from the left laser beam can only drive σ^- transitions and excite the atom to the $m_F = -1$ state, which is now shifted closer to resonance while state $m_F = +1$, which can only be reached via an absorption of a photon from the right laser beam, is being shifted further from resonance (opposite but same effect for an atom on the right hand side ($z > 0$)). The probability is higher to absorb a photon from the left beam rather than a photon from the right beam, therefore the resulting radiation pressure pushes the atom towards the magnetic field minimum, at which the absorption from both lasers is equal and is therefore the trap centre. As a result of this, any atom that isn't located at the trap centre will experience a force pointing to the centre of the MOT which allows confinement of the atoms.

2.3 Magnetic fields and atoms

To further cool an ensemble of trapped atoms, the constant light scattering in a MOT cannot be used. To overcome this the atom's magnetic moment can be used, and by applying an inhomogenous magnetic field, which results in an atom-magnetic field interaction, this can trap the atoms without the presence of light and allow further cooling by evaporative cooling techniques. The first experiment which utilised the idea of using magnetic fields to manipulate atoms was performed in 1921 by Stern and Gerlach [138]. In these experiments, the atomic beams yielded a small deflection in the presence of an inhomogenous magnetic field, which was highly dependent on the longitudinal velocity spread of the atoms and the magnitude of the magnetic field gradient. Since the development of laser cooling techniques, small clouds of atoms which have narrow velocity spreads have lead to magnetic confinement and manipulation of cold atomic ensembles [139].

2.3.1 Zeeman effect - atom-magnetic field interaction

In the absence of external magnetic fields all the magnetic m_F sublevels are degenerate for each hyperfine energy level F. However, their degeneracy is broken when an external magnetic field is applied. The Hamiltonian that describes the interaction with the magnetic field along the z-direction (atomic quantisation axis) is given by

$$H_B = \frac{\mu_B}{\hbar}(g_S S_z + g_L L_z + g_I I_z)B_z \ , \tag{2.12}$$

where g_S, g_L, and g_I are the electron spin, electron orbital and nuclear g-factors respectively [122]. If the energy shift from the magnetic field is small in comparison to the fine-structure splitting, then the interaction Hamiltonian can be written in terms of the quantum number J

$$H_B = \frac{\mu_B}{\hbar}(g_J J_z + g_I I_z)B_z \ , \tag{2.13}$$

where J is the total electronic momentum ($J = S + L$). Here, the Landé factor g_J is given by [140]

$$\begin{aligned} g_J &= g_L + g_S \\ &\simeq 1 + \frac{J(J+1) + S(S+1) - L(L+1)}{2J(J+1)} \ , \end{aligned} \tag{2.14}$$

for $g_L \simeq 1$ and $g_S \simeq 2$.

A similar approach can be taken if the energy shift due to the external magnetic field is small compared to the hyperfine splitting. In this case, the interaction Hamiltonian can be expressed in terms of the quantum number F [141]

$$H_{B(hfs)} = \mu_B g_F F_z B_z \ , \tag{2.15}$$

and the corresponding hyperfine Landé g-factor g_F is given by

$$\begin{aligned} g_F &= g_J + g_I \\ &\simeq g_J \frac{F(F+1) - I(I+1) + J(J+1)}{2F(F+1)} \ , \end{aligned} \tag{2.16}$$

for $g_I \ll g_J$. The energy shift from the Hamiltonian in Equation 2.15 takes the form

$$\Delta E_{B(hfs)} = \mu_B g_F m_F B_z \ . \tag{2.17}$$

There are two ground state energies for alkali atoms, which are a result of the total angular momentum $F = I \pm 1/2$, and can be described by the Breit-Rabi formula [142]

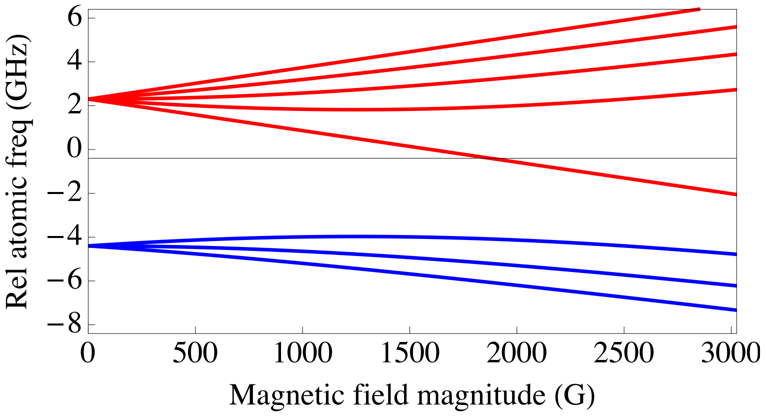

Figure 2.8: Ground state Breit-Rabi Diagram for ^{87}Rb showing the relative atomic frequency shifts dependence on the magnetic field, for each of the magnetic sublevels m_F. Upper red lines correspond to the $|F, m_F\rangle$ ground state energy levels $|2,2\rangle$,$|2,1\rangle$,$|2,0\rangle$,$|2,-1\rangle$,$|2,-2\rangle$ and for the lower blue lines $|F, m_F\rangle$ ground states $|1,-1\rangle$,$|1,0\rangle$,$|1,1\rangle$ (from top to bottom).

$$E_{|J\, m_J\, I\, m_I\rangle} = -\frac{\Delta E_{hfs}}{2(2I+1)} + g_I \mu_B m B \pm \frac{\Delta E_{hfs}}{2}\left(1 + \frac{4mx}{2I+1} + x^2\right)^{1/2} , \qquad (2.18)$$

where $\Delta E_{hfs} = A_{hfs}(I + 1/2)$ is the hyperfine splitting, $m = m_I \pm m_J = m_I \pm 1/2$ and $x = (g_J - g_I)\mu B/\Delta E_{hfs}$. The result of the Breit-Rabi formula shown in Figure 2.8 demonstrates the ground states dependence on magnetic field. The Zeeman effect produces two groups of atoms, which behave differently depending on their hyperfine state. Hyperfine states with $g_F m_F < 0$ are known as weak field seekers, and are attracted to the local minimum of the magnetic field whereas, states with $g_F m_F > 0$ are strong field seekers, and are attracted to the local maximum in the magnetic field. This is only true for low magnetic fields and when the splitting of the levels approaches the ground state splitting.

2.3.2 Rectangular and circular coils

There are many coil configurations for trapping atoms, and many of them rely on the same principle of how magnetic fields are produced. The simplest way to produce a magnetic field is one generated from a single current carrying wire and the magnetic

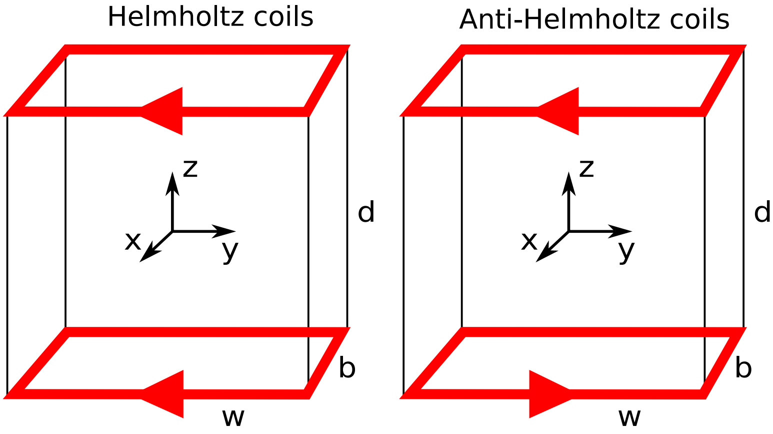

Figure 2.9: Square coils in Helmholtz and anti-Helmholtz configuration, with dimensions as indicated. Arrows indicate direction of current flow.

field can be determined from the Biot-Savart law

$$d\mathbf{B} = \frac{\mu_0 I}{4\pi} \frac{d\mathbf{l} \times (\mathbf{r} - \mathbf{r'})}{|\mathbf{r} - \mathbf{r'}|^3} \ , \tag{2.19}$$

where I is the current in a length of wire $d\mathbf{l}$, $d\mathbf{B}$ is the magnetic field at the point $\mathbf{r}$ that is generated at a position $\mathbf{r'}$ and μ_0 is the magnetic permeability of free space. The commonly used unit when talking abut magnetic trapping is the Gauss (1G $= 10^{-4}$ T), therefore the proportionality constant in Equation 2.19 is $\frac{\mu_0}{4\pi} = \frac{1}{10}$ GcmA^{-1}. These units are used throughout this section.

The magnetic field produced by a segment of wire along the z-axis, which has a length l, $(0, 0, \pm l/2)$, and has a current I flowing, is given by integrating Eq. 2.19

$$\mathbf{B} = \frac{I}{10(x^2 + y^2)} \left(\frac{-(z - l/2)}{\sqrt{x^2 + y^2 + (z - l/2)^2}} + \frac{(z + l/2)}{\sqrt{x^2 + y^2 + (z + l/2)^2}} \right) (x, -y, 0) \ . \tag{2.20}$$

Although there is no such thing as an isolated current carrying wire, the above equation can be extended to current carrying wires which are in a circuit or current loop.

The magnetic field generated from a pair of rectangular coils (Figure 2.9) of the same size in the Helmholtz configuration, current flowing in the same direction and spaced equal to the radius, has the Taylor expansion about the origin given by

$$\mathbf{B} = \frac{8NI}{5} \frac{wb(w^2 + b^2 + 2d^2)}{(w^2 + b^2)(b^2 + d^2)(w^2 + b^2 + d^2)^{1/2}} \ (0, 0, 1) \ , \tag{2.21}$$

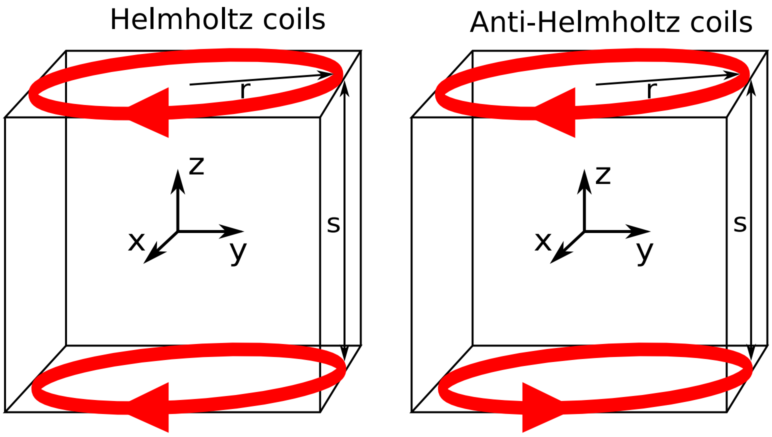

Figure 2.10: Circular coils in Helmholtz and anti-Helmholtz configuration, with separation s and radius r. Arrows indicate direction of current flow.

where N is the number of turns, I is the current, w, b and d are the dimensions of the rectangular coil (w=width, b= breadth, d=seperation). When the currents are flowing in opposite directions and the separation equal to the radius of the coils, known as anti-Helmholtz, the magnetic field Taylor expansion is given as

$$\mathbf{B} = \frac{8NI}{5}\frac{wbd}{(w^2+b^2+d^2)^{3/2}}(-B_{1x}x, -B_{1y}y, (B_{1x}+B_{1y})z) \ , \tag{2.22}$$

where $B_{1x} = \frac{3(w^2+b^2)+2d^2}{(w^2+b^2)^2}$ and $B_{1y} = \frac{3(b^2+d^2)+2w^2}{(b^2+d^2)^2}$.

The magnetic field generated from an N turn circular coil (Figure 2.10), along the z-axis has the form

$$B_z(0,z) = \frac{\pi NIr^2}{5(r^2+z^2)^{3/2}} \ , \tag{2.23}$$

where r is the radius of the coil, which is placed at $z = 0$. The magnetic field from a circular loop is a symmetric system and to second order the Taylor expansion over all space is given by

$$B(x,y,z) = B_0(0,0,1) + B_1\left(-\frac{x}{2}, -\frac{y}{2}, z\right) + \frac{B_2}{2}\left(-xz, -yz, z^2 - \frac{x^2+y^2}{2}\right) \ . \tag{2.24}$$

For two coils with radius r in the Helmholtz configuration, their magnetic field Taylor expansion has the even symmetric form

$$B_1 = B_3 = 0, \ \ B_0 = \frac{16\pi NIr^2}{5(4r^2+s^2)^{3/2}}, \ \ B_2 = \frac{668\pi NIr^2(4s^2-r^2)}{5(4r^2+s^2)^{7/2}} \ , \tag{2.25}$$

to second order for a coil separation of s. For coils in the anti-Helmholtz configuration, the Taylor expansion of their magnetic field has the odd symmetric form

$$B_0 = B_0 = 0,\ \ B_1 = \frac{96\pi N I r^2 s}{5(4r^2+s^2)^{5/2}}\ , \tag{2.26}$$

to third order. In the Strathclyde experiment a combination of rectangular and circular Helmholtz and anti-Helmholtz coils are used for the various steps in the experiment.

2.3.3 Quadrupole trap

The magnetic coil configuration which has a central minimum in $|\mathbf{B}|$ allows weak field seeking atoms to accumulate at the local minimum of the trap. All square and circular anti-Helmholtz coil pairs approximately generate a field of the form

$$\mathbf{B}_{quad}(r) = B_1(x, y, -2z)\ , \tag{2.27}$$

which results in a magnetic field magnitude of $|\mathbf{B}| = B_1(x^2+y^2+4z^2)^{1/2}$. This trap configuration was first demonstrated in 1985 [143] where sodium atoms where trapped for over 1 s. The resulting ground state energy from this trapping potential is given by

$$U(x, y, z) = \mu_B g_F m_F B_1(x^2+y^2+4z^2)^{1/2}\ . \tag{2.28}$$

The quadrupole trap has a zero-field point at the centre of the trap, which results in the atoms being able to ‘fall’ out of the trap. This loss process can by understood in the following way; at the zero point in the trap hyperfine degeneracy is present, so an atom that passes near will experience a change in orientation of its atomic moment and will no longer be aligned with the local field direction. This non-adiabatic spin-flip into a untrapped $g_F m_F < 0$ state is known as a Majorana spin-flip transition [24, 144]. The loss rate of the atoms from the trap increases with decreasing temperature, which can prove catastrophic when trying to reach the temperatures and densities required for Bose-Einstein condensation.

The major flaw of the quadrupole trap can be overcome by removing the zero-field point, hence removing the point of hyperfine degeneracy and thus stopping spin-flips. There are many configurations that do just this including ‘plugging’ the hole in the trap using a blue detuned laser beam [27, 145], which repels the atoms from the region of the trap where they can be lost. Another solution is to make the minimum of the trap position time-dependent, so the atoms 'chase' the hole but can never reach it. This is known as a time-averaged orbiting potential (TOP) trap [24, 146, 147]. In Strathclyde we don't use either of these techniques, but instead use a combination of rectangular and circular coils along with straight current carrying wires to form an Ioffe-Pritchard trap [23, 148, 149], as described below.

2.3.4 Ioffe-Pritchard trap

In Sec 2.3.2 the field produced by rectangular and circular coils was discussed. It is these fields that form the framework of the Ioffe-Pritchard (IP) trap. The IP trap is a static magnetic trap that creates a trapping potential which has a non-zero minimum, therefore preventing spin-flips and atoms being lost from the trap.

The 'traditional' IP trap consists of four long wires with current flowing in opposite direction for adjacent wires and a pair of Helmholtz circular coils. The four current carrying wires that are placed at equal distances from one another and from

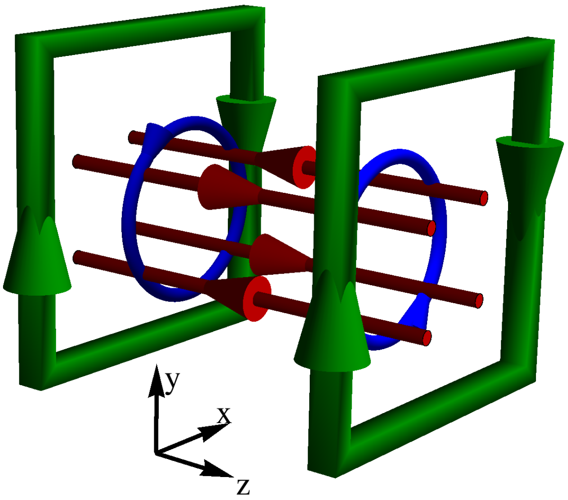

Figure 2.11: Ioffe-Pritchard trap geometry. The four straight current carrying wires (red) produce the 2D quadrupole trap in the x and y axis. Confinement along the z-axis comes from the two Helmholtz circular coils (blue) and the compensation magnetic field is generated from the square Helmholtz (green) coils. Arrows indicate the direction of current flow.

the symmetric z-axis of the circular coils can produce a a two-dimensional quadrupole field. Although this produces tight radial confinement, there is no such confinement along the axial direction so an additional magnetic field is required. This additional field is provided by the Helmholtz coil pair and are known as the pinch coils, shown in Figure 2.11. Such a trap for trapping neutral atoms was first introduced in 1983 [23], but was originally used for plasma physics [150].

Since the Ioffe-Pritchard trap was first proposed it has played a major role in not only trapping of neutral atoms, but also in the realisation of Bose-Einstein condensation. The combination of the pinch coils, which provide an axial harmonic minimum with curvature B_2, and the perpendicular quadrupole field with gradient B_1, results in a trap which has a large axial bias field B_{axial}, which can be cancelled by applying a magnetic field in the opposite direction. The magnetic field used to cancel this large axial bias is generated by a pair of Helmholtz coils [151] and are known as the compensation, nulling or IP 'bias' coils. With the addition of the IP 'bias' coils the effective total field at the centre of the trap is

$$\mathbf{B}_0 = \mathbf{B}_{axial} - \mathbf{B}_{IP\,bias} \ . \tag{2.29}$$

The bias offset at the trap minimum avoids any spin-flips, the field from pinch coils is given in equation 2.24 and a two dimensional quadrupole can be written as

$$\mathbf{B}(x, y, z) = B_1(-x, y, 0) \ . \tag{2.30}$$

The magnitude of the magnetic field from the IP trap, excluding the IP bias coils, is a combination of the four wires and two circular coils, this can be expressed as

$$B_{IP} = \sqrt{B_1^2(x^2+y^2) + \left(B_0 + \frac{B_2}{2}\left(z^2 - \frac{x^2+y^2}{2}\right)\right)^2} \ . \tag{2.31}$$

To second order the Taylor expansion is [152]

$$B_{IP} = B_0 + \frac{1}{2}\left(\frac{B_1^2}{B_0} - \frac{B_2}{2}\right)(x^2+y^2) + \frac{B_2}{2}z^2 \ , \tag{2.32}$$

and this produces (to second order) a harmonic, cylindrically symmetric trap.

2.3.5 Compression

The final stage of the cooling cycle is evaporation (see Section 2.4), but before this can be implemented there are certain parameters that need to reach a critical value for it to be efficient. The key parameter for efficient evaporation is the collision rate, so an adiabatic compression of the IP trap is performed to increase the density and temperature, both of which help maximises this parameter. The phase space density stays the same during this process as long as the compression is adiabatic.

The compression of the IP trap can be achieved by changing the current flowing through the IP trap and IP bias coils, which changes the potential energy of the magnetic trap and therefore changes the shape of the trap. During the compression the atoms are being 'squeezed' into a tighter trap, which in turn increases the collision rate and density of the ensemble of atoms, as well as heating them, which also increases the collision rate. As the magnetic trap is compressed the trap frequencies change, creating high confinement in the radial direction and due to the inherent cylindrically symmetric feature of the trap, this leads to an elongated cigar-shaped trap shown in Figure 2.12.

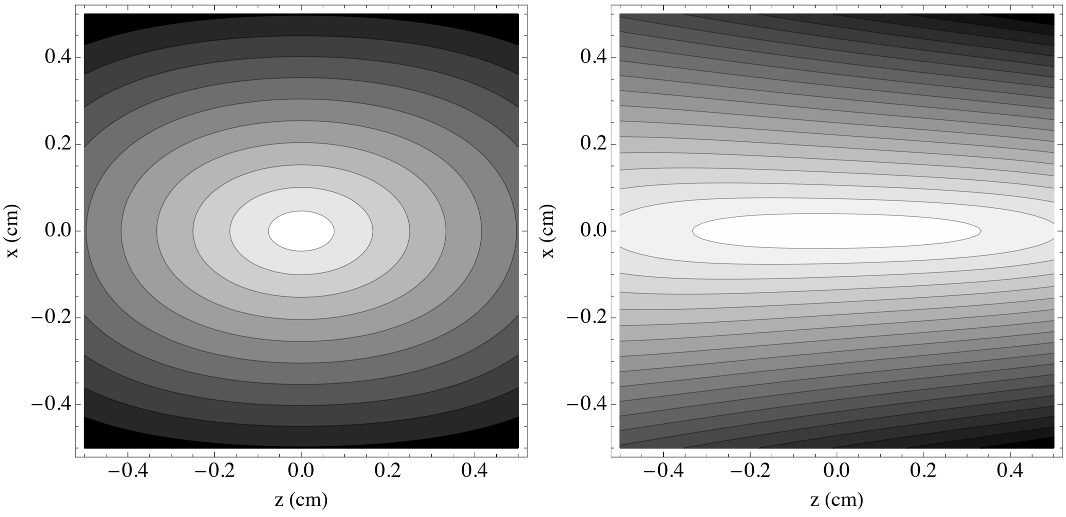

Figure 2.12: Contour plots of Strathclyde's uncompressed IP trap (left) and compressed IP trap (right). Contour intervals are smaller in the uncompressed trap. Compression increases collision rate and density of the cloud of atoms. Contours represent magnetic field, where the darker regions illustrate stronger magnetic field strength.

2.4 Evaporation

Adiabatic compression of the magnetic trap is an essential step for increasing the density and temperature of the atomic cloud, in turn increasing the collision rate. It's the fine interplay between 'good' elastic collisions and 'bad' inelastic collisions that holds the key to efficient evaporation. Evaporative cooling is a process that works by selectively removing the hotter atoms from the distribution, allowing it to rethermalise and therefore reduce the temperature of the atomic ensemble, as shown in Figure 2.13. In 1985, the idea of using evaporative cooling to reach the Bose-Einstein condensate phase transition was introduced by Hess [153]. In this paper evaporative cooling was used to attempt to create a hydrogen BEC, but this came with little success due to the poor efficiency of the evaporation. However the first hydrogen BEC was created in 1998 [28]. The main purpose of evaporative cooling is to reach the necessary phase space densities for the BEC transition and this can be done by slowly lowering the 'sides' of the magnetic trap [154], thus reaching ultra-low temperatures and at the same time high atomic densities ($> 10^{12}\text{cm}^{-3}$).

Two concerns, or downsides, of evaporation are the evaporated cloud's lifetime and the intrinsic atom losses. The evaporated clouds lifetime is fixed by any heating in

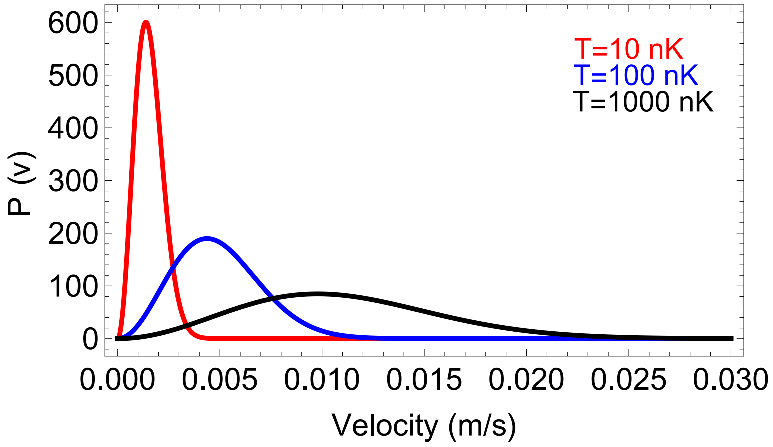

Figure 2.13: Basic principle of evaporative cooling where the hotter atoms are removed from the trap and after rethermalisation the ensemble is at a colder temperature. The hotter atoms are selectively 'cut' from the Maxwell Boltzmann distribution and once the remaining atoms rethermalise the average velocity, and therefore temperature, is reduced. This process results in a substantial decrease in temperature and an increase in density at the expense of atom number.

the trap, losses from the trap or inelastic collisions, therefore the ratio between elastic and inelastic collisions sets the efficiency of the evaporation. Atom loss is a necessary process in evaporation, e.g. in Strathclyde we start with $\approx 10^8$ atoms in the magnetic trap and when the atoms have been evaporated below the critical temperature and undergone the phase transition only $\approx 10^5$ atoms are left. This shows the magnitude of the loss process during evaporation, even with efficient evaporation we lose a factor of 1000 in atom number.

2.4.1 RF evaporative cooling

The lowering of the trap's 'walls' to selectively remove the hotter atoms can be done by applying an RF field to the atoms, as was first demonstrated experimentally in 1995 [24, 25, 155]. As discussed in Section 2.2.3, an atom trapped in a spatially varying magnetic field will experience an energy splitting of the excited state sublevels given by

$$\Delta E = g_F \mu_B m_F |B| \ , \tag{2.33}$$

where $|B|$ is the magnitude of the local magnetic field vector. An oscillating AC magnetic field is applied, which is perpendicular to the IP trap's magnetic field vector. This oscillating AC field is a superposition of σ^+ and σ^- polarised magnetic field and therefore drives the $|F, m_F\rangle \rightarrow |F, m_F \pm 1\rangle$ ground state transitions if the frequency of the RF field follows the relation

$$\upsilon_{RF} = g_F \mu_B |B| \ . \tag{2.34}$$

Since the magnetic field is spatially dependent, it also makes the RF induced transitions spatially dependent. Therefore if the RF is tuned to the the 'edges' of the trap, only the atoms which are at the 'edges' and furthest from the trap centre will undergo these transitions. This is due to the fact that only the more energetic, and therefore hotter atoms, can 'climb' up the potential and then be ejected from the trap as shown in Figure 2.14.

By sweeping down this spatially dependent RF field it allows the sides of the magnetic trap to be lowered, constantly enabling the hottest atoms to escape. This is known as an "RF knife" and it is this tool that 'chops' off the high velocity atoms in the Maxwell Boltzmann thermal distribution (Figure 2.13). For this RF knife to work

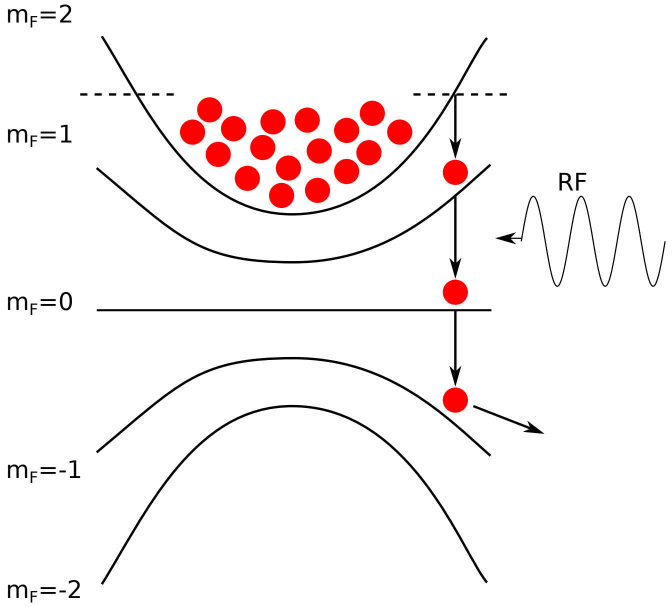

Figure 2.14: Principle behind RF evaporative cooling: an RF field is incident on the atoms, which is driving the $|2,2\rangle \rightarrow |2,1\rangle \rightarrow |2,0\rangle \rightarrow |2,-1\rangle \rightarrow |2,-2\rangle$ transitions. If an atom and RF photon (designated by dotted line) have exactly the same energy, the atom will be transitioned into an untrapped state ($m_F = 0, -1\,\mathrm{or} -2$) and be lost from the trap, and after thermalisation the ensemble is at a colder temperature.

the atoms that are left in the trap must redistribute their kinetic energy amongst each other in the form of collisions, thus returning close to thermal equilibrium. Waiting for the ensemble to fully equilibrate every time an atom is lost would take too much time, so instead the RF knife's frequency is continuously ramped down, which at each instant removes the hotter atoms. The time it takes for the atoms to approach thermal equilibrium therefore sets a time scale on how fast the RF knife can be swept at.

2.4.2 Dynamics of evaporative cooling

For atoms which are trapped in an external potential during evaporation, one of the key parameters is the potential depth, which is given as

$$U_{depth} = \eta k_B T \ , \tag{2.35}$$

where η is called the truncation parameter. For small values of η, evaporation happens fast since the trapping potential is low in comparison to the energy of the atoms, although fast evaporation doesn't necessary mean efficient evaporation. For evaporation to be efficient and result in an appreciable temperature drop for each escaping atom, the truncation parameter must be made time dependent, therefore relating it to the dynamics of the evaporation.

Evaporative cooling occurs on an exponential scale and consists of many finite steps in which the truncation parameter is altered and the remaining atoms in the trap rethermalise (shown in Davis *et al.*[156]). A measure of how much the temperature is reduced relative to the number of atoms lost from the trap can be expressed as [157]

$$\alpha = \frac{\ln(T^{'}/T)}{\ln(N^{'}/N)} \ , \tag{2.36}$$

where $T^{'} = T + \Delta T$ and $N^{'} = N + \Delta N$ [158]. If α is constant during the evaporation, then the decrease in temperature is $T(t)/T(0) = [N(t)/N(0)]^{\alpha}$.

In a power law potential which has d dimensions, $U(r) \propto r^{d/\delta}$ ($U(r) = 2$ for harmonic potential), during evaporation all quantities scale as $[N(t)/N(0)]^{x}$, where x is only a function of δ and α. In this case the relationship between the volume of the trapped atoms and the temperature is $V \propto T^{\delta}$ [159]. The value of the parameter δ depends on the trapping potential and on the dimenionality, for instance, $\delta = 0$ for a 3D box potential (with infinitely high walls), $\delta = 3/2$ for 3D harmonic potential and $\delta = 3$ for a 3D linear potential.

The key parameter in the whole process is α, this parameter indicates the temperature drop relative to atom loss. A full derivation can be found in Ref [16], in this thesis only the final equation is presented. The relationship between the average energy of an escaping atom, η and α can be expressed as

$$\alpha = \frac{\eta + \kappa}{\delta + 3/2} - 1 \ . \tag{2.37}$$

This equation results in a dimensionless quantity that indicates how much more than the average energy is removed by an evaporated atom. In principle there is no upper limit to the efficiency of evaporative cooling and α. This can be understood as follows: if η was large and long enough was waited until a single atom had all the energy of the system, then by evaporating this atom the system would be cooled down to zero temperature. Unfortunately this would take an almost infinite amount of time and not be conducive to any realistic experiment with a finite cloud lifetime.

2.4.3 Runaway evaporation

For alkali metals, where the main loss process is background gas collisions, it is important to maintain or increase the elastic collision rate, $n\sigma v$, which varies as [158]

$$\frac{d(n\sigma v)}{dt}/n\sigma v = \frac{1}{\tau_{el}}\left(\frac{\alpha(\delta - 1/2) - 1}{\lambda} - \frac{1}{R}\right) > 0 \ , \tag{2.38}$$

where n is the density, σ is the elastic collision cross section, v is the relative velocity between atoms, τ_{el} is the elastic collision time, λ is the ratio of the evaporation time and elastic collision time (τ_{ev}/τ_{el}) and R is the ratio between good and bad collisions (τ_{loss}/τ_{el}, where τ_{loss} is the time constant for an atom to be lost due to background gas collisions).

Evaporation at constant, or increasing collision rate, is known as “runaway evaporation” and requires

$$R \geq R_{min} = \frac{\lambda}{\alpha(\delta - 1/2) - 1} \ . \tag{2.39}$$

Equation 2.39 sets requirements on the initial conditions of the evaporation. In order to cool effectively and reach BEC in an harmonic potential there must be at least 150 good elastic collisions for every bad inelastic collision, a long time constant for an atom to be lost from the trap due to background collisions and an constant or increasing collision rate.

2.4.4 Phase-space density parameter

The parameter α describes the decrease in temperature due to atoms being lost from the trap during the evaporation process. However, to achieve a BEC it is important to not only decrease the temperature of the ensemble but also increase the phase-space density (PSD) of the atomic cloud. Maximising the PSD is critical in order to reach a BEC, the relative change in PSD with decreasing atom number in the trap is given by [158]

$$\gamma = -\frac{d(\ln PSD)}{d(\ln N)} = \frac{\alpha(\delta + 3/2)}{1 + \lambda/R} - 1 \ , \tag{2.40}$$

where γ is the efficiency parameter of the evaporation. In a harmonic trap γ must be ≥ 2 to be in the runaway evaporation regime. With a high γ, this opens up the possibility to reach high phase-space densities. Since the efficiency γ depends on the ratio of good to bad collisions R, if R is small (which isn't in the runaway regime) γ specifies that the PSD cannot be increased. However, if R is increased to above R_{min}, then γ will increase and therefore so will the PSD. If the collision rate required for runaway evaporation is satisfied, and if the PSD is increased, then Bose-Einstein condensation can take place.

From Equations 1.1 and 1.2, it can be seen that the PSD is proportional to both n and $T^{-3/2}$. As discussed earlier in this section, an atom trapped in a 3D harmonic potential experiences a relationship between the volume and temperature which follows $V \propto T^{3/2}$. By simply substituting V into the spatial density, the relationship between PSD with respect to temperature and number of atoms is found to be

$$PSD \propto \frac{N}{T^3} \; . \tag{2.41}$$

The average velocity of the atoms in the trap scales as $v_{av} \propto T^{1/2}$ and the density varies as $n \propto NT^{-3/2}$, so it can be seen that the elastic collision rate scales as $n\sigma v \propto N/T$. An efficient evaporation requires a constant or increasing elastic collision rate and if this is met it can be seen from the scaling relations that the PSD will increase. In the Strathclyde 3D harmonic trap, for efficient evaporation the temperature drop must be faster than the atom loss, therefore

$$d(n\sigma v) = d\frac{N}{T} = \frac{dN}{T} - \frac{NdT}{T^2} = \frac{N}{T}\left(\frac{dN}{N} - \frac{dT}{T}\right) > 0 \; . \tag{2.42}$$

for the drop in temperature to be greater than the loss of atoms $-dN/N < -dT/T$. Since when thinking about evaporation atom loss is considered, both $-dN$ and $-dT$ are positive.

2.5 Bose-Einstein condensation

The phenomena of BEC was first introduced by Einstein in 1924 [10] for a noninteracting gas, where he built on the ideas of Bose, which addressed photons [11]. Since the first experimental observation of BEC in dilute gases in 1995 [26, 27], interest in the field has grown dramatically due to the relative experimental ease and flexibility of these systems.

2.5.1 Mean-field theory

In order to describe the dynamics of a BEC, where interactions are present, one must address the quantum mechanics of a system containing N bosons in an external potential $V_{ext}(\mathbf{r}, t)$. An analogy with quantum optics can be made here: photons are bosons, and the electromagnetic field can be quantised in terms of harmonic oscillator modes [160]. To allow this to be used for BECs, the photon creation and annihilation operators are replaced with $\psi(\mathbf{r})$ and $\psi(\mathbf{r})^{\dagger}$, which are the boson field operators to annihilate and create a particle at position r [161]. By applying the second-quantised approach, the Hamiltonian of the system can be expressed as [162]

$$\begin{aligned} H &= \int d\mathbf{r}\psi^{\dagger}(\mathbf{r}) \left[\frac{\hbar^2}{2m}\nabla^2 + V_{ext}(\mathbf{r}) \right] \psi(\mathbf{r}) \\ &+ \frac{1}{2} \int d\mathbf{r}d\mathbf{r}'\psi^{\dagger}(\mathbf{r})\psi^{\dagger}(\mathbf{r}')V(\mathbf{r}-\mathbf{r}')\psi^{\dagger}(\mathbf{r}')\psi^{\dagger}(\mathbf{r}) \ , \end{aligned} \tag{2.43}$$

where the first term describes the kinetic energy and external potential, and the second term describes the interactions between atoms. Since BECs are dilute and extremely cold systems, only two body interactions contribute to the total interactions via the potential $V(\mathbf{r} - \mathbf{r}')$ and can be described by a single parameter, the s-wave scattering length a. This means the interatomic potential can be replaced with an effective delta-potential of the form [163]

$$V(\mathbf{r} - \mathbf{r}') = g\delta(\mathbf{r} - \mathbf{r}') \ , \tag{2.44}$$

where g is related to the scattering length a by the relation $g = 4\pi\hbar^2 a/m$.

In 1947, Bogoliubov formed the basis of mean-field theory for dilute gases in which the bosonic field operator Ψ is decomposed into two parts. The first creates a particle into a state in which Bose-Einstein condensation can occur, while the other creates a particle in one of all the other states [164]

$$\Psi(\mathbf{r}, t) = \Phi(\mathbf{r}, t) + \Psi'(\mathbf{r}, t) \ . \tag{2.45}$$

Assuming a macroscopic occupation of the ground state, the ground state operator $\Phi(\mathbf{r}, t)$ is now a complex number, which is defined as the total field operator's expectation value

$$\Phi(\mathbf{r},t) = \langle \Psi(\mathbf{r},t) \rangle \ . \tag{2.46}$$

The density distribution of the BEC is fixed by the relation $n_0(\mathbf{r},t) = |\Phi(\mathbf{r},t)|^2$, this can be thought of as the order parameter for the phase transition from a thermal to a condensed state. The function $\Phi(\mathbf{r},t)$ has a well-defined phase, which can be seen as the macroscopic phase of the BEC.

By writing the time evolution of the field operator $\Phi(\mathbf{r},t)$ using Heisenberg's equations of motion with the Hamiltonian (2.43), the result is the time-dependent Gross-Pitaevskii equation [165]

$$i\hbar \frac{\partial \Phi(\mathbf{r},t)}{\partial t} = \left[-\frac{\hbar^2}{2m}\nabla^2 + V_{ext}(\mathbf{r},t) + g|\Phi(\mathbf{r},t)|^2 \right] \Phi(\mathbf{r},t) \ . \tag{2.47}$$

By writing the order parameter as $\Phi(\mathbf{r},t) = \phi(\mathbf{r})^{-i\mu t/\hbar}$, where ϕ is real, this results in the time-independent Gross-Pitaevskii equation [166]

$$\left(-\frac{\hbar^2}{2m}\nabla^2 + V_{ext}(\mathbf{r}) + g\phi^2(\mathbf{r}) \right) \phi(\mathbf{r}) = \mu\phi(\mathbf{r}) \ , \tag{2.48}$$

which reduces to the usual Schrödinger equation in the absence of interactions.

2.5.2 The Thomas-Fermi approximation

In 1927, Thomas [167] and Fermi [168] independently devised a model to approximate the distribution of electrons in an atom, this is known as the Thomas-Fermi approximation and can be applied to atoms in a BEC.

As the number of bosons N increases, the kinetic energy contribution becomes less significant with respect to the interaction energy [169], once N is large enough the kinetic term can be neglected. The parameter that describes when the kinetic term can be discarded is the dimensionless parameter $\zeta = \frac{8\pi N a}{a_r}^{1/5}$, where $a_r = \sqrt{\frac{\hbar}{m\omega_r}}$ is the radial harmonic oscillator length [170]. The ratio between the kinetic and interaction energies is of the order $\zeta^{-4} \sim N^{-4/5}$, which means for just 1000 ^{87}Rb atoms the kinetic energy is only 0.4% of the interaction energy (only valid when using mean trap frequency). This is known as the Thomas-Fermi (TF) approximation and gives the density profile of the ground state in a harmonic trap [14]

$$n_{TF}(\mathbf{r}) = |\Phi^2(\mathbf{r})| = \frac{\mu - V_{ext}(\mathbf{r})}{g} \ . \tag{2.49}$$

For a harmonic trap, the TF approximation yields a density distribution in the shape of an inverted parabola, with the maximum density at the centre of the trap. The density distribution goes to zero at the Thomas-Fermi radius given by [171]

$$R_{r(z),TF} = \sqrt{\frac{2\mu}{m\omega^2_{r(z)}}} \ . \tag{2.50}$$

From Equation 2.49, the chemical potential can be derived in terms of the number of atoms N, the scattering length a and the geometric mean of the trapping potential $\bar{\omega} = (\omega_x \omega_y \omega_z)^{1/3}$ [172]

$$\mu = \frac{\hbar\bar{\omega}}{2}\left(15Na\sqrt{\frac{m\bar{\omega}}{\hbar}}\right)^{2/5} \ . \tag{2.51}$$

2.5.3 Condensate expansion

The formation of a Bose-Einstein condensate is usually observed by time-of-flight, where the cloud is released from the trap and allowed to expand. The condensate shows up as a sharp peak and has a bimodal distribution (see Figure 2.15), as it expands more slowly than a thermal cloud. To be able to model the dynamics of a condensate in a trapping potential, or during expansion, a solution of the GP equation is needed. However, in the Thomas-Fermi regime and using the scaling approach developed by Castin and Dum [173] and Kagan, Surkov and Shlyapnikov [174], the situation can be considered analytically.

In the method, the evolution of a classical gas at zero temperature in a time-dependent harmonic trap is considered. The classical gas initially has a Thomas-Fermi distribution and is in the steady state of the quantum system. Using Newton's equations of motion, and by considering the total force experienced by a particle in the gas, the time-dependent scaling parameter in each dimension, $\lambda_i(t)$ in the i_{th} dimension, can be calculated. The evolution of a condensate with initial size $r_i(0)$ in a time-dependent trap can be completely described by a set of coupled differential equations, where the scaling factors $\lambda_i(t)$ are solutions. This is significantly simpler than calculating a full

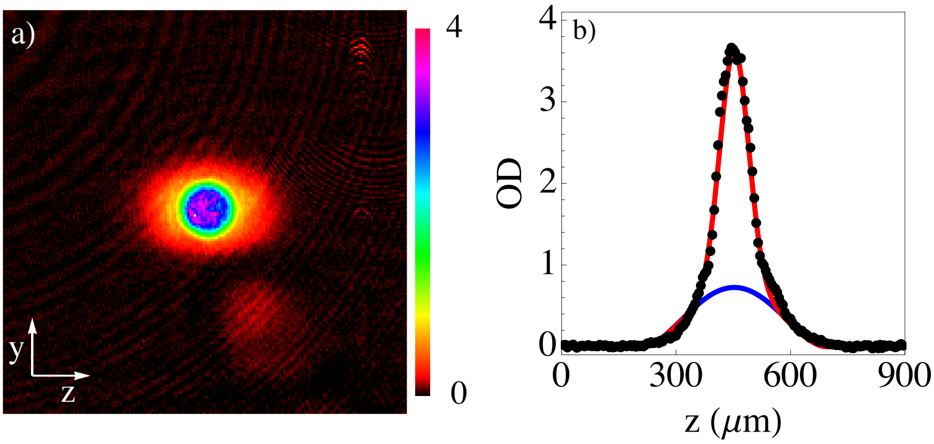

Figure 2.15: Absorption image, bimodal density distribution and fit of BEC. Scale bar represents optical density. a) is an absorption image (900 μm × 900 μm) of a BEC after 20 ms time-of-flight, b) shows the experimental data points of bimodal density distribution (black dots) fitted with a Thomas-Fermi+Gaussian function (solid red line) to the data summed over all rows. The solid blue curve indicates the thermal atoms, i.e. the atoms which are not condensed.

solution of the 3D GP equation.

The trap is described by an anisotropic time-dependent harmonic potential of the form

$$V(\mathbf{r},t) = \frac{1}{2}\sum_{i=x,y,z} m\omega_i^2(t) r_i^2 \ . \tag{2.52}$$

The force experienced by each particle in a classical gas is given by

$$F(\mathbf{r},t) = -\nabla(V(r,t) + g n_{cl}(r,t)) \ , \tag{2.53}$$

where n_{cl} is the spatial density, which is normalised to N. At $t = 0$, the gas is in equilibrium and so $F = 0$ whereas, for $t > 0$ it experiences dilatation and each particle will move along a trajectory given by

$$r_i(t) = \lambda_i(t) r_i(0) \qquad (i = x, y, z) \ . \tag{2.54}$$

Applying Newton's law for the condensate's trajectory implies

$$m\ddot{\lambda}_i(t) r_i(0) = -\frac{\partial V(r,t)}{\partial r_i} + \frac{1}{\lambda_j(t)\lambda_x(t)\lambda_y(t)\lambda_z(t)}\frac{\partial V(r(0),0)}{\partial r_i(0)} \ , \tag{2.55}$$

and by combining this with the trapping potential (2.52), the trajectory (2.54) is a solution of the equation of motion provided the scaling factors satisfy

$$\ddot{\lambda}_i(t) = \frac{\omega_i^2(0)}{\lambda_j(t)\lambda_x(t)\lambda_y(t)\lambda_z(t)} - \omega_i^2(t)\lambda_i(t) \ , \tag{2.56}$$

with the initial conditions $\lambda_i(0) = 1$. For a cylindrically symmetric trap, $\omega_x(0) = \omega_y(0) = \omega_r \gg \omega_z(0) = \omega_z$, and in the case of free expansion, all trap frequencies, $\omega_i(t)$, go to zero at $t = 0$. By introducing a dimensionless time, which has been scaled by the radial trap frequency $\tau = \omega_r t$, the evolution of the scaling parameters 2.56 reduce to

$$\frac{d^2}{d\tau^2}\lambda_r(\tau) = \frac{1}{\lambda_r^3\lambda_z} \ , \tag{2.57}$$

$$\frac{d^2}{d\tau^2}\lambda_z(\tau) = \frac{\varepsilon^2}{\lambda_r^2\lambda_z^2} \ , \tag{2.58}$$

where $\varepsilon = \omega_z/\omega_r$. In our trap where $\varepsilon \ll 1$, since $\omega_z \ll \omega_r$, these have analytic solutions

$$\lambda_r(\tau) \;=\; \sqrt{1+\tau^2} \tag{2.59}$$

$$\lambda_z(\tau) \;=\; 1 + \varepsilon^2(\tau \arctan\tau - \ln\sqrt{1+\tau^2}) \ . \tag{2.60}$$

In this case the condensate expands quickly in the radial direction due to the tighter confinement and interactions whereas the expansion in the axial direction is suppressed by a factor of ε^2.

2.6 Interference

The observation of an interference pattern proves that massive objects have wave characteristics and therewith shows the existence of a phase. Unlike the mass or velocity of particles, a global phase has no actual physical meaning, only the relative phase of two interfering particles has meaning and this manifests itself through interference experiments. However, it has been seen that the phase evolves through the particle coupling to potentials and external fields. By measuring the relative phase between two particles that are travelling in a potential allows conclusions to be drawn on the potential. For this reason, and the fact that atoms couple to electric, magnetic and gravitational fields, their phase opens up a tool to measure unknown quantities and is therefore of great interest. The relative phase between the two particles can be inferred from the interference pattern, but for this to work a source of coherent atoms is needed. The fact that in a BEC all atoms are in the same quantum ground state and can be described by the same wavefunction means that it has one global phase, therefore a BEC is an ideal source of coherent atoms.

2.6.1 Phase of a BEC

A dilute Bose gas which is trapped in an external potential $V_{ext}(\mathbf{r},t)$, and where the scattering length is much smaller than the average distance between particles, Gross [175] and Pitaevskii [176] derived the Gross-Pitaevskii (GP) equation

$$i\hbar\frac{\partial\Psi(\mathbf{r},t)}{\partial t} = -\frac{\hbar}{2m}\nabla^2\Psi(\mathbf{r},t) + V_{ext}(\mathbf{r},t)\,\Psi(\mathbf{r},t) + g|\Psi(\mathbf{r},t)|^2\,\Psi(\mathbf{r},t)\ . \tag{2.61}$$

The GP equation is valid for low temperatures and a large number of atoms in the condensate N_0. The final term describes the atom-atom interaction with the coupling constant $g = \frac{4\pi\hbar^2 a}{m}$, where a is the scattering length and m is the atomic mass. For $a < 0$ this corresponds to a repulsive force, whereas for $a > 0$ this describes an attractive interaction and when $a = 0$ the interactions vanish and the GP equations reverts to the Schrödinger equation. The function $\Psi(\mathbf{r})$, which describes a whole ensemble of atoms within the mean-field approximation, is a macroscopic Schrödinger wavefunction normalised to number of atoms N. This is known as the order parameter and can be written as [165]

$$\Psi(\mathbf{r},t) = \sqrt{n(\mathbf{r},t)}e^{i\phi(\mathbf{r},t)}\ . \tag{2.62}$$

The order parameter has a well-defined phase and the atomic density n is fixed by the relation $n(\mathbf{r},t) = |\Psi(\mathbf{r},t)|^2$ [177].

Under general time-dependent conditions, the phase gradient of a condensate is proportional to its velocity. In the regime where $Na/a_{ho} \gg 1$, the system can be described by the hydrodynamics of superfluids in the collisionless regime at zero temperature [12]. To understand the velocity of a BEC one can use the continuity equation, which is derived by multiplying equation 2.61 by $\Psi^*(\mathbf{r},t)$ and then subtracting the complex conjugate of the resulting equation to obtain [177]

$$\frac{\partial|\Psi(\mathbf{r},t)|^2}{\partial t} + \nabla\left[\frac{\hbar}{2mi}(\Psi^*(\mathbf{r},t)\nabla\Psi(\mathbf{r},t) - \Psi(\mathbf{r},t)\nabla\Psi^*(\mathbf{r},t))\right] = 0\ . \tag{2.63}$$

The above equation can be written in terms of particle density $n(\mathbf{r}, t)$

$$\frac{\partial n}{\partial t} + \nabla[n(\mathbf{r}, t)v(\mathbf{r}, t)] = 0 \ , \tag{2.64}$$

where the velocity of the condensate is defined as

$$v(\mathbf{r}, t) = \frac{\hbar}{2mi} \frac{(\Psi^*(\mathbf{r}, t)\nabla\Psi(\mathbf{r}, t) - \Psi(\mathbf{r}, t)\nabla\Psi^*(\mathbf{r}, t))}{|\Psi(\mathbf{r}, t)|^2} \ . \tag{2.65}$$

Simple expressions for the density and velocity can be obtained if Ψ is written in terms of its amplitude f and the phase ϕ ($\Psi = fe^{i\phi}$ and $n = f^2$), so the velocity of the condensate is now given by [171]

$$v(\mathbf{r}, t) = \frac{\hbar}{m}\nabla\phi(\mathbf{r}, t) \ . \tag{2.66}$$

The velocity field is fixed by the phase of the BEC. A trapped condensate (with no vortices) in the steady state has a vanishing velocity field and from equation 2.66 the phase is therefore constant over the whole BEC. Since, as discussed before, a BEC is a macroscopic occupation of the lowest ground state then intuitively one does indeed expect the atoms to form a uniform phase. Any change to the external potential, V_{ext}, will be the same for each atom in the condensate, therefore the whole BEC, or one of the wells in a double-well potential, will experience a total phase shift.

2.6.2 Matter-wave interference

The macroscopic phase coherence of BECs was first shown by the interference between atoms which were coupled out from a single BEC, now known as the atom-laser [58, 178]. Then Andrews *et al.* showed that two independent BECs interfere when they ballistically expand [64], and since then similar experiments where BECs have been released from optical lattices and interfered with one another have been performed [179, 180].

These experiments, and many others, are closely linked to the question raised by P. W. Anderson [181]: If two superfluids that have never 'seen' each other interfere do they have a definite relative phase? There is now a general agreement that even if the phase isn't initially defined, each experimental realisation will show a distinct phase [182]. This is known as spontaneous symmetry breaking and is a result of the quantum

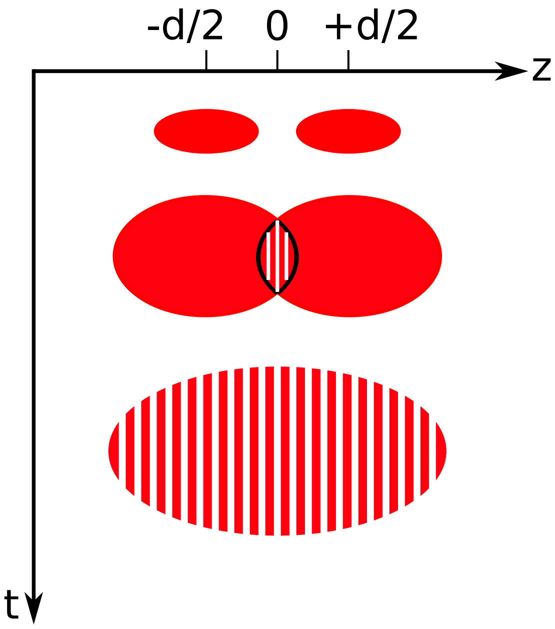

Figure 2.16: Schematic of two interfering BECs. As the two initially separated BECs are released from the trap and overlap with one another interference fringes start to become visible, until the whole cloud has clear spatial fringes across it.

measurement process. For two independent condensates overlapping, high contrast interference fringes are expected but the phase of the fringes should be random for each experimental realisation [183]. Since the nonlinear interactions are important in the system's evolution they lead to an effect known as phase diffusion, which sets a fundamental limit on the phase coherence of split BECs (see Section 2.6.4).

If two BECs, which are initially separated and independent from one another, are released from the trap at $t = 0$, schematically shown in Figure 2.16, and overlap during free fall, then the relative phase [182, 184] between the two clouds can be derived from the resulting interference pattern. The relative phase is defined as [65]

$$\phi_{rel} = \phi_1 - \phi_2 \ , \tag{2.67}$$

the difference of the two individual phases $\phi_{1,2}$. The interference fringes can be described by the mean field picture [185], where the equilibrium wave functions of the two independent condensates are

$$\Psi_{1,2} = \sqrt{n_{1,2}(\mathbf{r},t)} e^{i\phi_{1,2}(\mathbf{r},t)} \ . \tag{2.68}$$

The initial separation of the condensates is denoted by d, with condensate one centred around $z_1 = -d/2$ and condensate two centred at $z_2 = +d/2$. At $t = 0$, the system's initial order parameter is a linear combination of the two individual wavefunctions [177]

$$\Psi(\mathbf{r}) = \Psi_1(\mathbf{r}) + \Psi_2(\mathbf{r}) \ , \tag{2.69}$$

with the overlap of the wavefunctions

$$\int \Psi_1^*(\mathbf{r})\Psi_2(r)d^3\mathbf{r} \cong 0 \ . \tag{2.70}$$

If the interactions between the two condensates is neglected, and only the atom-atom interaction taken into consideration during the free expansion of the clouds, then the total density, $n = |\Psi|^2$, of the overlapping condensates takes the form

$$n(\mathbf{r},t) = n_1(\mathbf{r},t) + n_2(\mathbf{r},t) + 2\sqrt{n_1(\mathbf{r},t)n_2(\mathbf{r},t)}\cos[\phi_1(\mathbf{r},t) - \phi_2(\mathbf{r},t)] \ . \tag{2.71}$$

Equation 2.66 shows a condensate's phase is related to the velocity field, then by making the assumption that the condensate's velocity field asymptotically approaches the classical velocity of the particles, $v_{1,2} = r_{1,2}/t$, then from integration the phase of the condensates is given by

$$\phi_{1,2}(\mathbf{r},t) = \frac{1}{2}\frac{m}{\hbar t}(\mathbf{r} \pm \mathrm{d}) \cdot \mathbf{r} + \text{constant} \ . \tag{2.72}$$

The difference between the two phases at the point $\mathbf{r}$ is then given by

$$\phi_1(\mathbf{r},t) - \phi_2(\mathbf{r},t) = \frac{m}{\hbar t}\mathrm{d} \cdot \mathbf{r} + \phi_{rel} \ . \tag{2.73}$$

The integration constant has been replaced by the relative phase between the condensates, which is an initial and constant offset inside the trap. Since ϕ_{rel} doesn't exist for just one BEC, the properties of the two clouds after the release are the same and the relative phase is independent of position. Therefore equation 2.71 can be written as [65]

$$n(\mathbf{r},t) = n_1(\mathbf{r},t) + n_2(\mathbf{r},t) + 2\sqrt{n_1(\mathbf{r},t)n_2(\mathbf{r},t)}\cos\left(\frac{md}{\hbar t}x + \phi_{rel}\right) \ , \tag{2.74}$$

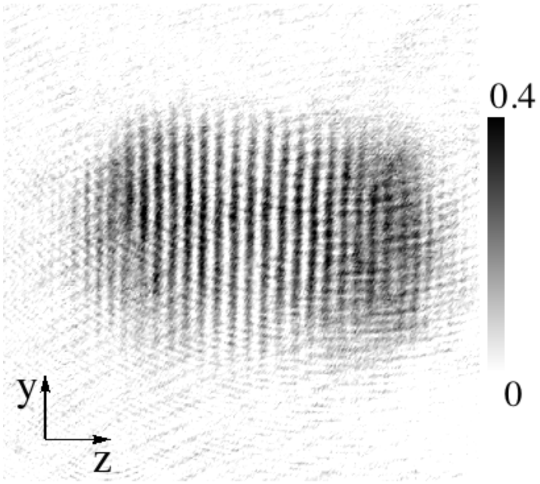

Figure 2.17: Absorption image (1.3×1.3 mm^2) from the Strathclyde experiment of the resulting interference from two condensates overlapping. Scale bar represents optical density. The condensates were initially separated by 40 μm and allowed to expand for 163 ms, this yields a fringe period λ=42 μm.

this shows that the interference fringes (see Figure 2.17) have a period given by

$$\lambda = \frac{ht}{md} \ , \tag{2.75}$$

where t is the time-of-flight and m is the mass of the particle. Since the initial relative phase, ϕ_{rel}, determines the fringe positions, the density distribution of the two overlapping condensates can be used to ascertain the relative phase. This is the basis of how phase measurements are performed using an interferometer.

2.6.3 Coherent splitting of a condensate

The main question that arises when talking about the relative phase between two interfering condensates is: can two BECs be prepared in such a way that for every single shot of an interference experiment there will be a fixed phase? To achieve this a single BEC is split in such a way that it preserves the phase, an analogy to an optical beam splitter. This is done by deforming the single-well potential into a double-well potential, which separates the condensate into two parts as shown in Figure 2.18. The condensate initially occupies the single ground state of the single-well, whilst the system

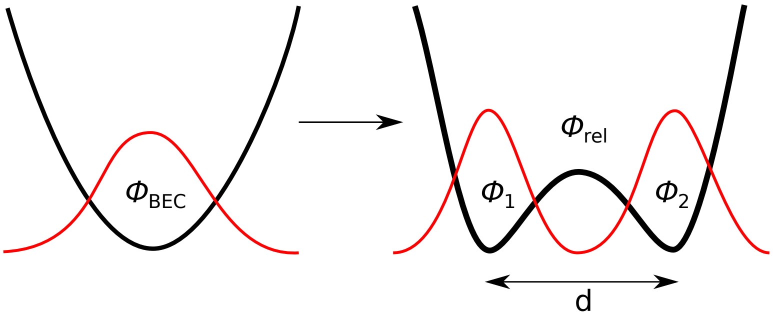

Figure 2.18: Schematic of BEC in a single-well potential being transformed into a double-well, with a BEC in each well where the separation between the two wells is given by d. The condensate in the single-well has a phase of ϕ_{BEC} and when the coherent splitting is performed the BECs have a 'phase memory' of each other and this introduces a relative phase ϕ_{rel}, which initially equals zero, between the two halves.

after the splitting process has two degenerate ground states which correspond to each of the two wells.

For finite splitting times the process cannot be truly adiabatic, which makes the process complicated and has led to many discussions on how best to describe it [186, 187]. However, there is general agreement that by dividing a single condensate into two parts prepares a phase coherent state, which by then interfering the two condensates will always result in the same relative phase. This process doesn't need the initial BEC to have a global phase, the splitting process itself introduces a fixed relative phase between the two condensates. So if the splitting of the condensate is done coherently, then the two halves will have a 'phase memory' of each other which will allow the interference fringes to be used in interferometry.

2.6.4 Phase diffusion

Even if the condensate is coherently split and the two halves have a fixed phase, their 'phase memory' of one another can be lost due to the fundamental process of phase diffusion. By coherently splitting the BEC the relative phase is initialised, this has a narrow distribution, which results in an uncertainty in the atom number in each of the two wells [188]. Assuming Poissonian noise, the fluctuations are of the order $\sqrt{N}$, where N is the total number of atoms. The total energy of the cloud depends on the interactions, therefore any fluctuations in atom number leads to fluctuations in the relative phase and this washes out the phase over many realisations of the experiment

[186]. For 3D condensates, the timescale for phase diffusion is given by [65, 186]

$$T_D = \frac{5\hbar\sqrt{N}}{2\mu} \ , \tag{2.76}$$

where μ is the chemical potential of the BEC. Therefore, the fact that phase diffusion is observed experimentally provides a major technological challenge. Not only does the splitting need to be done coherently, the coherence has to be maintained for long periods of time, unaffected by technical fluctuations or noise. In the Strathclyde experiment, under typical experimental parameters of the interferometry experiments ($\bar{\omega} = 2\pi(10 \times 100 \times 100)^{1/3}$, $N = 5 \times 10^5$) the phase diffusion time is 230 ms, whereas for phase fluctuations experiments ($\bar{\omega} = 2\pi(10 \times 400 \times 400)^{1/3}$, $N = 2 \times 10^5$) $T_D = 65$ ms.

2.7 Coherence - Phase fluctuations

Below the critical temperature T_c, and in equilibrium, fluctuations in the density and phase vanish and the condensate is phase coherent, however, in lower dimensions this is not the case. The Mermin-Wagner-Hohenberg [189, 190] theorem states that true condensation does not occur in 2D and 1D Bose gases at finite temperatures. In 1D traps, which have aspect ratios $\Lambda = \omega_r/\omega_z \gg 1$ between the radial trap frequency ω_r and the longitudinal trap frequency ω_z, density fluctuations are suppressed [191, 192]. However, phase fluctuations along the length of the cloud are present due to thermal excitations and can remain until the temperature drops significantly. The axial excitations with energies $\epsilon_v < \hbar\omega_r$ are the main contributors to the phase fluctuations and have excitation wavelengths which are smaller than the length of the condensate.

In the presence of phase fluctuations the BEC can no longer be thought of as a true condensate but rather now must be referred to as a quasicondensate. At this point, the coherence length is smaller than the condensate size and results in the condensate breaking up into domains with differing phase. After time-of-flight and expansion, the phase fluctuations transform into density fluctuations, which can be observed using absorption imaging. The result of this is matter-wave like interference fringes from the domains of different phase interfering with one another [192, 193]. Phase fluctuations causes the BEC to fragment into several quasicondensates of random phase and size, therefore the resulting matter-wave like interference fringes will have random phase and size with each experimental iteration.

2.7.1 BEC in a 3D elongated trap

Most Bose-Einstein condensate experiments are in a magnetic trap which are cylindrically symmetric, which gives rise to an elongated cigar shaped cloud. The level of the trap's anisotropy is given by the aspect ratio $\Lambda = \omega_r/\omega_z$. In such a system excitations with energies of the order μ can start to exhibit 1D character and result in domains of differing phase along the longitudinal axis of the condensate. In this regime the coherence length of the condensate is shorter than its size.

When a condensate is made in an elongated trap it can begin to cross over from a fully 3D regime to a 1D regime, in which the radial modes are frozen out. Similar to transitions between different quantum regimes in 1D and 3D systems, the crossover from fully 3D to an effective 1D system is very smooth also. F. Gerbier introduced a mean-field theory [194], which is based on a local density approximation, for the crossover regime. For a BEC the energy of the system isn't defined by the temperature T but by the chemical potential μ, therefore for a condensate to be in the 1D regime $\mu \ll \hbar\omega_r$. The dynamics of these systems have been studied in depth. For a more detailed description see Refs [170, 195, 196, 197].

2.7.2 Phase fluctuations in elongated BEC

The phenomena of phase fluctuations in a BEC were first introduced by Petrov *et al.* [198], where it was suggested that a highly elongated condensate could acquire 1D characteristics. The first experimental observation of phase fluctuations in an elongated quasicondensate was by Dettmer *et al.* [192, 193], where the aspect ratio of the condensate was changed and the density modulations after time-of-flight due to phase fluctuations were studied. Other methods that can be used to study phase fluctuations including condensate focussing [199] and Bragg spectroscopy [200, 201, 202]. These fluctuations have practical implications when trying to measure relative phases and perform interferometry, as they can interfere with the interference pattern.

The following analysis is a summary of the work by Petrov *et al* in Refs [191, 198, 203]. Under the condition where $\omega_r \gg \omega_z$, the radial size of the condensate R is much smaller than the axial size of the condensate L. The radial size R and axial size L take the form

$$R, L = \sqrt{\frac{2\mu}{m}} \left(\frac{1}{\omega_r}, \frac{1}{\omega_z} \right) \ , \tag{2.77}$$

where μ is the chemical potential, m is the mass and $\omega_{r,z}$ are the radial and axial trap frequencies. At finite temperature, fluctuations in the phase and density originate from excitations in the condensate. Excitations with energies of the order μ dominate density fluctuations with wavelengths shorter than the radial size of the condensate, hence they are small and have normal 3D character. The field operator for the atoms can be written as

$$\Psi(r) = \sqrt{n_0(r)} e^{-i\phi(r)} \ , \tag{2.78}$$

where $\phi(r)$ is phase operator. The single-particle correlation function can now be expressed through the mean square fluctuations of the phase

$$\langle \psi^\dagger(r) \psi(r') \rangle = \sqrt{n_0(r) n_0(r')} e^{-\Delta^2 \phi(r,r')/2} \ , \tag{2.79}$$

with $\Delta^2\phi(r, r') = \langle |\phi(r) - \phi(r')|^2 \rangle$. The phase operator $\phi(r)$ is given by

$$\phi(r) = \frac{1}{\sqrt{4n_0(r)}} \sum_j f_j^+(r) a_j + h.c. \ , \tag{2.80}$$

where a_j is the annihilation operator of an excitations with quantum number j and energy ϵ_j. The modes $f_j^+ = u_j + v_j$ are excitations of the BEC determined by the Bogoliubov-de Gennes equations.

The excitations can be split into two main groups, low energy axial excitations with energies $\epsilon_v < \hbar\omega_r$, and high energy excitations $\epsilon_v > \hbar\omega_r$. The high energy excitations have wavelengths smaller than the radial size R, these have 3D characteristics and don't contribute to the phase fluctuations. On the other hand, the low energy excitations have wavelengths which are larger than R and start to obtain 1D characteristics, it is these excitations which contribute greatly to the phase fluctuations. The main parameter that is related to experimental measurements is the mean squared amplitude of the phase fluctuations. At the central region of the condensate, $(|z|, |z'| \ll 1)$, the mean square amplitude is

$$\langle |\delta\phi(z, z')|^2 \rangle_T = \delta_L^2 \frac{|z, z'|}{L} \ , \tag{2.81}$$

where δ_L^2 is a measure of the phase fluctuations on a distance scale $|z - z'| \sim 1$ and is defined as

$$\delta_L^2(T) = \frac{32\mu k_B T}{15N_c(\hbar\omega_z)^2} \ , \tag{2.82}$$

where N_c is the number of condensed atoms. This equation can be written as

$$\delta_L^2(T) = \left(\frac{T}{T_c}\right)\left(\frac{N}{N_c}\right)^{3/5} \delta_c^2 \ , \tag{2.83}$$

where the transition temperature $k_B T_c \approx N^{1/3}\hbar\bar{\omega}$ and N is the total number of atoms. The 3D BEC transition in elongated traps requires the inequality $T_c \gg \hbar\omega_r$, this therefore sets a limit on the aspect ratio to $\omega_r/\omega_z \ll N$. The parameter δ_c^2 is defined as

$$\delta_c^2 = \frac{32\mu}{15N_c^{2/3}\hbar\bar{\omega}}\left(\frac{\omega_r}{\omega_z}\right)^{4/3} \ . \tag{2.84}$$

The number of atoms which aren't condensed is small, except from the narrow temperature window just below T_c, which reduces Equation 2.83 to $\delta_L^2 = (T/T_c)\delta_c^2$. This shows that phase fluctuations are prominent when δ_c^2 is large, whereas when $\delta_c^2 \ll 1$ they are small on any length scale and there is a true BEC.

When $\delta_c^2 \gg 1$, the behaviour of the condensate is temperature dependent, therefore a characteristic temperature is introduced

$$k_B T_\phi = \frac{15N_c(\hbar\omega_z)^2}{32\mu} \ , \tag{2.85}$$

at the point $\delta_L^2 \approx 1$. In the region $T_\phi < T < T_c$, the phase fluctuates on a length scale smaller than L. Thus, since the density fluctuations are suppressed, the condensed state is a condensate with fluctuating phase, also known as a quasicondensate. The phase coherence length is expressed as

$$l_\phi = L\left(\frac{T_\phi}{T}\right) \ , \tag{2.86}$$

which typically is bigger than the correlation length (or healing length), $l_c = \hbar/\sqrt{m\mu}$, of the BEC.

Equations 2.85 and 2.86 give the ratio $l_\phi/l_c \approx (T_c/T)(T_c/\hbar\omega_r)^2 \gg 1$, therefore the quasicondensate has the same density profile and local correlation properties as a true condensate but the phase coherence properties are drastically different. In the

Strathclyde experiments on phase fluctuations, typically the aspect ratio $\Lambda = 45$, which results in a condensate with a radial size $R = 2\,\mu$m and an axial size of $L = 82\,\mu$m. The characteristic temperature, T_ϕ, and transition temperature, T_c, were calculated to be $\sim 80\,$nK and $\sim 325\,$nK respectively. The temperature of the phase fluctuations after 58 ms is typically of the order of $\sim 150\,$nK, this results in a phase coherence length $l_\phi = 39\,\mu$m ($\sim L/2$), which is smaller than the axial size of the condensate, hence phase fluctuations are present.

2.7.3 Density fluctuations in time-of-flight

The density distribution of a BEC in the equilibrium state in a trap remains unaffected, even if its phase is fluctuating. The reason for this is that the mean-field interparticle interaction prevents the local field velocities, which come from the phase fluctuations, being transformed into modulations of the density [193]. However, once the condensate has been released from the trap, the mean-field interactions rapidly decrease and the axial velocity fields are then converted into the density distribution [203].

Since the velocity field of a BEC is proportional to the gradient of the phase, to first approximation, phase fluctuations can be mapped onto an initial velocity distribution along the length of the cloud. Density fluctuations at long time-of-flights are a result of interference between components of the BEC with different initial velocities and positions, shown in Figure 2.19. Since the initial phase distribution of these domains is random, the resulting density fluctuations will also vary with each experimental iteration. However average values, such as the mean square amplitude of the fluctuations, should be the same independent of the orientation of the density fluctuations.

For a condensate which is initially in the TF regime and has chemical potential μ, the radially integrated density fluctuations $\delta n(x)$ after time-of-flight t in the time interval $\mu/\hbar\omega_z^2 \gg t \gg \mu/\hbar\omega_r^2$ are given by [192]

$$\frac{\delta n(x)}{n_0(x)} = 2\sum_j \sin\left(\frac{\epsilon_j^2\tau}{\hbar\mu[1-(\frac{x}{L})^2]}\right)(\omega_r\tau)^{-(\epsilon_j/\hbar\omega_r)^2}\phi_j(x)\ , \tag{2.87}$$

where $n_0(x)$ is the radially integrated density for the unperturbed condensate, $\phi_j(x)$ is the phase operator for the jth mode, $\tau = \omega_r t$ and $\epsilon_j = \hbar\omega_z\sqrt{j(j+3)/4}$. The mean

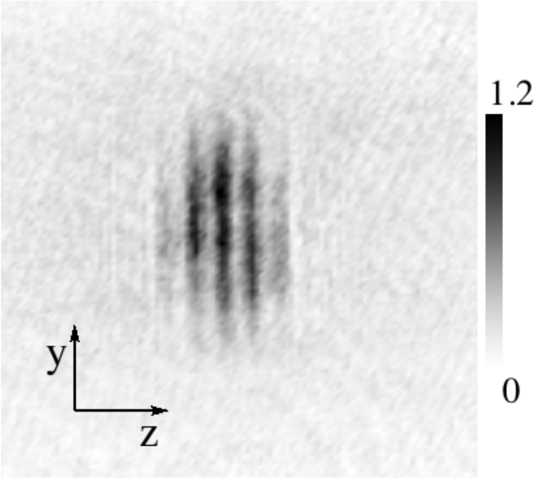

Figure 2.19: Absorption image ($600\,\mu$m $\times 600\,\mu$m) of phase fluctuations in an elongated condensate from the Strathclyde experiment. Scale bar represents optical density. A condensate is formed in a trap with an aspect ratio of 45, it is then allowed to expand for 58 ms. The ratio of the temperature and to the characteristic temperature (T/T_ϕ) was measured to be ~ 2. The matter wave like interference fringes are observed after expansion since phase fluctuations transform into density fluctuations.

square amplitude of the fluctuations, in the central part of the cloud, comes from averaging $(\delta n/n_0)^2$ over different initial phases and is given by

$$\left(\frac{\sigma_{BEC}}{n_0}\right)^2 = \frac{T}{\Lambda T_\phi}\sqrt{\frac{\ln\tau}{\pi}}\left(\sqrt{1+\sqrt{1+\left(\frac{\hbar\omega_r\tau}{\mu\ln\tau}\right)^2}}-\sqrt{2}\right) . \tag{2.88}$$

By measuring $(\sigma_{BEC}/n_0)^2$ in the lab, it can give a measure of how fragmented a condensate is due to the phase fluctuations. The temperature can also be estimated from this, as long as the trap frequencies, chemical potential and time-of-flight are known accurately, although if possible it is better and more accurate to calculate the temperature from the wings of the Gaussian.

Chapter 3

Experimental setup

3.1 The laser system

In laser cooling, one of the most important requirements for a good MOT is a stable laser system. The hyperfine structure of atoms sets underlying limits that the lasers must meet in order to be an effective light source for cooling and trapping. A MOT's atom number is extremely dependent on the frequency of the laser [204], therefore stable frequency is a necessity in laser cooling. The D2 transition in Rubidium has a line width of $\Gamma = 6.07$ MHz [122], therefore to be capable of addressing the individual transitions of the atom and obtain accurate detuning values for the various steps of the experimental sequence, MOT lasers must be stabilised to the 1 MHz level for effective laser cooling.

Although semiconductor diodes are relatively inexpensive, compact and simple devices, they still have a major role in optical and atomic physics. These diodes, combined with some additional components, can supply suitably stable light for laser cooling experiments. A basic laser diode, which has a short cavity, typically has a linewidth of $\sim$100 MHz and also has poor tunability [205]. The narrow linewidth and tunability required can be achieved by having an external, frequency selective, optical feedback using an external-cavity diode laser (ECDL) [206]. Another method for achieving narrow linewidths, which uses an acousto-optical modulator (AOM) to produce dispersion-like error signals to which the laser can be locked and stabilised to, was reported in Reference [207].

3.1.1 ECDL - Repump laser

An ECDL works by sending laser light from the diode back into the cavity, this is done using a diffraction grating, which is mounted in the Littrow configuration [208]. The angle of the grating can then be used to provide tunability by allowing the wavelength of the feedback to be selected. Using a piezo (PZT) allows a wide range of frequencies to be achieved very accurately, the resulting high level of tunability is key in selecting the correct wavelength. A schematic diagram of the ECDL is shown in Figure 3.1, which shows the three key ECDL components; the laser diode, the collimating lens and the diffraction grating. The laser diode is a Sanyo DL-LS1027 which lases at 780 nm with ∼50 mW, the collimating lens is an aspheric optic with a focal length of 6.2 mm and the diffraction grating is a gold-coated (1800 lines/mm) holographic grating on a $15 \times 15 \times 3$ mm^3 substrate. A more detailed description of how to construct a ECDL and technical information can be found in Reference [205]. It is this laser design that is used for our repump laser.

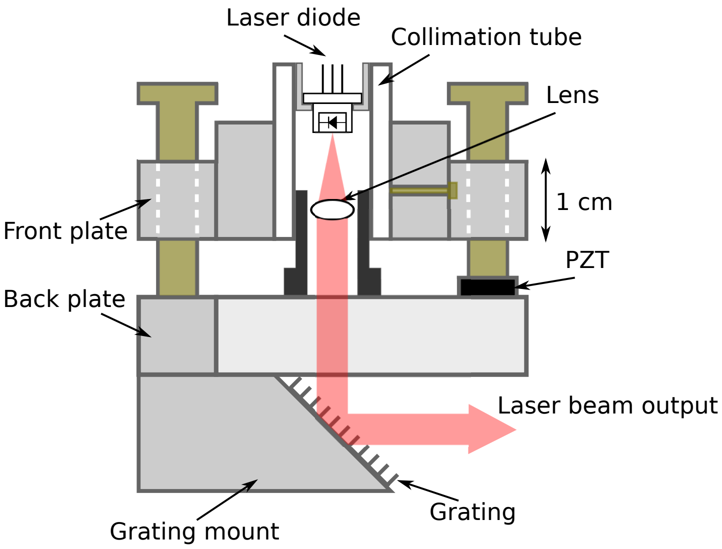

Figure 3.1: Schematic diagram, viewed from above, of a extended-cavity diode laser.

3.1.2 Trap and dipole beam lasers

The repump laser is ‘less important’, but still essential, in the laser cooling system and for this reason doesn’t require as much power. The reason for this is there is a smaller

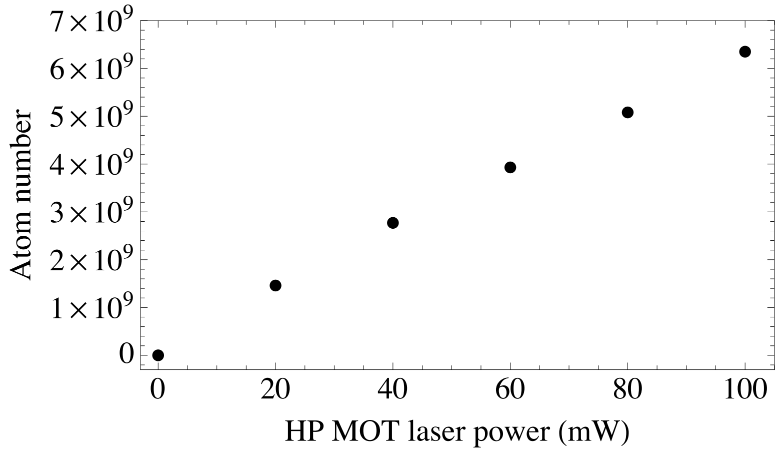

Figure 3.2: MOT atom number as a function of MOT beam power. Fluorescence was detected using a large area photo diode, the output of which was then converted into atom number. Beam power was changed by altering a $\lambda/2$ plate, which changed the amount of light sent to the MOT.

probability for an atom to decay to the $F = 1$ state and be lost from the cooling cycle, for ^{87}Rb, the repump is only needed once for every 1000 absorption cycles. However, the atom number increases with increasing cooling laser power (shown in Figure 3.2), for this reason a commercial laser is used for the cooling light. For cooling, a Toptica DLX100 is used, which lases at 780 nm with 1 W of power and supplies light to both the high pressure (HP) and low pressure (LP) MOTs simultaneously. One major advantage of the DLX is the built in optical fibre output, which not only helps with alignment but also improves the beam quality. Unlike diode lasers, which have a natural elliptical beam shape, the DLX output has a 1 : 1 aspect ratio eliminating the need for beam shape correction optics. We run the DLX at half power (for longevity of the laser diode) and at the output of the fibre this gives us ∼250 mW, which is then split between the HP, LP, push beam, optical pumping and imaging system.

The laser used to split the BEC is known as the dipole beam, which is a free running 658 nm laser diode with ∼ 100 mW of power. The large detuning from the atomic resonance of this beam means that such precise wavelength control is not needed and hence an ECDL is not used (as long as drifts in wavelength are within experimental noise). A more detailed description of the dipole beam setup will be discussed in Section 3.3.3.

3.1.3 Temperature and current controls

In order to have the appropriate laser frequency stability, attention needs to be paid to the temperature and current of the system, as small changes in these parameters can affect the laser frequency [209]. By placing the laser in a boxed enclosure one can isolate it from changes in environmental temperature and allow the laser to be locked, which actively stabilises the laser, to a known frequency using a rubidium saturated absorption spectrum as discussed in the following section.

Additional temperature control was created using using a FTP-4000 laser driver and temperature controller, which is connected to a Peltier thermoelectric cooler (PTC). By using a thermistor, which provides feedback to the temperature controller, the temperature can be measured accurately. The controller is dependent on a low noise power supply. Current is supplied to the diode via a Thorlabs LD1255R current controller, which is housed in an enclosed box; the driver allows a constant current, up to 250 mA, to be applied to the laser. Under usual experimental conditions it operates at ~150 mA.

3.1.4 Talking to the laser - absorption spectroscopy

To be able to 'talk' to the atoms, the laser has to be 'told' the correct frequency to use. Absorption spectroscopy allows the atomic transitions to be mapped out onto a photodiode. This frequency dependent signal provides a frequency reference for the laser [210]. The ground states of ^{87}Rb are connected to the excited states via the D1 and D2 absorption lines (see Figure 2.1), with cooling operating on the D2 transition. On this cooling transition the transition rules ($\Delta F = -1, 0, 1$) allow 3 atomic transitions for each of the hyperfine ground states. The frequency spacings between the excited hyperfine splittings of the 5p $^2\mathrm{P}_{3/2}$ are: $\sim$ 72 MHz between $F' = 0$ and $F' = 1$, $\sim$ 157 MHz between $F' = 1$ and $F' = 2$ and $\sim$ 267 MHz between $F' = 2$ and $F' = 3$ [122].

The resolvability of the hyperfine structure gives a stable and reliable frequency reference, which can then be used to lock the lasers frequency [211]. However, Doppler broadening of the absorption profile ($\sim$ 500MHz) hides the hyperfine structure and prevents acquisition of a reference frequency. To overcome this issue a Doppler-free spectrum is needed which will allow the hyperfine structure to be seen. Narrow absorption features on the scale of the natural linewidth can be achieved using saturated ab-

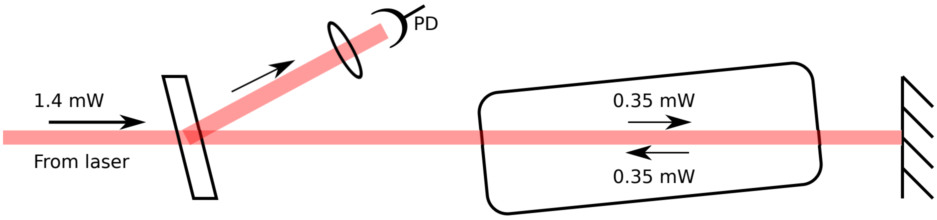

Figure 3.3: Trapping laser saturated absorption spectroscopy setup. The incoming single beam is a direct pick-off from the DLX (1.2 mW) which passes through a beam splitter to reduce the beam's intensity. The BS directs 0.35 mW through the absorption cell, which is retroreflected back by a mirror. The incoming beam is referred to as the pump beam and the reflected beam is known as the probe beams. The BS then sends a fraction of the pump beam through a lens into the photodiode.

sorption spectroscopy, hence allowing the three atomic transitions to be resolved from the Doppler-broadened profiles. This is achieved by counter-propagating the beam through a rubidium vapour cell in a pump-probe arrangement, the Strathclyde saturated absorption setup is shown in Figure 3.3. The resulting absorption signal on the photodiode gives a frequency 'map' that can be used to lock the laser's frequency. Corrections to the laser's frequency can be made by changing the diode's current or altering the cavity length via the piezo-electric transducer (PZT), which is attached to the diffraction grating.

When the laser passes through the cell, and is resonant with the atomic transition, the atoms will absorb photons. The pump beam makes all atoms resonant with the laser and reveals the Doppler broadened spectrum, then the counter-propagated probe beam can be used to resolve the hyperfine structure. Whilst the pump and probe beams have the same frequency, they interact with two different velocities of atoms due to the beams propagating in opposite directions

$$\mathbf{k} \cdot v_{\text{pump}} = -\mathbf{k} \cdot v_{\text{probe}} \ , \tag{3.1}$$

where v is the laser frequency. When the frequency from both beams matches the atom's resonance, then both lasers interact with the same atoms. At this point the pump beam saturates the transition (equal populations in ground and excited state) and makes the probe beam free from absorption, resulting in the hyperfine structure being resolved. The multiple excited states result in the existence of the useful phenomenon of crossover peaks. They occur when the frequency of the laser is equal to half of the

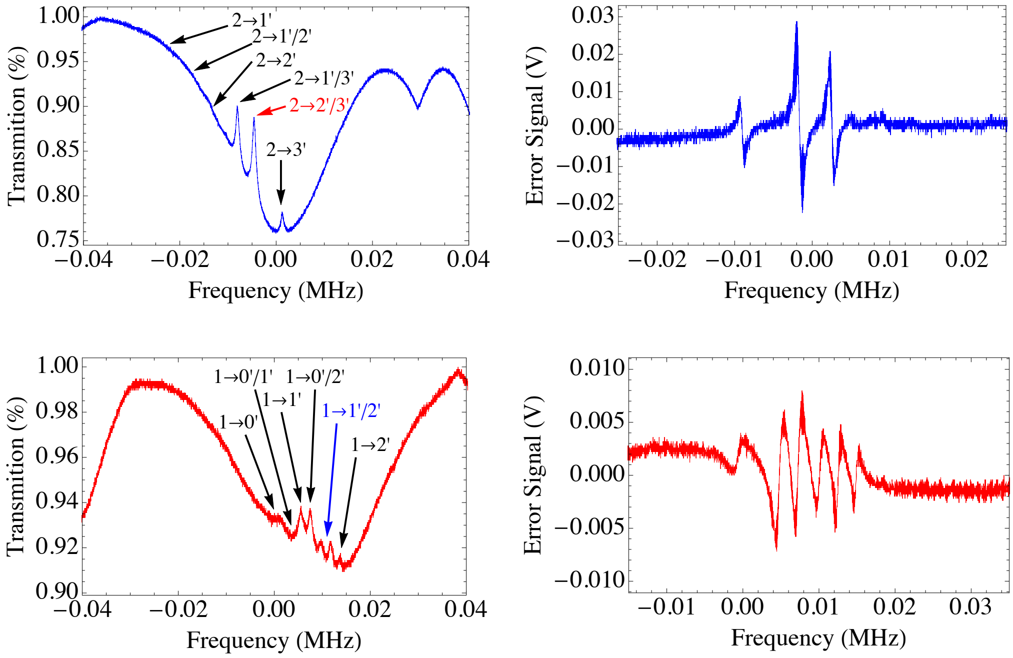

Figure 3.4: Experimental saturated absorption spectra of ^{87}Rb $F = 2 \rightarrow F'$ (top) and ^{87}Rb $F = 1 \rightarrow F'$ (bottom) and their corresponding error signals for locking the laser (right). Arrows represent transitions and cross-over peaks. Coloured arrows denote the peak at which the lasers are locked to.

spacing between two states, and can be used as frequency references as they produce the largest reduction of transmission (see Figure 3.4 for experimental saturated absorption spectra). For a more detailed explanation of saturated absorption spectroscopy see references [210, 211, 212].

The two important mechanisms when discussing saturated absorption spectroscopy are saturation and hyperfine pumping [212]. Both mechanisms are velocity dependent and alter the populations in the atomic states. In a two-level atom the saturation effect imposes a population limit between the ground and excited states, in the regime $I \gg I_{sat}$, a limit of 50% of the population in the excited state can be reached. Whereas, in a multi-level atom there is multiple ground states available from the excited states.

3.1.5 Locking the laser

Locking the laser to a saturated absorption feature is difficult due to a voltage offset in the lock, which if the beam's intensity fluctuates will change the laser frequency.

Moreover, the lock point will be near a turning point of the photodiode signal, making it incredibly sensitive to any drifts. For this reason, in Strathclyde we utilise a technique known as dither locking, which is based on frequency modulation of the PZT scan. By combining the photodiode signal with the frequency modulation, the derivative of the signal (i.e. dispersion curves) can be seen. Derivative signals are particularity useful as they have a linear response with frequency (and a zero crossing) near the centre of the absorption line. An integrator can then be used to lock to the zero crossings in the derivative signals [213], which correspond to the peaks of the absorption line. Applying a small modulation to the laser frequency used in the saturated absorption and by taking the product of the applied modulation and the modulation on the photodiode, this gives a signal proportional to the derivative of the saturated absorption signal. This signal can then be used as the error signal for the integrator, which then allows the lock point to account for any drifts in frequency, this assures a stable laser frequency.

3.1.6 Shifting the frequency

As mentioned in Section 3.1.4, when doing saturated absorption spectroscopy other useful features known as crossover peaks can be seen. The trap laser is locked to the $F = 2 \rightarrow F' = 2/3$ crossover peak, meaning it is 133.7 MHz red detuned from the main $F = 2 \rightarrow F' = 3$ resonant cooling transition. The frequency offset can be accounted for by using an acousto-optical modulator (AOM), which up-shifts the frequency of a beam passing through by an amount equal to that of the RF signal fed into the AOM. The AOM shifts the trap laser's frequency to the blue by $133.7 - \Delta_{\text{trap}}$ MHz, where Δ_{trap} corresponds to the detunings used for the HP and LP MOTs. The typical experimental detunings for the HP and LP MOTs are $\sim$ 22 MHz and $\sim$ 16 MHz respectively.

The repumper, just like the trap, needs to be adjusted to the correct frequency but as it interacts with different atomic states, another AOM is needed. The repump is locked to the $F = 1 \rightarrow F' = 1/2$ crossover peak, which is ± 78.4 MHz from the two closest $F' = 1$ and $F' = 2$ resonant transitions. The AOM shifts the repump 78.4 MHz to the blue to the main resonant repumping transition, $F = 1 \rightarrow F' = 2$.

The experiment has a total of five AOMs, three are used to control the trap and repump light for the HP and LP MOTs, one for transferring the atoms from the HP to LP MOT, known as the 'push beam', and a final AOM for controlling the dipole beam (see Section 3.3.3). The push beams AOM shifts the frequency by 133.7 MHz back to the resonant $F = 2 \rightarrow F' = 3$ transition, this pushes the atoms from the HP to LP MOT by resonant light scattering. This light is also used for imaging of the BEC, a polarising beam splitter (PBS) reflects a fraction of the light into a fibre for imaging and the transmitted is used for pushing the atoms. The light that is coupled into the fibre is not only used for imaging of the condensate, but also for optical pumping (see Section 4.2 for full details) into the desired m_F state. The $F = 2 \rightarrow F' = 2$ resonant transition is used for the optical pumping (σ_+) light, this is achieved by unlocking the laser and jumping the frequency by $\sim$ 270 MHz to the red, then jumped back to original frequency before being relocked. The laser lock can be broken by implementing a switch between the lock-in output and the integrator input. A digital signal from the computer unlocks the laser and then a current is injected into the laser using the 'scan' input through a 15 kΩ resistor such that 120 mV corresponds to $\sim$270 MHz. For optical pumping the laser is unlocked for 1 ms and then relocked when returned back to its original frequency, this technique is only possible due to good laser stability.

3.2 Double MOT setup - HP and LP MOTs

The idea behind having a double MOT setup is to differentially pump two experimental chambers and then seperate them by some distance. A general rule of thumb for magnetic lifetimes in a lab is that for a pressure of 10^{-9} Torr, a 1 s lifetime is expected [214]. As the pressure is lowered, the amount of background gas collisions decreases, meaning there is a strong dependence between the pressure and the magnetic lifetime. So for pressures of 10^{-10} and 10^{-11} Torr, lifetimes of 10 s and 100 s respectively can be achieved. The rubidium used in the experiment is supplied by heating rubidium dispensers (getters), which affects the high pressure (HP) chamber's pressure. So when atoms are being added to the vacuum by heating the getters the pressure increases. For this reason the getters are only run approximately once per day, which provides enough rubidium to produce BECs and run the experiment. While the getters are off, the pressure in the HP and low pressure (LP) chambers are $\sim 10^{-9}$ and $\sim 10^{-11}$ Torr respectively.

The Strathclyde vacuum system, depicted in Figure 3.5, is constructed from stainless steel, which is free from any magnetisation effects. The HP chamber's design allows trap and repump beams access through glass viewports, which are anti-reflection (AR)

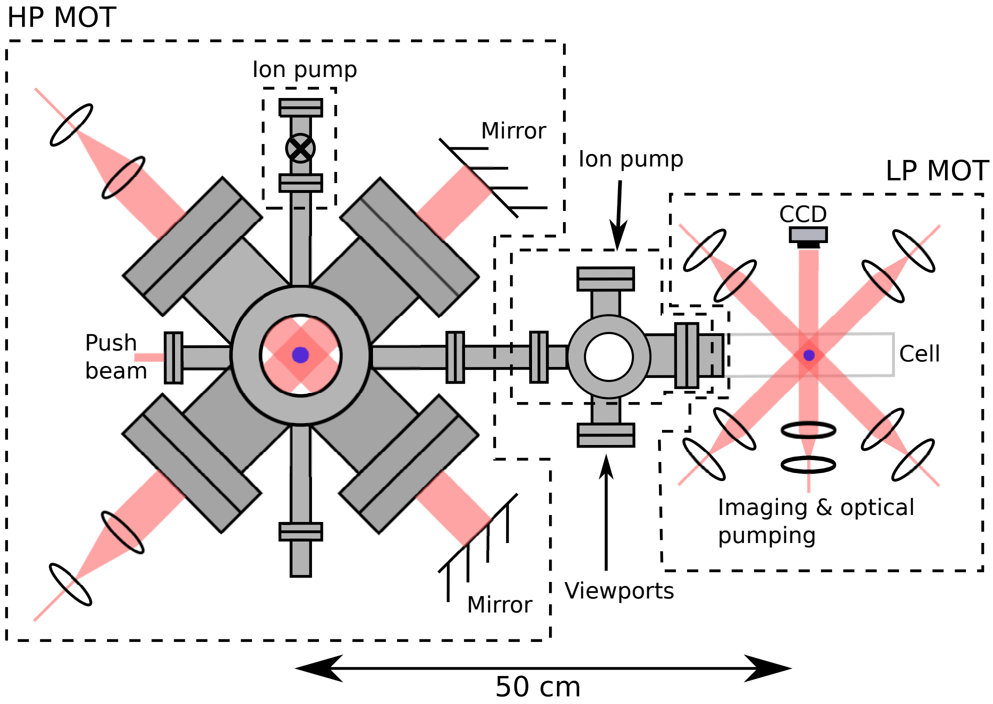

Figure 3.5: Strathclyde's double MOT optical setup viewed from above. The trap and repump lasers provide light for both the high pressure (HP) and low pressure (LP) MOTs. The push, optical pumping and imaging beams are derived from trap laser. The three trap and repump beams for the HP MOT are retroreflected by mirrors to provide a six beam MOT. The push beam pushes the atoms through a transfer tube into the LP MOT which has six trap and repump beams. The centres of both MOTs are separated by approximately 50 cm.

coated for normally-incident 780 nm light. In the double MOT arrangement, the HP MOT acts as the atom source for the LP MOT, and can be used to repeatedly load the LP chamber [215]. The loading rate of the LP MOT is dependent on the number of atoms in the chamber, this can be controlled by changing the current passing through the SAES alkali metal dispensers [216, 217]. The two MOTs are connected via a 30 cm transfer tube, a specially designed quartz vacuum cell is used at the LP MOT end instead of a stainless steal chamber. The LP MOT is formed within a 'square doughnut' shaped cell, which has $12.5 \times 12.5\,\mathrm{cm}^2$ sides as shown in Figure 3.6. The unique shape of the vacuum cell not only allows a MOT to be formed but is also ideal for a toroidal magnetic storage ring (Section 3.3.4).

Stable lasers and a good vacuum system are only the first step to creating a magneto-

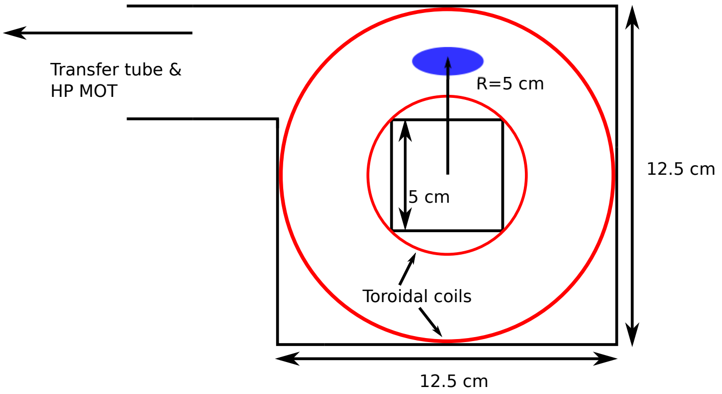

Figure 3.6: Strathclyde's 'square doughnut' quartz vacuum cell viewed from the side. The cell has side-lengths of 12.5 cm and a $5 \times 5\,\mathrm{cm}^2$ 'hole' in the middle. The toroidal coils (red) have diameters of 12.5 and 7.5 cm and the atom cloud forms $\sim$ 5 cm from the centre of the 'hole' in the cell.

optical trap, these elements must be combined with a variety of optical components, a schematic diagram of this is shown in Figure 3.7 (not all optical components are shown). All these elements must be implemented and aligned with a high level of precision in order to create a stable system and MOT.

As mentioned previously, the HP and LP MOT beams are derived from one repump ($\sim$ 45 mW ECDL) and one trap laser ($\sim$ 250 mW Toptica DLX). Both the HP and LP MOTs have separate beam expanders (10× for HP and 14× for LP), which allows a different beam size and collimation for each MOT. Periscopes are used to raise the horizontal MOT beams to $\sim$ 20 cm so they can enter the vacuum chamber through the viewports and interact with the atoms in the HP chamber and LP cell. The beam intensities of the individual trapping (repump) beams are measured frequently to ensure a consistent experiment, which was done using the photodiode head of a power meter. The 1 cm^2 square photodiode head was illuminated by each of the beams and the maximum power was recorded. The HP trap (repump) beams yield intensities of $I_x = 7.1$ (0.26) mW/cm^2, $I_z = 6.5$ (0.22) mW/cm^2 and $I_y = 5.8$ mW/cm^2. Similarly, the LP MOT beams were measured to be $I_{+x} = 2.2$ (0.32) mW/cm^2, $I_{-x} = 2.7$ (0.28) mW/cm^2, $I_{+z} = 2.5$ (0.29) mW/cm^2, $I_{-z} = 1.9$ (0.29) mW/cm^2, $I_{+y} = 2.1$ mW/cm^2 and $I_y = 2.4$ mW/cm^2. Note there is no vertical repump in either the HP or LP MOTs. The HP MOT uses three retroreflecting mirrors, hence the total intensity is given by $I_{HP(tot)} = 2(I_x + I_y + I_z)$. The number of atoms in the MOT is sensitive to the beam

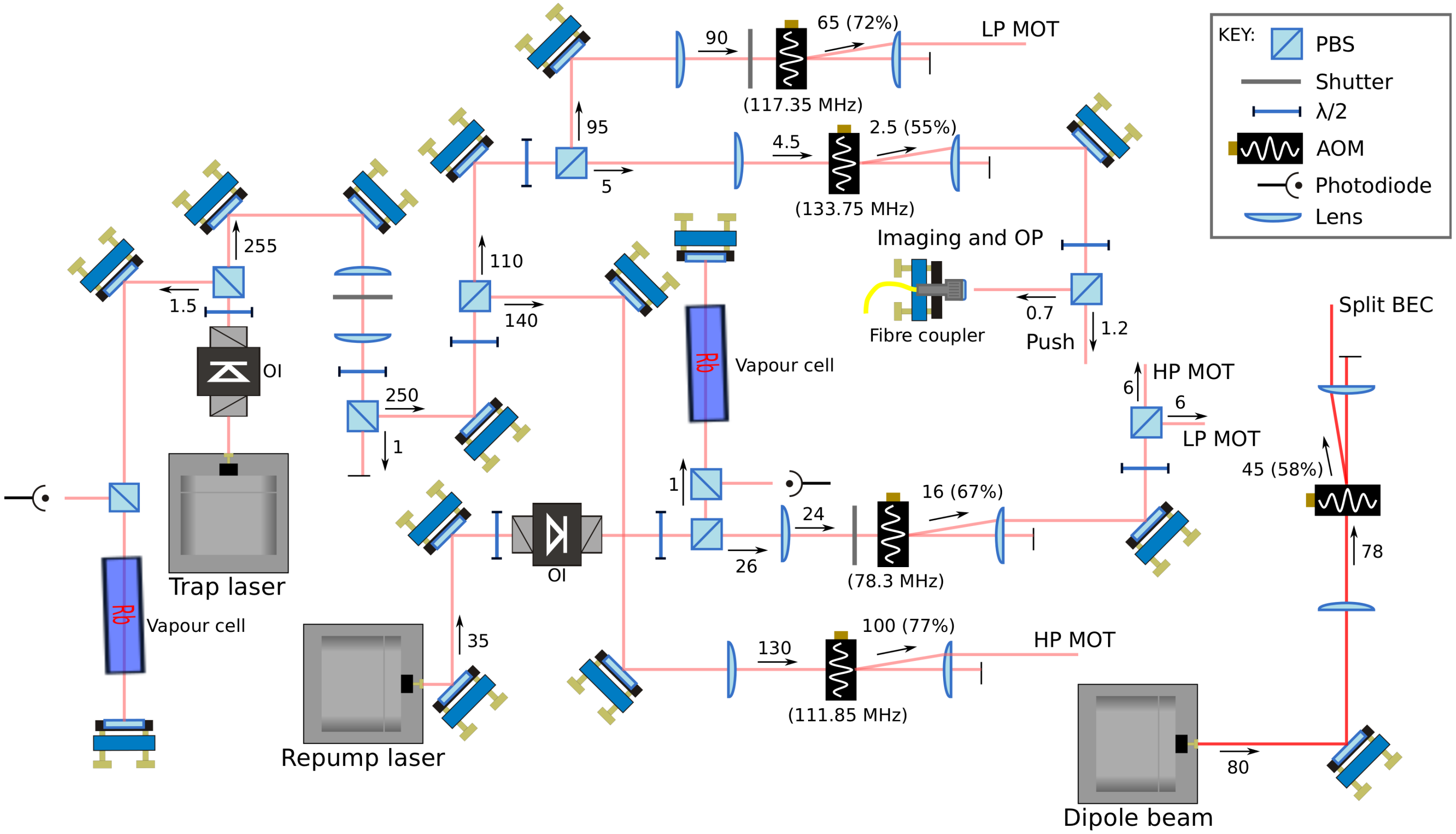

Figure 3.7: Strathclyde's optical setup: Schematic diagram of optical table showing the individual beam paths for the repump and trap lasers. Both HP and LP repump beams pass through same AOM whereas HP and LP trap beams pass through separate AOMs. Push, optical pumping and imaging beams are all derived from the trap laser. Arrows and numbers indicate the direction and amount of laser light and the numbers in brackets under AOMs indicate frequency of RF input.

alignment, but the intensity imbalance is relatively forgiving. Even with an imbalance of ∼ 20%, it is still possible to achieve a stable MOT with a large atom number.

As mentioned previously, the incoming HP beams are retroreflected back through the chamber to interact with the atoms and ensure an even restoring force towards the centre of the MOT. This process of retroflection can cause unwanted feedback via retroreflected MOT laser light entering the laser diode. To avoid this a -40 dB (LINOS FI-780-5 SV-BB) and a -60 dB (LINOS FI-790-TV) optical isolator (OI) are used in the repump and trap beam respectively. Another key component in the optical setup are shutters, which eliminate any stray unwanted light reaching the atoms, which is advantageous as stray resonant light can heat the the atoms in the MOT and decrease the magnetic lifetime. In the Strathclyde experiment three shutters are used (LS6T2 Uniblitz): one after the fibre in the trapping beam, one before the LP MOT AOM and one in the repump beam. The shutters, in combination with the AOMs, completely

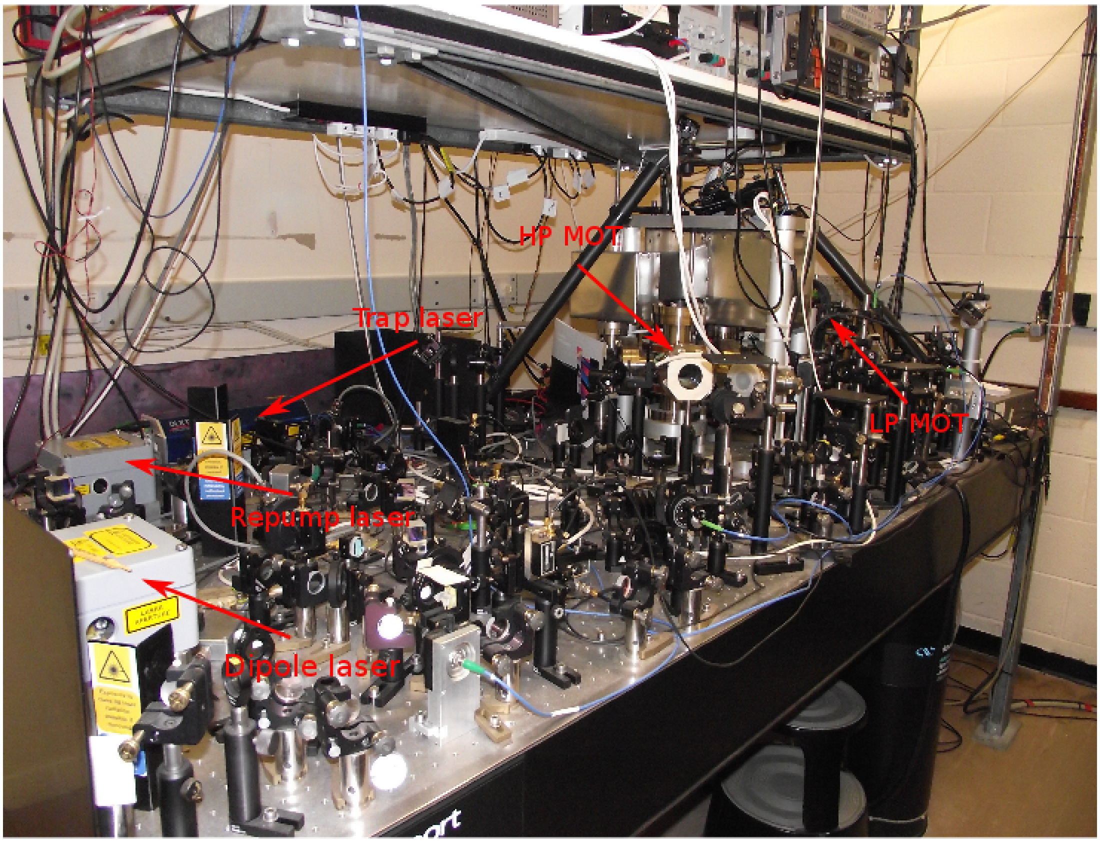

Figure 3.8: Strathclyde University BEC experiment optical setup (2015).

eliminate any stray light from reaching the atoms. Figure 3.8 shows the Strathclyde experiment's optical setup.

3.3 Four traps in one

In Section 3.2 the experimental setup of the double MOT was introduced, in which two separate quadrupole fields are used for trapping atoms in a MOT. The magnetic field used to create the HP MOT is generated from a pair of circular coils in the anti-Helmholtz configuration. However, the magnetic field which forms the LP MOT is produced from a combination of different coils. The Strathclyde coil configuration (Figure 3.9) allows the realisation of different magnetic geometries:

- 3D magnetic quadrupole field used for MOT
- Ioffe-Pritchard trap
- double-well potential to split BEC
- toroidal magnetic storage ring

This results in a high level of flexibility and control of the magnetic field at the LP end.

By using the hybrid trap, the lossy process of transferring the atoms from the MOT to a separate magnetic trap can be avoided. The unique setup allows ensembles of cold atoms and BECs to be created in a section of the ring, removing the need for transfer between the magnetic trap and the storage ring. Another advantage when using the hybrid trap is that it can be operated using the same power supplies. The Strathclyde hybrid trap consists of a combination of current carrying wires:

- four two-turn circular coils, 2 × 12.5 cm and 2 × 7.5 cm diameter
- four three-turn square coils, with side lengths of 7.5 cm
- a single straight wire

The schematic of the hybrid trap is shown in Figure 3.9.

The four two-turn circular coils are used to generate a 2D toroidal magnetic quadrupole field and to supply the ring confinement for the atoms. The four, three-turn, square coils, also known as the 'pinch' coils, are used for both the MOT and the Ioffe-Pritchard

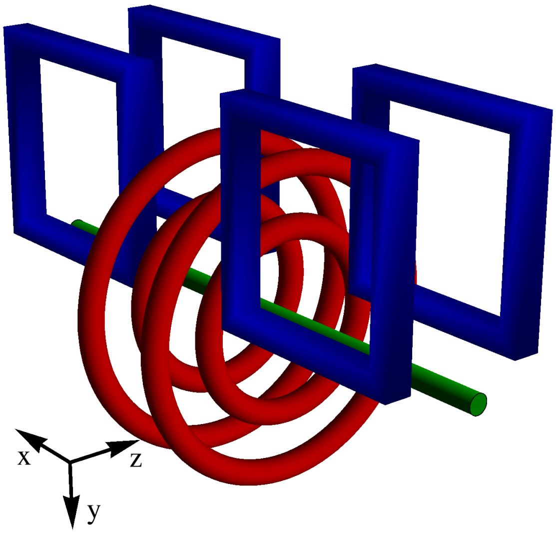

Figure 3.9: Schematic diagram of magnetic coil system of the Strathclyde storage ring. Four circular coils (red) with diameters of 12.5 and 7.5 cm generate the storage magnetic field minimum with average radius of 5 cm. The four square 'pinch' coils (blue), with side lengths of 7.5 cm, trap the atoms is the MOT or IP depending on their current direction. The straight azimuthal wire (green) adds an additional azimuthal magnetic field, which removes the zero field from the toroidal quadrupole field from the circular coils.

trap. Changing the current direction in the four pinch coils switches between the MOT and IP configurations. When the pinch coil pairs are in anti-Helmholtz configuration the trap operates in MOT mode, whereas when the pinch coil pairs the trap Helmholtz configuration the trap switches to IP mode. By having a different ratio of currents in the pinch coils this can produce a magnetic field gradient, which can be used to split the condensate inside the ring. The single straight wire produces a bias field at the centre of the toroidal quadrupole field. This azimuthal magnetic field is essential as it removes the zero field line, which is a result of the toroidal quadrupole field, and stops the atoms being lost due to Majorana spin-flips [144].

The four circular coils and four square coils, when operating at maximum current, produce magnetic fields using two-turn×500 A coils (circular) and three-turn× 500A coils (square), which produces a total power of 2.5 kW, therefore the power in the system must be dissipated and the heating reduced. The system is prevented from overheating by using copper rectangular cross section pipes, which allows internal cooling water to flow while the coils are in operation.

3.3.1 MOT configuration

When in the MOT configuration the hybrid trap creates a magnetic field using a combination of fields from the circular and square coils, which results in maximum field gradients of $(210, -170, -70)$ G/m in the (x, y, z) directions respectively. Using this combination of coils, and by adding a three-dimensional spatially constant offset field (bias field), the location of the MOT centre can be changed. The MOT magnetic field contours can be modelled using the Biot-Savart law for circular and square coils, as shown in Figure 3.10. The larger radial gradient when operating in the MOT configuration leads to a slightly elongated magnetic field, which results in the MOT atom cloud having a 3D ellipsoid shape. Ensuring the MOT's centre is aligned with the centre of the IP trap helps prevent any unwanted effects when loading the IP from the MOT.

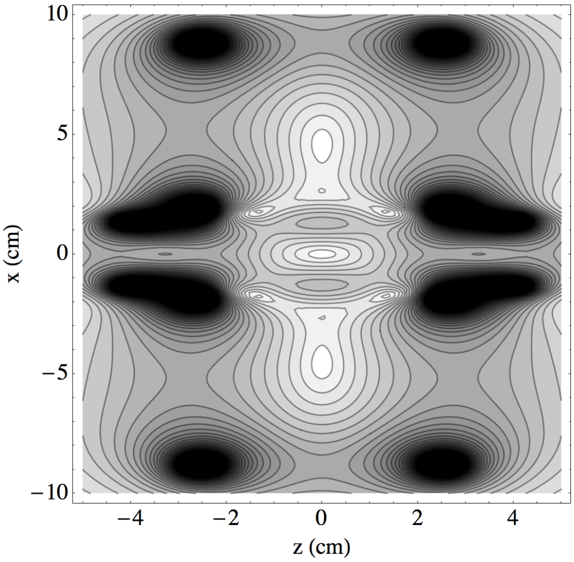

Figure 3.10: Top view of the magnetic field contour plot when coils are in MOT configuration (slice through magnetic field at $z = 4.8$ cm). Regions of black indicate the circular and pinch coils. Pair of square coils with current flowing in opposite directions create a 3D quadrupole with field minimum at the centre.

3.3.2 Ioffe-Pritchard configuration

The Ioffe-Pritchard (IP) magnetic trap is generated when the pinch coils operate in a Helmholtz configuration (i.e. current flowing ion the same direction), with an additional field from the compensation coils (typically $B_1 = 230$ G/cm and $B_2 = 60$

G/cm^2). Care must be taken to match not only the MOT and IP trap centres but also their curvatures to avoid any sloshing or breathing in the system. The theoretical magnetic contour plot of the trap in IP mode, without any magnetic field from the compensation coils, is shown in Figure 3.11.

The transition between the MOT and IP configurations is implemented experimentally after the atoms are further cooled during optical molasses. After this the IP trap is switched on and compressed over $\sim$ 400 ms, hence increasing the atomic ensembles density and temperature. Creating the compressed trap increases critical parameters and allows further cooling of the ensemble through evaporation procedures. Preparing the cold atom sample or condensate in the top section of the ring allows them to be either split into a double-well potential or launched into the magnetic storage ring, which is provided by the circular coils.

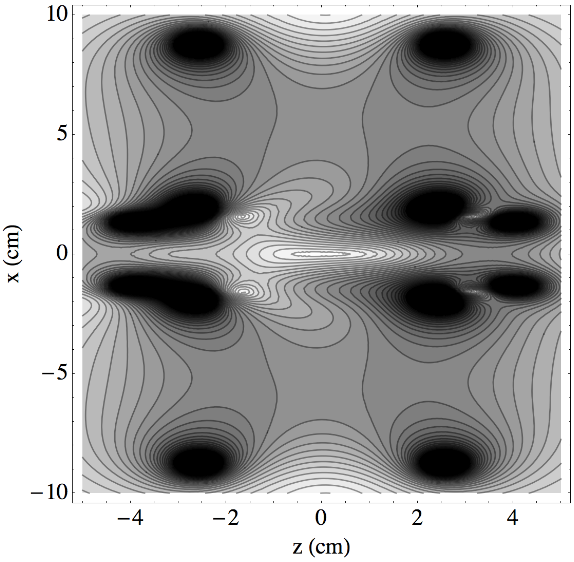

Figure 3.11: Top view of the magnetic field contour plot when coils are in IP configuration (slice through magnetic field at $z = 4.8$ cm). Regions of black indicate the circular and pinch coils. All square coils have current flowing in same direction to generate IP field. Note that symmetry is broken at ‘large’ distances from centre due to higher order terms.

3.3.3 Double-well potential configuration

In Strathclyde the double-well potential is created using a far blue-detuned optical dipole beam, which can be focussed onto the atoms in the IP trap. This allows for the creation of a pure double-well or the deforming of a single-well into a double-well trap. The limited space for an additional beam meant that the dipole beam was implemented at a slight angle ($\sim 10^\circ$) with respect to the $xy-$plane to avoid blocking the imaging beam. To achieve the required tilt for the focusing lens, a stable mount was designed, this had an adjustable tilt, as well as a fine adjustment micrometer attached to allow the focus to be accurately achieved (Figure 3.12).

The dipole beam consisted of a free-running 658 nm diode laser (Thorlabs HL6545MG) with an output power of $\sim$ 100 mW. The beam was then focused through an AOM, with a VCA controlled (Minicircuits ZAS-3) output to allow precise control over the beam's intensity. It was then focussed onto the atoms through a 80 mm focal length achromat lens, with a waist of 16 μm and 11 μm in the radial and axial directions respectively (measured outside of the cell). The dipole potential was aligned by overlapping the 658 nm dipole beam with a 780 nm 'tracer' beam (picked off from repump $F = 1 \rightarrow F' = 2$) to create a focussed beam with a much greater scattering rate and

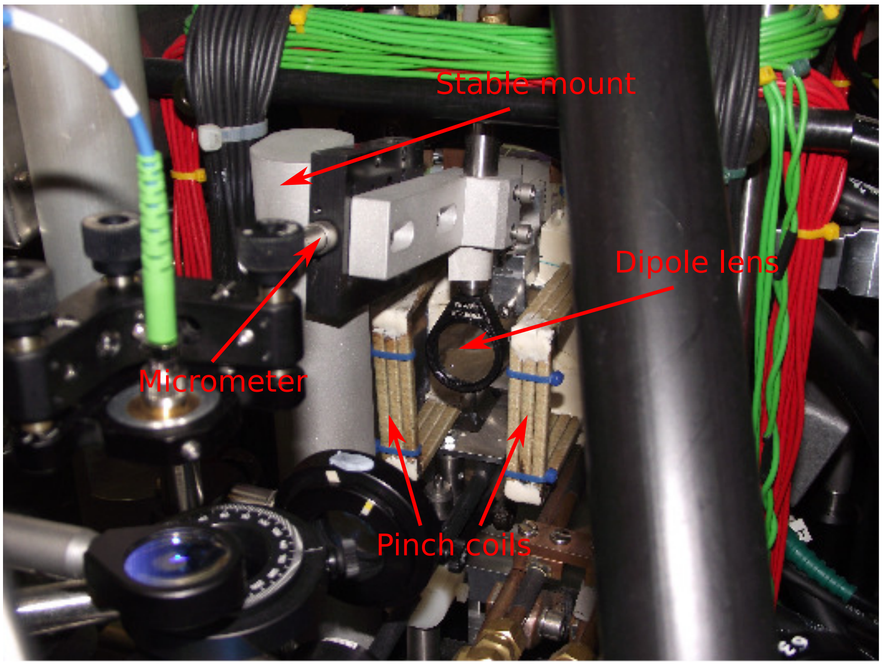

Figure 3.12: Strathclyde's dipole beam lens mount. A stable mount was used to reduce vibrations coupling into dipole beam as it passes through the lens. Micrometer enabled lens focus to be accurately achieved. The dipole beam lens is positioned between two pinch coils. Note the slight angle, this is due to limited optical access.

optical potential [218].

3.3.4 Toroidal magnetic storage ring

The Strathclyde storage ring is comprised of four concentric circular coils, which produce a toroidal quadrupole magnetic field of the form [115]

$$\begin{aligned}\mathbf{B}_{\text{ring}}(r,z) &= \mathbf{b}_{R-\delta_R}(r,z-\delta_z)-\mathbf{b}_{R-\delta_R}(r,z+\delta_z)-\mathbf{b}_{R+\delta_R}(r,z-\delta_z)\\ &+ \mathbf{b}_{R+\delta_R}(r,z+\delta_z). \qquad (3.2)\end{aligned}$$

The magnetic field generated by this coil setup is more symmetric compared to that produced by two concentric current carrying wires.

The storage ring has radius $R = 5.0\,\text{cm}$, radial displacement $\delta_R = 1.25\,\text{cm}$ and axial displacement $\delta_z = 1.35$ cm, which leads to a ring of zero-magnetic field at a radius $R_0 = 4.8\,\text{cm}$ (slightly smaller than the mean coil radius R). To avoid this field-zero an axial wire, which adds a $0 - 10\,\text{G}$ field, runs through the centre of the cell and toroidal quadrupole field. The straight axial wire adds a $1/r$ azimuthal magnetic field to Equation 3.2, which has negligible contribution to the ring radius, but results in a storage ring with completely nonzero-magnetic field.

Our 'BEC-friendly' ring has many advantages, as it can hold $\sim 5 \times 10^8$ atoms and has a magnetic lifetime of 55 s. The effective enclosed area of the ring is $72\,\text{cm}^2$, making it the biggest in the world and the shape allows a high level of optical access for imaging.

3.4 Current control

Having the ability to control the amount of current flowing through the coils is essential when trapping atoms in magnetic fields. In order to generate these current flows to create the MOT, IP and ring traps, a system which contained five water-cooled MOSFET banks was used, each of which contained 20 single PHP125NO6T MOSFETs. The sources were attached to two parallel copper bars (20×10 mm^2 cross section) and each of the individual MOSFETs bolted down onto the copper with thermal paste to increase the conductivity. In addition, the copper bar was connected to the water cooling system to help dissipate the heat power of the MOSFETs.

The experiment, when running at full current, produces a large amount of power

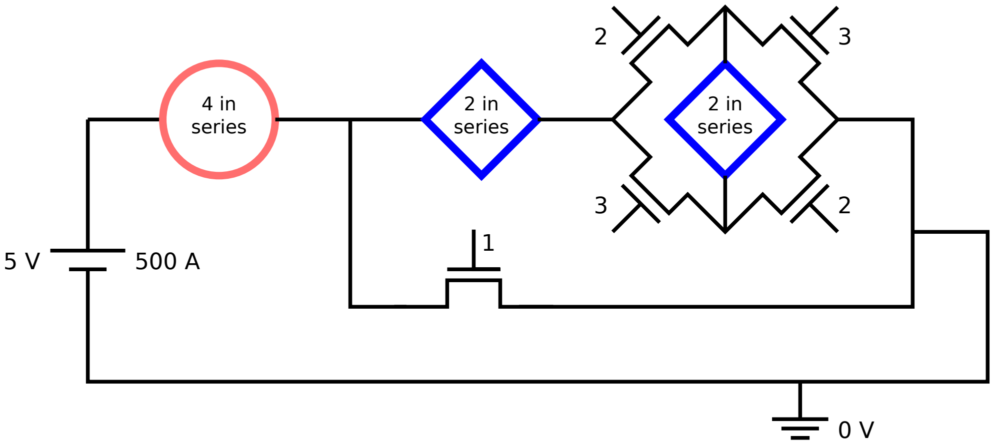

Figure 3.13: Strathclyde MOSFET bank arrangement. Current flows from the 5 V, 500 A power supply through the circular coils (red) and can either then flow through MOSFET bank marked 1, or through one set of square coils (blue) and either through both MOSFET banks marked 2 or both MOSFET banks marked 3.

($5\,\mathrm{V} \times 500\,\mathrm{A} = 2.5\,\mathrm{kW}$), so each of the MOSFET banks must be able to deal with this power dissipation. Each individual PHP125NO6T MOSFET has a rating of 55 V, 75 A, 187 W, so by placing 20 in parallel, each MOSFET has 125 W of power dissipated into it. The circuit used to control the MOSFET banks is shown in Figure 3.13. The coils are connected in series, which results in high stability and a high level of magnetic field noise cancellation [178].

3.4.1 Control circuit and DAC

To be able to control the flow of current through the coils a control circuit (which is based on an integrator) is needed where the input voltage is supplied via an analogue signal from the computer. The output voltage from the digital-to-analog convertor (DAC) was sent through a differential amplifier, which has the gain set to one to reduce any AC noise, before being fed into the feedback. A variable resistor was used on the input of the integrator, which allows the RC time constant to be adjusted and therefore switching speed of the coils to be changed. Having this flexibility allows fast switching ($\sim 1\,\mathrm{ms}$) while avoiding any undesirable oscillation of the voltage.

The current stabilisation was supplied by a fast feedback system, which consisted of a differential amplifier before the integrator and a high frequency response (150 kHz) current sensor. The current sensor was a non-invasive closed loop Hall effect sensor

(CSNR-161). The typical rms AC current noise on the sense resistor was $\sim 100\,\mu$V on top of a 8 V DC signal on the resistor, resulting in a relative current noise of 1×10^{-5}. The control circuit was powered by a ±16 V low-noise power supply and currents up to 500 A could be measured using a 33 Ω sense resistor. The control circuits used to regulate the current for the various coil configurations are shown in Appendix A.

The resolution of the control voltage is set by the hardware, in this case a 16-bit DAC card (National Instruments PCI-6733). Using a 16-bit DAC card gives 2^{16} steps in which the control voltage can be sent to the current drivers, i.e. the DAC output can be tuned between ±10 V with 16-bit resolution yielding step intervals of 0.3 mV.

3.5 Cameras

CCD cameras are some of the most essential components in cold atom labs as they have a variety of uses, which as optimisation and to gather experimental data. In Strathclyde there are four CCD cameras in use, three for general maintenance and optimisation and one for data acquisition using absorption imaging (Section 3.5.1).

The first of the three general purpose cameras is used to observe the atoms in the HP MOT. This camera sees the HP MOT through a PBS, which is also used for the push beam. This camera allows in situ alignment of the push beam and also proves helpful when locking the lasers. A cold sample is immediately observable when the lasers are locked to the correct transitions.

Another two cameras, which are set to continuous display mode, are positioned at the LP MOT and are used for beam alignment. The positioning of the two cameras enables the size, position and compression of the atomic ensemble to be observed in both the xy and yz planes. The camera arrangement also proves helpful at the final alignment stage of the optical molasses. Using long molasses expansion times of the order of ~ 1 s, these cameras can show any unwanted effects due to beam alignment, beam intensities or magnetic field imbalances when cooling in optical molasses.

The camera used for absorption imaging is the Andor Luca DL658M CCD camera. The Luca has a back-illuminated CCD array comprising of 658×496 pixels, each of which is $10 \times 10\,\mu\text{m}^2$. The maximum frame rate readout is 30 Hz, which is more than adequate for recording the three images in the absorption imaging sequence. The quantum efficiency at 780 nm is $\sim 25\,\%$.

3.5.1 Absorption imaging

Consider a near-resonant probe laser beam in the low intensity regime, $I < I_{sat}$, that is shining onto an atom cloud. Since the atoms will partially absorb the incident light, then by using a lens system, the atoms can be imaged as a shadow on the detector (CCD camera). This process is known as absorption imaging, and since photons are being scattered off the atoms as the picture is taken this is a destructive technique. The optical density is the relative amount of light the atoms absorb along a single ray through the atomic cloud. The observable optical depth (OD) can be expressed using the Beer's law relation.

$$I_{\text{out}} = I_{\text{in}} e^{-OD(r)} = I_0 e^{-\sigma_0 \int n(r) dx}, \tag{3.3}$$

where I_{in} is the intensity of the incident light, σ_0 is the absorption cross section and $n(r)$ is the atomic density at a position r in space.

The OD is calculated experimentally by taking three images: one of the probe light with atoms (I_{atoms}, shadow image), one of the probe light with no atoms (I_{probe}, normalisation image) and a final image with no light or atoms ($I_{\text{background}}$, background image). The experimental sequence of three images is shown in Figure 3.14. From the three images the relative absorption signal can then be interpreted, this is done by calculating the OD of each pixel, which is given by

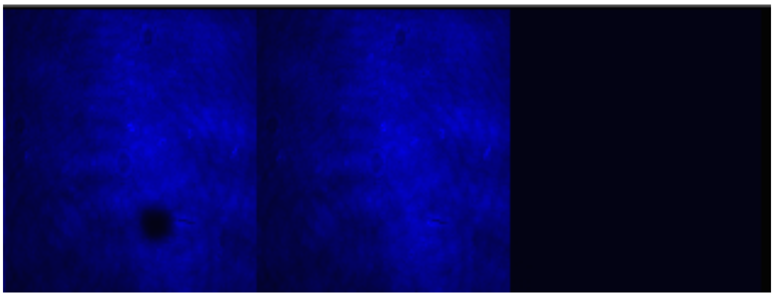

Figure 3.14: Experimental absorption imaging sequence. Left image is probe beam with atoms (note shadow), centre is probe beam without atoms and right is image with no light. Distortions on probe beam are due to aberrations from the glass of the LP MOT cell .

$$\text{OD} = \ln\left(\frac{\text{I}_{\text{probe}} - \text{I}_{\text{background}}}{\text{I}_{\text{atoms}} - \text{I}_{\text{background}}}\right). \tag{3.4}$$

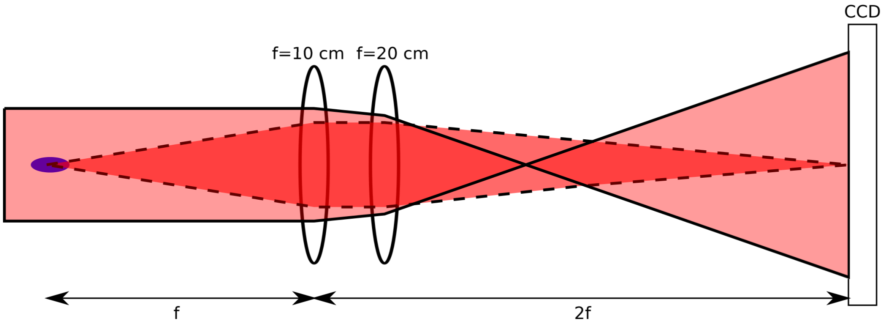

Figure 3.15: Schematic of Strathclyde's double lens absorption imaging setup. After the light passes through the atoms it passes through a two lens system and is then focussed onto the CCD.

The time between each of the three images is 40 ms, which was chosen to match the frequency of the lights in the lab. Allowing two periods of 50 Hz (1/50 Hz = 20 ms) ensures each of the three images has the same background conditions.

Before reaching the CCD the laser beam passes through a lens setup, which allows the image to be focussed onto the camera. Two lenses are used in the setup, as shown schematically is shown in Figure 3.15. The imaging beam is spatially filtered through an optical fibre (picked off the resonant push beam by a PBS) and then passes through a $\lambda/4$ waveplate to circularly polarise the beam before it probes the atoms in the LP

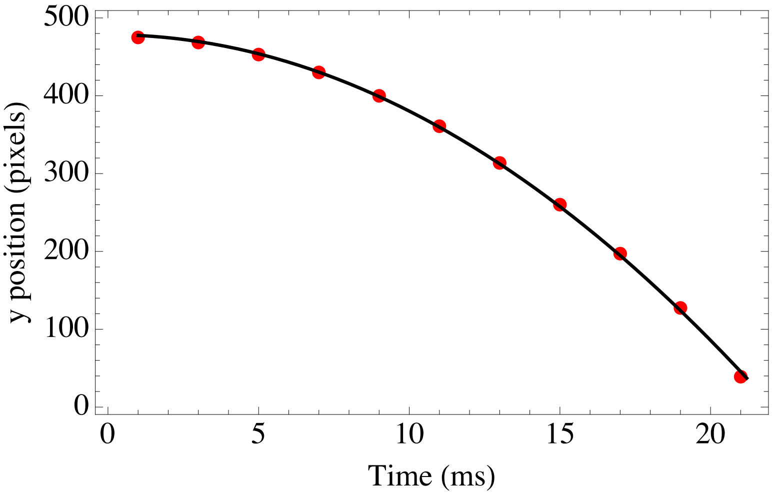

Figure 3.16: Ballistic expansion data used to calibrate magnification of the imaging beam. A condensate was formed and then allowed to drop and expand for variable time and the position recorded on CCD. Magnification was calculated to be 2.03 ± 0.05.

cell.

To be able to observe small objects like BECs or interference fringes, the imaging system must have a sufficiently high optical resolution. The Luca pixel size of $10\,\mu\mathrm{m}^2$ along with the imaging lens system, which has a magnification of ~ 2, resulted in a optical resolution of $\sim 5\,\mu$m. Experimental ballistic expansion data can be used to calibrate the magnification of the imaging camera. By comparing the expected $y = -gt^2/2$ motion with the experimental parabolic centre-of-mass motion of the condensate, a magnification factor of $\mathrm{M} = 2.03 \pm 0.05$ was obtained. Figure 3.16 presents the ballistic expansion data and corresponding fit used to calibrate the camera magnification. A BEC was created and then dropped from $1 \rightarrow 21$ ms in 2 ms steps to obtain an accurate camera calibration.

Chapter 4

Controlling the BEC

4.1 Loading the MOT

As discussed in Section 3.2, the Strathclyde experiment utilises a double MOT setup where the two chambers are connected by a transfer tube. Atoms are initially trapped in the HP MOT and then transferred to the LP MOT using a series of resonant light pulses. The resonant pulses accelerate the atoms to ~ 25 m/s through the transfer tube such that a large number of atoms ($\sim 10^9$) can be trapped. The push beam imparts a kinetic energy kick onto the atoms because the frequency matches the resonant transition for trapping atoms.

For this to occur, the HP MOT light is switched off when the push beam is pulsed on, allowing the atoms to be pushed out of the HP MOT, as they now only experience a scattering force from the push beam. The LP MOT loading sequence is shown in Figure

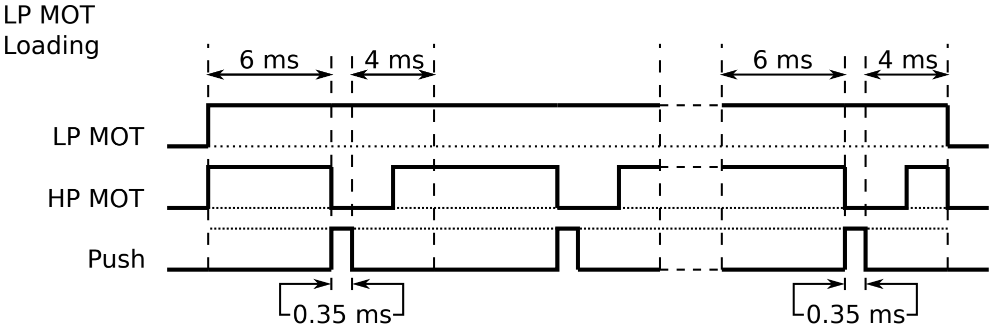

Figure 4.1: The LP MOT digital signal loading sequence and timings. Note that HP MOT light is switched off when the resonant push beam is pulsed on.

4.1. In order to efficiently load the LP MOT, one needs to avoid scattering atoms from this trap with the push beam. This is achieved by misaligning the push beam from the LP MOT centre, such that it is at a small angle to the horizontal but still aligned with the HP MOT centre. By having this angle, the atoms which are pushed have a parabolic trajectory allowing them to be collected in the LP MOT without being affected by any resonant light.

4.2 Optical pumping

Optical pumping (OP) is used after MOT loading and further cooling by optical molasses (red detuned, $\Delta_{\mathrm{molasses}} \sim 40\,\mathrm{MHz}$, for 10 ms). Without optical pumping, the atoms are distributed evenly amongst the magnetic sublevels of the ground state ($F = 2$). Optical pumping is a procedure that increases the population of atoms in a particular quantum state.

By using σ_+ polarised light that is resonant with the $|F = 2\rangle \rightarrow |F' = 2\rangle$ transition, photon absorption drives the $|F = 2, m_{\mathrm{F}}\rangle \rightarrow |F' = 2, m_{\mathrm{F}} + 1\rangle$ transition, which is then followed by spontaneous emission. After a series of absorption-emission cycles, the atoms will remain in the $|2, +2\rangle$ state. Once the atom reaches the $|2, +2\rangle$ ground state, any absorption from the σ_+ light is now forbidden so the state is now a dark. A schematic of this process is shown in Figure 4.2.

It is also possible to optically pump the $|F = 2\rangle \rightarrow |F' = 3\rangle$ transition using σ_+ light. This transition would make the repump redundant since the $|F' = 3\rangle \rightarrow |F = 1\rangle$ decay is forbidden, however this introduces heating, as photon emission is present even after the atoms are pumped into the $|2, +2\rangle$ state.

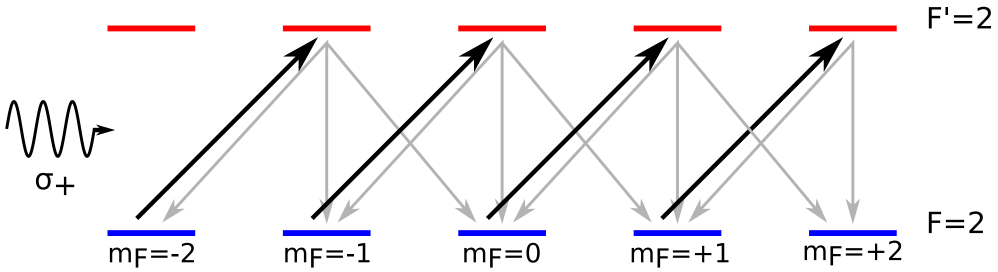

Figure 4.2: Optical pumping scheme. The black arrows indicate the $\Delta m_{\mathrm{F}} = 1$ transitions that lead to the dark state and the grey arrows show the allowed spontaneous emissions.

4.2.1 Magnetic field quantisation

The optical pumping must have a polarisation specified, in this case σ_+, therefore a magnetic field is needed. The optical pumping sequence is comprised of three steps: first is laser was unlocked and jumped $\sim 270\,\mathrm{MHz}$ to be resonant with the $|F=2\rangle \rightarrow |F'=2\rangle$ transition, with a time duration of 0.45 ms; the second step involves turning on a 1 G magnetic field (along OP axis) as well as the σ_+ OP light for a further 0.45 ms; finally, the laser is then jumped back and relocked to the $|F=2\rangle \rightarrow |F'=2/3\rangle$ crossover peak.

Once the optical pumping has been applied and the atoms are in the weak field seeking ($|2,2\rangle$) trappable state, it is essential to synchronise the magnetic trap switch on to catch the atoms. The timing of the magnetic field's switching is observed by monitoring the Hall effect sensor signal, this is shown in Figure 4.3.

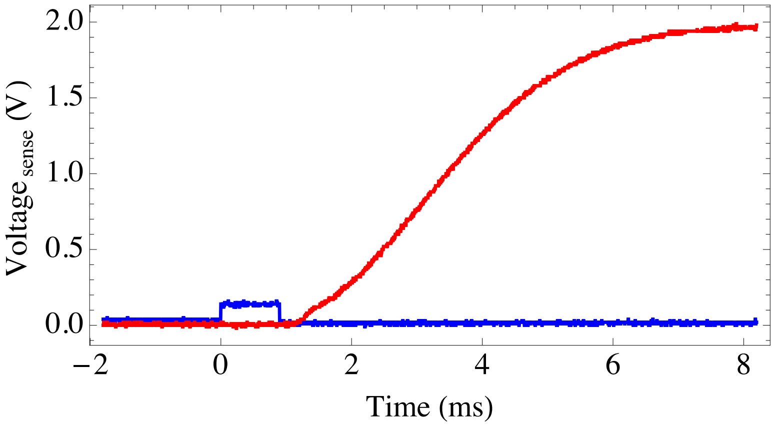

Figure 4.3: Current monitor during magnetic trap switch on. The blue curve shows the magnetic field generated along OP beam axis, this field is pulsed on prior to IP being switched for 0.9 ms. Red curve shows synchronised IP trap switch on, this catches the atoms which have been prepared in the $|2,2\rangle$ state by OP.

One can clearly see the effect that optical pumping has on a cloud of atoms in the magnetic trap by taking absorption images with and without OP. To do this, the MOT was loaded for 5 s (as short fill time avoids camera saturation), then the atoms were trapped in the compressed IP with (and without) the 0.45 ms OP pulse, and finally an absorption image was taken. Figure 4.4 shows the clouds profile and optical density (OD) with and without OP, it can be seen that the OD increases from ~ 2 to ~ 4.5

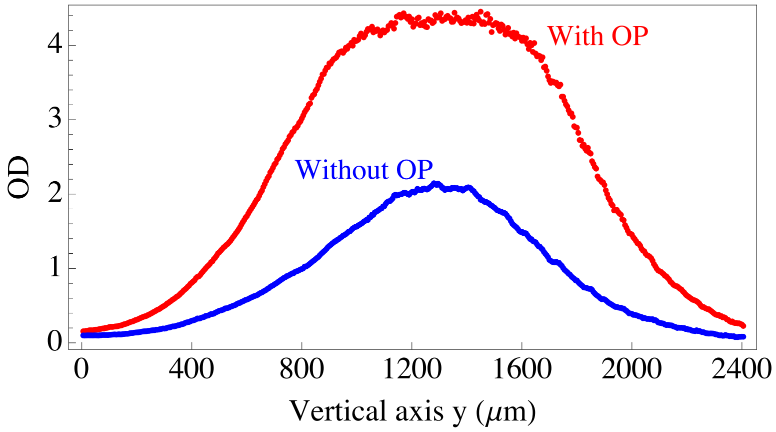

Figure 4.4: Demonstration of optical pumping efficiency through the cloud's profile along vertical y axis and optical depth. When OP is off (blue) the number of atoms is 2.8×10^7, whereas with OP (red) there are 7×10^7 atoms.

in the presence of OP. As well as increasing the OD, the number of atoms in the trap increases by a factor of ~ 2.5.

4.3 Trapping the atoms

As discussed in the previous section, optical pumping can be used to increase the number of atoms in the $|2, 2\rangle$ state, hence increasing the number of atoms in the magnetic trap. Once the atoms are trapped they can be controlled and manipulated to increase critical parameters or undergo further cooling. The atoms in the magnetic trap can also be used as a tool or diagnostic for the system.

4.3.1 Magnetic field compression

The compression of the magnetic trap is achieved by changing the current through the coils. After OP, the IP current controller is initially primed to 10 V to ensure a rapid switch on of the IP FET banks, then the current is increased from 125 → 450 A (2 V → 7 V DAC voltage) over 400 ms. During this compression stage, the compensation coils, which generate the bias field, are also switched on. Figure 4.5 shows the current through the coils, which were measured using the Hall-effect sensors, during the magnetic trap compression. The depth of the magnetic trap is deep enough to ensure that no atoms are lost during the process of compressing the trap.

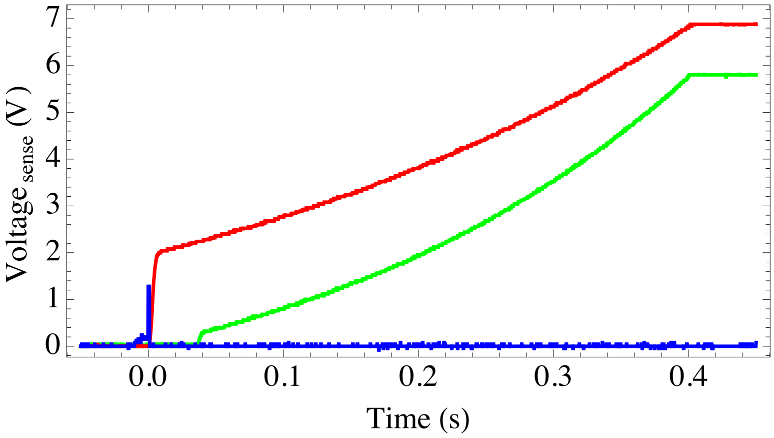

Figure 4.5: Current through the coils during magnetic trap compression. Red curve shows the current ramp of IP magnetic field (125 → 450 A) and green curve shows the current in the compensation bias field during compression. Blue curve is OP field (×10 to emphasise signal), which is applied immediately prior to IP field being switched on.

The adiabatic compression of the magnetic trap is the final step before implementing evaporative cooling. Compressing the trap increases the density and temperature of the atomic ensemble, and hence the ratio of elastic to inelastic collisions. At the end of the compression process, the critical parameters needed for runaway evaporation are satisfied.

4.3.2 Trap frequencies

The magnetic trap frequencies change during compression, due to the alteration of the shape of the trap. It is essential to know these frequencies accurately as they are used to calculate the temperature of the atoms once released from the trap. In this case the condensate is used as a tool to measure the trap frequencies of the IP trap.

At the centre of the IP trap the atoms experience a harmonic potential, which directly affects the behaviour of the trapped atoms. Atoms in this harmonic potential will experience a potential of the form

$$U(\mathbf{r},t) = \frac{1}{2}\sum_{i=x,y,z} m\omega_i^2(\mathbf{r})t_i^2 \ , \tag{4.1}$$

where ω_i is the trap frequency in the three spatial dimensions of the trap. The Strathclyde IP trap is approximately cylindrically symmetric about the axial axis, which

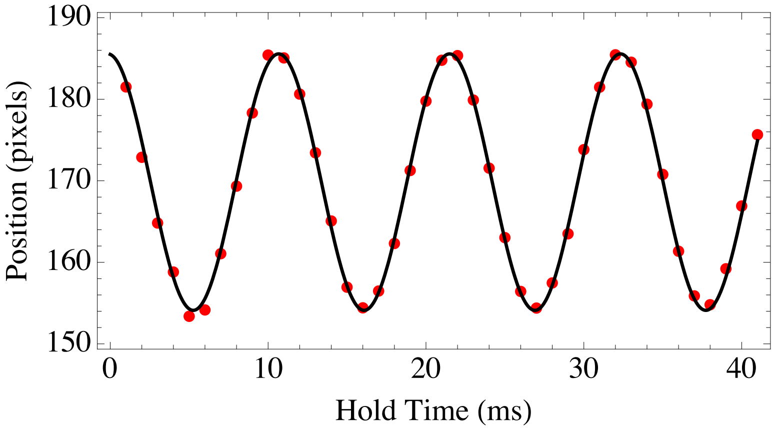

Figure 4.6: Radial magnetic trap frequency measurement. The hold time was varied from 0 → 41 ms in 1 ms steps to obtain four full oscillations to gain an accurate trap frequency measurement. Radial trap frequency was measured to 92.3(0.2) Hz.

implies that $\omega_x = \omega_y \equiv \omega_r$, and we can refer to this as the radial frequency. The axial confinement is an order of magnitude weaker, which results in a lower axial trap frequency ω_z due to the weaker confinement.

The trap frequencies were measured using an external perturbation to disturb the equilibrium position of the atoms in the trap, which results in spatial oscillations of the atoms in the magnetic trap. By recording the final position of the atomic cloud, after a variable hold time in the trap, the trap frequencies can be measured. Prior to the creation of an external perturbation, a BEC was prepared, with its equilibrium position measured as the peak of a 2D gaussian fit. To amplify the harmonic motion of the condensate a drop time of 15 ms was used.

The external perturbation was created using a magnetic field perturbation. The perturbation in radial direction was induced by dropping the total IP magnetic field, this changed the equilibrium gravitational sag. The total current in the IP coils was dropped from 450 → 385 A (7 → 6 V on DAC voltage) for 2.5 ms, which corresponded to a quarter of the expected oscillation period. Care was taken to ensure that the perturbation wasn't great enough for the atoms to reach the anharmonic regions of the trap. The radial trap frequency was measured to be 92.3(0.2) Hz, experimental data and the corresponding fit are shown in Figure 4.6. For the axial perturbation a field gradient was needed, this was supplied by the MOT coils. The magnetic perturbation was created by keeping both the IP and bias coils constant and pulsing on the MOT

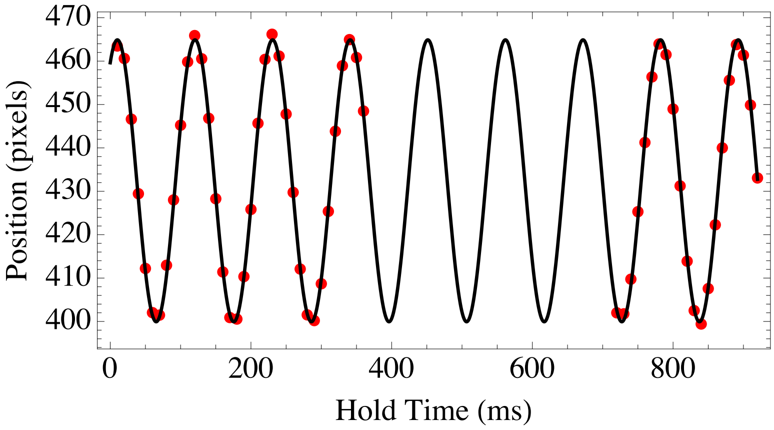

Figure 4.7: Axial magnetic trap frequency measurement. The hold time was varied from 0 → 820 ms in 10 ms steps for three full oscillations, three full oscillations were skipped before a final two oscillation data was recorded. This allowed more oscillations of the atoms to be sampled and ensured an accurate trap frequency measurement, with the axial trap frequency measured to be 9.11(0.01) Hz.

coils (0 → 0.2 V on DAC voltage) for 50 ms, again this was chosen to match half of the longer axial trap frequency. To create this pulsed MOT field, the current difference in the pinch coils was changed by switching the current direction in one of pinch coil pairs. The axial trap frequency was measured to be 9.11(0.01) Hz, experimental data and corresponding fit is shown in Figure 4.7.

4.4 Evaporative cooling

The final stage in creating a BEC is radio frequency (rf) evaporative cooling, this technique allows us to reach the required phase space density for macroscopic quantum degeneracy. The time required for rf evaporation, which continuously satisfies the critical parameters for runaway evaporation, in the Strathclyde experiment is ~ 32 s. The evaporation consists of a two-step continuous evaporation swept from 20 → 5 MHz, which is controlled by an external frequency generator (Agilent 33220A, 20 MHz Frequency Generator). The first step of the evaporation sweeps the frequency from 20 → 5.05 MHz in 30 s through a GPIB card, while the second step of the evaporation switches the Agilent to external frequency modulation (FM) and sweeps the frequency from 5.05 → 5 MHz in 2 s. The switch to external FM mode means that the rf evaporation is controlled by the DAC card, which is advantageous because the dipole beam and trap are

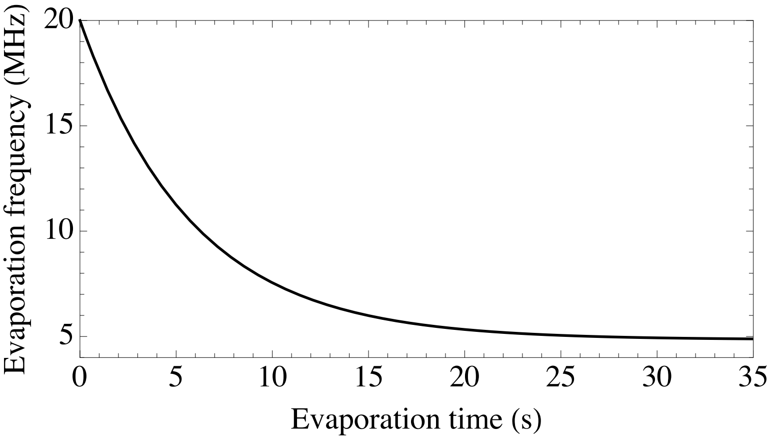

Figure 4.8: Experimental evaporative cooling frequency ramp. The curve shows typical 32 s frequency ramp for $\upsilon_{\mathrm{start}} = 20\,\mathrm{MHz}$, $\upsilon_{\mathrm{stop}} = 5\,\mathrm{MHz}$ and $\upsilon_{\mathrm{base}} = 4.85$.

also controlled by the DAC card. This eliminates any software jitter between the rf switching off and the dipole beam and magnetic trap, which is essential when trying to achieve stable phase locked interference fringes.

The rf evaporation interacts with the atoms via a two-turn (23×18 mm) copper coil that is placed on top of the cell in such a way that the vertical MOT beams pass through it. The frequency is ramped using an exponential curve, such that the time-dependent rf frequency is given by

$$\upsilon_{\mathrm{RF}} = (\upsilon_{\mathrm{start}} - \upsilon_{\mathrm{end}})\exp^{-t/\tau_{\mathrm{RF}}} + \upsilon_{\mathrm{base}} \; . \tag{4.2}$$

Equation 4.2 allows the evaporation to be modelled and optimised, and also allows for a linear ramp if the parameters are chosen correctly. The Strathclyde evaporation ramp is shown in Figure 4.8.

As the evaporation takes $\sim 32\,\mathrm{s}$, it is essential that the magnetic trap lifetime is long enough to ensure that background inelastic collisions don't interfere with the experiment and data. To measure the lifetime of the trap the atoms were loaded into the IP trap and held for a varying amount of time before an absorption image was taken. Once the data has been taken, it can then be fitted with a function of the form

$$f(x) = N_0 \exp^{x/t_{\mathrm{life}}} \; , \tag{4.3}$$

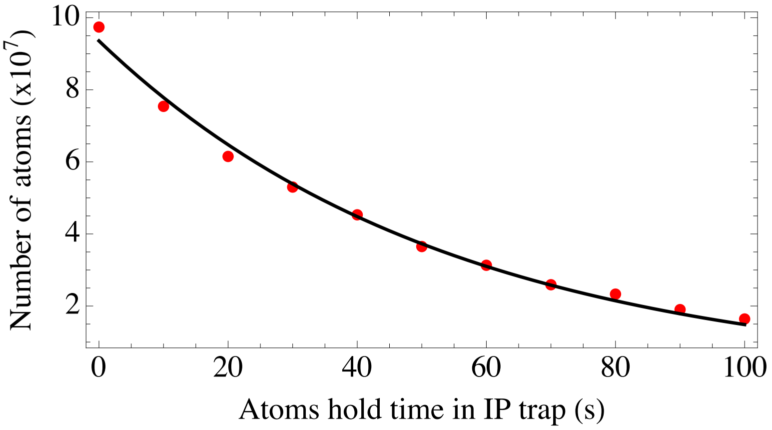

Figure 4.9: IP magnetic trap lifetime. The MOT was loaded for 15 s and then atoms were held for a variable time in the magnetic trap. Lifetime was measured to be 54 s.

where t_{life} is the magnetic trap lifetime. Using the above equation the IP magnetic trap lifetime was measured to be 54 s, which is more than sufficient for the 32 s evaporative cooling stage. The experimental data and fit are shown in Figure 4.9.

4.5 BEC

The evaporative cooling stage is the final step in creating a Bose-Einstein condensate. An abrupt increase in cloud density and the emergence of a bimodal distribution indicates the formation of a BEC. In addition, one can confirm the creation of a BEC through its anisotropic velocity distribution and agreement with predicted transition.

Figure 4.10 shows density plots (absorption images taken at 25 ms) of the formation of the BEC at different final trap depths at the final stage of evaporation. The atom number, condensate size and density is controlled by changing the trap depth, which can be achieved by changing the field from the bias (compensation) coils while keeping the RF knife at 5 MHz. The bias field is controlled by a DAC voltage and is calibrated in such a way that a 0.01 V change corresponds to a 25 kHz change in the trap depth, this method enables a high level of control over the final trap depth. Figure 4.10 shows the cloud shrinking in size as trap depth is lowered by altering the field from the bias coils, and peak density increasing as atoms condense into same state.

The appearance of a bimodal distribution once a condensate has been formed can be seen in Figure 4.11, where a 1D Thomas-Fermi+Gaussian curve has been fitted to

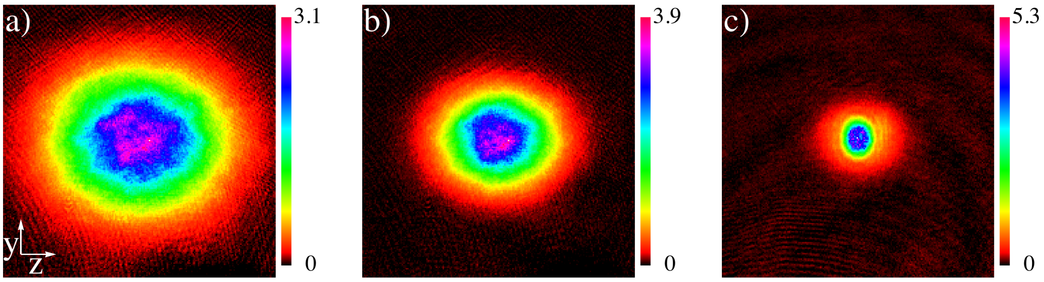

Figure 4.10: Density plots of the formation of a BEC as the trap depth is lowered by changing the field from the bias coils. Scale bars represent optical density. From a) to b) the trap depth was lowered by 25 kHz (bias 5.665 → 5.655 V) and from b) to c) it was lowered by a further 10 kHz (bias 5.665 → 5.651 V) to form a 80 % pure BEC. Each image is 0.8 mm^2 and image taken at 25 ms.

the experimental data. The bimodal (Thomas-Fermi+Gaussian) distribution used to the fit the data takes the form

$$\mathrm{Fit_{TF+G}} = \mathrm{A1} * \mathrm{H}\left(1 - \frac{\mathrm{x}-\mathrm{x_0}}{\sigma}\right)\left(1 - \frac{(x-x_0)^2}{\sigma^2}\right)^2 + \mathrm{A2}\exp\left(-\frac{(\mathrm{x}-\mathrm{x_0})^2}{2\sigma^2}\right), \quad (4.4)$$

where H represents the unit step function (equal to 0 for $\mathrm{x} < 0$ and 1 for $\mathrm{x} > 0$), $\mathrm{x_0}$ is the centre of the distribution and σ is the width. At first the atoms are in a thermal

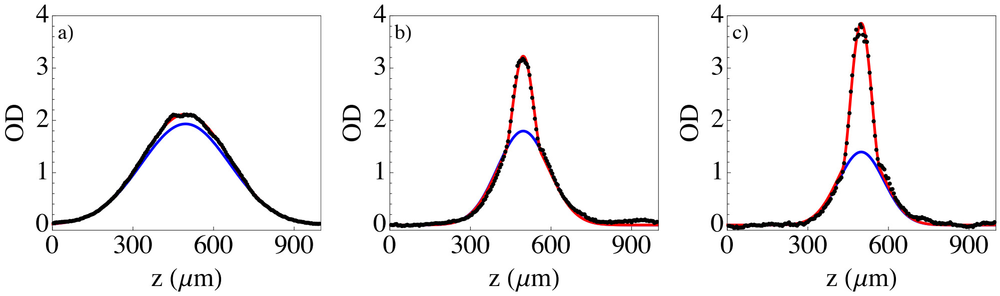

Figure 4.11: Density distributions and corresponding fits of the formation of a BEC as the trap depth is lowered. Density distributions correspond to BECs from Figure 4.10, i.e. a) is the density distribution of Figure 4.10 a) and so on. Black points are the experimental data, the red curve is the 1D Thomas-Fermi+Gaussian bimodal fit to the data and the blue curve is the thermal cloud. Note how the thermal component decreases and OD increases as the BEC is formed.

cloud, but as the trap depth is lowered the thermal component decreases as the OD of the condensed fraction increases. By dividing the area under the bimodal fit (red curve in Figure 4.11) by the area under the thermal fraction (blue curve in Figure 4.11) plus the area under fit, the BEC fraction can be calculated.

4.5.1 Ballistic expansion

Atoms in a BEC exhibit different ballistic expansion dynamics compared to a thermal cloud of atoms. This expansion of the condensate can be used to gain important information regarding the properties of the coherent matter wave, such as the velocity distribution and aspect ratio of the cloud.

The condensate's density can be written in the form of a time-dependent inverted paraboloid that is strongly dependent on trapping frequencies [173] (recall that the axial (ω_z) and radial (ω_r) trap frequencies are 9.1 Hz and 92.3 Hz respectively). When the Thomas-Fermi [12] regime applies, the ballistic expansion obeys [173, 219]

$$\frac{\iota_r(t)}{\iota_z(t)} = \frac{\sqrt{1+\tau^2}}{1+\varepsilon^2(\tau \arctan\tau - \ln\sqrt{1+\tau^2})}\ , \tag{4.5}$$

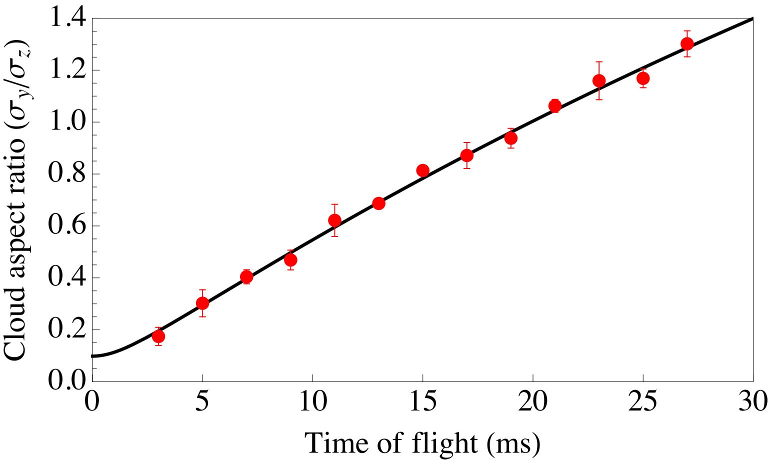

Figure 4.12: Ballistic expansion of BEC in free fall. The aspect ratio of the cloud was calculated after the condensate was released from the trap and allowed to expand for a varying time of flight. There is good agreement between the theoretical prediction (black solid line) from Equation 4.5 and the experimental data (red). The experimental trap frequencies used are $\omega_z = 2\pi \times 9.1$ Hz and $\omega_r = 2\pi \times 92.3$ Hz.

for a weakly interacting BEC, where $\tau = \omega_r t$ and $\varepsilon = \omega_z/\omega_r$. Figure 4.12 shows the experimental data of the BECs ballistic expansion in the presence of only gravity and the theoretical prediction from Equation 4.5, which are in good agreement.

4.6 Dipole beam

The Strathclyde experimental setup makes use of the optical dipole force to either create a condensate in a double-well potential or adiabatically deform a single-well into a double-well potential to a split BEC. This dipole beam is a blue detuned laser which is far detuned from the ^{87}Rb resonant transition and creates a potential barrier at the centre of the BEC.

4.6.1 Optical dipole potential

As with trapping atoms using radiation pressure and magnetic traps, it is also possible to make traps using laser beams. Such traps, which exploit electric dipole interactions, are known as optical dipole traps [220]. The potential generated in optical dipole traps has a strong dependence on detuning, therefore it is possible to create attractive and repulsive forces with the light. A far blue detuned laser repels atoms from the brightest parts of the beam, hence it is this repulsive force which can split the condensate.

An electric field $\mathbf{E}$ induces a dipole moment of $-e\mathbf{r} = \epsilon_0\chi_a \cdot \mathbf{E}$ in an atom with an interaction energy given by [97]

$$U = -\frac{1}{2}\epsilon_0\chi_a E^2 = \frac{1}{2}e\mathbf{r}\cdot\mathbf{E} \ , \tag{4.6}$$

where E is the amplitude of the electric field, U is the energy and $\epsilon_0\chi_a$ is the polarisability. The total force that the atom experiences is a combination of the dipole force and the scattering force, $F_{\text{total}} = F_{\text{dipole}} + F_{\text{scatt}}$. The dipole force takes the form [97]

$$F_{\text{dipole}} = -\frac{\hbar\delta}{2}\frac{\Omega}{\delta^2 + \Omega^2/2 + \Gamma^2/4}\frac{\partial\Omega}{\partial z} \ , \tag{4.7}$$

and the scattering force is given by

$$F_{\text{scatt}} = \hbar k\frac{\Gamma}{2}\frac{\Omega^2/2}{\delta^2 + \Omega^2/2 + \Gamma^2/4} \ , \tag{4.8}$$

where $\delta = \omega - \omega_0$ is the laser detuning and Ω is the Rabi frequency. The dipole force is zero on resonance ($F_{\text{dipole}} = 0$ for $\delta = 0$) and for $|\delta| \gg \Gamma$ the dipole force is equal to the derivative of the light shift ($\Delta\omega_{\text{light}} = \Omega^2/4\delta$). Therefore, the light shift, or a.c. Stark shift, for a ground state atom acts as a potential, U_{dipole}, which, in three dimensions, is given by [97]

$$\mathbf{F} = -\nabla U_{\text{dipole}} \ , \tag{4.9}$$

where

$$U_{\text{dipole}} \equiv \frac{\hbar\Omega^2}{4\delta} \equiv \frac{\hbar\Gamma}{8}\frac{\Gamma}{\delta}\frac{I}{I_{\text{sat}}} \ . \tag{4.10}$$

When δ is positive (blue detuning), the potential has a maximum where the intensity is highest, i.e. the atoms are repelled from regions of high intensity. In the opposite case when the frequency is detuned to the red (δ is negative), the atoms are attracted to the regions of high intensity. The dipole force either repels or confines the atoms at the focus of the beam and since dipole traps operate at large detunings, the scattering rate approximates to

$$R_{\text{scatt}} \simeq \frac{\Gamma}{8}\frac{\Gamma^2}{\delta^2}\frac{I}{I_{\text{sat}}}. \tag{4.11}$$

This scattering rate scales as I/δ^2, whereas the trap depth in Equation 4.10 scales as I/δ. Therefore, the use of large detuning reduces the scattering (heating) rate whilst maintaing a large trap depth.

4.6.2 Dipole beam position

To initially align the dipole beam it was overlapped with a 780 nm 'tracer' beam (picked off from $F = 1 \rightarrow F' = 2$ repump beam), which 'blew' away all of the atoms when aligned with them. Once this was achieved the 'tracer' beam was removed and fine alignment of the dipole beam realised. For the final alignment of the dipole beam maximum beam power (~ 40 mW) was used, which created the biggest optical dipole potential. The dipole beam was switched on before the evaporation and was present throughout the entire evaporation, which resulted in the clearest split signal. The atom number and cloud size was adjusted by changing the final DAC voltage of the compensation bias coils, Figure 4.13 shows the optical dipole potential's affect on two condensates with different atom numbers. In Figure 4.13 a) there is a sufficient number of atoms to continuously 'fill' the hole made by the dipole beam, which results in two

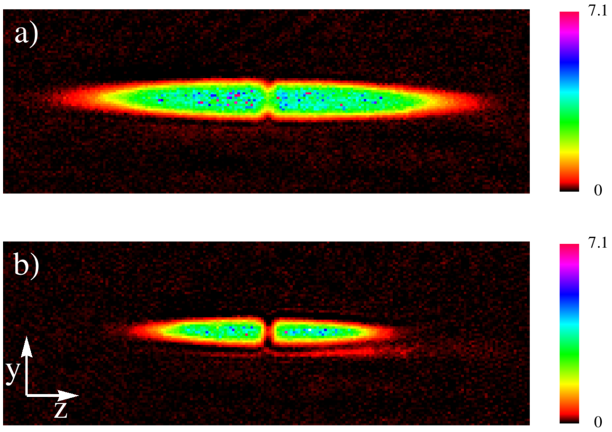

Figure 4.13: Absorption images of optical dipole potential effect on atoms in magnetic trap. Scale bars represent optical density. Two different final bias voltages a) 5.660 V and b) 5.680 V were used to determine that the centre of dipole beam was aligned. The two final bias voltages correspond to a change of 50 kHz at the trap bottom. Each image is 1.0 × 0.4 mm.

notches in the condensate, which indicate the dipole beam is positioned in the centre of the atomic cloud. For a smaller number of atoms in Figure 4.13 b) there are not enough atoms to 'fill' the hole, which results in the dipole beam completely splitting the condensate into two parts. By changing the intensity of the dipole beam the splitting between the two condensates can be adjusted.

The potential that the dipole beam creates is a function of the beam's power, waist

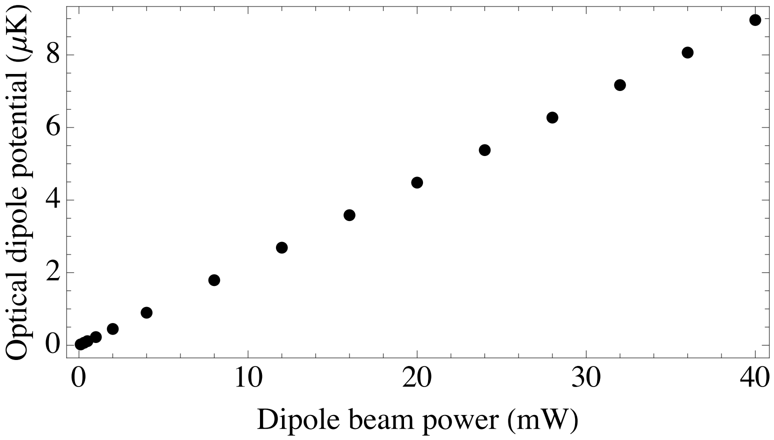

Figure 4.14: Theoretical optical dipole beam potential as a function of beam power.

and detuning from the resonant transition. The theoretical optical dipole potential as a function of dipole beam power is shown in Figure 4.14. The maximum dipole beam power achievable is $\sim 40\,\text{mW}$, the use of an AOM combined with a VCA allows any power from $0 \to 40\,\text{mW}$ to be used. Figure 4.14 shows that the potential scales linearly with power; hence, $0.1\,\text{mW}$ of power creates a $22\,\text{nK}$ potential and $40\,\text{mW}$ of power creates a $9\,\mu\text{K}$ optical dipole potential.

4.6.3 Controlling the dipole beam

By changing the rf frequency and power of an acousto-optic modulator (AOM), the deflection angle and intensity of a beam can be altered. These features have been previously used to create arbitrary patterns for BEC experiments using time-averaged optical dipole potentials [116, 221, 222]. Previously, potentials created for BECs using AOMs have used red-detuned light light, however blue-detuned light potentials [223] have much lower decoherence rates.

The dipole beam is focused through a 200 MHz AOM, which has a voltage-controlled amplifier (VCA) RF input, with an efficiency of $\sim 50\,\%$ (the poor efficiency is due to the beam being bigger than the active RF region). The VCA (attenuator/switch) allows the AOM to be controlled by a DAC line from the computer, which enables dipole beam to be ramped on/off in the experimental sequence. The VCA has an input from a frequency generator, a control input from a DAC voltage and a output

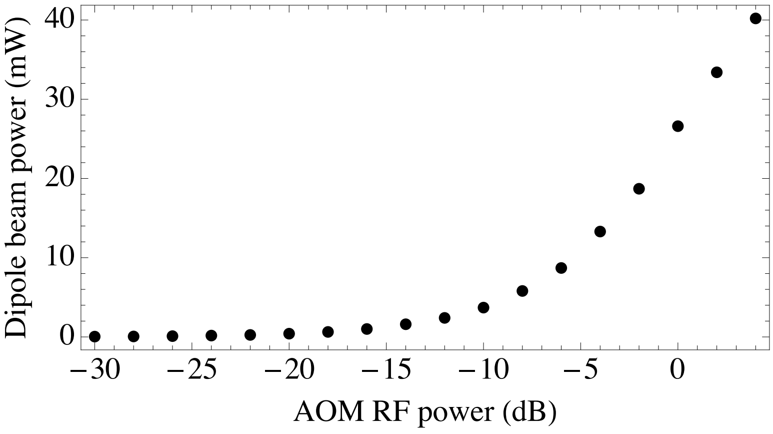

Figure 4.15: Dipole beam power as a function of RF power. The dipole beam illuminated the photodiode head of a power meter just before the dipole beam focussing lens at the cell and the maximum power was recorded. The DAC voltage was set to 5 V.

which gets amplified before being connected to the AOM.

The dipole beam's power is an extremely important parameter, as it alters the splitting between the two parts of the condensate and therefore the interference fringes (discussed in Section 5.3.2). In the experimental setup there are two ways in which to adjust the dipole beam's power, either through the power of the RF from the signal generator or the voltage from the DAC. Figure 4.15 shows the dipole beam's power as a function of the power of the applied RF from the signal generator. The second method to control the dipole beam's power is via the control voltage from the DAC, the dependence on which is shown in Figure 4.16.

Using both the RF power and DAC voltage means that the dipole beam's power can be controlled very accurately, which is essential when trying to perform ultra-stable interferometry experiments. Dipole beam's pointing stability is discussed in Section 5.8.3.

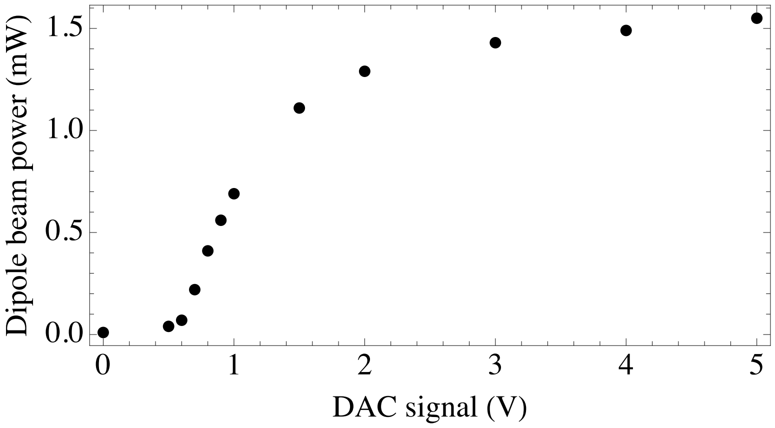

Figure 4.16: Dipole beam power as a function of control voltage from DAC. The dipole beam was incident on the photodiode head of a power meter just before the dipole beam focussing lens at the cell and the maximum power was recorded. RF power was set to −14 dB on signal generator.

4.6.4 Adiabatic splitting

In the Strathclyde experiment the splitting of the condensate can be achieved in two ways: either by creating a BEC in a trap with the presence of the dipole beam, or by ramping the dipole beam on after evaporation. The technique of continuous beam application (through the evaporation process) results in the creation of two independent

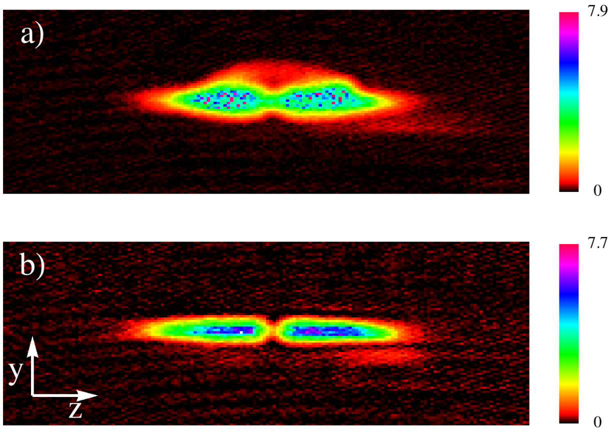

Figure 4.17: Density plots showing difference between adiabatic and rapid injection of dipole beam. Scale bars represent optical density. Image a) shows rapid injection of dipole beam over 1 ms and image b) shows adiabatic injection of dipole beam over 100 ms. Each image is 0.8 × 0.4 mm at 2 ms drop time.

BECs. For use in interferometry applications a single condensate needs to be smoothly (adiabatically) split into two condensates with a fixed relative phase [65, 184, 224] to prevent phase jitter in the interference fringes. Figure 4.17 shows the difference between rapid and adiabatic splitting of the condensate. Figure 4.17 a) shows a rapid injection of the dipole beam over a 1 ms linear ramp, which sends shock waves through the condensate and proves an obstacle when trying to generate interference fringes. However Figure 4.17 b) shows a linear dipole beam ramp over 100 ms which adiabatically splits the condensate and results in clear spatial interference fringes. Having the ability to adiabatically split the BEC allows both halves of the condensate to have a phase memory of each other, this is essential for interferometric techniques.

4.7 Levitation

Magnetic levitation [26, 41, 225] is a very useful tool in cold atom experiments and is used to overcome gravity, which allows for longer interaction times. Neutral atoms, which have been cooled, have magnetic moments that are parallel to a static magnetic field **B**, therefore using a superposition of the existing gravitational field and an additional magnetic field, they can be effectively levitated.

4.7.1 Importance of levitation

The importance of magnetic field levitation becomes apparent when considering the interference of two BECs. The period of the interference fringes λ in this experiment arises from the de Broglie waves of the two condensates and takes the form (Section 2.6.2)

$$\lambda = \frac{ht}{md} , \tag{4.12}$$

where h is Planck's constant, m is the atomic mass, d is the centre-of-mass splitting distance between the condensates and t is the expansion time. Ballistic expansion in free fall (t) is limited by the physical size of the vacuum cell and the imaging area (we note that times of 100 ms correspond to the BEC falling 49 mm). Magnetic levitation can be used to overcome this limitation and keep the atoms in the area of interest for long time intervals ($t > 80\,\mathrm{ms}$), allowing the interference fringes to become optically observable.

4.7.2 Creating the levitation field

The levitation field was generated using the quadrupole field produced by the four circular coils with an additional vertical constant field, $B_{4\text{ coils}} + B_{\text{vertical}}$. The mechanism of levitation uses weak-field seeking $|2,2\rangle$ atoms which are attracted to the local minimum of the magnetic field. Once a BEC has been formed, the anti-gravity conditions are achieved by applying a vertical magnetic field gradient. Since the force from gravity has to be compensated with a magnetic field gradient, the field required can be written as

$$F_{\mathrm{B}} = F_{\mathrm{g}} \implies \mu_B B = mg \implies B = \frac{mg}{\mu_B} , \tag{4.13}$$

therefore a vertical gradient of 15 G/cm is needed for the levitation field. Combining B_{vertical} with the quadrupole magnetic field reduces lensing in the vertical and imaging directions [226]. The additional vertical constant magnetic field B_{vertical} is generated from a pair of rectangular coils, which are used for optical molasses. The vertical bias field is parallel to gravity but has the opposite sign; the effect of adding this field to the field produced by the circular coils can be seen in Figure 4.18. The magnetic field causes focusing in the radial plane, while the axial dimensions display defocusing due to the magnetic field.

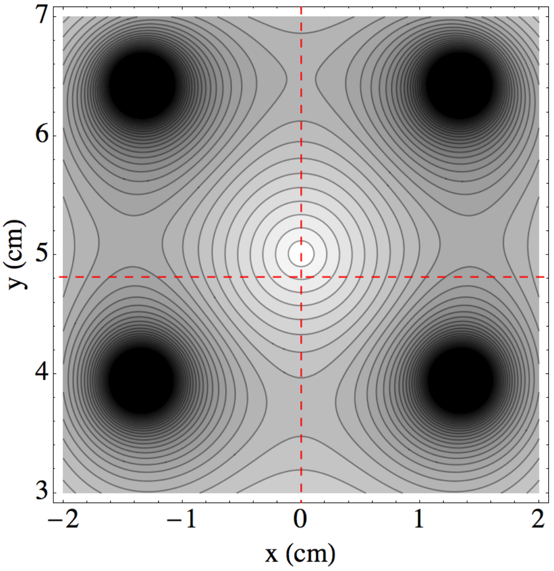

Figure 4.18: Magnetic field contours of the levitation field (slice through magnetic field at $z = 0\,\mathrm{cm}$). Contours represent magnetic field, where the darker regions indicate stronger magnetic field strength. The levitation field is generated from the four circular coils plus an additional vertical bias. The dashed line (red) indicates the original position of magnetic field minimum from the four circular coils.

4.7.3 Levitation timing

The effectiveness of the levitation field is very dependent on the accurate timing of the experimental sequence. Switching the field on too early or too late can lead to decoherence in the BEC or even atoms being lost. The levitation field is switched on after evaporation and immediately after the IP and bias coils have been switched off. Figure 4.19 shows the experimental timings of the quadrupole field from the toroidal coils and the vertical bias for levitation with respect to the magnetic trap switch off. The torus coils that produce the quadrupole field for levitation are pulsed to 10 V (on DAC) for 3 ms to ensure they are on just as the IP trap switches off, and then set to 0.75 V to support atoms against gravity. B_{vertical} requires a DAC voltage of 6.3 V to produce the necessary field for levitation.

4.7.4 Levitation field dynamics

The combined field $B_{4\ \text{coils}} + B_{\text{vertical}}$ compensates for gravity, therefore this linear field gradient can hold the atoms in a specific position for long times-of-flight. During levi-

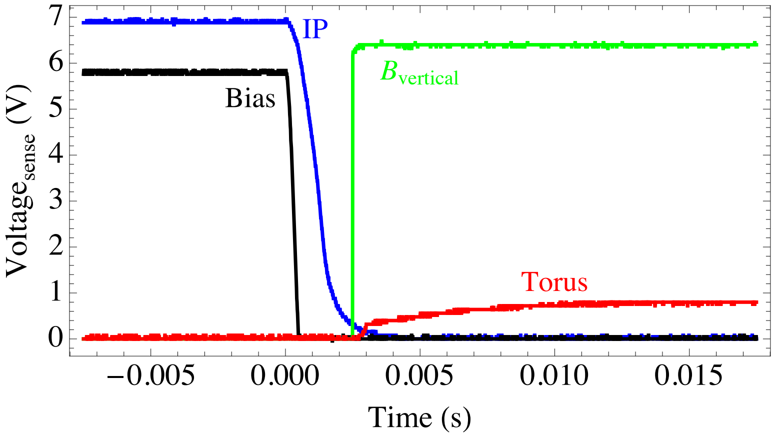

Figure 4.19: Magnetic levitation field timing. Bias (black) and IP (blue) switch off in ~ 3 ms at which point both the quadrupole (red) and B_{vertical} (green) have switched on. This method ensures a 'smooth' transfer from the magnetic trap to the levitation field.

tation the condensate experiences different expansion dynamics compared to a BEC in free fall as the levitation field causes the atoms to experience a weak outward force in the horizontal direction. Figure 4.20 shows the expansion of the atoms in the levitation field for various levitation times.

The nature of the modified expansion can be understood through considering the potential landscape of the field. Since the coils used to created the toroidal quadrupole field are circular, the axial (z) potential can be approximated to a weak inverted

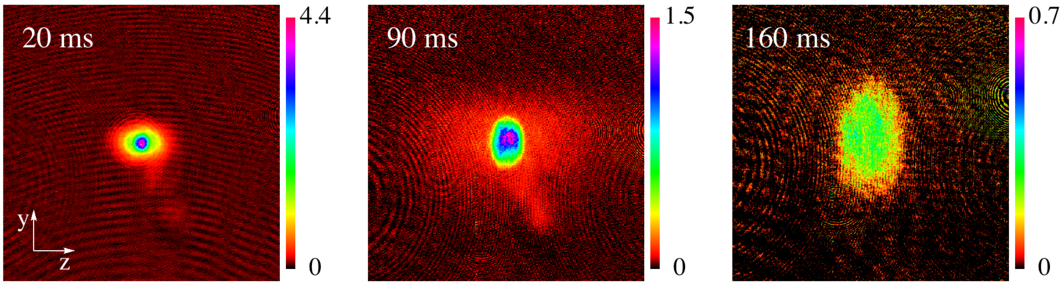

Figure 4.20: Density plots for BEC in levitation field. Scale bars represent optical density. Each image is $1.4 \times 1.4\,\text{mm}^2$ and the levitation time is given in top-left corners. Density plots show how the BEC expands and the OD density drops with time.

parabola, $U_z = -m\omega^2 z^2/2$. The magnitude of ω is that of a rigid pendulum, $\omega = \sqrt{g/r} = 14\,\mathrm{rad/s}$, where the acceleration due to gravity is g and r is the radius of the ring (5 cm). The classical motion of a particle with an initial velocity v_0 and horizontal position z_0 is given by

$$z(t) = z_0 \cosh(\omega t) + v_0 \sinh(\omega t)/\omega \; . \tag{4.14}$$

The anti-trapping potential that affects the horizontal motion can be defined by finding ω from Equation 4.14.

By analysing the cloud expansion during levitation the angular frequency of the anti-trapping potential can be found. After BEC formation, the BEC was then levitated

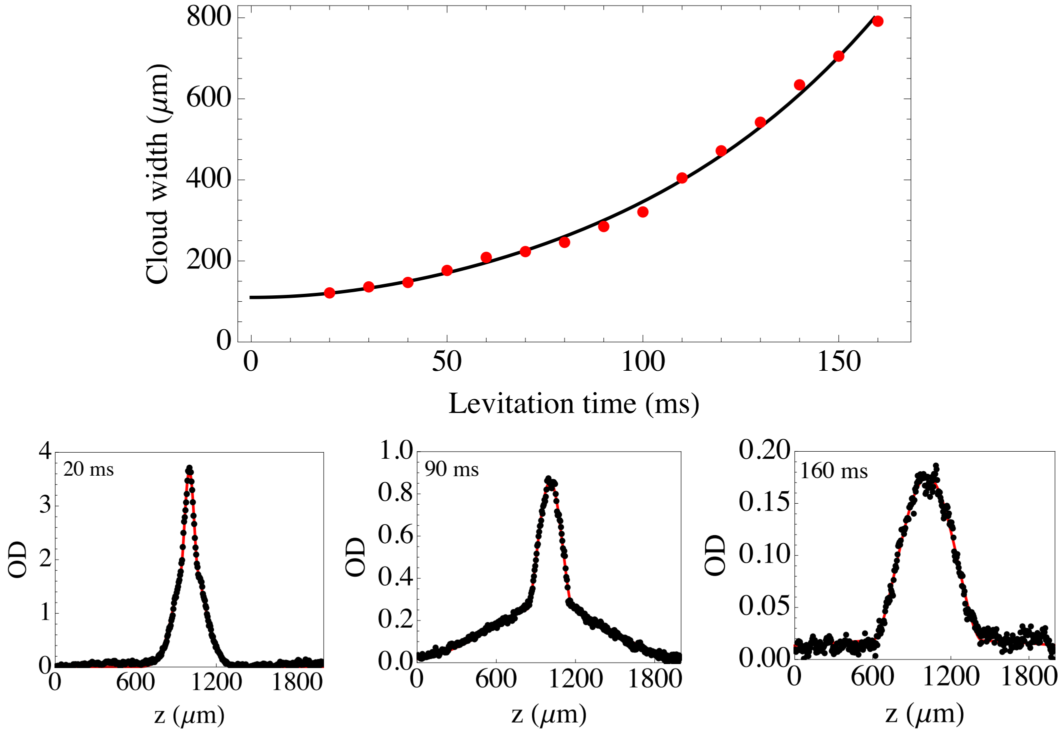

Figure 4.21: Axial cloud widths and distributions in levitation field. Top image shows how the width of the atomic cloud varies as a function of the levitation field. The fit function is of the form $\langle z(t)\rangle = (\langle z_0^2\rangle \cosh^2(\omega t) + \frac{1}{\omega^2}\langle v_0^2\rangle \sinh^2(\omega t))^{1/2}$. Bottom images are examples of 1D (Thomas-Fermi+Gaussian) fits using Equation 4.4 for different levitation times (shown in top-left corner), note the change of y-axis scale as cloud expands.

for a variable time and at each time an absorption image was taken. To observe the atomic distribution each absorption image was integrated along the y axis, resulting in determining the distribution along the axial direction of the condensate. For each levitation time a 1D Thomas-Fermi+Gaussian was fitted to the data and the width of the cloud obtained. Figure 4.21 shows the cloud widths (average of four images) as a function of the levitation time, along with some examples of the 1D fits to the experimental data using Equation 4.4.

The Magnitude of ω obtained from the fit to the data in Figure 4.21 was found to be $(14.1 \pm 0.4)\,\mathrm{rad/s}$, which agrees with the theoretical prediction from the geometric potential. The value of ω defines the anti-trapping potential and has a substantial effect on the interference fringes of two overlapping condensates that are in this levitated potential.

Chapter 5

Interferometry

By combining the Ioffe-Pritchard trap (discussed in section 2.3.4) and the dipole beam (discussed in section 4.6) a double well potential can be created, where two halves of the BEC, or two independent BECs, occupy both wells of the potential (Section 1.4.1). The recombination of the two wells is achieved by switching off the dipole and magnetic potentials and allowing the condensates to overlap with one another. After implementing the levitation field (Section 4.7) an interference pattern is optically observable after 80 ms. The levitation field enables interference fringes from 80 → 200 ms to be imaged using absorption imaging.

5.1 Interference fringes

Initially the interference fringes were obtained from two independent BECs as the dipole beam was present during the whole evaporation process. Once the two BECs had been created in each of the two wells, all dipole and trapping potentials were switched off and the anti-gravity conditions initialised for 160 ms. The levitation field was then switched off and an additional 2 ms free fall was applied before an absorption image was taken, which ensured there were no stray magnetic fields and resulted in a clearer image.

Figure 5.1 shows a typical interference pattern and density profile of two BECs that have overlapped during 160 ms levitation. From the absorption images some of the important properties of the coherent matter-wave can be interpreted, such as the fringe period, contrast and phase of the interference pattern. The period and contrast

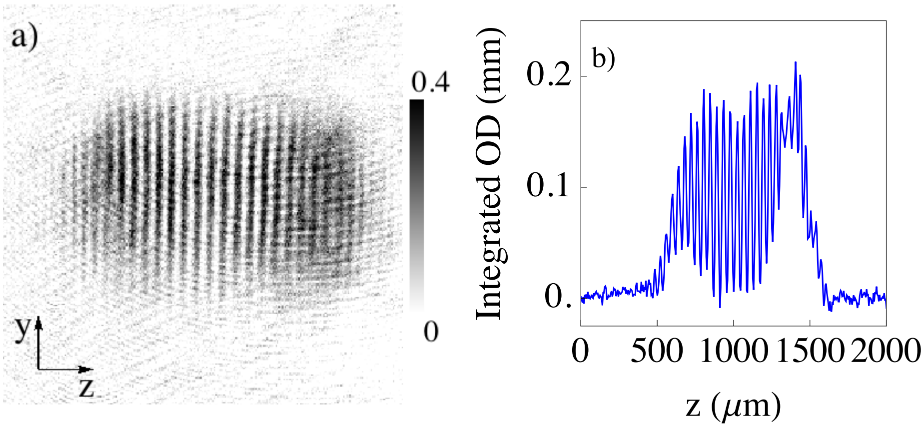

Figure 5.1: Interference pattern and integrated OD after 160 ms levitation. Scale bar represents optical density. a) Density plot (2×1.5 mm) of interference fringes from two initially separated BECs and b) is integrated optical density over the whole cloud.

of the interference fringes depend on a variety of experimental parameters, including the levitation time and the initial separation between the two condensates.

5.2 Fringe pattern processing

Once the absorption image has been taken, it has to be analysed to gain the period and contrast of the data. A technique known as Discrete Fourier Transform (DFT) is used to calculate the period of the interference pattern. The continuous Fourier transform is defined as [227]

$$\hat{f}(\omega) = \int_{-\infty}^{+\infty} f(t) e^{-2\pi i \omega t} dt \ , \tag{5.1}$$

where $f(t)$ is the inverse Fourier transform given by

$$f(t) = \int_{-\infty}^{+\infty} \hat{f}(\omega) e^{2\pi i \omega t} d\omega \ . \tag{5.2}$$

Now considering the case when the function is no longer continuous but takes discrete values, $\hat{f}(t) \rightarrow \hat{u_k}$, given N values $\hat{u_k}$ takes the values $u_0, u_1, ..., u_{N-1}$. This results in the discrete Fourier transform [228]

$$\hat{u_k} = \sum_{k=0}^{N-1} u_j e^{-2\pi i j k/N} \ , \tag{5.3}$$

the inverse transform is then

$$u_j = \frac{1}{N}\sum_{k=0}^{N-1} \hat{u_k} e^{2\pi ijk/N} \ . \tag{5.4}$$

Discrete Fourier transforms are particularly useful as they show periodicities in data as well as the relative strength of any periodic components. In general, the discrete Fourier transform of a real sequence of numbers will be a sequence of complex numbers of the same length. As the DFT is a complex function hence we can write the components as [229]:

$$\hat{u_k} = |\hat{u_k}|e^{i\phi(k)} \ . \tag{5.5}$$

By calculating the modulus of the Fourier transform's complex function $|\hat{u_k}|$, the amplitude spectrum can be obtained. The squared modulus of a Fourier complex function describes the spectral power density, therefore this results in the ratio of how different spectral elements contribute to the total power. if u_j is real, then $\hat{u}_{N-k}$ and $\hat{u}_k$ are related by

$$\hat{u}_{N-k} = \hat{u}_k \ , \tag{5.6}$$

for $k = 0, 1, ..., N-1$ and leads to a symmetric amplitude spectrum plot, only if the total number of components is odd.

5.2.1 Fourier transformation and fringe period

From the original image of the interference pattern only a section in the centre, the area of interest (AOI), is selected for further analysis. The Fourier spectrum was acquired by selecting all of the rows within the AOI $(R_1, R_2, R_3, ..., R_n)$, then the Fourier spectrum $\mathcal{F}_i(R_i)$ was calculated for each of the individual rows and finally the average $|\mathcal{F}_i(R_i)|/n$ was generated (assuming no tilt in the fringes).

Figure 5.2 b) shows the Fourier spectrum for the interference fringes in Figure 5.2 a). The original absorption image of the interference fringes was 400 × 400 pixels and the AOI was chosen from that image, this allows the period of the fringes to be seen more clearly. The AOI was chosen to be a 50 × 50 pixel submatrix in the centre of the original image, shown in Figure 5.2 a), and the amplitude of the Fourier spikes corresponds to the contrast of the fringe pattern.

The Fourier spike can be transformed into the fringe period using

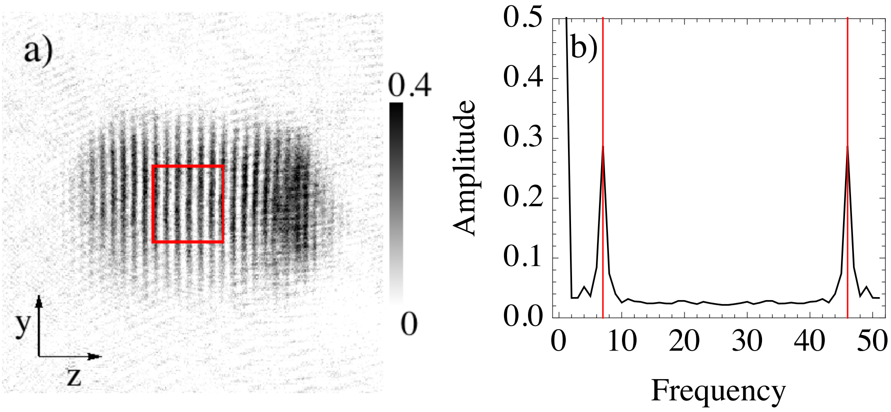

Figure 5.2: Submatrix and Fourier spectrum for experimental interference pattern after 160 ms levitation. Scale bar represents optical density. a) Original absorption image is 400 × 400 pixels and submatrix 50 × 50 pixels (red box), which is used to calculate period. b) Fourier spectrum of the submatrix in a), fringe period was calculated to be $\sim 45\,\mu$m.

$$\lambda = \frac{N_{\text{total}}}{N_{\text{peak}} - 1} P_{\text{size}} \ , \tag{5.7}$$

where N_{peak} is the frequency at which the fringes occur within the AOI, with total width N_{total}, and P_{size} is the pixel size. It is this formula that is used to calculate the fringe period for all the experimental data, although as discussed in Sectopn 5.4 this needs to be modified due to the inverted parabola axial potential.

Ideally the interference pattern will be aligned with the CCD camera, however experimental interference fringes may be tilted with respect to the pixel array. Interference fringes possess phase information, by applying phase related correction the fringes can be straightened. Figure 5.2 presents the raw image with the 50 × 50 pixel submatrix and the corresponding Fourier spectrum used to calculate the fringe period and density maxima. The Fourier spectrum has peaks at 7 and 46, which have opposite phase and are most sensitive when straightening the fringe pattern. The tilt of the fringes directly corresponds to the phase change along the fringes. The phase, ϕ_i, for each of the rows (from bottom to top) in the AOI is obtained from the Fourier transform, Figure 5.3 presents the phase change for each row in the AOI.

The phase change with respect to the rows was fit using the function $\phi_{\text{cor}} = A\text{x}+\phi_0$, the gradient A was found to be -0.006 rad/row and ϕ_0 was found to be 0.97 rad. The

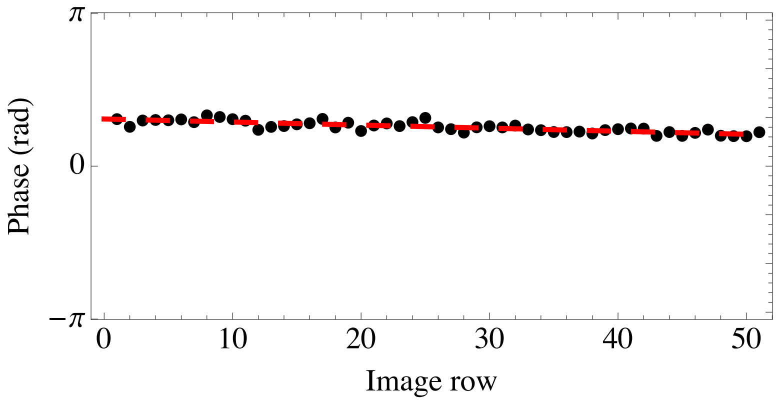

Figure 5.3: Phases of the Fourier components of interference pattern with the AOI from Figure 5.2 a). Data points (black) are shown along with corresponding linear phase shift fit (red dashed) to the phases of the Fourier components. The slope was determined to be −0.006 rad/row.

phase correction factor is then applied to the peaks in the Fourier spectrum (with opposite phase $e^{-i\phi_{\mathrm{cor}}}$ and $e^{i\phi_{\mathrm{cor}}}$), this results in the phase correction shift and the interference fringes being straightened.

Once the fringe period has been calculated from the Fourier spectrum the contrast is then obtained by averaging the phase corrected rows in the AOI and fitting the data.

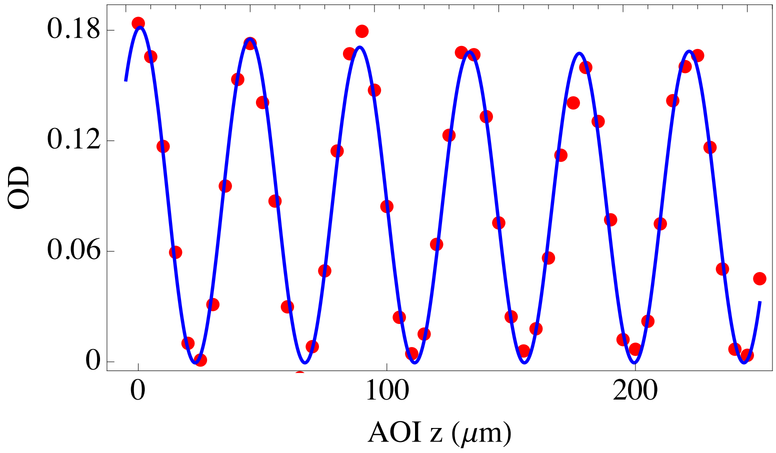

Figure 5.4: Density profile and sinusoidal fit of the interference pattern. The density profile (red points) is obtained by averaging the rows in the AOI, which are then fitted (blue curve) with a sine wave that has a quadratically varying amplitude and offset (Equation 5.8). The sinusoidal fit to the data demonstrated a high contrast of 95%.

The fringes are fitted with a sine wave that has a quadratically varying amplitude of the form

$$\mathrm{Fit}_{\mathrm{fringes}} = \left(1 + C(\mathrm{x} - D)^2\right)\left(A + B\cos\left[2\pi\left(\mathrm{x} - \frac{\mathrm{leng} - 1}{2}\right)(\mathrm{spi} - 1)/(\mathrm{leng}) + \phi\right]\right) \tag{5.8}$$

where leng is the number of the columns in the AOI and spi is the position of the first Fourier spike in the AOI. Figure 5.4 shows the density profile and fit (using Equation 5.8) of the interference fringes within the AOI in Figure 5.2 a). When calculating the fringe visibility the background level was measured and subtracted from the data. There is a striking agreement between the averaged row experimental data and the fit, this increases the confidence in the calculated values of the fringe period and contrast.

5.3 Fringe period - initial separation

The initial separation between the two wells of the potential is a critical parameter, as it can not only influence the fringe period but also the contrast of the interference pattern. The initial separation can be changed by altering the power in the dipole beam, effectively changing the potential barrier thickness between the two wells.

5.3.1 Focusing the dipole beam

The dipole beam is linked to the initial separation between the two wells of the potential, therefore it is essential that the dipole beam is focussed at the BEC. Similar to Section 4.3.2 where the BEC was used as a tool to measure the trap frequencies, the BEC can be used to identify if the dipole beam is in focus. Using the equation for the fringe period (Equation 4.12), it can be seen that the fringe period is inversely proportional to the initial separation. Therefore, the largest fringe period should correspond to when the the dipole beam is focussed at the condensate.

Figure 5.5 shows the experimental fringe separation (and corresponding contrast) as a function of the dipole beam lens position. The lens was attached to a micrometer, this gave accurate control over the lens position. Two independent condensates were created and levitated for 150 ms and the fringe period calculated from the image of the fringes. The largest fringe separation occurred when the lens was at 8.3 mm on the micrometer, this corresponded to a fringe separation of $\sim 35\,\mu$m.

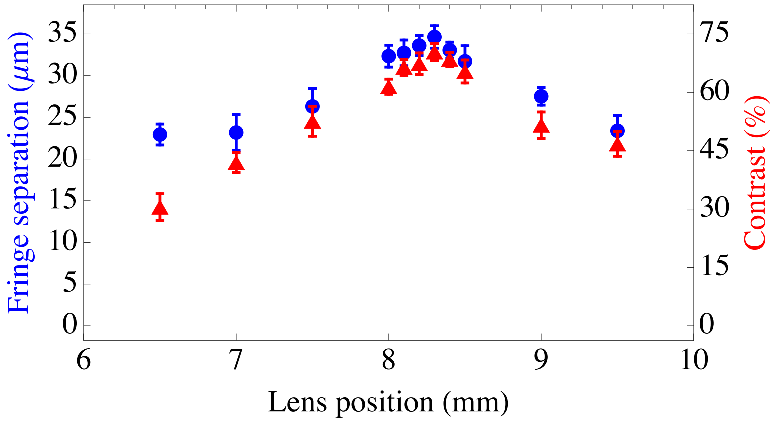

Figure 5.5: Dipole beam lens focus. Two independent BECs were created and levitated for 150 ms before an absorption image was taken. The lens was attached to a micrometer and this was used to vary the lens position. Blue (circles) corresponds to fringe separation and red (triangles) corresponds to contrast. The fringe period is inversely proportional to the initial separation, therefore the lens was in focus at 8.3 mm as this gave the largest fringe period. Each point is an average of five experimental data points.

5.3.2 Dipole beam power

For a fixed drop time the power of the dipole beam is linked to the initial separation of the condensate. Increasing the power in the dipole beam makes a linearly larger Gaussian potential at the bottom of the parabolic IP trap, pushing the two condensates apart. The fringe period's dependence on dipole beam power is shown Figure 5.6 and it agrees well with the fringe period formula. Two independent condensates were generated since the dipole beam was on throughout evaporation, the BEC was then levitated for 160 ms and the dipole beam power varied. Lower intensities, ≤ 1 mW, result in the largest fringe period since effectively this corresponds to the thinnest optical barrier between the two parts of the condensate. The fringe spacing ranges from $\sim 22.9\ \mu$m to $\sim 55.1\ \mu$m, note the first two images have curved fringes which is similar to Reference [64] (see Figure 5.7). Figure 5.7 shows absorption images of the interference pattern for various dipole beam powers, note discernible change in the period of the fringes and their contrast.

When dealing with interference patterns, not only is the fringe period taken into account but also the fringe contrast (visibility), which is written as

$$\text{Contrast} = \frac{S_{\max} - S_{\min}}{S_{\max} + S_{\min}}\ , \tag{5.9}$$

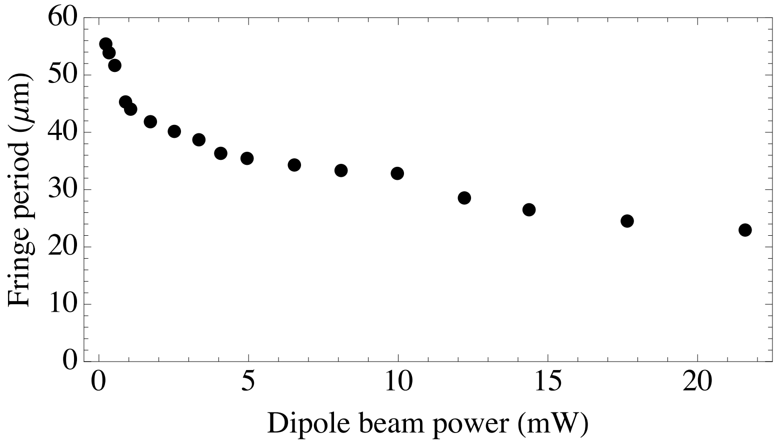

Figure 5.6: Fringe period dependence on dipole beam power. The dipole beam is present throughout whole evaporation, then the BECs were levitated for 160 ms and the dipole beam power was varied. Each point is an average of five experimental data runs.

where $S_{\max}$ is the maximum signal of the oscillations and $S_{\min}$ the minimum of the oscillations. The dipole beam power also affects the contrast of the interference pattern, this dependence is shown in Figure 5.8 and the reason discussed below. The same set of experimental data was used for Figures 5.6 and 5.8.

The contrast starts to drop as the dipole beam power is increased, as at higher beam powers the part of the Gaussian dipole potential experienced by the BEC is increasingly steep. As the condensate is in the Thomas-Fermi regime there is a correspondingly

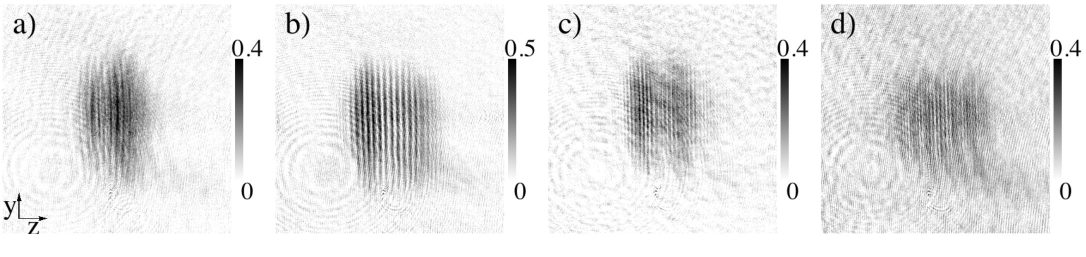

Figure 5.7: Absorption image of interference fringes for various dipole beam powers, taken after 150 ms of levitation. Scale bars represent optical density. The beam power for each interference pattern was a) 0.2 mW, b) 0.9 mW, c) 6.5 mW and d) 14.4 mW. The fringe periods and contrasts were measured to be: a) 55 μm and 15 %, b) 46 μm and 94 %, c) 34 μm and 74 %, d) 24 μm and 65 %.

steep atomic density gradient, which further increases the broken symmetry of the system prior and during expansion. The largest fringe period and contrast occur at low dipole beam power which lends itself perfectly to interferometry, This is because smaller changes in the potential permit faster adiabatic splitting of the condensate, ideally leading to longer phase memory in the halved BEC.

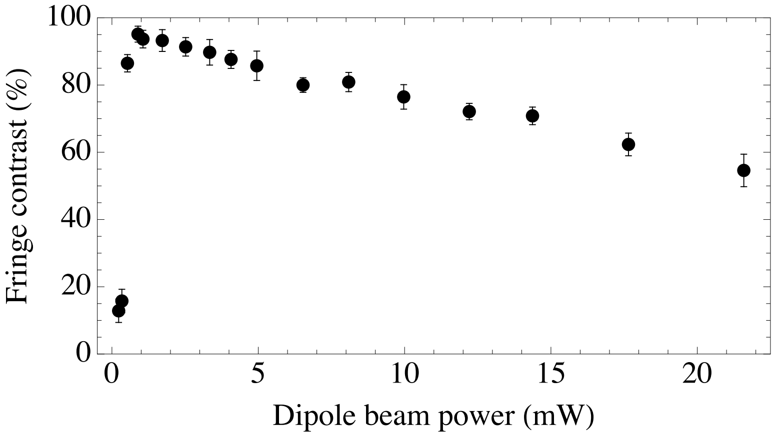

Figure 5.8: Fringe contrast dependence on dipole beam power. The dipole beam is present throughout whole evaporation, then the BECs were levitated for 160 ms and the dipole beam power was varied. Each point is an average of five experimental data runs.

5.4 Fringe period - levitation time

Altering the initial separation between the condensates by changing the potential which splits them isn't the only method of changing the fringe period. Using fringe period formula from Equation 4.12, it can be seen the ballistic expansion results in a linearly increasing fringe spacing with time. With a fixed initial centre-of-mass separation between the condensates, the fringe period is directly proportional to the duration of the ballistic expansion. The solid red curve in Figure 5.9 is how the fringe period should depend on the ballistic expansion time however, it is clear that the data significantly deviates from the predicted curve.

The reason for the deviation from the ballistic expansion theory can be understood when considering the levitation field applied during the ballistic expansion of the BECs. As discussed in Section 4.7.4, the atoms experience an inverted parabola axial potential

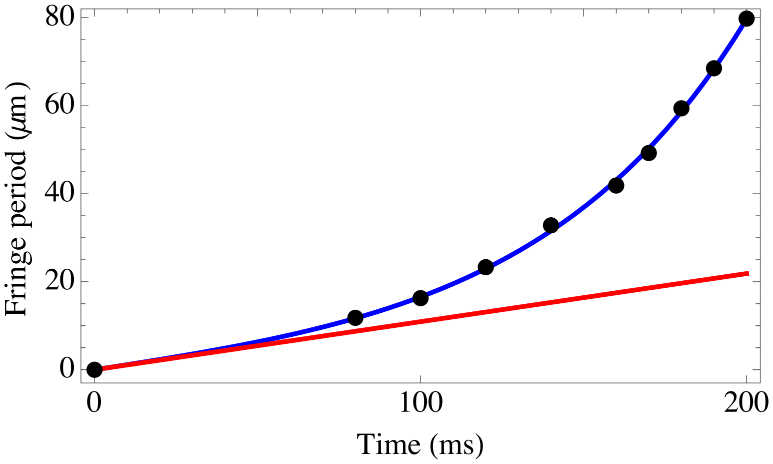

Figure 5.9: Fringe period as a function of levitation time. BECs were initially separated by $\sim 40\,\mu$m and then levitated for a varying time. Ballistic expansion theory (red), experimental data (black points) and modified fringe period formula (blue) are all shown for levitation times up to 190 ms. The experimental data agrees well with the model for the fringe period in an inverted parabola potential (a geometrical ring property), with $\omega = 15.3\,$rad/s.

during levitation due to the circular nature of the quadrupole field. By solving the one-dimensional time-dependent Schrödinger equation, it can be shown that the fringe separation in a potential $U_z = -m\omega_z^2 z^2/2$ should be modified relative to the fringe period from ballistic expansion theory, $\lambda = ht/md$, to

$$\lambda' = \lambda \frac{\sinh(\omega_z t)}{\omega_z t} \ . \tag{5.10}$$

The levitational potential has a nonlinear 'magnifying' effect on the fringes and with 200 ms levitation fringe periods of $80\,\mu$m can be observed, which can be clearly seen in Figure 5.9. It should be noted that to achieve the equivalent maximum fringe period by ballistic expansion it would take 800 ms, which corresponds to 3 m of free-fall.

5.5 Maximum contrast interference

The theoretical maximum contrast that is possible can be modelled and then compared to the experimental data. If you assume two perfect matter-wave point sources that interfere, they will produce an interference signal in the form of sinusoidal fringes

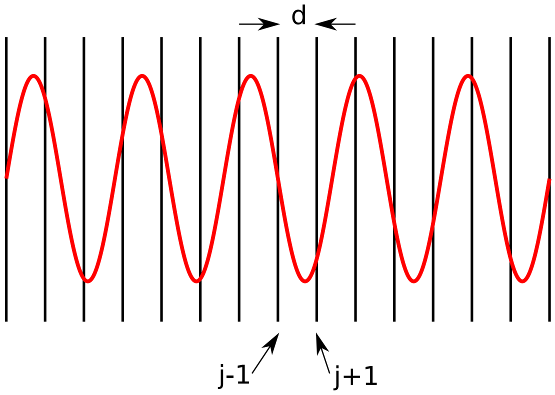

Figure 5.10: Schematic diagram of sinusoidal fringes on pixels of the CCD. Interference fringes (red) spanning over the pixels of the camera (black) with a pixel size $d = 5\,\mu$m. Adjacent pixels in the CCD are defined as $J - 1$ and $J + 1$.

$$F(x) = A \sin\left(\frac{2\pi x}{\lambda_f}\right) \ , \tag{5.11}$$

where λ_f is the fringe period. By integrating how much of the sine wave is in each of the pixels the theoretical maximum contrast can be calculated. When the interference fringes hit the j^{th} pixel of a perfect CCD, which has a pixel size of d (schematic shown in Figure 5.10), the fringe signal averaged over the range $(j - 1/2)d \leq x \leq (j + 1/2)d$ is

$$F_{\text{CCD}} = \text{sinc}\left(\frac{\pi d}{\lambda_f}\right) A \sin\left(\frac{2\pi j d}{\lambda_f}\right) = CF(jd) \ . \tag{5.12}$$

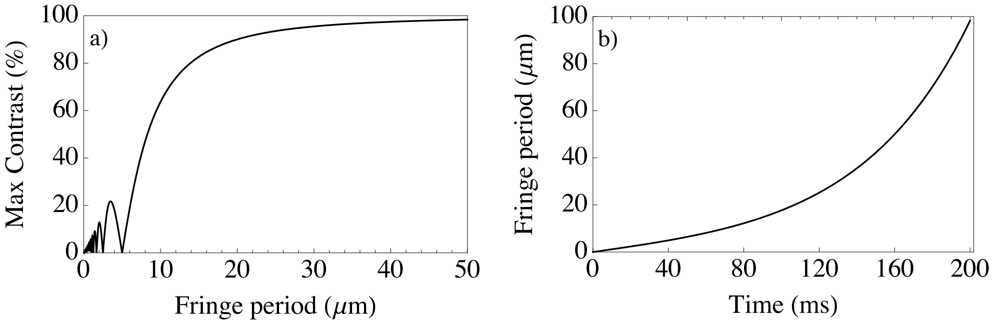

Figure 5.11: Maximum contrast as a function of fringe period theory curves. a) Theoretical plot of the variation of contrast as a function of time using Equation 5.13. b) Theoretical plot of fringe period as a function of levitation time in the inverted parabola axial potential using Equation 5.10.

Therefore, the original fringe signal is modulated by the reduced contrast

$$\mathrm{C} = \mathrm{sinc}\left(\frac{\pi d}{\lambda_f}\right) . \tag{5.13}$$

In our experimental setup the size of the pixels d is constant, therefore the contrast only depends on the period of the time-dependent interference fringes. Figure 5.11 shows the theoretical plots for both the contrast as a function of the fringe period and the fringe period as a function of levitation time. Figure 5.11 b) used the formula for the modified fringe period (Equation 5.10) due to the axial inverted parabola potential during levitation and the calculated $\omega = 15.3\,\mathrm{rad/s}$ from the fit in Figure 5.9.

Knowing how the contrast depends on the fringe period, and how the fringe period varies with time, allows the theoretical maximum contrast sinc curve due to the pixellation of sinusoidal fringes on the CCD camera to be determined. Figure 5.12 shows the theoretical maximum fringe contrast as a function of time in the levitation field. For levitation times $> 150\,\mathrm{ms}$ the contrast reaches $95 - 100\%$.

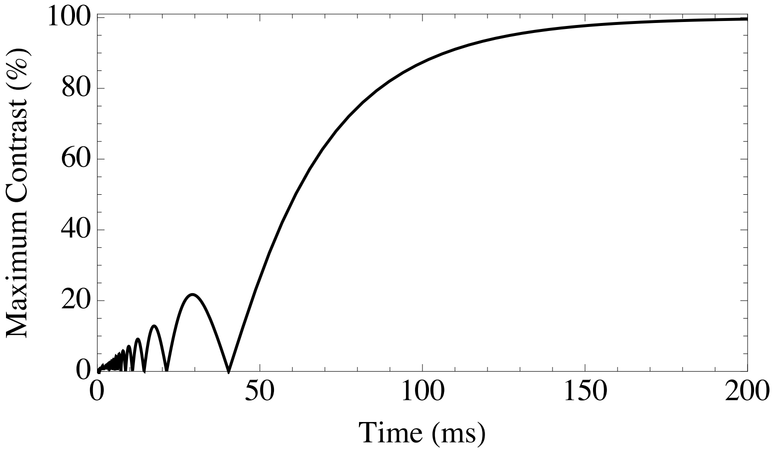

Figure 5.12: Theoretical maximum contrast as a function of time, due to pixellation of sinusoidal fringes on the CCD camera. Theory curve (black) uses both plots in Figure 5.11 to calculate the maximum contrast in the levitation field.

5.5.1 Contrast - Experimental fringes

As discussed theoretically in the previous section, the contrast of the interference fringes varies as a function of levitation time. A BEC was created and then split by $\sim 40\,\mu\mathrm{m}$ using the dipole beam, the two halves were allowed to expand in the levitation field

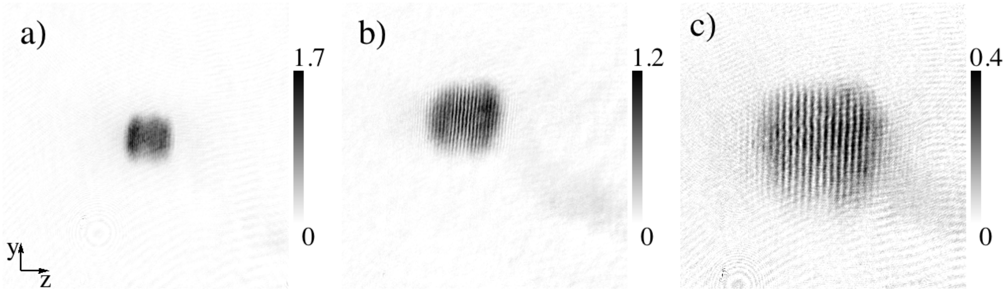

Figure 5.13: Absorption image of interference fringes for various levitation times. Scale bars represent optical density. Image a) is after 80 ms with a contrast of 30%, b) is after 120 ms levitation with a contrast of 65% and c) is after 160 ms with a contrast of 95%. Each individual image is 1.8 × 1.8 mm.

and an absorption image was taken. Figure 5.13 shows absorption images of the interference fringes at various points during levitation: a) 80 ms, b) 120 ms and c) 160 ms. From these images it is clear to see not only the contrast increasing with time but also the noticeable change in the fringe period, which agrees with the model for the experimental setup.

Figure 5.14 shows how the contrast of the interference fringes varies as a function

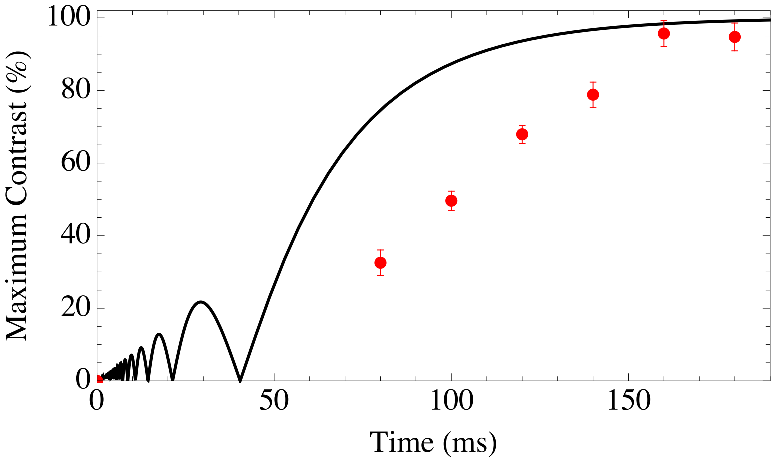

Figure 5.14: Experimental fringe contrast as a function of time using −3 MHz detuned imaging beam light. Experimental data points (red) and theory curve (black) are shown for levitation times up to 190 ms. Each point is an average of five experimental data runs.

of time, using $-3\,\mathrm{MHz}$ detuned imaging light (discussed in next section), as well as the theoretical maximum contrast curve. The reason for the increasing contrast up to levitation times of 150 ms is that there are fewer pixels per fringe, i.e. lower fringe resolution. As the fringe period grows with levitation time it fills more pixels, therefore the fringe resolution increases and the contrast becomes more evident. Another reason for the increasing contrast with time is that at short time of flights the spatial distribution dominates, whereas at longer times the velocity distribution dominates. A result of this is that the matter wave fringes become increasing planar. At 160 ms single-shot interference contrast $\geq 95\%$ has been observed, which is the highest contrast reported in this type of interferometer, and is only limited by the pixellation of the sinusoidal fringes on the CCD camera.

There is good agreement between the experimental data and the theory, which is quite remarkable as the theory assumes two perfect matter wave point sources. The theory also has no allowance for our non-tomographic imaging which is susceptible to any spatial asymmetry in the source BECs and hence 3D curvature of the fringes. The agreement between the experimental data and theory is made all the more impressive considering the BEC is far from a perfect point source, it is an elongated condensate split in half with broken symmetry.

5.5.2 Contrast - Imaging beam detuning

The frequency of the light used to image the BEC is an important parameter, as absorption imaging is a function of detuning. As discussed in Section 3.5.1, the Strathclyde experiment uses resonant absorption imaging, so any magnetic fields on during imaging must be accounted for. During the imaging sequence there is a $\sim 2\,\mathrm{G}$ magnetic field along the imaging direction, this causes a 3 MHz relative Zeeman shift of the $|2,2\rangle \leftrightarrow |3,3\rangle$ transition. To calibrate the imaging beam frequency and the applied magnetic field during imaging, the frequency of the light was changed and the number of atoms in the IP trap recorded.

Figure 5.15 shows the atom number in the IP trap as a function of the imaging beam frequency and the corresponding Lorentzian fit. From the fit the maximum in atom number occurs at an AOM frequency of 136.5 MHz with a linewidth of 6.4 MHz. The imaging beam AOM is set to be on resonance at 133.7 MHz, therefore as expected the AOM frequency needs to be adjusted by $\sim 3\,\mathrm{MHz}$ to be resonant with the

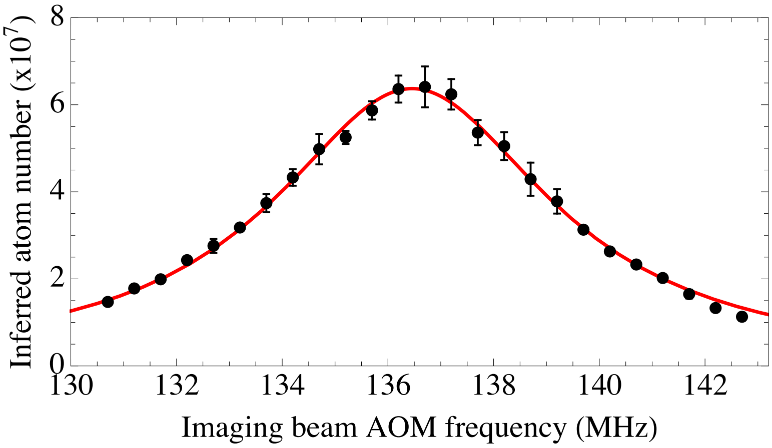

Figure 5.15: Atom number as a function of imaging beam frequency. Imaging beam frequency was adjusted by changing the RF input to the AOM and MOT was loaded for 5 s to avoid the camera saturating. The data was fit with a Lorentzian function, centre frequency and linewidth from fit are 136.5 MHz and 6.4 MHz respectively. Each point is an average of five experimental data runs.

$|2,2\rangle \leftrightarrow |3,3\rangle$ imaging transition. Not having the imaging beam on resonance results in a drop in optical density and contrast as the focal point of the camera changes with imaging beam frequency.

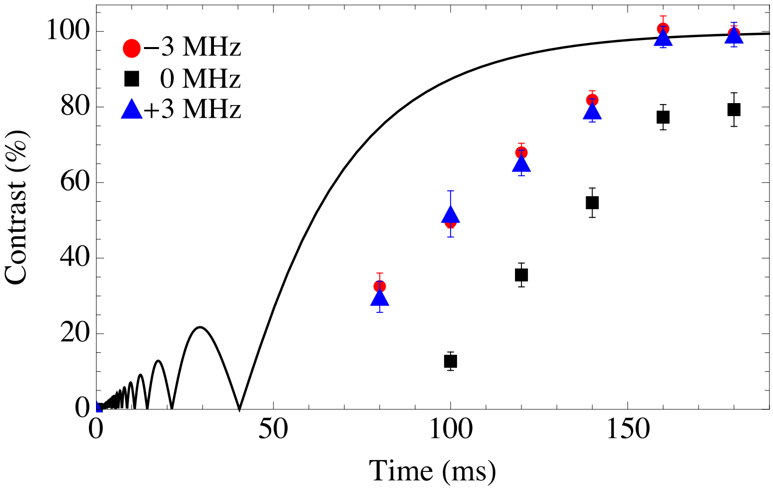

Figure 5.16: Contrast as a function of time for different imaging beam detunings. Two BECs were created, then levitated for a varying time and the contrast of the resulting interference pattern analysed. The fringes were focused separately for all three detunings. Each point is an average of five experimental data runs.

As mentioned previously, the focal position of the camera changes depending on the frequency of the imaging beam. The fringes were focused for -3, 0 and +3 MHz detuning from the imaging resonance and the contrast of the interference fringes as a function of time was performed for all 3 detunings. The experimental data is presented in Figure 5.16, where it is clear to see that there is $\sim 20\%$ increase in contrast for both the -3 and $+3$ MHz detuning. The reason for the increase in contrast when the imaging beam is detuned can be attributed to the spatial Talbot effect of the imaging light interacting with the periodic BEC fringes, The Talbot effect converts phase amplitude into intensity amplitude, which results in an increase of the observed contrast of the interference pattern. This Talbot effect and enhancement of contrast will be discussed in more detail in the next section.

5.6 Talbot enhanced interference

5.6.1 Talbot effect

A well known phenomenon in classical optics is the Talbot effect, the self-imaging of a periodic structure in near-field diffraction at certain regular distances. The Talbot effect was first observed in 1836 by Talbot [230], when a diffraction grating was illuminated with white light, and behind the structure repeated images of the grating were observed [231]. In 1881, Lord Rayleigh explained the Talbot effect in terms of wave optics [232], where he proved the phenomenon was a result of the diffraction interference of highly spatially coherent waves, i.e. plane waves, by the grating.

When light with wavelength λ is incident on a periodic structure (a grating) with period d, the intensity pattern of the light forms a self image of the structure behind the grating. These self images occur at particular periodic positions, with a period given by the Talbot length [76]

$$L_{\mathrm{Talbot}} = \frac{d^2}{\lambda} \ , \tag{5.14}$$

and then again at all multiples of the length. At even multiples of the Talbot length an exact self image of the structure is reproduced, whereas at odd multiples the reproduced self image is shifted by half the period of the grating (see Figure 5.17). In between the revivals of the images, patterns with smaller periods are formed, this effect is known

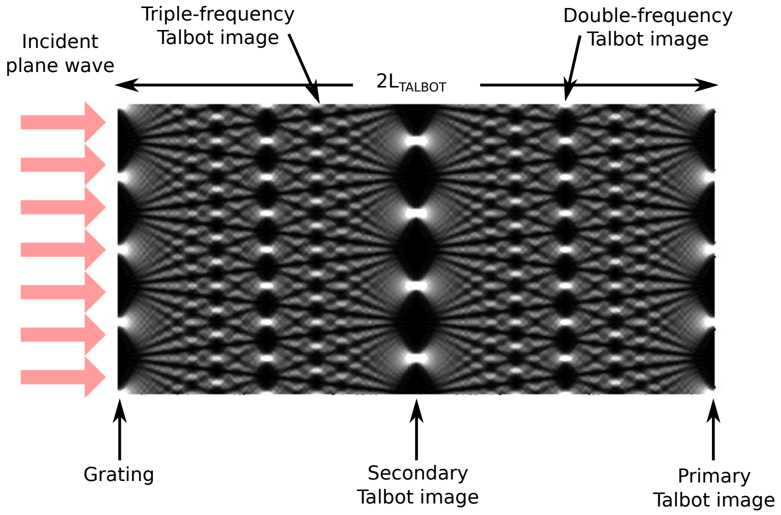

Figure 5.17: The Talbot effect, figure taken and adapted from [231], shown as a "Talbot carpet". An incident plane wave diffracts though the grating and this exact image is reproduced behind the grating at $2L_{\text{Talbot}}$. Another exact self image of the grating occurs at L_{Talbot} but is shifted by half a period of the grating. At regular fractions of the Talbot length higher frequency images are also present.

as the fractional Talbot effect [233]. Figure 5.17 schematically shows the Talbot effect for plane light waves incident on a periodic grating. It is clear to see the identical self image of the structure at $2L_{\text{Talbot}}$, the self image shifted by half a period as well as the higher frequency Talbot effects.

The Talbot effect has many applications in imaging processing and synthesis, optical testing and optical metrology [234], and has been studied extensively both theoretically and experimentally [235, 236, 237]. The Talbot effect has also been observed with spatially incoherent light [238] to form a Talbot-Lau interferometer [239], which is used in atomic and molecular interferometry [240, 241]. In the case of atom optics, where matter waves replace light waves, the Talbot effect has also been observed [239, 242, 243]. As regards to macroscopic matter waves, i.e. BECs, the temporal Talbot effect has been observed in the time domain [244, 245]. The Talbot effect is also important for pattern formation [246].

5.6.2 Spatial Talbot effect - BEC interferometry

In atom optics the Talbot effect is due to matter waves imaging and reimaging at the Talbot distance ($\Lambda_{\mathrm{T}} = 2d^2/\lambda$). The Talbot effect has been observed using hot atomic beams, which have de Broglie wavelengths of tens of picometers. For BECs, to date the Talbot effect has been seen in the time domain, in systems with additional 1D standing waves. In Strathclyde there is a strong dependence of the interference fringe contrast with the focal location of the camera, which can be clearly attributed to the Talbot effect. This is the first observation of the spatial Talbot effect of imaging light interacting with periodic BEC fringes and this effect can have a drastic influence on the interference signal, which is discussed below.

The CCD camera is on a translation stage, which has a total range of 25 mm, so by moving the camera in 1 mm steps interference patterns from multiple different focal locations can be analysed. By moving the camera over the full range of 25 mm, the observed contrast of the interference fringes increases and decreases, as shown in Figure 5.18. In this experiment two BECs were created, then levitated for 160 ms before an absorption image was taken on resonance at the various camera positions. From this it is clear to see that the contrast of the interference pattern increases and decreases as the camera is swept through the full range of the translation stage. The three density plots were chosen at the peak, trough and middle point to display the contrast visibly changing and demonstrate the drastic effect on the interference signal.

The magnification of the imaging system modifies the observed Talbot period, which is therefore given by

$$\Lambda = \frac{(M\lambda_f)^2}{\lambda} \ , \tag{5.15}$$

where M is the magnification, λ_f is the period of the fringes and λ is the wavelength of the imaging light. Due to the magnification of 2.03(0.05) (measured in Section 3.5.1) at a camera position of 12.5 mm in the setup, the Talbot period appears four times longer when imaged onto the camera. The observed fringe period under these experimental conditions was calculated to be 41(1) μm (camera position of 12.5 mm) after 160 ms, using Equation 5.15 this corresponds to a theoretical Talbot period of 8.6(4) mm. The Talbot period from the fit to the data in Figure 5.18 was measured to be 8.0(1) mm, which agrees well with the theoretical predictions.

The Talbot effect depends on the magnification, fringe period and wavelength of the imaging light. To confirm the observed effect was the Talbot effect the period of the interference fringes was changed and the same experiment was carried out. The fringe period was altered by changing the total levitation time, 140 ms and 170 ms were chosen

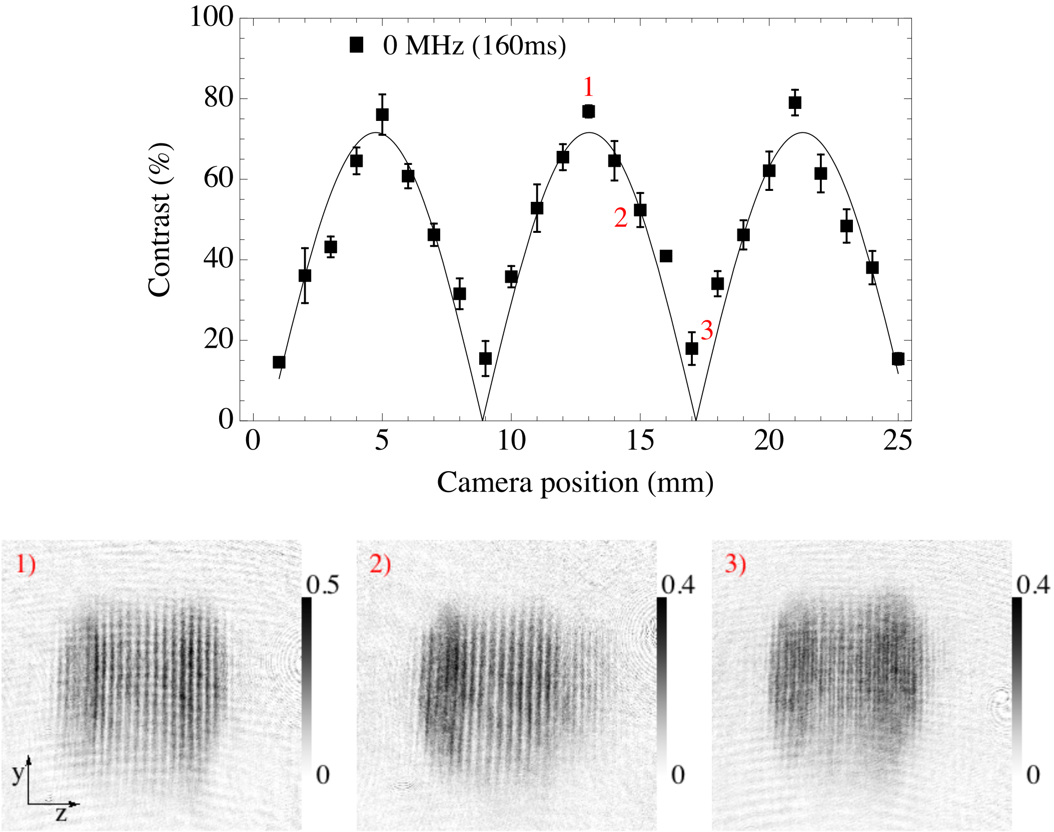

Figure 5.18: Talbot effect - Contrast as a function of camera position for a resonant imaging beam and density plot of fringes at three camera positions for 160 ms levitation. Scale bars represent optical density. Contrast of interference signal drops and then rises as the camera's position is scanned across the full range. Red numbers on graphs correspond to red numbers in the corner of the density plots. Density plots of fringes show the contrast visibly changing as the camera's focal location is changed. Each data point is an average of five experiment iterations and images are single shots with 1.2×1.2 mm.

as they would both produce a noticeable change in the observed Talbot period. The same experiment was performed for both 140 ms and 170 ms: two BECs were created, then levitated for either 140 ms or 170 ms and the contrast as a function of camera position was analysed. Figure 5.19 shows the experimental data and fits to the data, which also exhibit a periodic variation in the contrast of the interference signal as the camera's location is varied. It is expected that the Talbot period will be extended for larger fringe periods and shortened when the fringe period becomes smaller, this effect

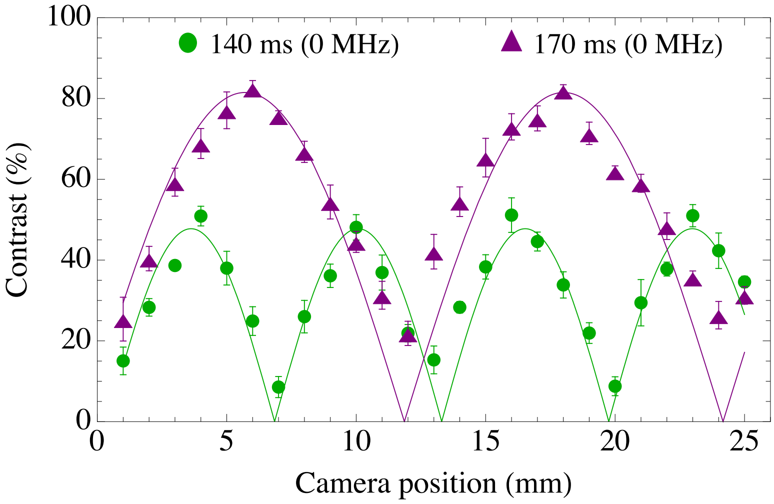

Figure 5.19: Talbot effect - Fringe contrast as a function of camera position for resonant imaging light for 140 and 170 ms levitation. Talbot period increases with larger fringe periods and gets shorter with smaller fringe periods. With the camera at 12.5 mm, the fringe periods at 140 ms and 170 ms were measured to be 35(1) μm and 49(1) μm, respectively, which results in theoretical Talbot periods of 6.3(3) mm for 140 ms and 12.3(4) mm for 170 ms. Talbot period from the fits were measured to be 6.4(1) mm for 140 ms and 11.8(1) mm for 170 ms. Each point is an average of five experimental data runs.

is observed in Figure 5.19. The fringe periods under the experimental conditions for 140 ms was found to be 35(1) μm and 49(1) μm for 170 ms with the camera at 12.5 mm, which results in a theoretical Talbot period of 6.3(3) mm and 12.3(4) mm for 140 ms and 170 ms respectively. The Talbot periods from the fits to the data were measured to be 6.4(1) mm for 140 ms and 11.8(1) mm for 170 ms, both of these are in good agreement with the theoretical prediction.

The striking agreement between the theoretically predicted Talbot periods and the measured Talbot periods from the fits to the experimental data strongly verifies that the observed effect is indeed the Talbot effect. This is the first reported observation of the spatial Talbot effect of imaging light interacting with periodic BEC fringes. This effect is relevant to all BEC interferometers and can be used as a tool to optimise and focus interference fringes. Figure 5.20 presents the observed Talbot period as a function of fringe period for three different magnifications and demonstrates the relevance and importance this effect has on BEC interferometry. Depending on the magnification of the imaging system and the interference pattern's fringe period the Talbot period can

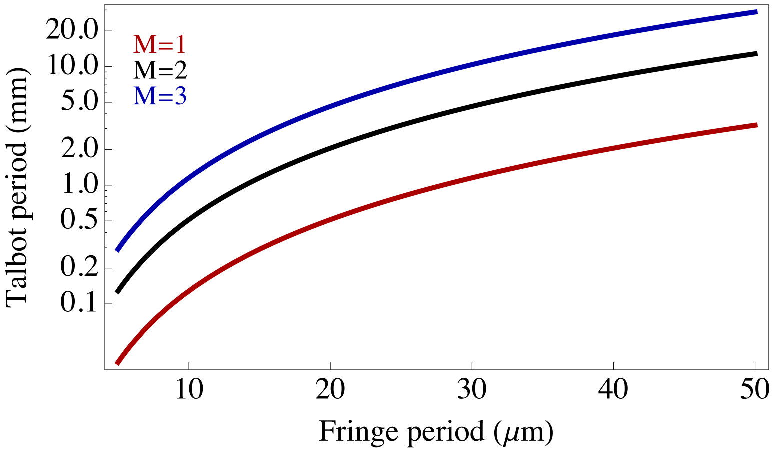

Figure 5.20: Theoretical Talbot period as a function of fringe period for three different magnifications. Theoretical Talbot periods calculated using Equation 5.15. This demonstrates how sensitive the Talbot period is to experimental parameters. Depending on fringe period and magnification, the Talbot period can be either small or large, which can have a major effect on the interference signal. Note y-axis is on a log scale.

be either extremely short or long. If the fringe period is small, when the BEC appears to be in focus the interference signal could potentially be at a trough in the Talbot period, therefore the resulting fringes will appear to have a low contrast. By moving the camera a small amount, while still keeping the BEC in focus, the fringes would rise to a peak in the Talbot period, in turn increasing the contrast of the interference signal. This phenomenon offers a technique to focus interference fringes and obtain the highest possible contrast the system allows and is important for all BEC interferometers.

The spatial Talbot effect of light interacting with periodic interference fringes was also studied using positive and negative detuned imaging light. The contrast as a function of camera position after 160 ms levitation was performed for both $+3\,\mathrm{MHz}$ and $-3\,\mathrm{MHz}$ imaging beam detuning. Figure 5.21 presents the experimental data for the contrast as a function of camera position for $+3/0/-3\,\mathrm{MHz}$ detuned imaging light. The enhancement in the contrast can be understood by considering what happens to the imaging light as it passes through the fringes. When light passes through the interference fringes, the atoms attenuate and phase shift the light depending on the detuning and optical density. The phase delay due to the detuning and optical density

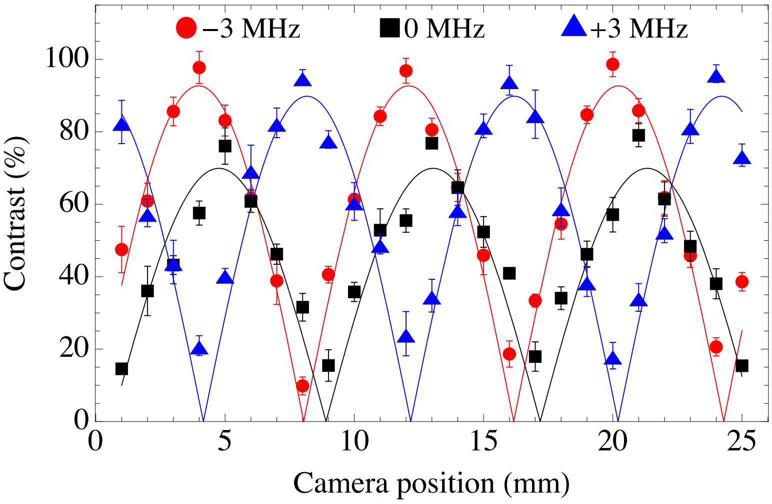

Figure 5.21: Talbot effect - Fringe contrast as a function of camera position for +3/0/−3 MHz detuned imaging light after 160 ms levitation. Contrast is enhanced for both the negative and positive detunings, which are also anti-correlated (π out of phase). The phase of the Talbot period curves for both the +3 and −3 MHz is shifted, this is due to the imaging light being phase shifted through the fringes. With the camera position at 12.5 mm, the observed fringe periods were 41(1) μm and Talbot periods of 8.6(4) mm, which agree well with the theoretically predicted period of 8.0(1) mm. Each point is an average of five experimental data runs.

can be described by the following

$$\phi_{\text{delay}} = \text{OD}\left(\frac{\Delta}{1 + (I/I_{\text{sat}}) + 4\Delta^2}\right) , \tag{5.16}$$

where OD is the condensate's optical density, I is the intensity of the light, I_{sat} is the saturation intensity ($I/I_{\text{sat}} \sim 0.25$ in the Strathclyde experiment) and Δ is the light's detuning measured in linewidths (δ/Γ). Figure 5.22 demonstrates the phase shift of the imaging light as a function of detuning. It can be seen that the largest phase shift occurs at ± 3 MHz ($\delta/\Gamma = 0.5$). The phase delay as a function of the optical density is presented in Figure 5.23. The phase shift increases linearly for both the −3 and +3 MHz detuning as a function of the optical density. The phase delay of the imaging light as it passes through BEC fringes, with a period of 42 μm, for $-3, 0$ and $+3$ MHz is presented in Figure 5.24. It can be seen that the light acquires a phase shift as it passes through the atoms for both the positive and negative detunings. Due to the finite linewidth of the laser used for imaging (~ 1 MHz), experimentally the 0 MHz detuning

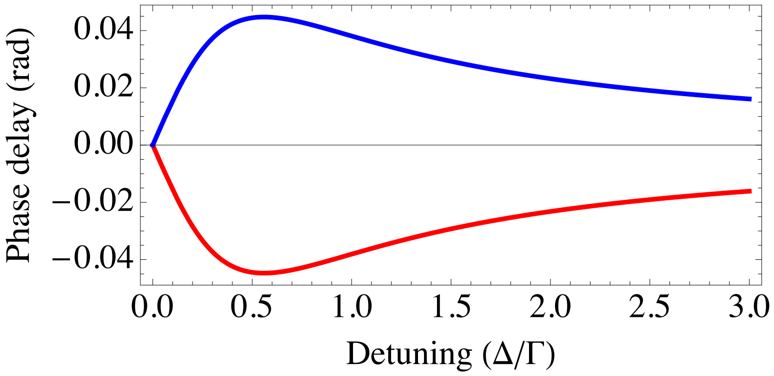

Figure 5.22: Phase shift of imaging light as a function of detuning with an optical density of 0.2. Imaging light experiences largest phase shift at −3 MHz (red) and +3 MHz (blue) detuning. Phase delay was calculated using Equation 5.16.

will experience a slight phase shift. The Talbot effect causes an enhancement of the observed contrast for detuned light due to the phase variation in the initial conditions converting reversibly into intensity variation upon propagation. Another phenomenon which contributes to the enhancement of contrast is focusing and defocusing of the light as it passes through the BEC fringes due to the different refractive index of the BEC depending on the imaging beam's detuning. This phenomenon, along with the Talbot effect, results in the regions with light (i.e. peak of the fringes) to be even brighter and the regions with no light (i.e. trough of fringe) to be even darker. The Phase of the −3 and +3 MHz Talbot period curves are shifted compared to the 0 MHz because the

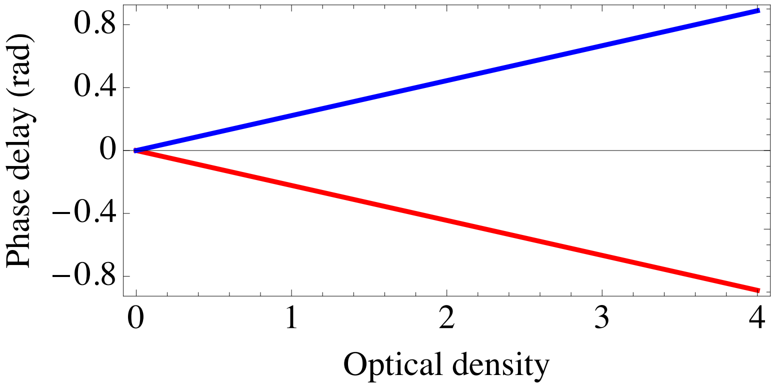

Figure 5.23: Phase shift of imaging light as a function of condensate's optical density. Phase shift increases linearly as a function of optical density for both the −3 MHz (red) and +3 MHz (blue) detuning. Phase delay was calculated using Equation 5.16.

phase of the light is delayed as it passes through the condensate. The Talbot period curves for -3 and $+3$ MHz detuning are π out of phase, this is due to the positive and negative refractive index of the condensate depending on detuning of the imaging beam. The fractional Talbot effect (higher frequency images) isn't observed in the experiment because our light sources aren't localised.

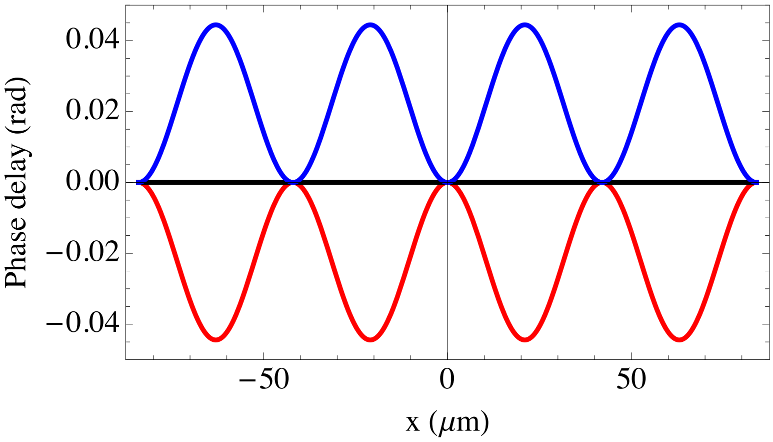

Figure 5.24: Phase shift of imaging light from passing through BEC fringes with optical density of 0.2. No phase delay occurs at 0 MHz detuning (black), whereas for -3 MHz (red) and $+3$ MHz (blue) the atoms phase shift the imaging light. The phase delay is dependent on the detuning of the light and the optical density of the condensate.

5.6.3 Spatial Talbot effect - BEC interferometry theory

The spatial Talbot effect of imaging light interacting with periodic BEC fringes can be modelled by calculating the propagation of the electromagnetic (EM) waves. It is easier to propagate the field in Fourier space or k-space, the Fourier transform of the spatial field distribution is known as the angular spectrum. The general method is: calculate the angular spectrum, propagate over a distance z and then use the inverse Fourier transform to covert back to a real space distribution. A detailed description of how to propagate the electromagnetic waves in Fourier space can be found in [247, 248, 249]. The figures in this section are taken from the theory and code developed by Dr. Aidan Arnold.

Figure 5.25 represents the theoretical Talbot effect of imaging light interacting with periodic BEC fringes from propagating electromagnetic waves with 0 MHz detuned imaging light. The theoretical propagation of light interacting with matter-wave fringes

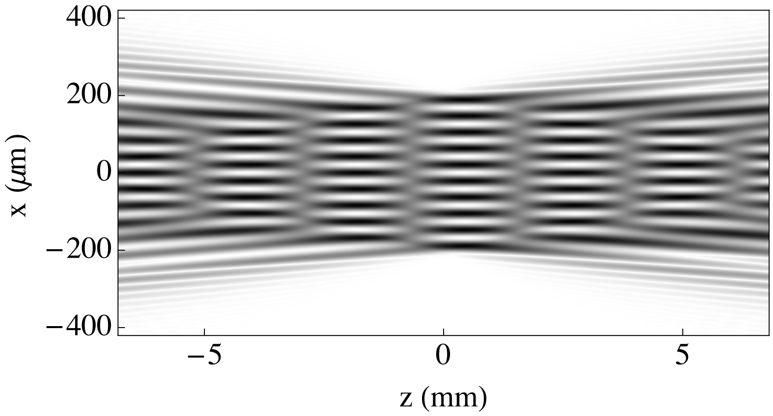

Figure 5.25: Theoretical Talbot effect pattern from propagating electromagnetic waves for 0 MHz detuning. Theoretical propagation of light interacting with matter-wave fringes is modelled for a BEC at $z = 0$ with ten fringes of peak OD = 0.4. Primary (exact self-image) and secondary (exact self-image shifted by half the period of the grating) Talbot image are both observed. Note Talbot period is four times longer after the imaging system (Equation 5.15).

is modelled for a BEC at $z = 0$ with ten fringes of peak OD = 0.4, from this it is clear to see the primary Talbot image (exact self-image) and secondary Talbot image (exact self-image shifted by half the period of the grating). The Talbot period appears four times longer in the experiment due to an extra factor of four from the magnification of the imaging system (Equation 5.15). In Figure 5.26, the central fringe of the theoretical

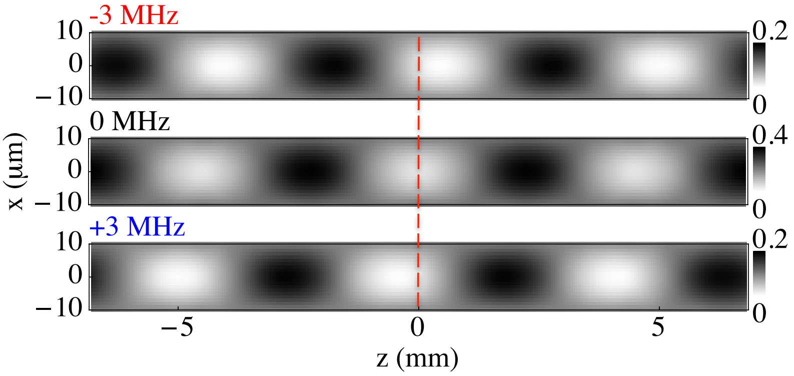

Figure 5.26: Theoretical propagation of light interacting with matter-wave fringes for ±3 and 0 MHz detuned light for a BEC at $z = 0$ with ten fringes of peak OD = 0.4. Central fringe is displayed for ±3 and 0 MHz, illustrating how detuning not only phase-shifts the fringes in z, but can enhance contrast relative to the initial optical density.

propagation of light interacting with matter-wave fringes is shown for ±3 MHz and 0 MHz detunings. This clearly illustrates how detuning not only phase-shifts the fringes in z, but can also enhance contrast relative to the initial optical density. By taking slices through Figure 5.25 the contrast as a function of z can be obtained, this is shown in Figure 5.27. The contrast is enhanced from 80 % for the 0 MHz detuning to 100 % for both the positive and negative detunings, which is in excellent agreement with the experimental data. This enhancement for detuned light is due to phase variation in the initial conditions converting reversibly into intensity variation upon propagation. The phase of the -3 and $+3$ MHz detunings are $\sim 0.8\pi$ out of phase, unlike the π out of phase in the experimental data, however, overall there is good agreement between the theory and the experimental data.

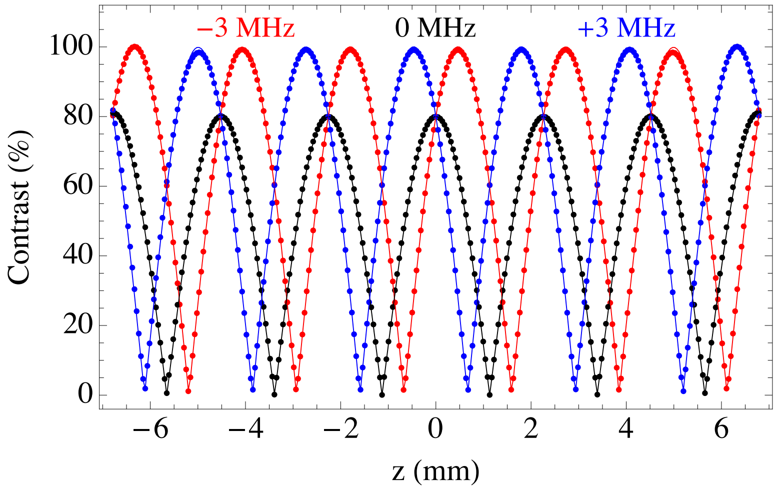

Figure 5.27: Theoretical Talbot effect - contrast as a function of z obtained by taking slices through Figure 5.25. The contrast is enhanced from 80 % to 100 % for both the positive and negative detunings, which is in excellent agreement with the experimental data in Figure 5.21. The phase of the ±3 MHz Talbot periods are shifted compared to the 0 MHz detuning due to the phase delay when the light passes through the fringes, which is also in good agreement with experimental data. Note Talbot period is four times longer after the imaging system (Equation 5.15).

5.7 Interference fringes lifetime

The Strathclyde magnetic storage ring has a total enclosed area of $\sim 72\,\mathrm{cm}^2$, which lends itself perfectly for Sagnac interferometry as the sensitivity is proportional to the enclosed area [115]. The storage ring is also a fully coherent system, i.e. after a full propagation around the ring the atomic cloud is still a BEC and the heating rate is less than 50 nK/s [250]. The atoms travelling around the ring (one revolution) need to travel ∼ 30 cm, so not only does the BEC lifetime need to be sufficiently long, the lifetime of the interference fringes must also be long enough.

To measure the lifetime of the interference fringes an experiment was carried out where two BECs were created, then a varying hold time was implemented before the condensate was levitated. The BEC lifetime was measured by monitoring the BEC fraction and the fringe lifetime was measured by analysing the contrast of the interference signal. BECs with 5×10^5 atoms and a ∼ 60% condensate fraction were alternately created with (without) the dipole beam, RF evaporation was then stopped and the atoms were held in the IP trap for a varying time. The atoms were then allowed to expand for 160 ms (20 ms) and an absorption image was taken. The data without the dipole beam, and with short time-of-flight, allowed the relative remaining BEC fraction to be accurately determined. The long levitation time data with the dipole beam was used to calculate the fringe contrast, which is a measure of the fringe lifetime.

Figure 5.28 shows the experimental data for the BEC fraction and fringe lifetime as a function of hold time in the IP trap. A BEC lifetime of around 1 s was determined, with a similar fringe coherence time which only appears to be limited by the BEC life-

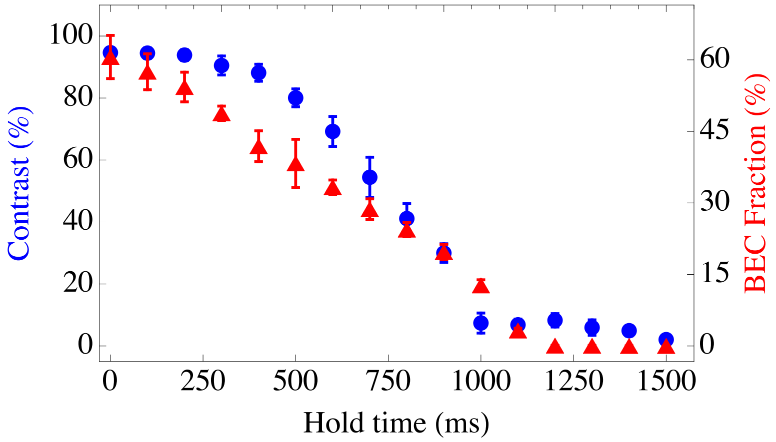

Figure 5.28: Experimental interference fringes lifetime. The BEC fraction (red) and fringe lifetime (blue) are shown as a function of hold time in the IP trap. The BEC fraction was calculated using 20 ms time-of-flight and the fringe contrast was determined using 160 ms time-of-flight. Each data point is an average of ten experimental data runs.

time. By leaving a weak RF evaporation knife on during the ‘hold’ time [62], the fringe lifetime could no doubt be extended. This result is a proof of principle that interference will be possible between condensates travelling around the magnetic storage ring. As it appears the fringe lifetime is limited by the BEC lifetime, and since the heating rate of the ring is sufficiently low that after multiple revolutions the atomic cloud is still a BEC, interferometry around the ring should be possible.

5.8 The search for phase locked fringes

The crucial element of any kind of sensor is to be able to obtain a stable and consistent measurement. This is essential as if the system is stable and reproducible there is a reference point from which quantities can be measured against. For atom interferometry to be used as a measuring device it requires the matter-wave interference pattern to be ultra stable. Unfortunately the spatial fluctuations of the Strathclyde BEC and interferometer prevents the observation of reproducible interference fringes, i.e. the position of the interference pattern changes with each nominally identical realisation of the experiment.

5.8.1 Spatial fluctuations

Since the fringes move from shot to shot, there is no stable reference point from which to make measurements. Spatial fluctuations in the location of the centre of the BEC can be caused by

- magnetic trap/current noise
- magnetic switch off
- dipole beam movement

each of which was studied.

First the final cloud position with no dipole beam, i.e. just BEC, after 160 ms levitation was monitored for several iterations of the experiment and centre-of-mass of the condensate was found. The centre of the BEC was found by fitting a Gaussian in both the y and z axis and the peak of the Gaussian was taken as the centre of the condensate. Figure 5.29 shows how the centre of the condensate fluctuates from the

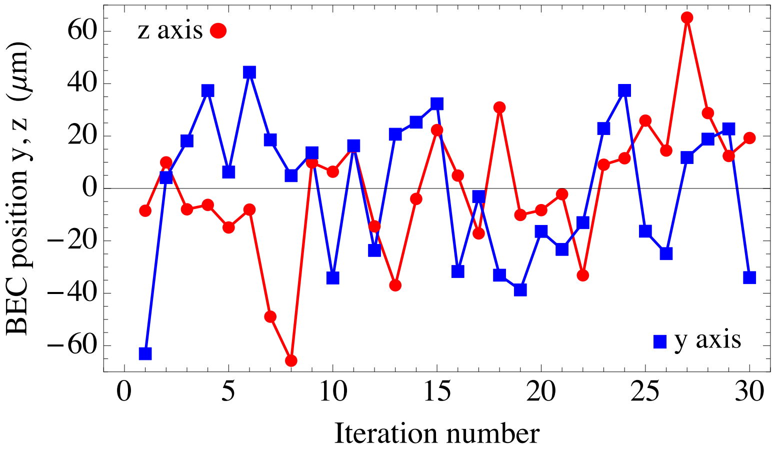

Figure 5.29: Spatial fluctuations of final BEC position in y and z axis after 160 ms levitation. The centre of mass of the condensate was calculated for 30 consecutive experimental iterations and the centres subtracted from the average cloud centre. The standard deviation demonstrates by how much the centre of the cloud fluctuates from the average centre over a period of $\sim$ 30 minutes (each experimental iteration takes $\sim$ 1 minute).

mean cloud centre of mass with each iteration of the experiment (each experimental iteration lasts ~ 60 s).

To attribute the fluctuation in the BEC location to a change in the initial velocity or position, the same experiment was carried out for various levitation times. The data and corresponding fit of this experiment is presented in Figure 5.30. From this experiment it is clear to see that the standard deviation of the condensate centre to the mean cloud centre increases with increasing levitation time. This result points towards the cause being fluctuations in initial conditions (position or velocity) since the jitter in BEC location increases with time. However, it is difficult to distinguish between fluctuations in the initial velocity or position, from the fit to the data shown in Figure 5.30, z_0 and v_0 were found to be 1.187(0.707) and 0.098(0.109) respectively for the z-axis(y-axis). When using long levitation times of the order 100 ms, the spatial fluctuations become significant when compared to the size of the condensate, or more importantly the period of the interference fringes. Therefore the size of our interference pattern in comparison to our centre-of-mass uncertainty currently prevents us from ascertaining our degree of phase stability. The initial conditions of the condensate are set by the turn-off of the magnetic trap, which starts the ballistic expansion or magnetic levitation, hence the

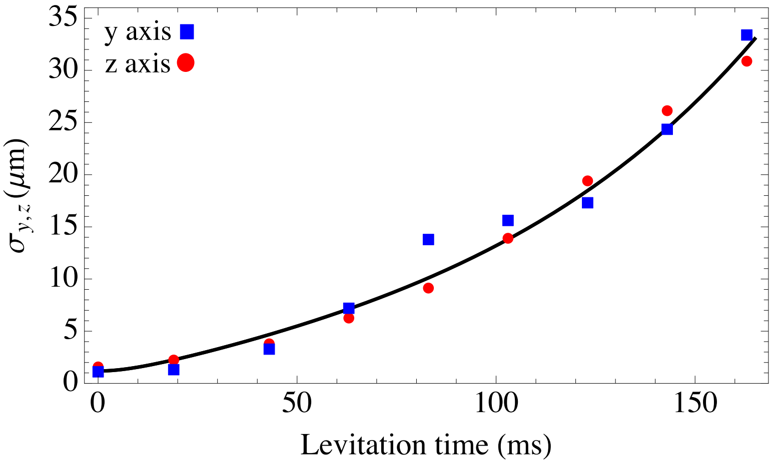

Figure 5.30: Spatial fluctuations of final BEC position in y and z axis as a function of levitation time. For each levitation time 30 iterations of the experiment were carried out with no dipole beam. Points are averaged standard deviation of the condensates centre from the mean centre for the z (red) and y (blue) axis. The data was fit using a function of the form $\langle z(t)\rangle = (\langle z_0^2\rangle \cosh^2(\omega t) + \frac{1}{\omega^2}\langle v_0^2\rangle \sinh^2(\omega t))^{1/2}$, with $z_0 = 1.187(0.707)$ and $v_0 = 0.098(0.109)$ for the z-axis(y-axis). These results demonstrate jitter in the BEC's centre increasing as a function of time.

fluctuations in BEC location are present from the moment the atoms are released from the trap.

5.8.2 Spatial fluctuations - Magnetic switch off

Changes in the initial conditions of the condensate at the moment that the atoms are released from trap can result in a different spatial position after each experimental run. During the magnetic trap switch off an initial velocity or position can be imparted onto the atoms, which will not only result in a different spatial location but also will increase with time. The advantage of the inverted parabola axial potential providing a magnifying effect on the fringes also has the disadvantage of magnifying any initial velocity or position that the atoms have. To study if the magnetic switch has an effect on the final position of the BEC's centre, the switch off time was varied and the jitter as a function of time analysed.

Typically the Bias and IP coils switch off in 1 ms and 2.5 ms respectively (Bias must switch off before IP to avoid spin-flips), which is due to slightly different time constants

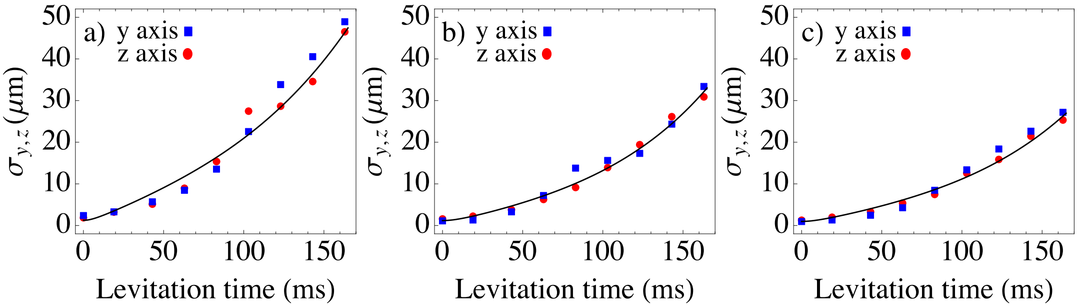

Figure 5.31: Spatial fluctuations of final BEC position in y (blue) and z (red) axis as a function of levitation time for different magnetic trap switch off timings. a) Fast timings; bias and IP are switched off in 0.5 ms and 1 ms respectively, jitter in condensate centre increases. b) Typical experimental timings; bias and IP are switched off in 1 ms and 1.5 ms respectively. c) Slow timings; bias and IP are switched off in 3.5 ms and 4.5 ms respectively, standard deviation of condensates centre decreases. The initial position and velocity z_0 and v_0 from the fit were calculated to be; a) 1.245(1.562) and 0.171(0.158), b) 1.187(0.707) and 0.098(0.109) and c) 0.988(0.501) and 0.085(0.096) for the z-axis(y-axis). Each point is comprised of averaged standard deviation of the clouds centre from the average centre for 30 experimental iterations.

of the control circuits and coil inductance. By either changing the time constant of the circuit or DAC line voltages and timings, the speed of the switch off can be varied. To avoid ringing in the circuit the time constant wasn't changed, instead the switch of speed was adjusted solely using the DAC line. Figure 5.31 shows the spatial fluctuations as a function of time for both extremes of the magnetic switch off, i.e. a fast and slow switch off, and the typical experimental switch off timings. In Figure 5.31 a) the bias and IP were switched off in 0.5 ms and 1 ms respectively, and it is clear to see that this has an undesired effect as the standard deviation of the clouds centre increased by a noticeable amount. This result is expected as the faster the trap is switched off the more instantaneous and nonadiabatic the release from the trap becomes. This means the atoms experience a large change in magnetic field over a short period so therefore they gain an initial unwanted velocity. In Figure 5.31 c) the bias was switched in 3.5 ms and the IP in 4.5 ms, which resulted in the overall jitter in the condensate's location to decrease. Again this can be understood in the following way: as the trap is switched off over a longer period the atoms experience a less abrupt change in magnetic field and the release from the trap becomes more adiabatic. Also, some of the initial kinetic energy of the atoms is absorbed by the trap as it is being slowly switched off. Overall,

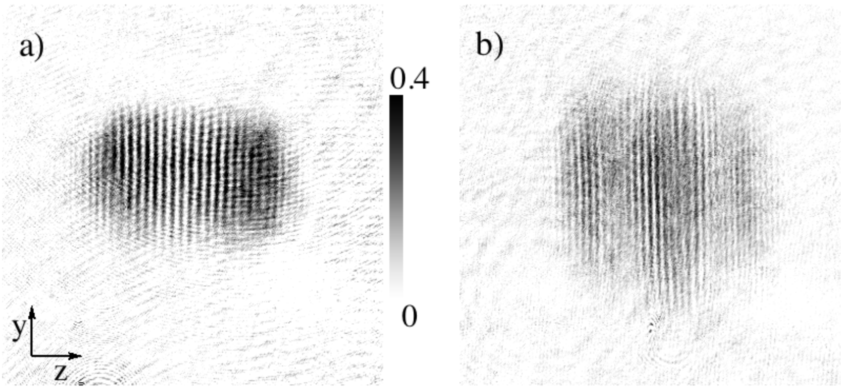

Figure 5.32: Density plots of fringes with different magnetic trap switch off times after 160 ms levitation. Scale bars represent optical density. a) Typical magnetic switch off (bias=1 ms and IP=2.5 ms) and b) slow magnetic trap switch off (bias=3.5 ms and IP=4.5 ms). Contrast drops from $\geq 95\,\%$ in a) to $\sim 65\,\%$ in b). Not only did the slower magnetic trap switch off reduce the contrast, it also changed the expansion dynamics of the condensate. Each image is $1.8 \times 1.8\,\mathrm{mm}^2$.

the initial position x_0 and velocity v_0 from the fits in Figure 5.31 both decrease as the switch off time is increased, this coincides with the standard deviation of the cloud's centre also decreasing at slower switch off speeds.

Using the slower magnetic switch off reduced the standard deviation of the condensate's centre from $\sim 32\,\mu$m (Figure 5.31 b), bias=1 ms and IP=2.5 ms) to $\sim 25\,\mu$m (Figure 5.31 c), bias=3.5 ms and IP=4.5 ms) in both the y and z directions for a drop time of 160 ms. It was then investigated if the slower switch off had an effect on the resulting interference pattern, Figure 5.32 shows density plots of the interference fringes with the typical and the slower magnetic trap switch off times after 160 ms levitation. The contrast of the interference pattern drops from $\geq 95\,\%$ (Figure 5.32 a)) to $\sim 65\,\%$ (Figure 5.32 b)) with the slow magnetic trap switch off. Not only did the contrast reduce when using the slower magnetic trap switch off, the expansion dynamics of the condensate were also altered. A possible reason for this is that the interference fringes arise from the momentum distribution of the two condensates de Broglie wavelength's overlapping, so by slowly switching off the potential the momentum distribution is disrupted. As the condensates are released from the trap some of the initial kinetic energy is absorbed by the 'walls' of the trap, therefore meaning the momentum distribution is changed and the contrast of the resulting interference pattern decreases.

By switching the trap off over a longer period (3.5 ms and 4.5 ms for bias and IP), the standard deviation in the condensate's centre is reduced by $\sim 20\,\%$ although the contrast drops by $\sim 35\,\%$. It was found that by switching the coils over an even longer period further reduced the centre-of-mass motion but the contrast of the interference pattern washed out. Even though the longer switch off time decreased the BEC's location, it came at a price as the contrast dropped by a significant amount compared to the reduction in the jitter of the cloud. From this it was inferred that the magnetic trap switch off has some contribution to the spatial fluctuations but it is difficult to eliminate form the experiment without effecting the resulting interference pattern.

5.8.3 Spatial fluctuations - Dipole beam

Another possible cause of the fluctuations in the final location of the condensate is the optical dipole beam, which could impart a velocity or position onto the atoms. The dipole beam could cause an initial velocity or position in the atoms via instabilities in either the intensity or position. To investigate any instabilities in the dipole beam a photodiode was placed in the beam just before the focusing lens, this was the closest point to analyse before the atoms. Then scope traces were taken over various time bases (to ensure all frequency components were covered) with the full beam illuminating the photodiode for intensity noise and with a knife edge over half the beam for position noise.

The knife edge measurement was performed for the vertical and horizontal motion of the dipole beam and any motion was converted into a position. This was done

Time base	**Vertical** (μm)	**Horizontal** (μm)	**Intensity** ($\times 10^{-3}$)
1 ms	3.49	3.24	1.42
100 ms	4.15	3.41	1.46
10 s	5.21	4.13	1.49

Table 5.1: Dipole beam's vertical and horizontal RMS position noise and relative intensity noise. Vertical and horizontal position noise was calculated using knife edge measurement, i.e. half of the photodiode was illuminated, and relative intensity noise was measured with the full photodiode illuminated. RMS signal of the scope trace was converted into position by multiplying by a conversation factor for both the vertical and horizontal, whereas intensity is relative noise (RMS/DC voltage). Three time bases were taken to ensure that all frequency components are included.

by calculating the RMS of the signal from the scope trace and multiplying it by a conversion factor, which converts the voltage change on the photodiode into a position change. The conversion factor was found to be $(\sqrt{\pi/2}/w)/\mathrm{V}_{\mathrm{max}}$, where w is the beam's waist and $\mathrm{V}_{\mathrm{max}}$ is the maximum DC voltage on the photodiode. Intensity noise was calculated by dividing the RMS of the scope trace by the voltage on the photodiode ($\mathrm{RMS}/\mathrm{V}_{\mathrm{max}}$), which results in a relative intensity noise. Table 5.1 presents the RMS position noise of the dipole beam in the vertical and horizontal axis as well as the relative intensity noise. Figure 5.33 shows the scope trace for the knife edge measurement in the vertical axis with a time base of 1 ms. Position error of the dipole beam was calculated by taking the RMS of the trace and converting into movement at the dipole beam. Similar traces were used for all dipole beam jitter measurements.

As well as calculating the instabilities of the dipole beam using photodiode measurements, an experiment was carried out using the hole which the dipole makes when splitting the BEC. In this experiment a BEC was created, then the dipole beam was ramped on to split the condensate in half and an absorption image taken after 0.1 ms expansion. From the resulting images the minimum in the density distribution was found, this was taken to be the centre of the hole created by the dipole beam. The jitter in the minimum of the hole between the two condensates can be converted into position change of the beam. Using this method the jitter in dipole beam's position in

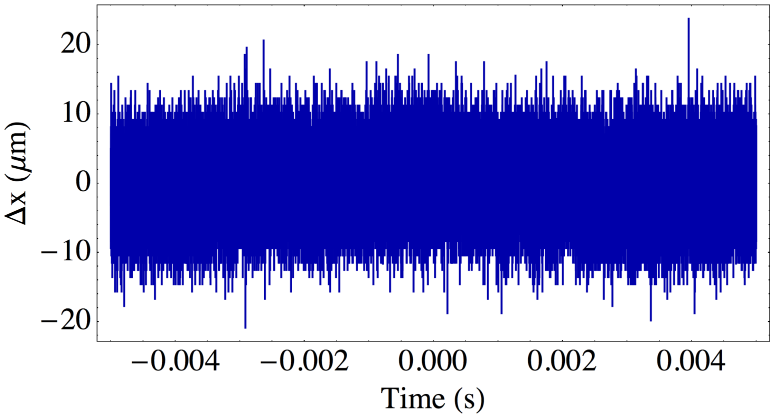

Figure 5.33: Dipole beam knife edge measurement scope trace for vertical axis with time base of 1 ms. RMS jitter is calculated from this trace and then converted into a position motion at the dipole beam. All scope traces had one million data points. Similar traces were used for all jitter in position calculations.

	Vertical (μm)		**Horizontal** (μm)		**Intensity** ($\times 10^{-3}$)	
Time base	0- 5Hz	5 Hz-5 kHz	0-5 Hz	5 Hz-5 kHz	0-5 Hz	5 Hz-5 kHz
1 ms	0.88	3.37	0.97	3.08	0.44	1.35
100 ms	2.84	3.01	1.98	2.77	0.56	1.35
10 s	3.43	3.93	2.36	3.39	0.25	1.47

Table 5.2: Dipole beam's vertical and horizontal RMS position noise and relative intensity noise in particular frequency ranges. The Fourier transform was calculated for all of the traces, then the RMS position and relative intensity noise was calculated for both frequency regions. Photodiode had DC voltage of 240 mV for vertical and horizontal measurements, whereas intensity measurement had a 480 mV DC on photodiode. Noise in both regions add in quadrature, i.e. $((0\text{-}5\,\text{Hz})^2+(5\,\text{Hz-}5\,\text{kHz})^2)^{1/2}$=total noise (Table 5.1). Three timebases were taken to ensure all frequency components were covered.

the vertical and horizontal axis was calculated to be 3.87 μm and 3.54 μm respectively, which is consistent with the measured values in Table 5.1.

Next the Fourier transform of each of the scope traces was taken to investigate if there was any noise at a particular frequency. Table 5.2 shows the RMS position and intensity noise within the ranges of $0-5$ Hz and $5\,\text{Hz}-5\,\text{kHz}$ for each of the time bases for the vertical, horizontal and intensity traces. The relative RMS position noise in all frequency ranges is $< 5\,\mu$m, which is smaller than a pixel on the CCD camera. Figure 5.34 presents the Fourier transforms for all of the time bases in the vertical axis, note the change in frequency range between the three Fourier transforms (similar transform were taken for horizontal and intensity noise). From this it can be interpreted that

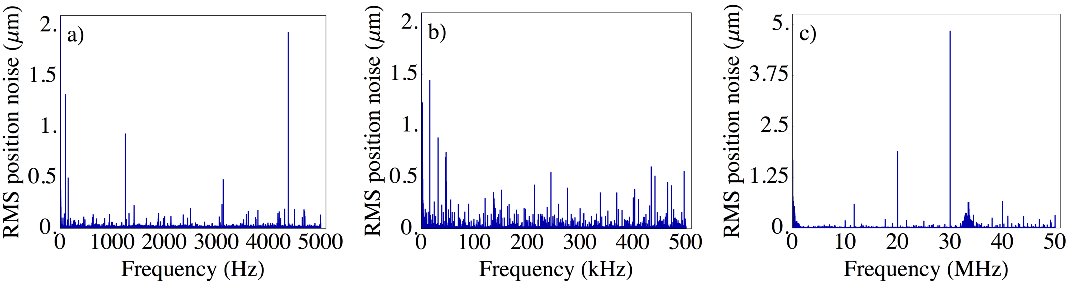

Figure 5.34: Fourier transform of vertical knife edge measurement for various times bases, which enables a wide range of frequencies to be analysed. Time bases are a) 10 s, b) 100 ms, and c) 1 ms. Overall the RMS position noise is greater at higher frequencies. Fourier transforms were also taken for the horizontal position noise and relative intensity noise, which resulted in similar transforms.

RMS position and relative intensity noise from the dipole beam has very little, if any, effect on the standard deviation of the BEC's centre.

5.8.4 Spatial fluctuations - Magnetic trap noise

An experiment was carried out to study if noise on the magnetic trap bottom had any influence on the final location of the BEC. Fluctuations in the position of the trap bottom could couple into an initial velocity when the atoms are released from the trap. Typical noise on the IP current sense resistor is $\sim 100\,\mu$V, this results in a relative current noise (i.e. by dividing by 7 V usual IP setting) of the $\sim 1 \times 10^{-5}$ current level. Typically the fluctuation in the condensate's position at 25 ms is $2/2.5\,\mu$m in both the y and x axis, which is $\sim 1/2$ of the $5\,\mu$m pixel size of the CCD camera. Noise was added into the circuit after the integrator (see Appendix A) via the noise function on a Agilent 33250A signal generator, which adds random noise at a known frequency and amplitude. A BEC was created in the magnetic trap, which had noise added at a known frequency and amplitude, then it was released from the trap and allowed to expand for 25 ms to amplify its affect on the condensate's centre-of-mass jitter. The longest time-of-flight possible without the need for levitation, 25 ms, was chosen.

	Noise added to trap		**COM motion**	
Frequency (Hz)	Agilent (mV$_{\text{pp}}$)	Resistor (mV)	y-axis (μm)	z-axis (μm)
5	500	14.2	2.45	3.58
10	75	1.8	2.14	12.84
12	150	6.5	3.11	6.47
50	800	31.2	3.34	2.82
85	150	4.5	6.15	1.72
90	50	1.5	52.79	3.07
100	150	4.4	5.84	2.21
110	550	17.2	2.94	3.84

Table 5.3: Centre-of-mass motion of condensate with various known frequency and amplitude noise added to magnetic trap. The amplitude of the noise signal sent to the circuit is shown along with the resulting noise on the current sense resistor. The centre-of-mass motion was measured for both the y and z axis for all frequencies of added noise. Standard deviation of the cloud's centre from the mean cloud centre was calculated from 20 experimental runs for each frequency. Note that more noise must be added at frequencies which aren't near the trap frequency for there to be a noticeable change in the condensate's location compared to the typical centre-of-mass motion.

Table 5.3 presents the results from adding various known frequencies and amplitudes of noise to the magnetic trap and analysing the condensate's final position. From this experiment it can be seen that the standard deviation of the final location of the condensate is extremely sensitive when the frequency of the noise added is near the trap frequency. The centre-of-mass jitter has the most notable increase in the z-axis for frequencies of 10 and 12 Hz, whereas the most noticeable increase occurs at 85, 90 and 100 Hz in the y-axis. This can be understood by considering the the trap frequencies: the radial trap frequency is 92.3 Hz, so therefore when the frequency of the noise approaches this more noise will be coupled into the radial axis and result in the jitter in the y-axis increasing. The same can be said about the axial trap frequency, which is 9.2 Hz, and when the noise frequency approaches this it couples more into the z-axis motion.

It was surprising that it was possible to still create BECs with so much noise being added to the magnetic trap. Typically the IP current sense resistor has 0.1 mV noise and even with $> 30\,\mathrm{mV}$ noise on the sense resistor it was still possible to create BECs. It is impressive that the evaporation still worked when effectively it was only 'nibbling' into the BEC at the modulation frequency of the noise. Converting the noise at 50 Hz into $31.2\,\mathrm{mV}/7\,\mathrm{V}\times 28\,\mathrm{G}\times 0.7\,\mathrm{MHz/G}= 90\,\mathrm{kHz}$ RMS oscillation in the trap bottom, which is massive relative to our normal evaporation sensitivity. When the frequency of the noise wasn't near the trap frequencies a larger amplitude was needed to see a notable change in the final BEC position compared to the typical COM motion at 25 ms. This implies that the jitter in the condensate's centre is more sensitive to noise with frequencies close to the frequencies of the magnetic trap.

5.8.5 Spatial fluctuations - Phase

As well as the final location of the condensate fluctuating with each iteration of the experiment, the phase of the interference pattern also changes with each realisation. This proves detrimental when trying to produce stable interference fringes to use in precision metrology. Figure 5.35 presents two typical sets of data and demonstrates how the phase fluctuates with each iteration of the experiment. In these experiments a BEC was created, it was then adiabatically split (Section 4.6.4) before being levitated for 160 ms and an absorption image taken. It is clear to see that the phase fluctuates randomly with each realisation of interference fringes and it is believed that the splitting

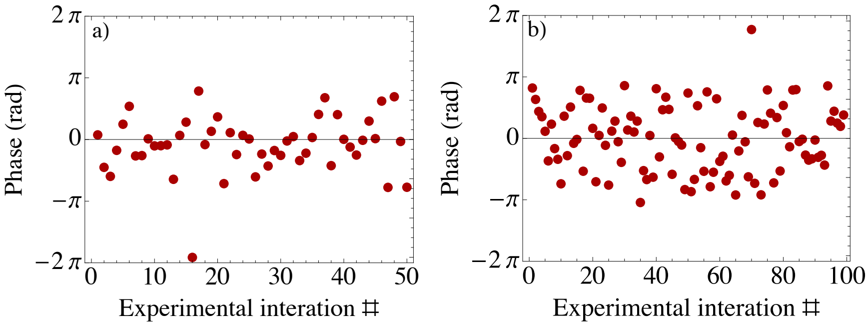

Figure 5.35: Fluctuation in phase of interference pattern with time. Phase was calculated for each of the interference patterns and plotted as a function of time to demonstrate how the phase fluctuates. a) 50 interference patterns were used and b) 100 interference patterns.

dynamics causes this unwanted effect. Currently the condensate is trapped magnetically and split optically, this means that when the IP moves with respect to the dipole beam the split changes. By changing the splitting dynamics (split ratio), the phase of the two halves evolve differently with each experimental realisation, this leads to the phase of the interference pattern fluctuating from shot to shot. There are two obvious solutions to this, either reduce the magnetic trap noise or decouple the magnetic trap and the split.

5.8.6 Spatial fluctuations - Solutions

A potential cause of the spatial fluctuations is sloshing in the magnetic trap, which can originate from loading the magnetic trap off centre, compressing the magnetic trap or the evaporation. If the atoms are sloshing in the trap, then each time they are released from the trap the atoms could be at a different point in their oscillation, therefore having different initial conditions and velocity. Another probable cause is noise on the levitation field, so atoms acquire a velocity kick during the levitation procedure causing the final position of the condensate to fluctuate from shot to shot. If the magnetic levitation is noisy and ‘shaking’, then even atoms released with perfect initial conditions, i.e. no velocity component, will exhibit spatial fluctuations that will grow with the amount of time in the levitation field.

A solution which could be used to investigate sloshing in the magnetic trap and decrease the influence of any noise that may be gained during the levitation process is RF dressing. RF dressed double-well potentials have been produced on atom chips and used for BEC interferometry [102, 103, 251, 252], which are ideal due to the high trap frequencies and magnetic field gradients. However, initial calculations suggest that it will be possible to RF dress our standard macroscopic IP trap and create a double-well potential interferometer (see Appendix B). The advantage of RF dressing is that the initial separation between the condensates will decrease, and from the fringe period equation ($\lambda = ht/md$) this means the time-of-flight needed to obtain the same size fringes ($\sim 40\,\mu$m) will also decrease. Therefore, the time the atoms spend in the levitation field will decrease, so any noise and centre-of-mass jitter the atoms acquire during levitation will be reduced. Using RF dressing to split the condensate decouples the magnetic and optical noise, which is advantageous when trying to create stable fringes. Currently the trap is magnetic and the split is optical, therefore when the magnetic trap moves the split changes. However, using RF dressing to split the condensate means when the magnetic trap moves the split also moves.

To be able to observe the interference fringes from the RF dressed double-well potential a vertical imaging system is needed (Appendix C). Not only will this allow the interference pattern to be observed, it will also enable sloshing in the x-axis to be investigated, which may be contributing to the condensate jitter. Having the horizontal and vertical imaging system will allow all three axes of the condensate to be probed and investigated, hopefully leading to the centre-of-mass motion of the condensate being removed from the system. Another solution in which the magnetic and optical noise would be decoupled is for the axial confinement and split to be all optical. This could be achieved by using the AOM to paint arbitrary potentials and create "ω" dipole beam potential, which could be used to axially confine the condensate as well as split it. A final solution is instead of using the existing toroidal coils for levitation a separate coil could be implemented, with its sole use being to apply the magnetic levitation. Due to limited space on the optics table this would be difficult to implement into the system.

Chapter 6

Phase Fluctuations

The phenomenon of phase fluctuations in elongated condensates was introduced in Section 2.7. It was shown that in an elongated condensate, $\Lambda = \omega_r/\omega_z \gg 1$, excitations can show 1D character, which results in domains of differing phase along the longitudinal axis of the condensate. At this point the condensate can no longer be thought of as a true BEC but as a quasicondensate, which when allowed to expand results in matter wave like interference fringes due to the different phases interfering.

The aspect ratio of the cloud is the ratio between the radial and axial trap frequencies, ω_r/ω_z, so by altering the magnetic trap frequencies the aspect ratio can be varied. In Strathclyde, the aspect ratio of the cloud is adjusted by changing the position of the trap bottom, this is achieved by altering the field from the bias coils. By lowering the trap bottom, and the final RF evaporation frequency, the curvature of the trap, and therefore trap frequency, can be changed and the aspect ratio of the cloud can be varied from $\Lambda = 10 \rightarrow 45$. Figure 6.1 shows a schematic diagram (not to scale) of how lowering the trap bottom alters the curvature of the trap and therefore the aspect ratio of the BEC.

The number of atoms and the total RF evaporation time both change as the trap bottom is varied. As the trap bottom is lowered the effective volume of the magnetic trap shrinks and three body collisions start to dominate, this results in atoms being lost from the trap at a higher rate and leads to smaller BECs. To over come the effect of three body losses the total RF evaporation time is decreased, this allows the atoms to condense before being lost from the trap.

Figure 6.2 demonstrates how the BEC atom number varies as a function of the

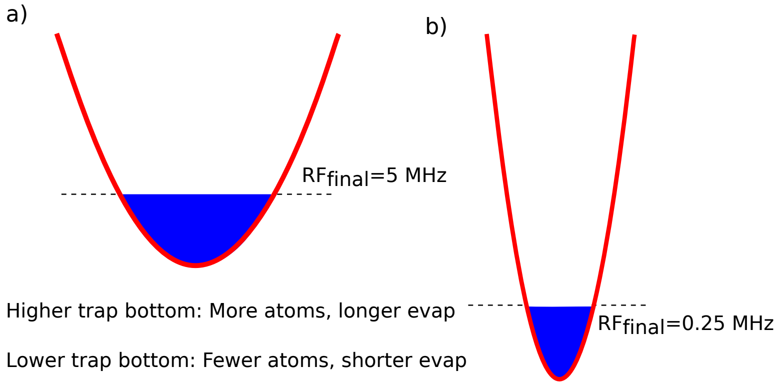

Figure 6.1: Schematic diagram trap bottom changing curvature of magnetic trap. Lowering the trap bottom increases the radial trap frequency, which allows the aspect ratio to be varied from 10 → 45. As the trap bottom is lowered the number of inelastic collisions increases, this results in the number of atoms in the BEC decreasing. The evaporation time also decreases with decreasing trap bottoms as three-body collisions start to dominate as the atoms are being 'squeezed' into a tighter trap.

magnetic trap's aspect ratio, i.e. the trap's curvature. For aspect ratios < 7 the curvature isn't sufficient to maintain the collision rate required for runaway evaporation, therefore the BEC number falls sharply. For aspect ratios > 7, large condensates are achievable since the parameters for runaway evaporation are maintained until $\Lambda \geq 20$, at this point three-body inelastic collisions increase and BEC atom number falls.

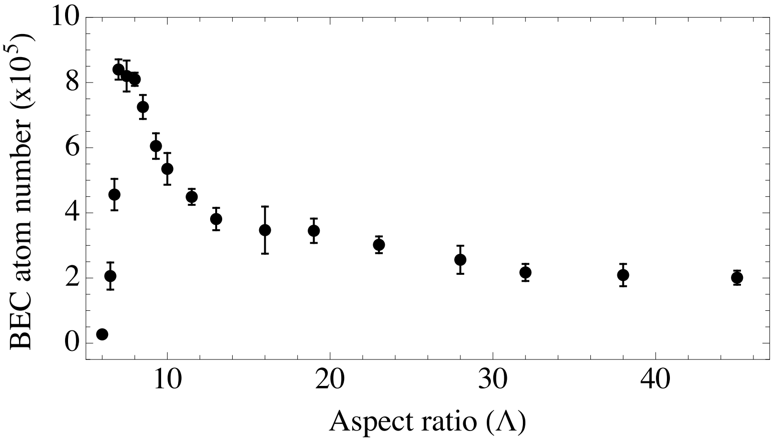

Figure 6.2: BEC atom number as function of the magnetic trap's aspect ratio. The number of atoms in the BEC increases from $\Lambda = 45 \rightarrow 7$, at which point the atom number drops drastically due to the trap being so weak there aren't enough collisions for efficient evaporation. Each point is an average of five experimental data runs.

6.1 Calibrating trap bottom and aspect ratio

The aspect ratio is altered by lowering the trap bottom, which modifies the trap frequencies by changing the curvature the atoms experience at the centre of the trap. The aspect ratio comes from the ratio of the radial and axial trap frequencies, lowering the trap bottom changes the radial trap frequency whereas the axial frequency is left unchanged. The total field produced by the IP trap can be expressed as (Equation 2.32)

$$B_{IP} = B_0 + \frac{1}{2}\left(\frac{B_1^2}{B_0} - \frac{B_2}{2}\right) r^2 + \frac{B_2}{2} z^2 \ , \tag{6.1}$$

where $r^2 = (x^2 + y^2)$. The radial trap frequency $\omega_r \propto \left(\frac{B_1^2}{B_0} - \frac{B_2}{2}\right)$ and the axial trap frequency $\omega_z \propto B_2$, therefore the aspect ratio can be expressed as

$$\Lambda = \sqrt{\frac{B_1^2}{B_0 B_2} - \frac{1}{2}} \ , \tag{6.2}$$

where B_0 is the trap bottom, $B_1 \sim 200\,\text{G/cm}$ and $B_2 \sim 70\,\text{G/cm}$. Using this expression the aspect ratio is 10 and 47 for the 5 MHz and 0.25 MHz trap bottom respectively. There is a finite difference between the final RF evaporation frequency and the actual trap bottom, which needs to be taken into account when calculating the aspect ratio. For a RF frequency of 5 MHz, there is another $\sim$ 20 kHz to the actual trap bottom, whereas for an RF frequency of 0.25 MHz, there is $\sim$ 40KHz. The difference between the RF frequency and trap bottom increases as the trap is tightened since the same amount of chemical potential is being 'squeezed' into a tighter trap. An approximation that allows the new radial trap frequency to be calculated follows

$$\omega_{r(\text{new})} \approx \omega_{r(5\,\text{MHz})} \left(\frac{5\ \text{MHz}}{\text{RF}_{\text{new}}}\right)^{1/2} \ , \tag{6.3}$$

where ω_r is the trap frequency at 5 MHz, which was measured to be 92.3(0.2) Hz (Section 4.3.2) and RF_{new} is the value of the new trap bottom.

To confirm the relationship gives an accurate value for how the radial trap frequency changes as a function of trap bottom, trap frequency measurements were performed for various curvatures (shown in Figure 6.3). Particular care had to be taken when applying the magnetic field perturbation, especially at 0.25 MHz, since when the curvature is increased the harmonic region of the trap decreases. From equation 6.3, the new radial

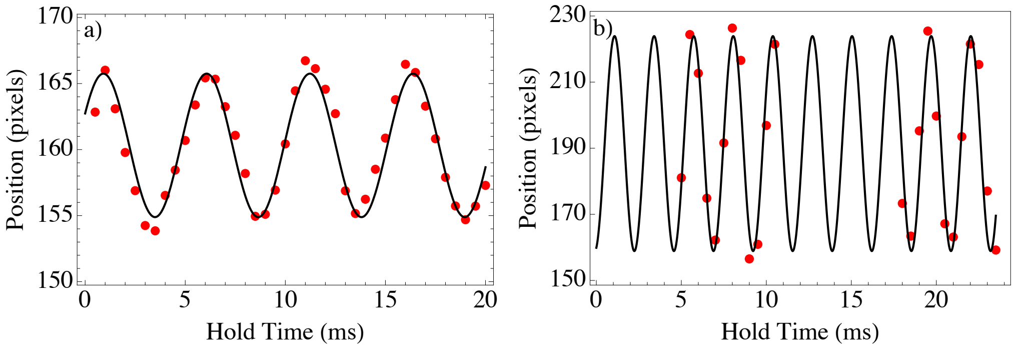

Figure 6.3: Radial trap frequencies for 1 MHz and 0.25 MHz trap bottom. a) Radial trap frequency for 1 MHz trap bottom, measured to be 204(2) Hz. b) Radial trap frequency at 0.25 MHz, measured to be 428(2) Hz.

trap frequency was calculated to be (using $\omega_r = 92.3\,\text{Hz}$) 208 Hz and 430 Hz for the 1 MHz and 0.25 MHz trap bottom respectively. This is in good agreement with the measured trap frequency values of 204(2) Hz and 428(2) Hz from Figure 6.3.

The assumption when calculating the aspect ratio is that the axial trap frequency doesn't change as the trap bottom is altered, to confirm this, an axial trap frequency measurement at 0.25 MHz was carried out. Figure 6.4 presents the axial trap frequency data and fit, with the trap frequency measured to be 9.0(0.1) Hz, this is almost identical to the axial trap frequency of 9.11(0.01) Hz at 5 MHz. Finally to calculate the aspect ratio the radial frequency must be divided by the axial, which results in aspect ratios of 10, 23 and 47 for 5, 1 and 0.25 MHz respectively.

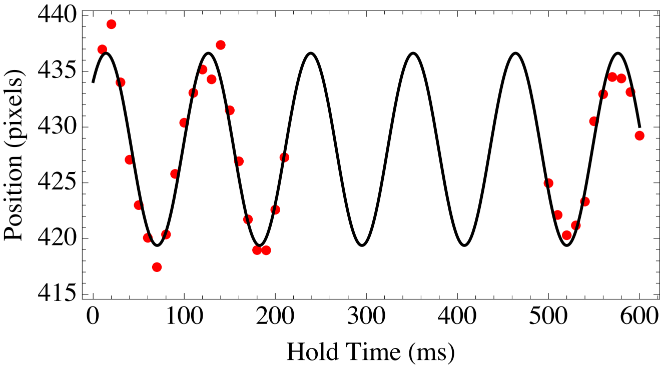

Figure 6.4: Axial trap frequency for 0.25 MHz trap bottom. Axial trap frequency for 0.25 MHz was measured to be 9.0(0.1) Hz.

6.2 Phase fluctuations in time-of-flight

Phase fluctuations show up as density fluctuations in time-of-flight, which is a result of the domains of differing phase interfering once the cloud has been released from the trap. The phase fluctuations, σ_{BEC}, are characterised by fitting a bimodal Thomas-Fermi+Gaussian distribution to the experimental data and then calculating the standard deviation between the fit and data in the central region of the BEC (full width half maximum). The bimodal distribution used to fit the data takes the form

$$\mathrm{Fit}_{\mathrm{TF+G}} = \mathrm{A1} * \mathrm{H}\left(1 - \frac{\mathrm{x} - \mathrm{x}_0}{\sigma}\right)\left(1 - \frac{(x - x_0)^2}{\sigma^2}\right)^2 + \mathrm{A2}\exp\left(-\frac{(\mathrm{x} - \mathrm{x}_0)^2}{2\sigma^2}\right) , \quad (6.4)$$

where H represents the unit step function (equal to 0 for $\mathrm{x} < 0$ and 1 for $\mathrm{x} > 0$), x_0 is the centre of the distribution and σ is the width. This method enables a value to be assigned which defines the level of fragmentation along the length of the condensate, therefore allowing the dynamics to be studied.

Figure 6.5 presents typical density plots of BECs with and without phase fluctuations after 58 ms levitation, both showing the experimental data points and fit. The

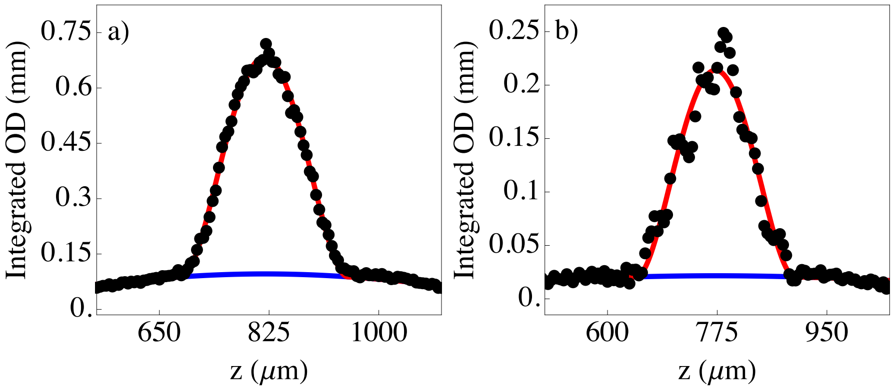

Figure 6.5: Density plots of BECs with and without phase fluctuations. Experimental data points (black) are shown along with Thomas-Fermi+Gaussian fit (red) and thermal component (blue) zoomed into Thomas-Fermi radius to emphasise effect of phase fluctuations. a) BEC in 18:1 aspect ratio trap, b) BEC made in 45:1 aspect ratio trap. Note how data points follow fit in a) when there are no phase fluctuations whereas in the presence of fluctuations the data deviates considerably from the fit. OD y-axis scale changes as number of atoms in BEC decreases for tighter trap (b)), which is consistent with Figure 6.2.

fragmentation along the length of the cloud causes a noticeable change in the density plot and can have a considerable affect on the performance of matter-wave interferometers. However, when the quasicondensate is imaged along the longitudinal axis the fragmentation due to the phase fluctuations becomes less important [103, 251].

6.2.1 Fluctuations - time

Under typical experimental parameters $\omega_r/\omega_z \sim 10$, phase fluctuations are suppressed and no fragmentation along the length of the cloud is observed. However, as the aspect ratio of the cloud is increased there is a smooth transition from a fully 3D system to an effective 1D system. Phase fluctuations can be mapped onto the initial velocity distribution along the condensate, these then appear as density modulations after time-of-flight.

The level of fragmentation of the condensate is a function of time, i.e. the number of stripes across the condensate increases with increasing time. The sensitivity to phase fluctuations increases with time, therefore the levitation field is a precise tool to study phase fluctuations. To study the phase fluctuation's dependence on time, condensates were created in traps where phase fluctuations were and weren't expected. The experiment was carried out by creating $18:1$ and $45:1$ aspect ratio BECs, then the BECs were allowed to expand for a varying amount of time and the standard deviation between data and fit calculated.

Figure 6.6 presents σ_{BEC} as a function of time for both a $18:1$ and $45:1$ aspect ratio BEC. For the $18:1$ there is a constant statistical offset value of σ_{BEC}, whereas for a $45:1$ aspect ratio cloud σ_{BEC} increases and continues to grow with time. To establish a baseline for the phase fluctuations the same analysis was performed on thermal atoms, i.e. data was fit using Equation 6.4 and the standard deviation of the data from the fit calculated. Thermal atoms aren't susceptible to phase fluctuations so are ideal to obtain a constant statistical offset. By averaging over ten experimental realisations of thermal atoms, the statistical offset was found to be 0.021 ± 0.004. The value of σ_{BEC} for the $18:1$ aspect ratio condensate is similar to the constant statistical offset, therefore indicating that no phase fluctuations where present. Having the ability for long time-of-flight allows the build-up and formation of phase fluctuations to be studied with high levels of sensitivity. Figure 6.7 shows density plots of a BEC in the presence of phase fluctuations for various levitation times. It is clear to see the stripes

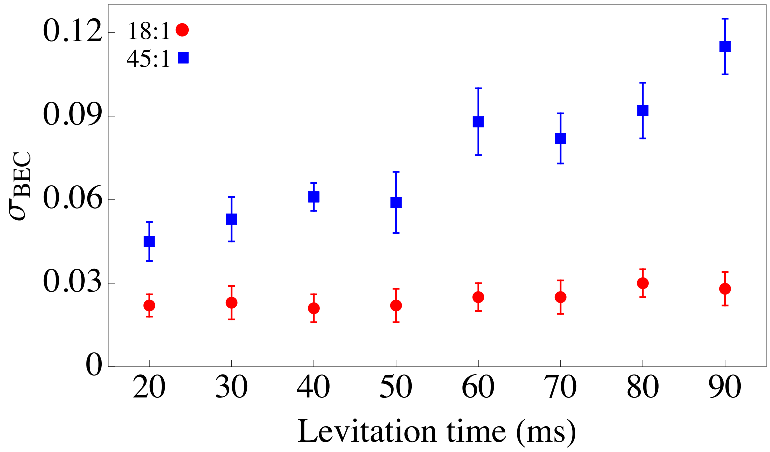

Figure 6.6: Phase fluctuations as a function of time for 18 : 1 and 45 : 1 aspect ratio BECs. For the 18 : 1 initial aspect ratio BEC (red) there are only constant statistical fluctuations (similar value to $\sigma_{\mathrm{BEC}} = 0.021$ for thermal atoms) whereas for a 45 : 1 aspect ratio (blue) fluctuations are always present and grow with time. Each point is an average of five experimental data runs.

in the condensate and how they become more and more pronounced with increasing levitation time. Although, initial data suggest that the period of the phase fluctuations doesn't increase with time, this indicates that the condensate breaks up into chunks of differing phase from the start, which then interfere with one another. However, more experiments must be performed to confirm this. The levitation field not only

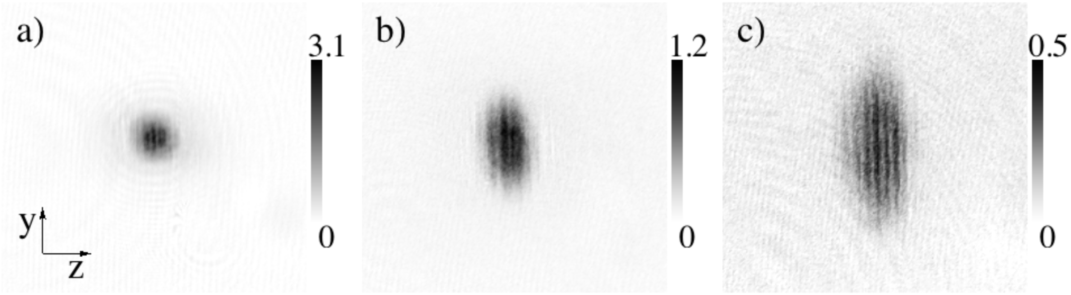

Figure 6.7: Density plots of BECs with phase fluctuations at various levitation times. Scale bars represent optical density. Levitations times are: a) 20 ms, b) 50 ms and c) 90 ms. Note how the density fluctuations from the phase fluctuations continue to grow in time-of-flight and become more pronounced. Each image is $1 \times 1\,\mathrm{mm}^2$.

enables long time-of-flight, it also amplifies the stripes due to the inverted parabola axial potential, this offers new levels of sensitivity to investigate the aspect ratio in which the system undergoes a transition from a 3D to an effective 1D system.

6.2.2 Fluctuations - aspect ratio

As the condensate is elongated it can begin to cross over from a 3D to an effective 1D system and start to exhibit phase fluctuations. The levitation field enables long time-of-flight, which allows the range of aspect ratios at which the condensate transitions from a 3D to a 1D system to be studied more precisely. Using a fixed levitation time, 58 ms as it yielded the best signal-to-noise, and by varying the aspect ratio, the phase fluctuations dependence on the cloud's aspect ratio could be studied.

Figure 6.8 presents the phase fluctuation's dependence on the trapping potential aspect ratio for a fixed levitation time of 58 ms. It can be seen that for $\Lambda < 20$ fluctuations are suppressed as σ_{BEC} lies in the constant statistical offset of 0.021 ± 0.004. The offset was calculated from the average of ten standard deviations of the data from the fit (Equation 6.4) using thermal atoms. However, for $20 < \Lambda < 30$, the value of σ_{BEC} increases above the statistical offset, at this point the BEC undergoes a phase

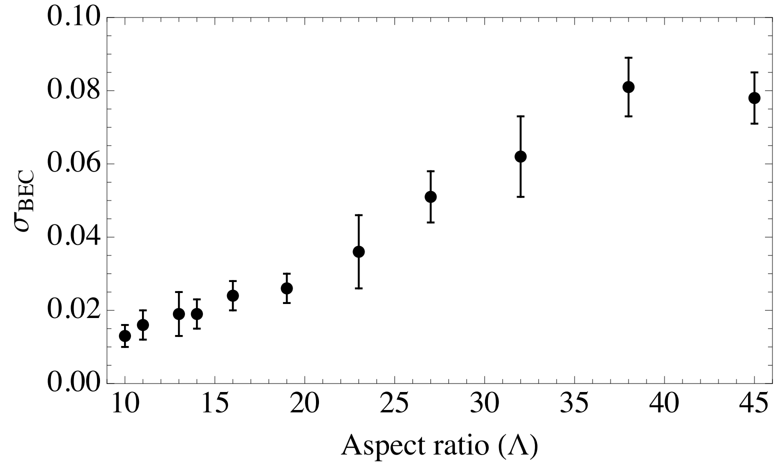

Figure 6.8: Phase fluctuations as a function of aspect ratio at 58 ms levitation time. For initial $\Lambda < 20$, no phase fluctuations are present as σ_{BEC} falls within the constant statistical offset of 0.021 ± 0.004, which was calculated from thermal atoms (average of ten experimental iterations). However, for $20 < \Lambda < 30$, σ_{BEC} grows out of the statistical offset and there is a changeover and the BEC acquires 1D characteristics leading to phase fluctuations. Each point is an average of five experimental data runs.

'transition' and acquires 1D characteristics leading to phase fluctuations.

Phase fluctuations are extremely sensitive to temperature and atom number, σ_{BEC} continuously reduces with decreasing temperature and increasing atom number [192]. Due to this it isn't possible to determine a cutoff point in which phase fluctuations cease, rather they continue to decrease until they cannot be resolved from the statistical fluctuations (low level noise). Therefore, it can be said that phase fluctuations are always present in experiments with BECs in tightly confining elongated potentials at finite temperature. For aspect ratios where phase fluctuations have previously not been observed, this may be due to the fluctuations not being able to be optically resolved by the imaging setup. The Strathclyde experiment's levitation field and wide range of trapping potential aspect ratios offers a new tool to probe the dynamics of phase fluctuations formation with advanced levels of sensitivity.

6.3 Regular phase fluctuations

Phase fluctuations are mapped onto density fluctuations once the condensate has been released from the trapping potential and allowed to expand. Phase fluctuations in one-dimensional systems are random and lead to fragmentation into several quasicondensates of random size and phase. Therefore, each experimental iteration will result in matter wave like interference fringes that have a different phase and size.

However, in the Strathclyde experiment elongated Bose gases, which should normally result in random phase fluctuations, can give rise to a large regular spatial period during expansion. This result indicates the existence of regular phase fluctuations in an elongated BEC, which as far as we know has never been reported in 1D quasicondensates. This observation was made possible by utilising the long time-of-flight made possible by the levitation field.

Figure 6.9 demonstrates a typical quasicondensate that exhibits regular phase fluctuations after 58 ms levitation. The atomic distribution of the condensate is shown with the data points joined (dash blue line Figure 6.9 b), it is clear to see the periodic character of the phase fluctuations. To analyse the regular phase fluctuations first a Thomas-Fermi+Gaussian (Equation 6.4) was fit to the data to obtain the centre and the width of the distribution. Then a sine wave modulated by a Gaussian amplitude

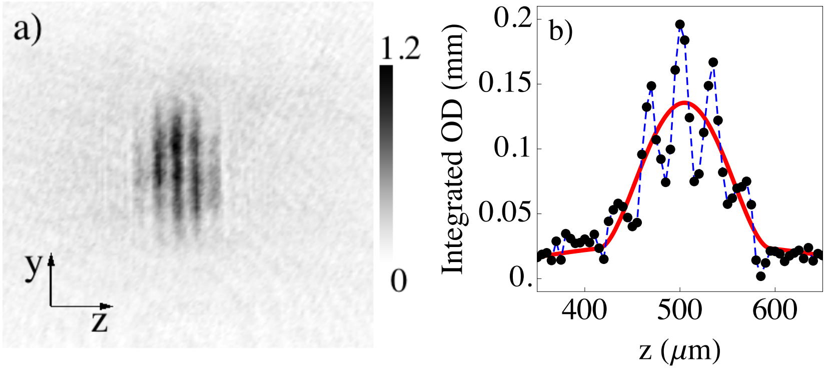

Figure 6.9: Density plot and distribution of BEC with regular phase fluctuations. a) Typical density plot of condensate exhibiting regular phase fluctuations after 58 ms levitation. b) Experimental density distribution (black) along with corresponding Thomas-Fermi+Gaussian fit (red), data points have been joined together (dashed blue) to emphasise the periodic nature of the fluctuations.

was fitted only to the data within the width of the condensate (i.e. σ_{BEC} in the Thomas-Fermi radius) and the period of the fluctuations was calculated from the fit. The sine wave modulated by a Gaussian amplitude was of the form

$$\lambda\,\sigma_{\mathrm{BEC}} = A(1 + B\sin[\frac{2\pi}{\lambda}\mathrm{x} + \phi])\exp\left(-\frac{\mathrm{x}-\mathrm{x}_0}{2\sigma^2}\right) + C\ , \tag{6.5}$$

where λ is the period of the fluctuations, x_0 is the centre of the distribution and σ is the width. Another method for extracting the period of the phase fluctuations was to take the Fourier transform within the width of the condensate where the fluctuations where present. Figure 6.10 shows both methods of calculating the periodicity of the fluctuations after 58 ms levitation. Using the sine wave fit (Figure 6.10 a) the period was determined to be 33.4 μm and using the Fourier transform (Figure 6.10 b) it was calculated to be 33.3 μm.

To establish that the regular phase fluctuations aren't a result of the levitation field, vertical imaging was implemented in the experiment (see Appendix C). The new imaging system was realised by Dr. Yueyang Zhai and Victoria Henderson, and confirmed that the regular fluctuations weren't a consequence of the levitation field. This was made possible since the vertical imaging can image from 0 → 60 ms without the need

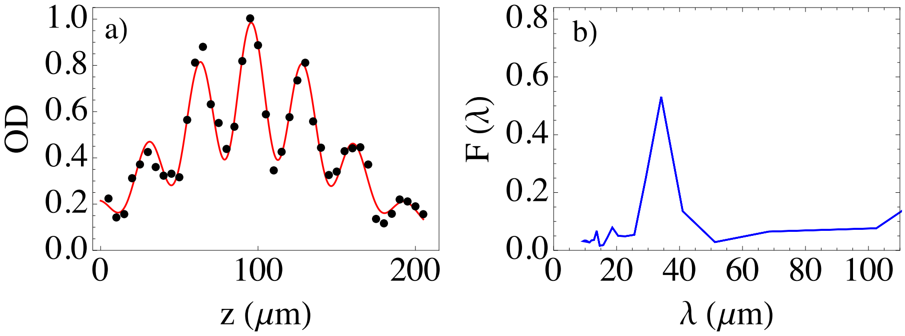

Figure 6.10: Modulated sine wave fit and Fourier transform of condensate exhibiting regular phase fluctuations after 58 ms levitation. a) Experimental data (back) and sine wave fit (red) to phase fluctuations within the Thomas-Fermi radius. b) Fourier transform of condensate within the Thomas-Fermi radius, the Fourier transform displays one strong peak which indicates a periodic density distribution of the phase fluctuations. The period of the fluctuations was calculated from the fit and the Fourier transform and found to be 33.4 μm and 33.3 μm respectively.

for levitation (only limited by physical size of cell) or the need to launch the atoms vertically. Figure 6.11 presents typical experimental data using the vertical imaging

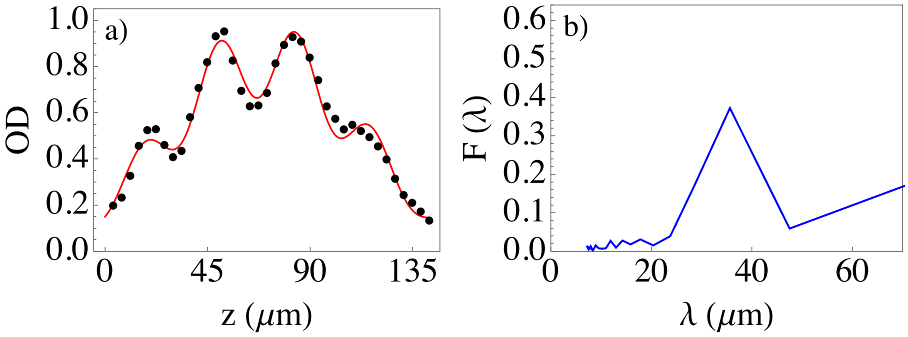

Figure 6.11: Modulated sine wave fit and Fourier transform of condensate exhibiting regular phase fluctuations after 58 ms time-of-flight using vertical imaging system (no levitation). a) Experimental data (back) and sine wave fit (red) to phase fluctuations and b) Fourier transform of condensate. Period of the fluctuations from the was calculated to be 32.5 μm and from the Fourier transform 33.6 μm. Condensate expansion is smaller in vertical direction in the absence of inverted parabola potential from levitation. Since regular phase fluctuations are seen in both imaging system, initial experimental data indicates periodicity of fluctuations isn't a consequence of the levitation field.

system of a condensate after 58 ms time-of-flight (no levitation field) displaying regular phase fluctuations. Since this effect is seen in both the horizontal and vertical imaging axis, this confirms that the periodicity of the fluctuations isn't a result of the levitation. Initial data in Figure 6.11 was taken before full calibration of the vertical imaging system, signal-to-noise and contrast of phase fluctuations should increase when camera has been fully calibrated.

6.4 Phase coherence revival

Phase fluctuations in elongated BECs are a direct result of axial excitations, which have wavelengths that are smaller than the length of the condensate. At this point the condensate becomes a quasicondensate since the coherence length is smaller than the size of the condensate and results in domains of differing phase. The system undergoes a phase transition and the coherence of the system is lost due to the fragmentation which occurs along the length of the condensate. This raises the question: can quasicondensates be re-cohered after dephasing and exhibiting phase fluctuations?

To answer this question a phase revival experiment was carried out, which takes advantage of being able to dynamically change the aspect ratio of the trapping potential during an experimental sequence. In this experiment the radial trap frequency is dynamically changed from a small value to a large value and then back again, accessing a large range of BEC aspect ratios in a controlled manor. The compensation bias

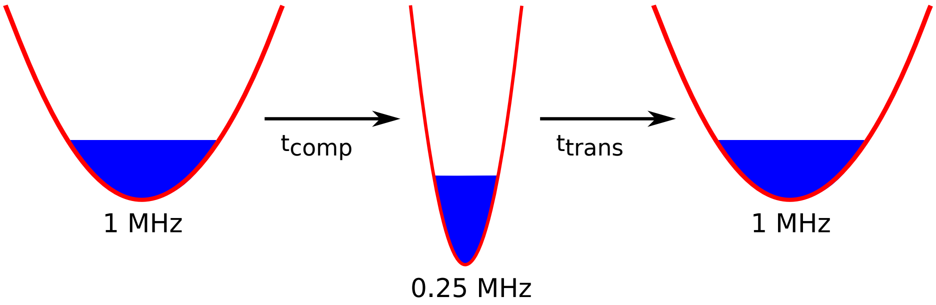

Figure 6.12: Schematic diagram of phase coherence revival experiment. A BEC is created in a 22 : 1 aspect ratio trap, which is then dynamically compressed by changing the field from the compensation bias coils over a time t_{comp}, this 'squeezes' the condensate into a tighter 45 : 1 aspect ratio trap. The condensate is then held in the tighter trap for a variable amount of time before the trap is transformed back into the original 22 : 1 trapping potential over a time t_{trans}.

field is controlled via a DAC voltage and can be used to manipulate the trap bottom (discussed in Section 4.5). So by creating a BEC in a trap and then increasing the bias field, the condensate is ‘squeezed’ into a tighter trap. Being able to dynamically change the aspect ratio in a controlled way once the condensate has been created allows the loss and then subsequent revival of coherence of a quasicondensate to be observed. A schematic diagram of the phase revival experiment, which demonstrates the aspect ratio increasing and then relaxing, is shown in Figure 6.12.

Figure 6.13 shows the experimental sequence of the phase revival experiment as well as experimental data at various points throughout the experiment. Firstly a BEC was generated in a trap with an aspect ratio of 22 (Figure 6.13a, $\sigma_{\mathrm{BEC}} = 0.024$ after 58 ms levitation), then the aspect ratio was slowly ramped up to 45 in 100 ms. The condensate is then held in the tighter 45 : 1 aspect ratio trap for varying hold times of 10, 20 and 70 ms, and the phase fluctuations analysed. As the hold time is increased a growing value of σ_{BEC} is observed, this implies that the longer the condensate is held in a trap in which its coherence length is shorter than its size, then the more fragmented the condensate becomes. Figure 6.13 d), e) and f) demonstrate this, as the hold time increases so does the the value of σ_{BEC}, which are 0.069, 0.071 and 0.107 for 10, 20 and 70 ms, respectively.

This phenomenon of the build up of phase fluctuations as the trap is elongated and σ_{BEC} increasing as the condensate is held in the elongated trap agrees well with both prior experimental results [192, 200, 253, 254] and theoretical predictions [255, 256, 257]. As a contrast, to probe the revival of coherence across the condensate, the aspect ratio was linearly ramped back down to the original 22 : 1 trap. The linear ramp back to the original trap was performed over two different times, which are 80 ms and 130 ms (Figure 6.13 b) and c)). It was found that density fluctuations across the condensate from the phase fluctuations were removed within statistical uncertainty when the aspect ratio was relaxed, no extra RF evaporative cooling was used. The phase fluctuations for the 80 ms and 130 ms linear ramp are ≤ 0.031 in both situations. This experiment demonstrates a controlled generation and removal of phase fluctuations in BECs as the trap is elongated and then relaxed, and can be used to further investigate and understand the dynamics of low-dimensional Bose gases.

To further study the loss of coherence and then removal of phase fluctuations in BECs as the aspect ratio is increased and then relaxed, a phase fluctuation evolution

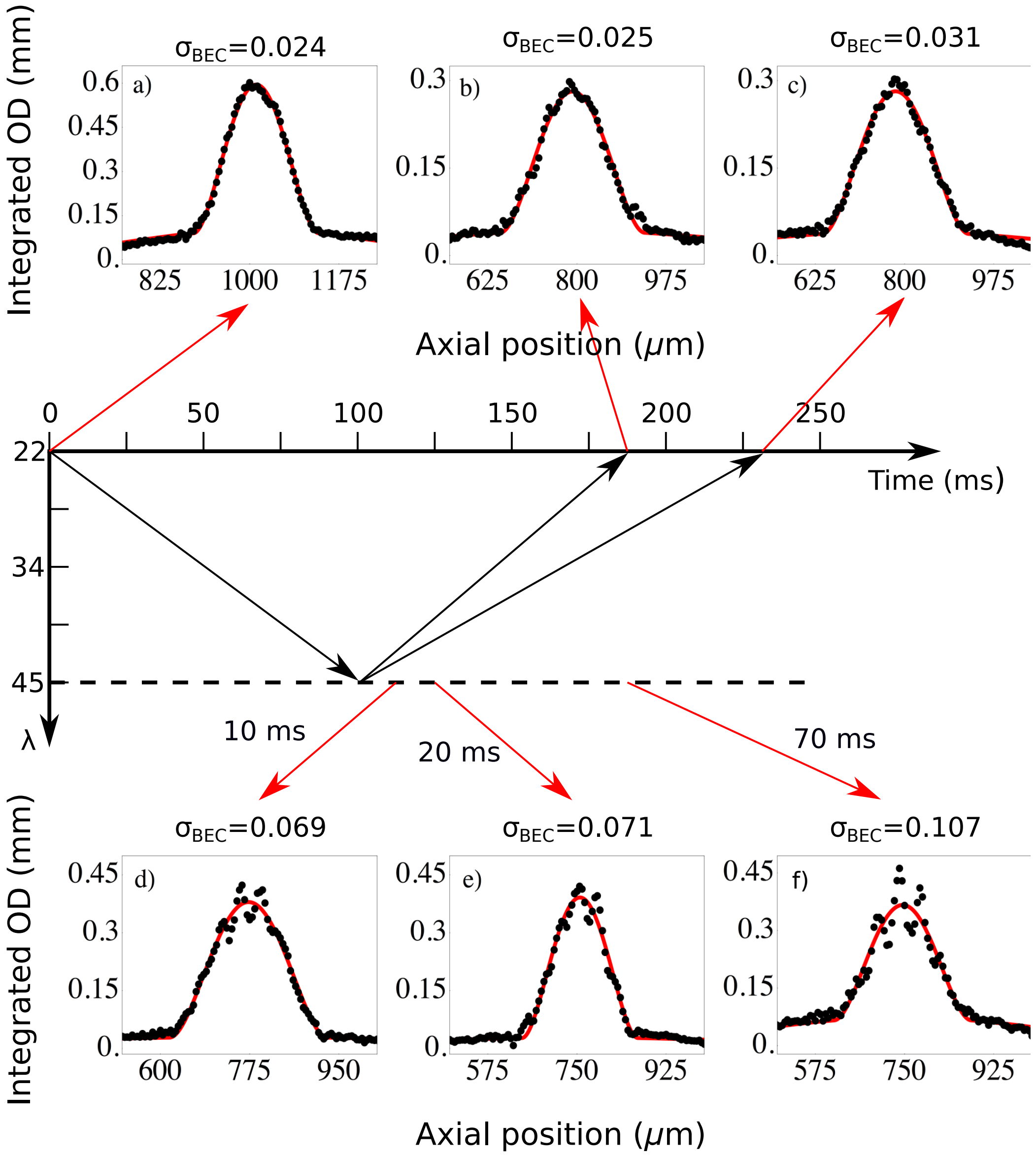

Figure 6.13: Formation of phase fluctuations and subsequent revival of coherence. Time is shown along the horizontal axis and aspect ratio is shown along the vertical axis. Density profiles are shown zoomed into the Thomas-Fermi radius to demonstrate phase fluctuations more evidently. Data points (black) and corresponding Thomas-Fermi+Gaussian fits (red) are presented along with σ_{BEC}. First a BEC is made in a 22 : 1 aspect ratio trap a) where no phase fluctuations are present, the BEC is then linearly compressed into a 45 : 1 aspect ratio trap in 100 ms. A variable hold time from 10 ms to 70 ms, permits phase fluctuations to build up d), e) and f), then the BEC is transformed back into the original trap over two different times of 80 ms b) and 130 ms c) with $\sigma_{\text{BEC}} = 0.025$ and 0.031 respectively.

experiment was carried out. In this experiment a BEC was created in a 22 : 1 aspect ratio trap, the aspect ratio was then linearly ramped to 45 and then the condensate was held in this trap to allow the phase fluctuations to build up. Finally, after the hold time, the aspect ratio was linearly ramped back down to 22 : 1 and the condensate was levitated for 58 ms and an absorption image taken. Both the linear ramp compressing and relaxing the trap were performed over 100 ms and the condensate was held in the tight trap for 30 ms, allowing enough time for a noticeable increase in σ_{BEC}. The phase fluctuations were analysed at various points throughout the compress-hold-decompress process by stopping the experiment at certain times, i.e. 20 ms into linear compression, and then levitating the BEC for 58 ms and calculating σ_{BEC}.

Figure 6.14 presents the evolution of experimental phase fluctuation data as the aspect ratio of the trapping potential is altered. During the linear compression from $\Lambda = 22 \rightarrow 45$ the process was stopped at multiple different times (16, 33, 50, 66, 84 and 100 ms) to observe the build up of fluctuations as the condensate 'squeezed' into a tighter trap. σ_{BEC} was evaluated after 10 ms and 30 ms hold time before the aspect ratio was linearly ramped from 45 back to 22, again σ_{BEC} was determined at several points through the decompression (35, 40, 50, 60, 70, 80, 100 ms).

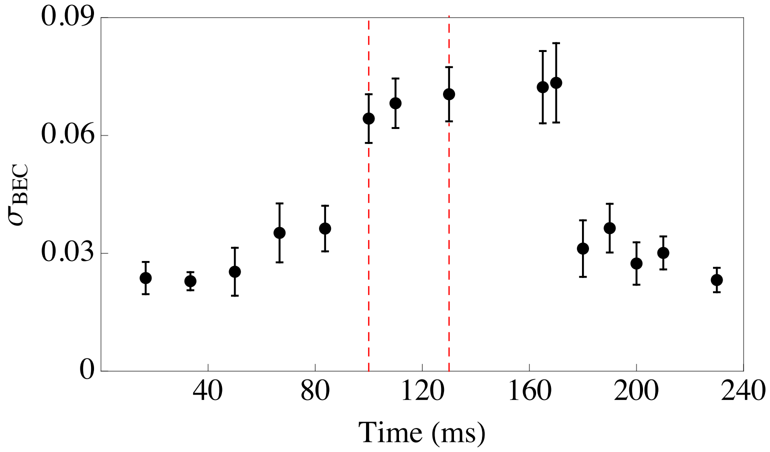

Figure 6.14: Phase fluctuation evolution as aspect ratio is dynamically varied. The aspect ratio is linearly ramped from 22 → 45 in 100 ms, then the BEC is held for 30 ms in the 45 : 1 trap. From 130 ms to 230 ms the trap is linearly ramped back to an aspect ratio of 22. The dashed red lines indicate the hold time. Each data point is an average of five experimental iteration, taken after 58 ms levitation to enhance the density fluctuations.

From the phase fluctuation evolution experiment it is clear to say that there is a noticeable increase in phase fluctuations σ_{BEC} once the aspect ratio reaches $45 : 1$. The phase fluctuations increase as the condensate is held in the tighter trap, then as the trap is linearly decompressed there is a notable delay of ~ 50 ms before the phase fluctuations are removed from the condensate. This shows a controlled loss of and then recovery of coherence as the trap is tightened and then loosened. To the best of our knowledge this phenomenon shows a whole new result of the coherence re-build process after the BEC reaches a quasicondensate state. There is a noticeable time delay for the phase fluctuation removal as the elongation of the BEC is reduced, this indicates a time scale for the excitation and dissipation of phase fluctuations.

Chapter 7

Conclusions

7.1 Summary

The outcome of the research during my PhD has led to two papers to be published, the first on the spatial Talbot effect in condensate interferometry [258], and the second on the existence regular phase fluctuations in elongated condensates and the revival of phase coherence of a quasicondensate [259].

The thesis began with an introduction of Bose-Einstein condensates (BECs) and a brief description of the history and first experimental observation before discussing the some of the various studies and practical uses of BECs. Next the concept of interferometry, both using light and atoms, was introduced and then some of the advantages and disadvantages of using cold atoms and BECs in interferometers were considered. Finally, the basic principles of double-well and guided-wave BEC interferometers were presented.

The basic theory behind creating a BEC was the subject of Chapter 2. The chapter begins with a description of the quantum structure of rubidium before providing a brief outline of laser cooling, from the light force on atoms to magneto-optical trapping. The general properties of atoms in magnetic fields was described as well as theoretical models of the magnetic field produced from various coil geometries, before the practical Ioffe-Pritchard trap was considered. This was followed by a description of evaporative cooling, the final step before the creation of a BEC. The dynamics of a BEC, such as mean-field theory and the condensate's expansion, was discussed in the next section. The idea of matter-wave interference was the introduced, as well as the coherent splitting of a condensate and phase diffusion. Finally, the last topic of the chapter was phase fluctuations in elongated BECs and how they manifest themselves in the experiment.

Chapter 3 described the Strathclyde BEC experimental setup, including the laser system, double MOT optical setup, the various magnetic geometries possible from the hybrid trap and the imaging system.

In Chapter 4 the various experimental methods for ‘controlling’ the BEC were discussed, these included the MOT loading sequence, optical pumping, the magnetic traps and evaporative cooling. The experimental generation of a BEC and its expansion dynamics was then described and compared with theory. The later stages of Chapter 4 introduced the methods used to manipulate the condensate, such as the dipole beam and levitation field. Within the dipole beam section the optical dipole potential was discussed as well as the dipole beam's alignment, how to control the dipole beam and the process of adiabatic splitting. In the final section the magnetic levitation field was described as well as the condensate's expansion dynamics in the field.

Bose-Einstein condensate interferometry was reported in Chapter 5, where the interference signal's dependence on a variety of experimental parameters was discussed. First the fringe pattern processing technique was introduced before the fringe period's dependence on the dipole beam and levitation time were discussed. The next section introduced maximum contrast interference, both the theoretically and experimental results, and then demonstrated how imaging beam detuning could affect the contrast of the interference pattern. Talbot-enhanced interference was the topic of the next section, here the Talbot effect was introduced and the experimental results of the spatial Talbot effect of light interacting with periodic BEC fringes was described as well as the corresponding theory for this observed effect. The lifetime of the interference fringes was presented, before finally Chapter 5 concluded with a discussion on the possible causes (magnetic switch off, dipole beam noise, magnetic trap noise) and solutions (vertical imaging to investigate sloshing, RF dressing, new levitation coil) to the spatial fluctuations in the final condensate position. This thesis presents the first experimental observation of the spatial Talbot effect of imaging light interacting with periodic BEC fringes, and also discusses the drastic effect it can have on the interference signal. This is the topic of the first paper from my PhD [258].

Chapter 6 gives a description of the experiments involving phase fluctuations in elongated condensates. How to calibrate the aspect ratio of the trap was introduced first before the phase fluctuation's dependence on time-of-flight and aspect ratio was discussed. The observation of regular phase fluctuations was described in the next section, which also contained experimental data showing that this wasn't a result of the levitation field. The final result in Chapter 6 was the phase revival of quasicondensates, in this section it was shown that a elongated condensate exhibiting phase fluctuations can be re-cohered. All of these results are the subject of the second paper from my PhD [259].

Finally in this chapter possible improvements to the existing Strathclyde BEC experiment and will be discussed. Also, future potential experiments and possible directions of the project will be considered.

7.2 Outlook and future improvements

The current problem with the spatial fluctuation in the condensate's final location, and the variation of the interference pattern's phase with each experimental realisation, opens up the possibility of future improvements for the experiment. Some of the experimental improvements have been started by myself and continued by the current postdoc in the lab Dr. Yueyang Zhai and the new PhD student Ms. Victoria Henderson, these include new coil driver circuits, vertical imaging system and RF dressing.

The new coil driver circuit is based on the circuit in Figure A.2, with some new features to help improve stability. The new circuits are all housed in the same enclosed box, are attached to a heat sink and have a low temperature coefficient sense resistor, all of which will help increase stability of the current in the coils. Care was taken to design a system that has low thermal drifts with time, this is essential when trying to obtain stable phase locked fringes. The new circuits have now been made and are ready to be tested before being implemented into the experiment. Figure 7.1 presents a Fourier transform of the coil power supplies during the RF evaporation sequence. It was recently discovered that there is a resonance at 400 kHz, it is believed that this is an inherent resonance due to the fact the power supplies are driving RLC circuit, however it would be preferable to investigate this further and remove from the experiment. As well as the circuits to control the current in the coils, there is also a new simplified coil setup. This setup would use three MOSFET banks instead of the five and enable more control over the magnetic fields.

The vertical imaging system will enable the condensate to imaged in all three axes

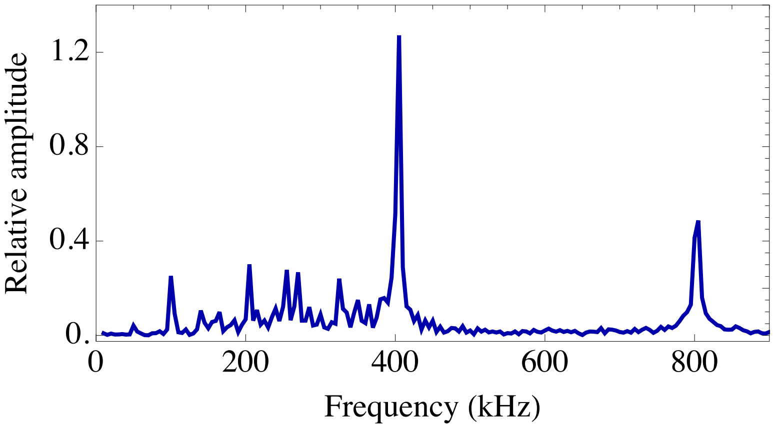

Figure 7.1: Response of coil power supplies as a function of frequency showing a resonance in the circuit. The Fourier transform of coil power supplies during RF evaporation, shows a resonance in the circuit at 400 kHz. It is believed that this is an inherent resonance since the power supplies are driving a RLC circuit.

and allow any sloshing in the magnetic trap to be investigated (discussed briefly in Appendix C). Potential sloshing in the magnetic trap could lead to an initial velocity or position in the condensate, which could contribute to the fluctuations in the BEC's final position. Having the ability to image the condensate vertically allows sloshing to be eliminated (if present) from the experiment, which increases the chances of obtaining reproducible interference fringes. It will also allow the resulting interference pattern from a RF dressed double-well potential to be imaged (briefly discussed in Appendix B). Using an RF dressed double-well potential has two main advantages: 1) The initial split is smaller so one can achieve the same sized interference fringes ($\sim 40\,\mu$m) with less expansion time, therefore there is less time for any velocity or position noise to build up. 2) The trap and split are both magnetic and therefore decoupled, i.e. if the trap moves the split also moves. Both these improvements in the experiment can help towards achieving stable phase locked interference fringes.

Another potential improvement is to paint arbitrary potentials onto the dipole beam and use this to split and trap the condensate axially, which also decouples the trap and split. This is achieved by sending a carrier RF frequency mixed with sidebands, with multiple RF components to the AOM. This method splits the beam into various components, which are spaced close enough that the atoms see it as a smooth continuous potential. This method can be used to make linear v-potentials and parabolic

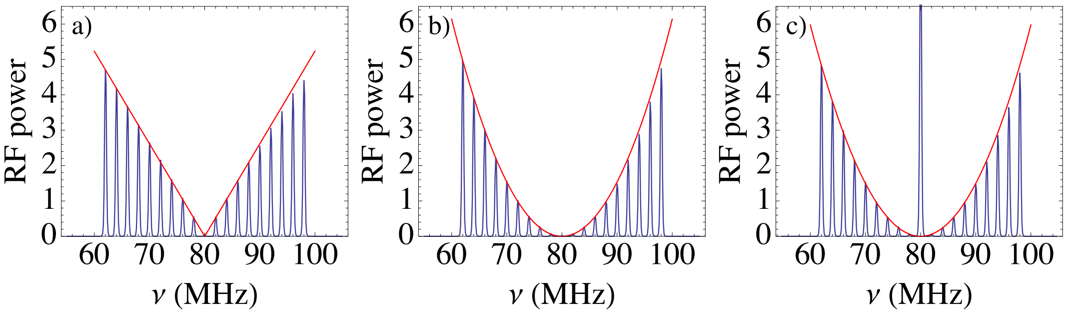

Figure 7.2: Various RF arbitrary potentials. Each RF potential has a central carrier frequency of 80 MHz and nine sidebands each side spaced 2 MHz apart. a) Linear v-potential, b) parabolic potential and c) parabolic potential with high amplitude component in middle to split condensate ($\omega-$potential).

potentials and by having a high amplitude component in the centre it can also split the condensate. Figure 7.2 presents the RF spectrum for a linear v-potential a), a parabolic potential b) and a parabolic potential with a component for splitting c). Each spectrum has a central carrier frequency of 80 MHz with nine sidebands each side spaced 2 MHz apart, this is still close enough together so that the atoms will see a continuous potential. This RF spectrum is then amplified before being fed into the the AOM and the potential is painted onto the dipole beam. Due to nonlinear effects when amplifying the RF spectrum, a correction factor was needed to fix the potential on the dipole beam. Once the RF spectrum has been painted onto the dipole beam it was imaged

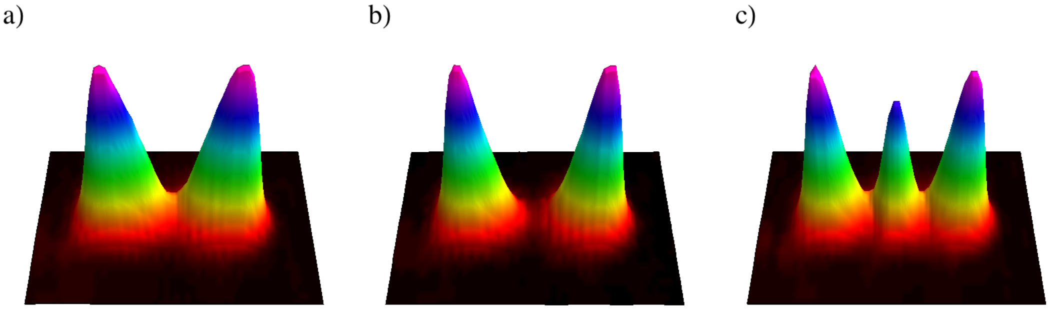

Figure 7.3: Various arbitrary dipole beam potentials.Dipole beam potentials in a), b) and c) correspond to the RF spectrums in Figure 7.2 a), b) and c). Dipole beam potentials were imaged using a beam profiler. a) Linear v-potential, b) parabolic potential and c) parabolic potential with splitting component in the middle.

on a CCD beam profiler to analyse the dipole beams's potential, this data is shown in Figure 7.3. Figure 7.3 a), b) and c) correspond to the RF spectrums in Figure 7.2, it can be seen that the potential painted onto the beam is similar to the RF spectrum. This is very preliminary data, but it shows the potential to use this method to trap the condensate axially as well as split it, which as mentioned previously decouples the trap and split and could help to achieve reproducible interference fringes. This method could be extended to 2D or 3D by the use of additional AOMs, this could potentially make trap and split completely optical.

Appendix A

Electronic Circuits

A.1 Dipole beam VCA controller

The dipole beam was controlled via a digital signal from the computer, which was converted into an analog line using a digital-to-analog convertor (DAC). The analog line was sent into a VCA, this allowed precise control of the beams intensity.

VCAs typically require ~ 25 mA to operate. The 5 mA DAC voltage was converted into a 25mA signal that controlled the VCA, which was connected to the input of the AOM. Figure A.1 shows the VCA control circuit, which is based on a differential amplifier, with an adjustable offset that enables fine tuning of the signal send to the VCA.

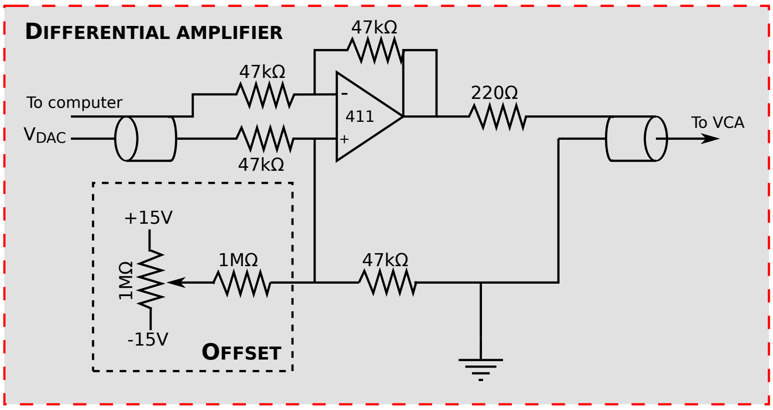

Figure A.1: Dipole beam VCA control signal circuit diagram. 411 (LF 411), Low Offset, Low Drift JFET Input Operational Amplifier (output source current of 25 mA). The 5 mA DAV voltage was converted into a 25 mA signal, which controls the VCA, that is connected to the AOM. The offset was used for fine tuning of the AOM controller.

A.2 MOSFET banks driver

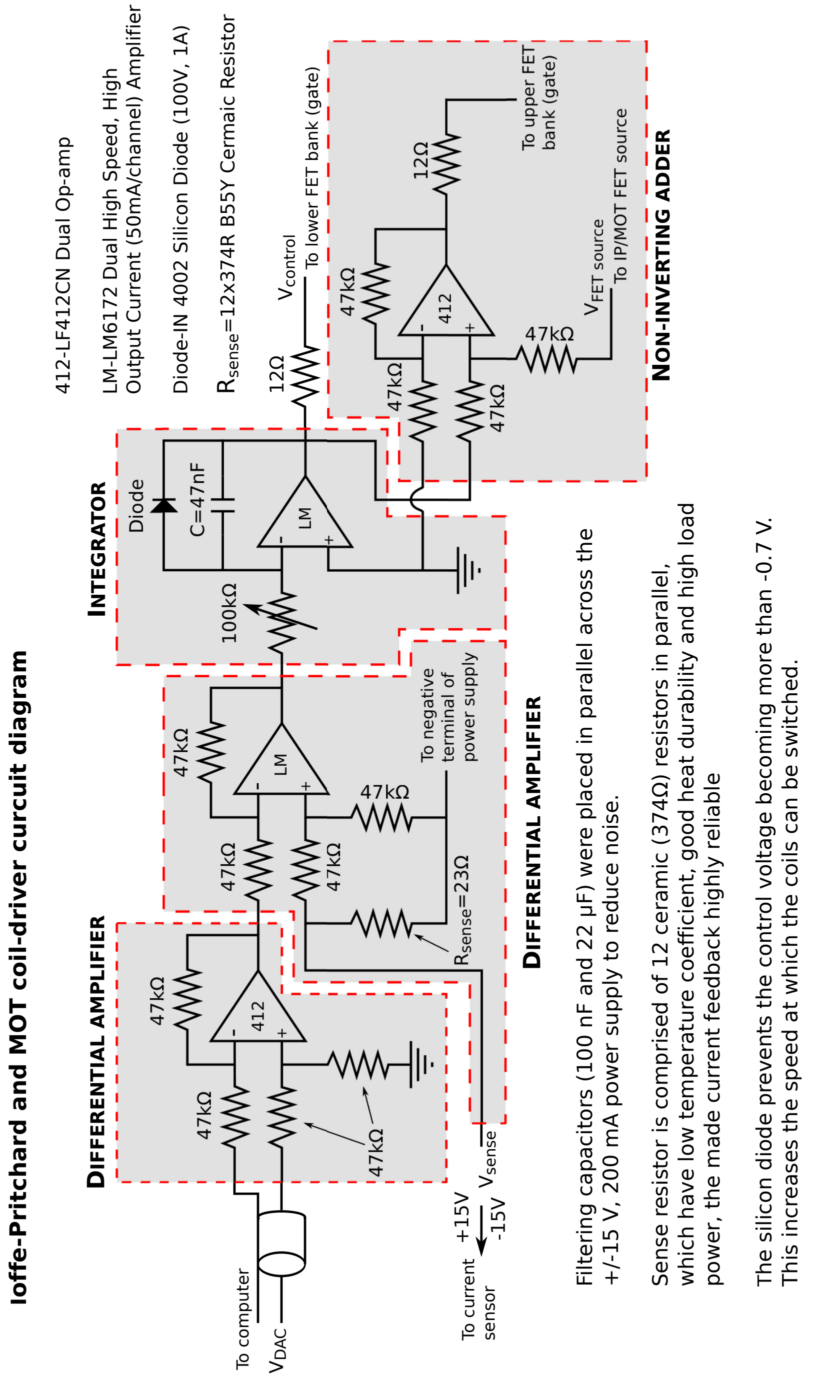

Figure A.2: Circuit diagram for Ioffe-Pritchard and MOT coil-driver.

A.3 The coil-driver circuit

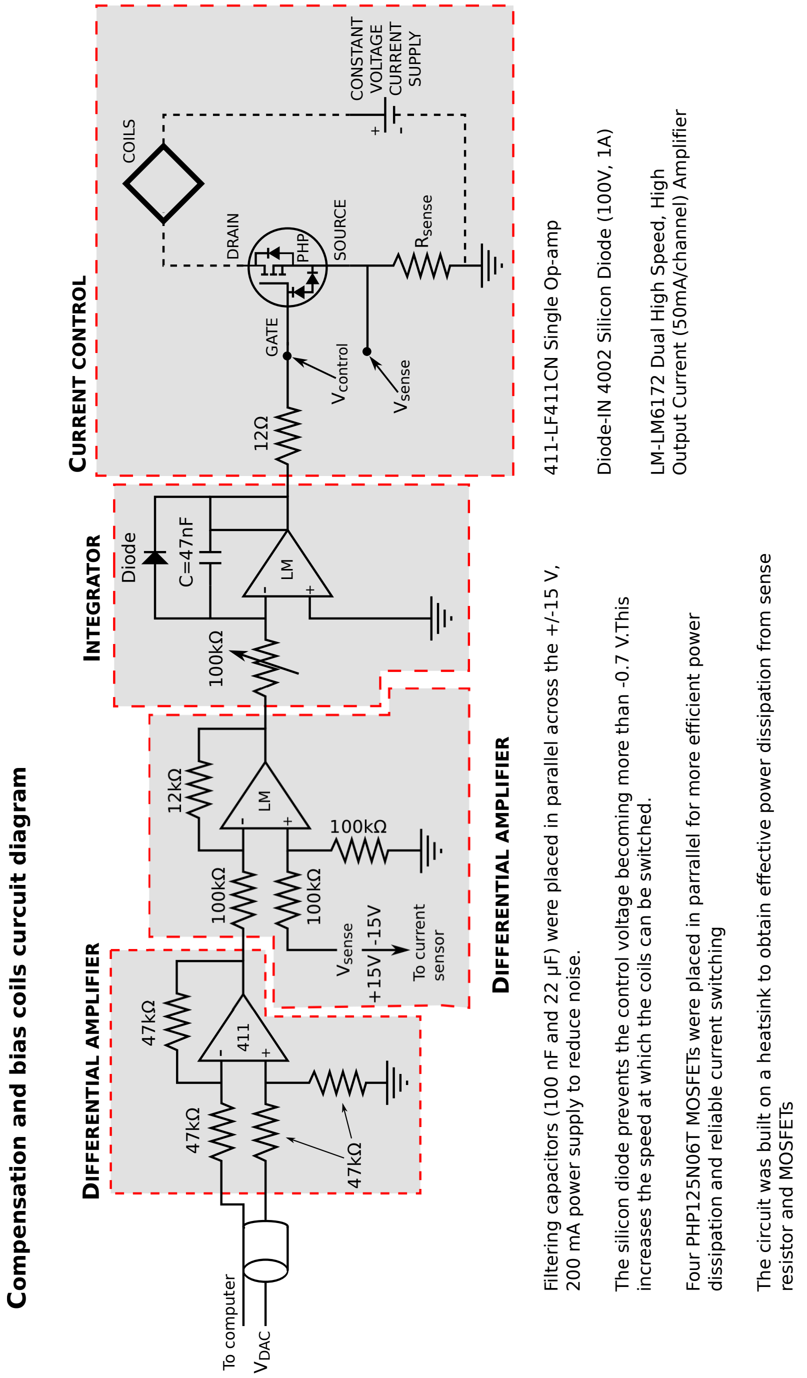

Compensation and bias coils curcuit diagram

411-LF411CN Single Op-amp

Diode-IN 4002 Silicon Diode (100V, 1A)

LM-LM6172 Dual High Speed, High Output Current (50mA/channel) Amplifier

Filtering capacitors (100 nF and 22 µF) were placed in parallel across the +/-15 V, 200 mA power supply to reduce noise.

The silicon diode prevents the control voltage becoming more than -0.7 V.This increases the speed at which the coils can be switched.

Four PHP125N06T MOSFETs were placed in parrallel for more efficient power dissipation and reliable current switching

The circuit was built on a heatsink to obtain effective power dissipation from sense resistor and MOSFETs

Figure A.3: Coil-driver circuit for compensation and bias coils.

Appendix B

RF dressing

The basic principle of magnetic trapping utilises the Zeeman effect, which shifts the energy of a spin state $|m_F\rangle$ by an amount depending on the local magnetic field. Normally a coupling of various $|m_F\rangle$ states is used for RF evaporative cooling to reach the BEC transition but can also be used to create traps for atoms. Instead of using RF fields to eject the hotter atoms from the trap, Zobay and Garraway [104] introduced the idea of dressing the $|m_F\rangle$ states to create new trapping geometries. Figure B.1 presents the basic principle of RF dressing with atoms in a 1D harmonic trap. An RF field will be resonant at two points in space, left and right of the trap minimum. Atoms in the static magnetic trap are dressed by a strong near-resonant RF field. In this case the $|m_F\rangle$ states are no longer the eigenstates, instead the dressed states become the eigenstates of the system, which are a combination of the photons in the RF field and the atom's internal state

On resonance the RF field is resonant at two points (Figure B.1a), in the dressed state regime the bare states cross at these points. The RF field then couples them so that this becomes an anti-crossing and the atoms are trapped in the minima that is formed at this anti-crossing. If the RF field is detuned from resonance the bare states do not cross, however the states are still coupled by the RF field, which pushes them apart. The coupling is strongest at the centre of the trap, this results in the states being pushed further than the surrounding points, which results in a spatially varying coupling. This can also be understood in the following way: when the RF field is detuned it causes an AC stark shift in the trap which is spatially-dependent, i.e. larger stark shift near the centre and smaller at the sides of the trap. Both setups can be used to implement a double-well potential for the atoms, this eliminates the need for a

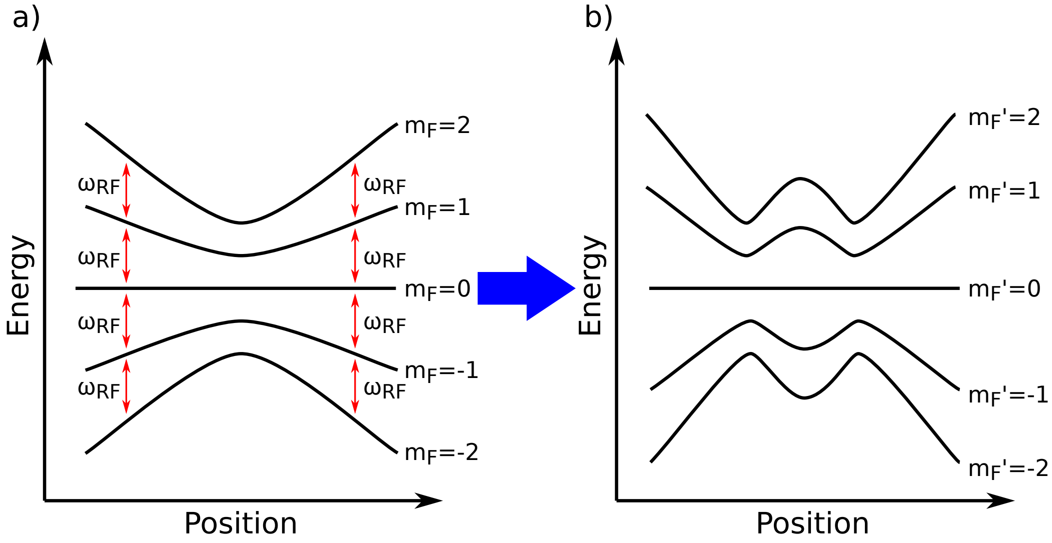

Figure B.1: Adiabatic RF potentials for $F = 2$ system. Coupling between different $|m_F\rangle$ states of atoms in a 1D harmonic magnetic potential. RF field of frequency ω_{RF} is resonant to energy gap between states at two points and when off resonant causes a AC stark shift, which various depending on position. On resonance the states are coupled to each other and the atoms experience a new trap geometry, the so called dressed states, which are labelled $|m_F{}'\rangle$.

optical dipole beam.

Dressed double-well trap interferometers have been achieved on atom chips but never in a macroscopic Ioffe-Pritchard trap. The reason for this is that atom chip trap have extremely high trap frequencies, which lead to the large magnetic field gradients needed to couple the different $|m_F\rangle$ states. However, initial theoretical simulations predict predict that the required magnetic field gradients and coupling strengths can be achieved in the Strathclyde experiment to allow the IP trap to RF dressed and a double-well potential created. Figure B.2 shows the theoretical plots of an harmonic potential with and without the presence of RF dressing, the plots were determined using achievable parameters in the Strathclyde experiment. From the initial simulations it appears that RF dressing is possible in Strathclyde's macroscopic IP trap. Also, the initial separation between the two halves of the condensate will be reduced to at least 15 μm, half of what it is using the optical dipole beam. By reducing the centre-of-mass splitting, then the expansion time needed to obtain the same period fringes reduces, therefore there is less time for the atoms to gain noise which could lead to

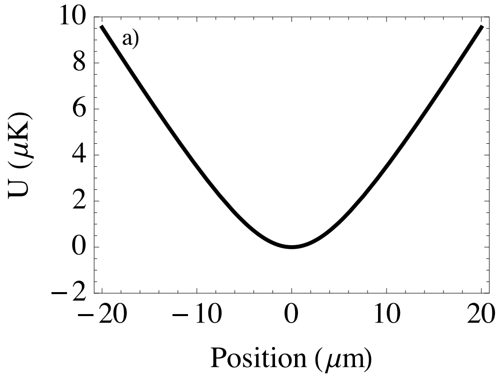

Figure B.2: Theoretical plot of harmonic potential with and without RF dressing. a) presents harmonic IP trap without RF dressing and b) is same harmonic trap trap in the presence of RF dressing. Both plots were determined using achievable parameters in the Strathclyde experiment, this confirmed that using RF dressing to create a double-well potential interferometer is possible.

spatial fluctuations in their final position. Using the modified fringe period formula ($\lambda' = \lambda \sinh(\omega_z t)/\omega_z t$), the time needed to to obtain 41 μm period fringes decreases from 160 ms (40 μm splitting) to 95 ms (15 μm splitting). If the centre-of-mass splitting turns out to be > 15 μm, then this could eradicate the need for the levitation field completely.

Appendix C

Vertical imaging

Having both a vertical and horizontal imaging system will allow all axes of the condensate to be probed and studied, as well as enabling a 3D image of the condensate to be constructed. The vertical imaging system was implemented by picking off light (using a PBS) from the horizontal imaging system and then overlapping it with the vertical MOT beam. Figure C.1 shows a schematic diagram of the vertical imaging's optical setup. Once the condensate is released from the trapping potential it starts to expand and fall under gravity ($1/2gt^2$), this means that the focal position of the first

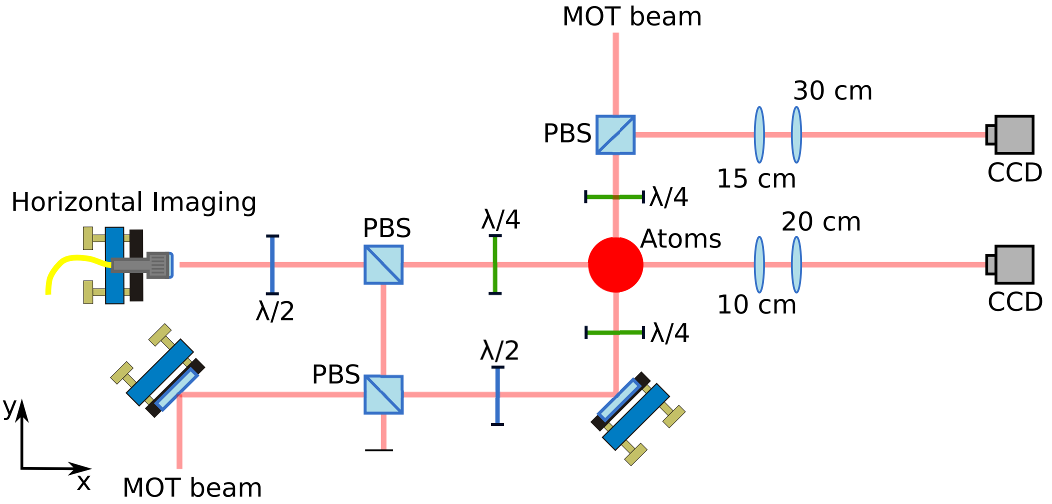

Figure C.1: Schematic diagram of vertical imaging optical setup. Half of the horizontal imaging light is picked off using a PBS and is then overlapped with the vertical MOT beam. The polarisation is set in such a way that the MOT beam is transmitted through the PBS after the atoms and the imaging light is reflected by the same PBS. Both imaging systems use a two lens setup, which results in a magnification equal to two.

lens changes depending on drop time. To account for this the first lens was mounted on a translation stage, which was attached to a micrometer for fine adjustment, and lens position depending on drop time was calibrated. It was calculated that the condensate would drop by 18 mm in 60 ms, using this all drop times in-between could be calculated and the lens position calibrated.

Once the lens position was calibrated and the condensate focussed for all drop times, absorption images were taken in both the horizontal and vertical direction and the resulting profiles compared. From the trapping potential geometry it was expected that the condensates size and width should be the same for both imaging directions. Figure C.2 presents the same condensate imaged in both the horizontal and vertical direction. The width of the condensate was determined from the fit and was found to be 115 μm and 127 μm for the horizontal and vertical direction imaging systems respectively. The difference in the width of the condensate between the imaging systems is contributed to be due to slightly different magnifications. When an absorption image is taken a field must be applied along the imaging axis to ensure the correct polarisation of the imaging light. However, when imaging in both axis, magnetic fields in both directions can't be applied, this results in a drop in optical density in the axis which hasn't had the magnetic field applied. The resulting absorption image of the condensate will have

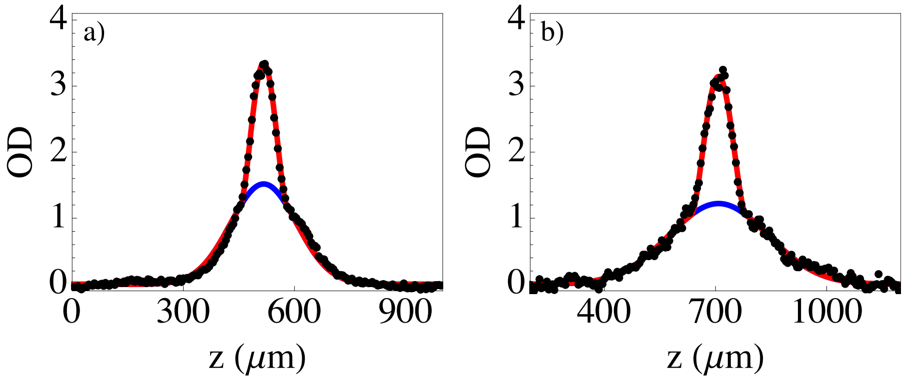

Figure C.2: Density profiles of BEC after in using horizontal and vertical imaging system. a) BEC after 20 ms expansion using horizontal imaging beam and b) same BEC using vertical imaging system. Condensate was fit using Thomas-Fermi+Gaussian distribution and the widths were calculated to be a) 115 μm and b) 127 μm. Difference in the width of the condensate is contributed to slightly different magnification between both imaging systems.

the same parameters (i.e. width, temperature, PSD) but will appear to have a much lower optical density. The apparent reduced optical density can be accounted for by using a scale factor, which once calibrated will allow the true optical density of the condensate to be observed.

The vertical imaging system allows the potential sloshing in the magnetic trap to be studied, and if present be eliminated from the experiment. It also enables the interference fringes from the RF dressed double-well potential to be observed.

References

[1] M. Gong, S. Tewari, and C. Zhang, *BCS-BEC crossover and topological phase transition in 3D spin-orbit coupled degenerate Fermi gases*, Physical Review Letters **107**, 195303 (2011).

[2] K. Baumann, C. Guerlin, F. Brennecke, and T. Esslinger, *Dicke quantum phase transition with a superfluid gas in an optical cavity*, Nature **464**, 1301 (2010).

[3] I. Bloch, J. Dalibard, and W. Zwerger, *Many-body physics with ultracold gases*, Reviews of Modern Physics **80**, 885 (2008).

[4] M. Lewenstein *et al.*, *Ultracold atomic gases in optical lattices: mimicking condensed matter physics and beyond*, Advances in Physics **56**, 243 (2007).

[5] I. Bloch, J. Dalibard, and S. Nascimbène, *Quantum simulations with ultracold quantum gases*, Nature Physics **8**, 267 (2012).

[6] H.-J. Briegel, T. Calarco, D. Jaksch, J. Cirac, and P. Zoller, *Quantum computing with neutral atoms*, Journal of Modern Optics **47**, 415 (2000).

[7] J. J. Cooper, D. W. Hallwood, and J. A. Dunningham, *Entanglement-enhanced atomic gyroscope*, Physical Review A **81**, 043624 (2010).

[8] J. E. Debs *et al.*, *Cold-atom gravimetry with a Bose-Einstein condensate*, Physical Review A **84**, 033610 (2011).

[9] J. Dunningham, K. Burnett, and W. D. Phillips, *Bose–Einstein condensates and precision measurements*, Philosophical Transactions of the Royal Society of London A: Mathematical, Physical and Engineering Sciences **363**, 2165 (2005).

[10] A. Einstein, *Quantentheorie des einatomigen idealen Gases* (Akademie der Wissenshaften, in Kommission bei W. de Gruyter, 1924).

[11] S. N. Bose, *Plancks gesetz und lichtquantenhypothese*, Z. Phys **26**, 178 (1924).

[12] F. Dalfovo, S. Giorgini, L. P. Pitaevskii, and S. Stringari, *Theory of Bose-Einstein condensation in trapped gases*, Reviews of Modern Physics **71**, 463 (1999).

[13] A. Griffin, W. D. Snoke, and S. Stringari, *Bose-Einstein Condensation* (Cambridge University Press, Cambridge, 1996).

[14] W. Ketterle, D. Durfee, and D. Stamper-Kurn, *Making, probing and understanding Bose-Einstein condensates*, arXiv preprint cond-mat/9904034 **5** (1999).

[15] V. Bagnato, D. E. Pritchard, and D. Kleppner, *Bose-Einstein condensation in an external potential*, Physical Review A **35**, 4354 (1987).

[16] J. H. Metcalf and P. van der Straten, *Laser Cooling and Trapping* (SpringerVerlag, New York, 1999).

[17] J. C. Pethick and H. Smith, *Bose-Einstein Condensation in Dilute Gases* (Cambridge Uni. Press, Cambridge, 2002).

[18] T. W. Hänsch and A. L. Schawlow, *Cooling of gases by laser radiation*, Optics Communications **13**, 68 (1975).

[19] S. Chu, L. Hollberg, J. E. Bjorkholm, A. Cable, and A. Ashkin, *Three-dimensional viscous confinement and cooling of atoms by resonance radiation pressure*, Physical Review Letters **55**, 48 (1985).

[20] A. Ashkin, *Trapping of Atoms by Resonance Radiation Pressure*, Physical Review Letters **40**, 729 (1978).

[21] S. Chu, J. E. Bjorkholm, A. Ashkin, and A. Cable, *Experimental Observation of Optically Trapped Atoms*, Physical Review Letters **57**, 314 (1986).

[22] E. L. Raab, M. Prentiss, A. Cable, S. Chu, and D. E. Pritchard, *Trapping of Neutral Sodium Atoms with Radiation Pressure*, Physical Review Letters **59**, 2631 (1987).

[23] D. E. Pritchard, *Cooling neutral atoms in a magnetic trap for precision spectroscopy*, Physical Review Letters **51**, 1336 (1983).

[24] W. Petrich, M. H. Anderson, J. R. Ensher, and E. A. Cornell, *Stable, Tightly Confining Magnetic Trap for Evaporative Cooling of Neutral Atoms*, Physical Review Letters **74**, 3352 (1995).

[25] K. B. Davis, M.-O. Mewes, M. A. Joffe, M. R. Andrews, and W. Ketterle, *Evaporative Cooling of Sodium Atoms*, Physical Review Letters **74**, 5202 (1995).

[26] M. H. Anderson, J. R. Ensher, M. R. Matthews, C. E. Wieman, and E. A. Cornell, *Observation of Bose-Einstein condensation in a dilute atomic vapor*, Science **269**, 198 (1995).

[27] K. B. Davis *et al.*, *Bose-Einstein condensation in a gas of sodium atoms*, Physical Review Letters **75**, 3969 (1995).

[28] D. G. Fried *et al.*, *Bose-Einstein condensation of atomic hydrogen*, Physical Review Letters **81**, 3811 (1998).

[29] A. Robert *et al.*, *A Bose-Einstein condensate of metastable atoms*, Science **292**, 461 (2001).

[30] F. P. Dos Santos *et al.*, *Bose-Einstein condensation of metastable helium*, Physical Review Letters **86**, 3459 (2001).

[31] C. C. Bradley, C. A. Sackett, and R. G. Hulet, *Bose-Einstein Condensation of Lithium: Observation of Limited Condensate Number*, Physical Review Letters **78**, 985 (1997).

[32] G. Roati *et al.*, *K 39 Bose-Einstein Condensate with Tunable Interactions*, Physical Review Letters **99**, 010403 (2007).

[33] S. Kraft, F. Vogt, O. Appel, F. Riehle, and U. Sterr, *Bose-Einstein Condensation of Alkaline Earth Atoms: Ca40*, Physical Review Letters **103**, 130401 (2009).

[34] G. Modugno *et al.*, *Bose-Einstein condensation of potassium atoms by sympathetic cooling*, Science **294**, 1320 (2001).

[35] A. Griesmaier, J. Werner, S. Hensler, J. Stuhler, and T. Pfau, *Bose-Einstein Condensation of Chromium*, Physical Review Letters **94**, 160401 (2005).

[36] S. Stellmer, M. K. Tey, B. Huang, R. Grimm, and F. Schreck, *Bose-Einstein Condensation of Strontium*, Physical Review Letters **103**, 200401 (2009).

[37] Y. N. M. de Escobar *et al.*, *Bose-Einstein Condensation of Sr84*, Physical Review Letters **103**, 200402 (2009).

[38] S. L. Cornish, N. R. Claussen, J. L. Roberts, E. A. Cornell, and C. E. Wieman, *Stable 85Rb Bose-Einstein Condensates with Widely Tunable Interactions*, Physical Review Letters **85**, 1795 (2000).

[39] S. Stellmer, M. K. Tey, R. Grimm, and F. Schreck, *Bose-Einstein condensation of Sr86*, Physical Review A **82**, 041602 (2010).

[40] P. G. Mickelson, Y. N. Martinez de Escobar, M. Yan, B. J. DeSalvo, and T. C. Killian, *Bose-Einstein condensation of Sr88 through sympathetic cooling with Sr87*, Physical Review A **81**, 051601 (2010).

[41] T. Weber, J. Herbig, M. Mark, H.-C. Nägerl, and R. Grimm, *Bose-Einstein condensation of cesium*, Science **299**, 232 (2003).

[42] Y. Tang, N. Q. Burdick, K. Baumann, and B. L. Lev, *Bose-Einstein condensation of 162Dy and 160Dy*, arXiv preprint arXiv:1411.3069 (2014).

[43] M. Lu, N. Q. Burdick, S. H. Youn, and B. L. Lev, *Strongly Dipolar Bose-Einstein Condensate of Dysprosium*, Physical Review Letters **107**, 190401 (2011).

[44] T. Fukuhara, S. Sugawa, Y. Takasu, and Y. Takahashi, *All-optical formation of quantum degenerate mixtures*, Physical Review A **79**, 021601 (2009).

[45] K. Aikawa *et al.*, *Bose-Einstein Condensation of Erbium*, Physical Review Letters **108**, 210401 (2012).

[46] T. Fukuhara, Y. Takasu, M. Kumakura, and Y. Takahashi, *Degenerate Fermi gases of ytterbium*, Physical Review Letters **98**, 030401 (2007).

[47] Y. Takasu *et al.*, *Spin-Singlet Bose-Einstein Condensation of Two-Electron Atoms*, Physical Review Letters **91**, 040404 (2003).

[48] J. Klaers, J. Schmitt, F. Vewinger, and M. Weitz, *Bose-Einstein condensation of photons in an optical microcavity*, Nature **468**, 545 (2010).

[49] S. Inouye *et al.*, *Observation of Feshbach resonances in a Bose–Einstein condensate*, Nature **392**, 151 (1998).

[50] J. Stenger *et al.*, *Strongly Enhanced Inelastic Collisions in a Bose-Einstein Condensate near Feshbach Resonances*, Physical Review Letters **82**, 2422 (1999).

[51] S. Kato, S. Sugawa, K. Shibata, R. Yamamoto, and Y. Takahashi, *Control of Resonant Interaction between Electronic Ground and Excited States*, Physical Review Letters **110**, 173201 (2013).

[52] M. Edwards, P. A. Ruprecht, K. Burnett, R. J. Dodd, and C. W. Clark, *Collective Excitations of Atomic Bose-Einstein Condensates*, Physical Review Letters **77**, 1671 (1996).

[53] D. S. Jin, J. R. Ensher, M. R. Matthews, C. E. Wieman, and E. A. Cornell, *Collective Excitations of a Bose-Einstein Condensate in a Dilute Gas*, Physical Review Letters **77**, 420 (1996).

[54] M.-O. Mewes *et al.*, *Collective Excitations of a Bose-Einstein Condensate in a Magnetic Trap*, Physical Review Letters **77**, 988 (1996).

[55] D. S. Rokhsar, *Vortex Stability and Persistent Currents in Trapped Bose Gases*, Physical Review Letters **79**, 2164 (1997).

[56] M. R. Matthews *et al.*, *Vortices in a Bose-Einstein Condensate*, Physical Review Letters **83**, 2498 (1999).

[57] C. Raman, J. R. Abo-Shaeer, J. M. Vogels, K. Xu, and W. Ketterle, *Vortex Nucleation in a Stirred Bose-Einstein Condensate*, Physical Review Letters **87**, 210402 (2001).

[58] I. Bloch, T. W. Hänsch, and T. Esslinger, *Atom laser with a cw output coupler*, Physical Review Letters **82**, 3008 (1999).

[59] S. Inouye *et al.*, *Phase-coherent amplification of atomic matter waves*, Nature **402**, 641 (1999).

[60] M. Andrews *et al.*, *Direct, nondestructive observation of a Bose condensate*, Science **273**, 84 (1996).

[61] H.-J. Miesner *et al.*, *Bosonic stimulation in the formation of a Bose-Einstein condensate*, Science **279**, 1005 (1998).

[62] C. Ryu *et al.*, *Observation of persistent flow of a Bose-Einstein condensate in a toroidal trap*, Physical Review Letters **99**, 260401 (2007).

[63] A. Ramanathan *et al.*, *Superflow in a Toroidal Bose-Einstein Condensate: An Atom Circuit with a Tunable Weak Link*, Physical Review Letters **106**, 130401 (2011).

[64] M. R. Andrews *et al.*, *Observation of Interference Between Two Bose Condensates*, Science **275**, 637 (1997).

[65] Y. Shin *et al.*, *Atom Interferometry with Bose-Einstein Condensates in a Double-Well Potential*, Physical Review Letters **92**, 050405 (2004).

[66] Y. Shin *et al.*, *Interference of Bose-Einstein condensates split with an atom chip*, Physical Review A **72**, 021604 (2005).

[67] J. A. Dunningham and K. Burnett, *Sub-shot-noise-limited measurements with Bose-Einstein condensates*, Physical Review A **70**, 033601 (2004).

[68] T. Young, *The Bakerian lecture: On the theory of light and colours*, Philosophical transactions of the Royal Society of London , 12 (1802).

[69] J. C. Maxwell, *A dynamical theory of the electromagnetic field*, Philosophical Transactions of the Royal Society of London , 459 (1865).

[70] P. Hariharan, *Optical interferometry*, Reports on Progress in Physics **54**, 339 (1991).

[71] L. d. Broglie, *XXXV. A tentative theory of light quanta*, Philosophical Magazine Series 6 **47**, 446 (1924).

[72] C. Davisson and L. H. Germer, *Diffraction of electrons by a crystal of nickel*, Physical Review **30**, 705 (1927).

[73] G. Thomson, *Experiments on the diffraction of cathode rays*, in *Proceedings of the Royal Society of London A: Mathematical, Physical and Engineering Sciences*, volume 117, pp. 600–609, The Royal Society, 1928.

[74] L. Marton, A. J. Simpson, and A. J. Studdeth, *Electron Interferometer*, Review of Scientific Instruments **25:1099** (1954).

[75] H. Maier-Leibnitz and T. Springer, *Ein interferometer für langsame neutronen*, Zeitschrift für Physik **167**, 386 (1962).

[76] A. D. Cronin, J. Schmiedmayer, and D. E. Pritchard, *Optics and interferometry with atoms and molecules*, Reviews of Modern Physics **81**, 1051 (2009).

[77] D. W. Keith, C. R. Ekstrom, Q. A. Turchette, and D. E. Pritchard, *An interferometer for atoms*, Physical Review Letters **66**, 2693 (1991).

[78] O. Carnal and J. Mlynek, *Young's double-slit experiment with atoms: A simple atom interferometer*, Physical Review Letters **66**, 2689 (1991).

[79] M. Kasevich and S. Chu, *Atomic interferometry using stimulated Raman transitions*, Physical Review Letters **67**, 181 (1991).

[80] F. Riehle, T. Kisters, A. Witte, J. Helmcke, and C. J. Bordé, *Optical Ramsey spectroscopy in a rotating frame: Sagnac effect in a matter-wave interferometer*, Physical Review Letters **67**, 177 (1991).

[81] S. R. Jefferts *et al.*, *Accuracy evaluation of NIST-F1*, Metrologia **39**, 321 (2002).

[82] J. M. McGuirk, M. J. Snadden, and M. A. Kasevich, *Large Area Light-Pulse Atom Interferometry*, Physical Review Letters **85**, 4498 (2000).

[83] S. Gupta, K. Dieckmann, Z. Hadzibabic, and D. E. Pritchard, *Contrast Interferometry using Bose-Einstein Condensates to Measure h/m and α*, Physical Review Letters **89**, 140401 (2002).

[84] M. J. Snadden, J. M. McGuirk, P. Bouyer, K. G. Haritos, and M. A. Kasevich, *Measurement of the Earth's Gravity Gradient with an Atom Interferometer-Based Gravity Gradiometer*, Physical Review Letters **81**, 971 (1998).

[85] H. Müller, A. Peters, and S. Chu, *A precision measurement of the gravitational redshift by the interference of matter waves*, Nature **463**, 926 (2010).

[86] S. Dimopoulos, P. W. Graham, J. M. Hogan, and M. A. Kasevich, *Testing General Relativity with Atom Interferometry*, Physical Review Letters **98**, 111102 (2007).

[87] S.-Y. Lan *et al.*, *A clock directly linking time to a particle's mass*, Science **339**, 554 (2013).

[88] H. Müller, S.-w. Chiow, S. Herrmann, S. Chu, and K.-Y. Chung, *Atom-Interferometry Tests of the Isotropy of Post-Newtonian Gravity*, Physical Review Letters **100**, 031101 (2008).

[89] S. M. Dickerson, J. M. Hogan, A. Sugarbaker, D. M. S. Johnson, and M. A. Kasevich, *Multiaxis Inertial Sensing with Long-Time Point Source Atom Interferometry*, Physical Review Letters **111**, 083001 (2013).

[90] T. L. Gustavson, P. Bouyer, and M. A. Kasevich, *Precision Rotation Measurements with an Atom Interferometer Gyroscope*, Physical Review Letters **78**, 2046 (1997).

[91] A. Lenef *et al.*, *Rotation Sensing with an Atom Interferometer*, Physical Review Letters **78**, 760 (1997).

[92] B. Anderson and M. A. Kasevich, *Macroscopic quantum interference from atomic tunnel arrays*, Science **282**, 1686 (1998).

[93] A. Peters, K. Y. Chung, and S. Chu, *Measurement of gravitational acceleration by dropping atoms*, Nature **400**, 849 (1999).

[94] M. S. Chapman *et al.*, *Photon Scattering from Atoms in an Atom Interferometer: Coherence Lost and Regained*, Physical Review Letters **75**, 3783 (1995).

[95] B. Canuel *et al.*, *Six-Axis Inertial Sensor Using Cold-Atom Interferometry*, Physical Review Letters **97**, 010402 (2006).

[96] T. Müller *et al.*, *A compact dual atom interferometer gyroscope based on laser-cooled rubidium*, The European Physical Journal D **53**, 273 (2009).

[97] C. J. Foot, *Atomic physics* (Oxford University Press, 2004).

[98] T. Gustavson, A. Landragin, and M. Kasevich, *Rotation sensing with a dual atom-interferometer Sagnac gyroscope*, Classical and Quantum Gravity **17**, 2385 (2000).

[99] K. Bongs and K. Sengstock, *Physics with coherent matter waves*, Reports on Progress in Physics **67**, 907 (2004).

[100] E. W. Streed *et al.*, *Large atom number Bose-Einstein condensate machines*, Review of Scientific Instruments **77**, 023106 (2006).

[101] E. Hinds, C. Vale, and M. Boshier, *Two-wire waveguide and interferometer for cold atoms*, Physical Review Letters **86**, 1462 (2001).

[102] I. Lesanovsky, S. Hofferberth, J. Schmiedmayer, and P. Schmelcher, *Manipulation of ultracold atoms in dressed adiabatic radio-frequency potentials*, Physical Review A **74**, 033619 (2006).

[103] T. Schumm *et al.*, *Matter-wave interferometry in a double well on an atom chip*, Nature Physics **1**, 57 (2005).

[104] O. Zobay and B. Garraway, *Two-dimensional atom trapping in field-induced adiabatic potentials*, Physical Review Letters **86**, 1195 (2001).

[105] M. E. Zawadzki, P. F. Griffin, E. Riis, and A. S. Arnold, *Spatial interference from well-separated split condensates*, Physical Review A **81**, 043608 (2010).

[106] Y.-J. Wang *et al.*, *Atom Michelson Interferometer on a Chip Using a Bose-Einstein Condensate*, Physical Review Letters **94**, 090405 (2005).

[107] O. Garcia, B. Deissler, K. J. Hughes, J. M. Reeves, and C. A. Sackett, *Bose-Einstein-condensate interferometer with macroscopic arm separation*, Physical Review A **74**, 031601 (2006).

[108] M. Horikoshi and K. Nakagawa, *Dephasing due to atom-atom interaction in a waveguide interferometer using a Bose-Einstein condensate*, Physical Review A **74**, 031602 (2006).

[109] J. A. Sauer, M. D. Barrett, and M. S. Chapman, *Storage Ring for Neutral Atoms*, Physical Review Letters **87**, 270401 (2001).

[110] J. H. T. Burke and C. A. Sackett, *Scalable Bose-Einstein-condensate Sagnac interferometer in a linear trap*, Physical Review A **80**, 061603 (2009).

[111] S.-Y. Lan, P.-C. Kuan, B. Estey, P. Haslinger, and H. Müller, *Influence of the Coriolis Force in Atom Interferometry*, Physical Review Letters **108**, 090402 (2012).

[112] S. Beattie, S. Moulder, R. J. Fletcher, and Z. Hadzibabic, *Persistent Currents in Spinor Condensates*, Physical Review Letters **110**, 025301 (2013).

[113] S. Moulder, S. Beattie, R. P. Smith, N. Tammuz, and Z. Hadzibabic, *Quantized supercurrent decay in an annular Bose-Einstein condensate*, Physical Review A **86**, 013629 (2012).

[114] S. Gupta, K. W. Murch, K. L. Moore, T. P. Purdy, and D. M. Stamper-Kurn, *Bose-Einstein Condensation in a Circular Waveguide*, Physical Review Letters **95**, 143201 (2005).

[115] A. S. Arnold, C. S. Garvie, and E. Riis, *Large magnetic storage ring for Bose-Einstein condensates*, Physical Review A **73**, 041606 (2006).

[116] K. Henderson, C. Ryu, C. MacCormick, and M. Boshier, *Experimental demonstration of painting arbitrary and dynamic potentials for Bose–Einstein condensates*, New Journal of Physics **11**, 043030 (2009).

[117] I. Lesanovsky and W. von Klitzing, *Time-Averaged Adiabatic Potentials: Versatile Matter-Wave Guides and Atom Traps*, Physical Review Letters **99**, 083001 (2007).

[118] P. F. Griffin, E. Riis, and A. S. Arnold, *Smooth inductively coupled ring trap for atoms*, Physical Review A **77**, 051402 (2008).

[119] J. D. Pritchard, A. N. Dinkelaker, A. S. Arnold, P. F. Griffin, and E. Riis, *Demonstration of an inductively coupled ring trap for cold atoms*, New Journal of Physics **14**, 103047 (2012).

[120] B. E. Sherlock, M. Gildemeister, E. Owen, E. Nugent, and C. J. Foot, *Time-averaged adiabatic ring potential for ultracold atoms*, Physical Review A **83**, 043408 (2011).

[121] W. Heathcote, E. Nugent, B. Sheard, and C. Foot, *A ring trap for ultracold atoms in an RF-dressed state*, New Journal of Physics **10**, 043012 (2008).

[122] D. A. Steck, *Rubidium 87 D line data*, 2001.

[123] M. Matthews *et al.*, *Dynamical response of a Bose-Einstein condensate to a discontinuous change in internal state*, Physical Review Letters **81**, 243 (1998).

[124] Y. Torii, Y. Suzuki, M. Kozuma, and T. Kuga, *Realization of Bose-Einstein condensation in a rubidium vapor using a simple double magneto-optical trap*, in *Lasers and Electro-Optics, 1999. CLEO/Pacific Rim'99. The Pacific Rim Conference on*, volume 3, pp. 608–609, IEEE, 1999.

[125] D. Hall, M. Matthews, J. Ensher, C. Wieman, and E. Cornell, *Dynamics of component separation in a binary mixture of Bose-Einstein condensates*, Physical Review Letters **81**, 1539 (1998).

[126] D. Hall, M. Matthews, C. Wieman, and E. Cornell, *Measurements of relative phase in two-component Bose-Einstein condensates*, Physical Review Letters **81**, 1543 (1998).

[127] B. Anderson, P. Haljan, C. Wieman, and E. Cornell, *Vortex precession in Bose-Einstein condensates: Observations with filled and empty cores*, Physical Review Letters **85**, 2857 (2000).

[128] E. F. Nichols and G. Hull, *A preliminary communication on the pressure of heat and light radiation*, Physical Review **13**, 307 (1901).

[129] R. Frisch, Z. Phys **86**, 42 (1933).

[130] D. Wineland and H. Dehmelt, *Principles of the stored ion calorimeter*, Journal of Applied Physics **46**, 919 (1975).

[131] W. D. Phillips and H. Metcalf, *Laser deceleration of an atomic beam*, Physical Review Letters **48**, 596 (1982).

[132] P. D. Lett *et al.*, *Optical molasses*, Journal of the Optical Society of America B **6**, 2084 (1989).

[133] A. Ashkin, *Acceleration and trapping of particles by radiation pressure*, Physical Review Letters **24**, 156 (1970).

[134] A. Ashkin, *Atomic-beam deflection by resonance-radiation pressure*, Physical Review Letters **25**, 1321 (1970).

[135] F. Reif, *Fundamentals of statistical and thermal physics* (Waveland Press, 2009).

[136] C. S. Adams and E. Riis, *Laser cooling and trapping of neutral atoms*, Progress in Quantum Electronics **21**, 1 (1997).

[137] C. Cohen-Tannoudji, B. Diu, and F. Laloë, *Quantum Mechanics, Vol. I*, I (J. Wiley & Sons, Paris, France, 1977) (1977).

[138] W. Gerlach and O. Stern, *Das magnetische moment des silberatoms*, Zeitschrift für Physik A Hadrons and Nuclei **9**, 353 (1922).

[139] E. A. Hinds and I. G. Hughes, *Magnetic atom optics: mirrors, guides, traps, and chips for atoms*, Journal of Physics D: Applied Physics **32**, R119 (1999).

[140] H. A. Bethe and E. E. Salpeter, *Quantum mechanics of one-and two-electron atoms*volume 168 (Plenum Publishing Corporation New York, 1977).

[141] E. B. Aleksandrov, G. I. Khvostenko, and M. P. Chaika, *Interference of atomic states*, Interference of atomic states Izdatel'stvo Nauka, 256 p. **1** (1991).

[142] A. Corney, *Atomic and laser spectroscopy* (Clarendon Press Oxford, 1978).

[143] A. L. Migdall, J. V. Prodan, W. D. Phillips, T. H. Bergeman, and H. J. Metcalf, *First observation of magnetically trapped neutral atoms*, Physical Review Letters **54**, 2596 (1985).

[144] D. Brink and C. Sukumar, *Majorana spin-flip transitions in a magnetic trap*, Physical Review A **74**, 035401 (2006).

[145] D. Naik and C. Raman, *Optically plugged quadrupole trap for Bose-Einstein condensates*, Physical Review A **71**, 033617 (2005).

[146] V. G. Minogin, J. A. Richmond, and G. I. Opat, *Time-orbiting-potential quadrupole magnetic trap for cold atoms*, Physical Review A **58**, 3138 (1998).

[147] E. Hodby *et al.*, *Bose-Einstein condensation in a stiff TOP trap with adjustable geometry*, Journal of Physics B: Atomic, Molecular and Optical Physics **33**, 4087 (2000).

[148] U. Ernst, A. Marte, F. Schreck, J. Schuster, and G. Rempe, *Bose-Einstein condensation in a pure Ioffe-Pritchard field configuration*, EPL (Europhysics Letters) **41**, 1 (1998).

[149] M.-O. Mewes *et al.*, *Bose-Einstein condensation in a tightly confining dc magnetic trap*, Physical Review Letters **77**, 416 (1996).

[150] Y. Gott, M. Ioffe, and V. Telkovsky, *Nuclear Fusion, 1962 Suppl., Pt. 3*, (1962).

[151] N. R. Thomas, A. C. Wilson, and C. J. Foot, *Double-well magnetic trap for Bose-Einstein condensates*, Physical Review A **65**, 063406 (2002).

[152] A. S. Arnold, *Preparation and Manipulation of an 87Rb Bose-Einstein Condensate*, PhD thesis, University of Sussex, 1999.

[153] R. Lovelace, C. Mehanian, T. Tommila, and D. Lee, *Magnetic confinement of a neutral gas*, Nature **318**, 30 (1985).

[154] H. F. Hess, *Evaporative cooling of magnetically trapped and compressed spin-polarized hydrogen*, Physical Review B **34**, 3476 (1986).

[155] C. S. Adams, H. J. Lee, N. Davidson, M. Kasevich, and S. Chu, *Evaporative cooling in a crossed dipole trap*, Physical Review Letters **74**, 3577 (1995).

[156] K. B. Davis, M.-O. Mewes, and W. Ketterle, *An analytical model for evaporative cooling of atoms*, Applied Physics B **60**, 155 (1995).

[157] O. Luiten, M. Reynolds, and J. Walraven, *Kinetic theory of the evaporative cooling of a trapped gas*, Physical Review A **53**, 381 (1996).

[158] W. Ketterle and N. Van Druten, *Evaporative cooling of trapped atoms*, Advances in Atomic, Molecular, and Optical Physics **37**, 181 (1996).

[159] J. Walraven, *Quantum dynamics of simple systems*, Proceedings of the 44th Scottish University Summer School in Physics (1996).

[160] R. Loudon, *The quantum theory of light* (Oxford university press, 2000).

[161] A. Parkins and D. F. Walls, *The physics of trapped dilute-gas Bose–Einstein condensates*, Physics Reports **303**, 1 (1998).

[162] V. Yukalov, *Basics of Bose-Einstein condensation*, Physics of Particles and Nuclei **42**, 460 (2011).

[163] J. Weiner, V. S. Bagnato, S. Zilio, and P. S. Julienne, *Experiments and theory in cold and ultracold collisions*, Reviews of Modern Physics **71**, 1 (1999).

[164] N. N. Bogoliubov, *On the theory of superfluidity*, J. Phys. (USSR) **11**, 23 (1947).

[165] F. Dalfovo, S. Giorgini, L. P. Pitaevskii, and S. Stringari, *Theory of Bose-Einstein condensation in trapped gases*, Reviews of Modern Physics **71**, 463 (1999).

[166] A. J. Leggett, *Bose-Einstein condensation in the alkali gases: Some fundamental concepts*, Reviews of Modern Physics **73**, 307 (2001).

[167] L. H. Thomas, *The calculation of atomic fields*, in *Mathematical Proceedings of the Cambridge Philosophical Society*, volume 23, pp. 542–548, Cambridge Univ Press, 1927.

[168] E. Fermi, *Un metodo statistico per la determinazione di alcune priorieta dell'atome*, Rend. Accad. Naz. Lincei **6**, 32 (1927).

[169] M. Ueda, *Fundamentals and new frontiers of Bose-Einstein condensation* (World Scientific, 2010).

[170] G. Baym and C. Pethick, *Ground-state properties of magnetically trapped Bose-condensed rubidium gas*, Physical review letters **76**, 6 (1996).

[171] P. Meystre, *Atom optics*volume 33 (Springer Science, 2001).

[172] Y. Castin, *Bose-Einstein condensates in atomic gases: simple theoretical results*, in *Coherent atomic matter waves*, pp. 1–136, Springer, 2001.

[173] Y. Castin and R. Dum, *Bose-Einstein condensates in time dependent traps*, Physical Review Letters **77**, 5315 (1996).

[174] Y. Kagan, E. Surkov, and G. Shlyapnikov, *Evolution of a Bose gas in anisotropic time-dependent traps*, Physical Review A **55**, R18 (1997).

[175] E. P. Gross, *Structure of a quantized vortex in boson systems*, Il Nuovo Cimento Series 10 **20**, 454 (1961).

[176] L. Pitaevskii, *Vortex lines in an imperfect Bose gas*, Sov. Phys. JETP **13**, 451 (1961).

[177] C. Pethick and H. Smith, *Bose-Einstein condensation in dilute gases* (Cambridge university press, 2002).

[178] M.-O. Mewes *et al.*, *Output coupler for Bose-Einstein condensed atoms*, Physical Review Letters **78**, 582 (1997).

[179] M. Greiner, O. Mandel, T. Esslinger, T. W. Hänsch, and I. Bloch, *Quantum phase transition from a superfluid to a Mott insulator in a gas of ultracold atoms*, Nature **415**, 39 (2002).

[180] Z. Hadzibabic, S. Stock, B. Battelier, V. Bretin, and J. Dalibard, *Interference of an array of independent Bose-Einstein condensates*, Physical Review Letters **93**, 180403 (2004).

[181] P. W. Anderson, *Measurement in quantum theory and the problem of complex systems*, in *The Lesson of quantum theory*, volume 1, p. 23, 1986.

[182] J. Javanainen and S. M. Yoo, *Quantum phase of a Bose-Einstein condensate with an arbitrary number of atoms*, Physical Review Letters **76**, 161 (1996).

[183] D. Durfee and W. Ketterle, *Experimental studies of Bose-Einstein condensation*, Optics Express **2**, 299 (1998).

[184] Y. Castin and J. Dalibard, *Relative phase of two Bose-Einstein condensates*, Physical Review A **55**, 4330 (1997).

[185] L. Pitaevskii, S. Stringari, and A. Leggett, *Bose-Einstein condensation*, Physics Today **57**, 74 (2004).

[186] J. Javanainen and M. Wilkens, *Phase and phase diffusion of a split Bose-Einstein condensate*, Physical Review Letters **78**, 4675 (1997).

[187] J. Javanainen and M. Y. Ivanov, *Splitting a trap containing a Bose-Einstein condensate: Atom number fluctuations*, Physical Review A **60**, 2351 (1999).

[188] M. Lewenstein and L. You, *Quantum phase diffusion of a Bose-Einstein condensate*, Physical Review Letters **77**, 3489 (1996).

[189] N. D. Mermin and H. Wagner, *Absence of ferromagnetism or antiferromagnetism in one-or two-dimensional isotropic Heisenberg models*, Physical Review Letters **17**, 1133 (1966).

[190] P. Hohenberg, *Existence of long-range order in one and two dimensions*, Physical Review **158**, 383 (1967).

[191] D. Petrov, G. Shlyapnikov, and J. Walraven, *Regimes of quantum degeneracy in trapped 1D gases*, Physical Review Letters **85**, 3745 (2000).

[192] S. Dettmer *et al.*, *Observation of phase fluctuations in elongated Bose-Einstein condensates*, Physical Review Letters **87**, 160406 (2001).

[193] D. Hellweg *et al.*, *Phase fluctuations in Bose–Einstein condensates*, Applied Physics B **73**, 781 (2001).

[194] F. Gerbier, *Quasi-1D Bose-Einstein condensates in the dimensional crossover regime*, EPL (Europhysics Letters) **66**, 771 (2004).

[195] C. Menotti and S. Stringari, *Collective oscillations of a one-dimensional trapped Bose-Einstein gas*, Physical Review A **66**, 043610 (2002).

[196] J.-N. Fuchs, X. Leyronas, and R. Combescot, *Hydrodynamic modes of a one-dimensional trapped Bose gas*, Physical Review A **68**, 043610 (2003).

[197] V. Dunjko, V. Lorent, and M. Olshanii, *Bosons in cigar-shaped traps: Thomas-Fermi regime, Tonks-Girardeau regime, and in between*, Physical Review Letters **86**, 5413 (2001).

[198] D. Petrov, G. Shlyapnikov, and J. Walraven, *Phase-fluctuating 3D Bose-Einstein condensates in elongated traps*, Physical Review Letters **87**, 050404 (2001).

[199] I. Shvarchuck *et al.*, *Bose-Einstein condensation into nonequilibrium states studied by condensate focusing*, Physical Review Letters **89**, 270404 (2002).

[200] S. Richard *et al.*, *Momentum spectroscopy of 1D phase fluctuations in Bose-Einstein condensates*, Physical review letters **91**, 010405 (2003).

[201] M. Hugbart *et al.*, *Coherence length of an elongated condensate*, The European Physical Journal D-Atomic, Molecular, Optical and Plasma Physics **35**, 155 (2005).

[202] F. Gerbier *et al.*, *Momentum distribution and correlation function of quasicondensates in elongated traps*, Physical Review A **67**, 051602 (2003).

[203] D. Petrov, *Bose-Einstein condensation in low-dimensional trapped gases*, PhD thesis, Van der Waals-Zeeman Institute, 2003.

[204] K. Lindquist, M. Stephens, and C. Wieman, *Experimental and theoretical study of the vapor-cell Zeeman optical trap*, Physical Review A **46**, 4082 (1992).

[205] A. Arnold, J. Wilson, and M. Boshier, *A simple extended-cavity diode laser*, Review of Scientific Instruments **69**, 1236 (1998).

[206] C. E. Wieman and L. Hollberg, *Using diode lasers for atomic physics*, Review of Scientific Instruments **62**, 1 (1991).

[207] P. D. McDowall and M. F. Andersen, *Acousto-optic modulator based frequency stabilized diode laser system for atom trapping*, Review of Scientific Instruments **80**, 053101 (2009).

[208] R. Wyatt and W. Devlin, *10 kHz linewidth 1.5 μm InGaAsP external cavity laser with 55 nm tuning range*, Electronics Letters **19**, 110 (1983).

[209] D. A. Neamen and B. Pevzner, *Semiconductor physics and devices: basic principles*volume 3 (McGraw-Hill New York, 2003).

[210] K. MacAdam, A. Steinbach, and C. Wieman, *A narrow-band tunable diode laser system with grating feedback, and a saturated absorption spectrometer for Cs and Rb*, American Journal of Physics **60**, 1098 (1992).

[211] W. Demtröder, *Laser spectroscopy*volume 3 (Springer, 1982).

[212] D. A. Smith and I. G. Hughes, *The role of hyperfine pumping in multilevel systems exhibiting saturated absorption*, American Journal of Physics **72**, 631 (2004).

[213] C. Pearman *et al.*, *Polarization spectroscopy of a closed atomic transition: applications to laser frequency locking*, Journal of Physics B: Atomic, Molecular and Optical Physics **35**, 5141 (2002).

[214] K. Weatherill *et al.*, *A versatile and reliably reusable ultrahigh vacuum viewport*, Review of Scientific Instruments **80**, 026105 (2009).

[215] K. Gibble, S. Chang, and R. Legere, *Direct observation of s-wave atomic collisions*, Physical Review Letters **75**, 2666 (1995).

[216] U. D. Rapol, A. Wasan, and V. Natarajan, *Loading of a Rb magneto-optic trap from a getter source*, Physical Review A **64**, 023402 (2001).

[217] C. Wieman, G. Flowers, and S. Gilbert, *Inexpensive laser cooling and trapping experiment for undergraduate laboratories*, American Journal of Physics **63**, 317 (1995).

[218] K. O'Hara *et al.*, *Ultrastable CO 2 laser trapping of lithium fermions*, Physical Review Letters **82**, 4204 (1999).

[219] C. Shuai *et al.*, *Analysis of Runaway Evaporation and Bose–Einstein Condensation by Time-of-Flight Absorption Imaging*, Chinese Physics Letters **21**, 2105 (2004).

[220] R. Grimm, M. Weidemüller, and Y. B. Ovchinnikov, *Optical dipole traps for neutral atoms*, Advances in Atomic, Molecular, and Optical Physics **42**, 95 (2000).

[221] S. Schnelle, E. Van Ooijen, M. Davis, N. Heckenberg, and H. Rubinsztein-Dunlop, *Versatile two-dimensional potentials for ultra-cold atoms*, Optics express **16**, 1405 (2008).

[222] R. Onofrio *et al.*, *Surface excitations of a Bose-Einstein condensate*, Physical Review Letters **84**, 810 (2000).

[223] N. Houston, E. Riis, and A. Arnold, *Reproducible dynamic dark ring lattices for ultracold atoms*, Journal of Physics B: Atomic, Molecular and Optical Physics **41**, 211001 (2008).

[224] G.-B. Jo *et al.*, *Long phase coherence time and number squeezing of two Bose-Einstein condensates on an atom chip*, Physical Review Letters **98**, 030407 (2007).

[225] D. Han, M. T. DePue, and D. S. Weiss, *Loading and compressing Cs atoms in a very far-off-resonant light trap*, Physical Review A **63**, 023405 (2001).

[226] I. Bloch, M. Köhl, M. Greiner, T. W. Hänsch, and T. Esslinger, *Optics with an atom laser beam*, Physical Review Letters **87**, 030401 (2001).

[227] G. Kaiser, *A friendly guide to wavelets* (Springer Science & Business Media, 2010).

[228] C. E. Heil and D. F. Walnut, *Continuous and discrete wavelet transforms*, Society for Industrial and Applied Mathematics Review **31**, 628 (1989).

[229] M. Rahman, *Applications of Fourier transforms to generalized functions* (WIT Press, 2011).

[230] H. F. Talbot, *LXXVI. Facts relating to optical science. No. IV*, The London and Edinburgh Philosophical Magazine and Journal of Science **9**, 401 (1836).

[231] J. Wen, Y. Zhang, and M. Xiao, *The Talbot effect: recent advances in classical optics, nonlinear optics, and quantum optics*, Advances in Optics and Photonics **5**, 83 (2013).

[232] L. Rayleigh, *XXV. On copying diffraction-gratings, and on some phenomena connected therewith*, The London, Edinburgh, and Dublin Philosophical Magazine and Journal of Science **11**, 196 (1881).

[233] M. V. Berry and S. Klein, *Integer, fractional and fractal Talbot effects*, Journal of Modern Optics **43**, 2139 (1996).

[234] K. Patorski, *The Self-Imaging Phenomenon and its Applications*, Progress in Optics **27**, 1 (1989).

[235] J. Clauser and M. Reinsch, *New theoretical and experimental results in Fresnel optics with applications to matter-wave and X-ray interferometry*, Applied Physics B **54**, 380 (1992).

[236] O. Carnal, Q. Turchette, and H. Kimble, *Near-field imaging with two transmission gratings for submicrometer localization of atoms*, Physical Review A **51**, 3079 (1995).

[237] K. Banaszek, K. Wodkiewicz, and W. P. Schleich, *Fractional Talbot effect in phase space: A compact summation formula*, Optics Express **2**, 169 (1998).

[238] E. Lau, *Interference phenomenon on double gratings*, Ann. Phys **6**, 417 (1948).

[239] J. F. Clauser and S. Li, *Talbot-vonLau atom interferometry with cold slow potassium*, Physical Review A **49**, R2213 (1994).

[240] B. Brezger *et al.*, *Matter-wave interferometer for large molecules*, Physical Review Letters **88**, 100404 (2002).

[241] S. Gerlich *et al.*, *A Kapitza–Dirac–Talbot–Lau interferometer for highly polarizable molecules*, Nature Physics **3**, 711 (2007).

[242] M. S. Chapman *et al.*, *Near-field imaging of atom diffraction gratings: The atomic Talbot effect*, Physical Review A **51**, R14 (1995).

[243] S. Nowak, C. Kurtsiefer, T. Pfau, and C. David, *High-order Talbot fringes for atomic matter waves*, Optics Letters **22**, 1430 (1997).

[244] L. Deng *et al.*, *Temporal, matter-wave-dispersion Talbot effect*, Physical Review Letters **83**, 5407 (1999).

[245] M. J. Mark *et al.*, *Demonstration of the temporal matter-wave Talbot effect for trapped matter waves*, New Journal of Physics **13**, 085008 (2011).

[246] G. Labeyrie *et al.*, *Optomechanical self-structuring in a cold atomic gas*, Nature Photonics **8**, 321 (2014).

[247] A. McDonald, G. McConnell, D. C. Cox, E. Riis, and P. F. Griffin, *3D mapping of intensity field about the focus of a micrometer scale parabolic mirror*, Optics Express **23**, 2375 (2015).

[248] L. Novotny and B. Hecht, *Principles of nano-optics* (Cambridge university press, 2012).

[249] J. W. Goodman *et al.*, *Introduction to Fourier optics*volume 2 (McGraw-hill New York, 1968).

[250] M. E. Zawadzki, *Bose–Einstein condensate manipulation and interferometry*, PhD thesis, University of Strathclyde, Glasgow, 2010.

[251] S. Hofferberth, I. Lesanovsky, B. Fischer, J. Verdu, and J. Schmiedmayer, *Radiofrequency-dressed-state potentials for neutral atoms*, Nature Physics **2**, 710 (2006).

[252] T. Berrada *et al.*, *Integrated Mach–Zehnder interferometer for Bose–Einstein condensates*, Nature Communications **4** (2013).

[253] G.-B. Jo *et al.*, *Matter-wave interferometry with phase fluctuating bose-einstein condensates*, Physical Review Letters **99**, 240406 (2007).

[254] D. Kadio, M. Gajda, and K. Rzażewski, *Phase fluctuations of a Bose-Einstein condensate in low-dimensional geometry*, Physical Review A **72**, 013607 (2005).

[255] H.-P. Stimming, N. Mauser, J. Schmiedmayer, and I. Mazets, *Dephasing in coherently split quasicondensates*, Physical Review A **83**, 023618 (2011).

[256] R. Scott, D. Hutchinson, T. Judd, and T. Fromhold, *Quantifying finite-temperature effects in atom-chip interferometry of Bose-Einstein condensates*, Physical Review A **79**, 063624 (2009).

[257] Y. Hao and S. Chen, *Density-functional theory of two-component Bose gases in one-dimensional harmonic traps*, Physical Review A **80**, 043608 (2009).

[258] C. H. Carson, Y. Zhai, P. F. Griffin, E. Riis, and A. S. Arnold, *Talbot-Enhanced Maximum-Contrast Condensate Interference*, in preparation (2015).

[259] Y. Zhai, C. H. Carson, P. F. Griffin, E. Riis, and A. S. Arnold, *Regular phase fluctuations in an elongated Bose-Einstein condensate*, in preparation (2015).